HYBRID METAL OXIDE NANOARRAYS: FABRICATION, PROPERTIES AND ENERGY CONVERSION APPLICATIONS

BY

IBRAHIM

A Dissertation Presented to the

DEANSHIP OF GRADUATE STUDIES

KING FAHD UNIVERSITY OF PETROLEUM & MINERALS

DHAHRAN, SAUDI ARABIA

In Partial Fulfillment of the

Requirements for the Degree of

DOCTOR OF PHILOSOPHY

In

CHEMISTRY

APRIL 2018

KING FAHD UNIVERSITY OF PETROLEUM & MINERALS

DHAHRAN- 31261, SAUDI ARABIA

DEANSHIP OF GRADUATE STUDIES

This thesis, written by **IBRAHIM** under the direction his thesis advisor and approved by his thesis committee, has been presented and accepted by the Dean of Graduate Studies, in partial fulfillment of the requirements for the degree of **DOCTOR OF PHILOSOPHY IN CHEMISTRY.**

Dr. Ahsanulhaq Qurashi
(Advisor)

3/5/2018

Dr. Abdulaziz Al-Saadi
Department Chairman

Dr. Anvarhusein Isab
(Member)

Dr. Salam A. Zummo
Dean of Graduate Studies

Dr. Nisar Ullah
(Member)

٨/٥/١٩

Date

Dr. Abdallah Abulkibash
(Member)

Dr. Mazen Mohammad Khaled
(Member)

DEDICATED TO MY BELOVED WIFE (ATIA IBRAHIM), ADORABLE KIDS (MALAIKA, AAHEL AND AAYAN), AND HONOURABLE PARENTS

ACKNOWLEDGMENTS

Writing Ph.D. dissertation was a long journey and many important life events and people were associated with this. During these years, I was thoroughly supported by my family, friends, colleagues, and teachers, where needed. I am grateful to my siblings and family members for provided me moral and emotional support throughout.

I would like to express my special appreciation and thanks to my Ph.D. dissertation advisor Dr. AHSAN-UL-HAQ QURASHI, you have been a tremendous mentor for me, and I am giving you full credit for transforming me to a complete researcher and taught me the basic skills and ethics of research. Your advice on both research as well as on my career have been priceless. I would also like to thank Prof. ABDALLAH ABULKIBASH, Prof. ANVARHUSSEIN ISAB, Prof. NISAR ULLAH and Dr. MAZEN KHALED for serving as my committee members even at hardship. I want to thank you for letting my defense be an enjoyable moment, and for your brilliant comments and suggestions. I would like to extend my thank to Dr. ZAIN H. YAMANI (Director of CENT, KFUPM) and Dr. ABDUL AZIZ AL-SAADI (Chairman of Chemistry Department, KFUPM) for providing me sufficient support during my experimental work in the form of various research facilities.

I would also like to appreciate the efforts and support of my friends, especially Dr. SHAHID ALI, Dr. MUHAMMAD MANSHA, and Mr. IBRAR AHMAD. I like to express deep love for my sweet kids MALAIKA IBRAHIM, AAHEL IBRAHIM, AAYAN IBRAHIM, and PARENTS. Last but not least, I would like to express heartiest appreciation to my beloved wife ATIA IBRAHIM, who motivated me towards this definite goal of my life from the very start i.e. to be a Doctor of Philosophy (Ph.D.)..

TABLE OF CONTENTS

LIST OF TABLES

LIST OF FIGURES

LIST OF ABBREVIATIONS

1D	:	One dimensional
ALD	:	Atomic LASER deposition
BTU	:	British thermal unit
CB	:	Conduction band
CV	:	Cyclic voltammetry
EDS	:	Energy dispersion spectroscopy
EIS	:	Electronic impedance spectroscopy
FESEM	:	Field emission scanning electron microscopy
FTIR	:	Fourier transform infrared
LSPR	:	Localized surface plasmon resonance
LSV	:	Linear sweep voltammetry
NAs	:	Nanoarrays
NPs	:	Nanoparticles
NRE	:	Normal hydrogen electrode
NRs	:	Nanorods
NTS	:	Nanotubes
NWAs	:	Nanowire arrays
NWs	:	Nanowires
PEC	:	Photoelectrochemical
PIRET	:	Plasmon-induced resonance energy transfer
PL	:	Photoluminescence

PVDF	**:**	Polyvinylidene fluoride
rGO or RGO	**:**	Reduced graphene oxide
RHE	**:**	Standard hydrogen electrode
SCE	**:**	Saturated calomel electrode
STH	**:**	Solar to hydrogen efficiency
US-EIA	**:**	United States energy information administration
UV-Vis/DRS	**:**	UV-Vis/diffuse reflectance spectroscopy
VB	**:**	Valence band
XPS	**:**	X-ray photoelectron spectroscopy
XRD	**:**	X-ray diffraction

ABSTRACT

Full Name : Ibrahim

Thesis Title : Hybrid Metal Oxide Nanoarrays: Fabrication, Properties and Energy Conversion Applications

Major Field : Chemistry

Date of Degree : April 2018

Alternative energy generation is an evolving field of research to meet the future energy demands and environmental sustainability, as the fossil fuels burning caused tremendous anthropogenic devastations, lately. Therefore, the main objective of this Ph.D. dissertation is to develop advance heterostructure and hybrid nanoarrays (NAs) materials for energy conversion applications. We especially explored the photoelectrochemical (PEC) water splitting characteristics of various NAs, which were directly fabricated on the self-supported photoelectrode. The potential materials choose for this purpose include Ag/α.Fe_2O_3/TiO_2, RGO/ZnO, GaON/ZnO, RGO/ZnO/PVDF, and Au/In_2O_3. Ag/α.Fe_2O_3/TiO_2, and Au/In_2O_3 NAs were developed by modified electrochemical anodization technique. Whereas RGO/ZnO, GaON/ZnO, RGO/ZnO/PVDF NAs have been synthesized by sonochemical assisted wet chemistry methods. Various characterization techniques were applied to explore the physicochemical properties. The morphological features were investigated using a field emission scanning electron microscopy (FESEM). Energy dispersion spectroscopy (EDS or EDX) and X-ray photoelectron spectroscopy (XPS) used to determine chemical states and bonding, elemental confirmation, and distribution of the constituent elements. X-ray diffraction

(XRD) analysis was performed to investigate the crystallinity, phase, and facet arrangement of the NAs. Fourier transform infrared (FTIR) and Raman spectroscopies were utilized to study the vibrational bands and phonon modes. The photoluminescence (PL) and UV-Vis/diffuse reflectance spectroscopy (DRS) were found useful to explore the optoelectronic behaviors of the NAs such as the charge recombination behavior of photoinduced electrons/holes, optical band gaps and bands positions, respectively. The electrochemical techniques such as cyclic voltammetry (CV), linear sweep voltammetry (LSV), chronoamperometry (I-t), electronic impedance spectroscopy (Nyquist plot) were used to measure the performance of the as-synthesized NAs for energy harvesting applications in terms of photocurrent densities (mA/cm^2), stability, charge transfer capacity and solar to hydrogen (STH) efficiencies. Additionally, the elastic RGO/ZnO/PVDF NAs were also tested for piezoelectric applications via oscilloscope and related techniques. Finally, we also proposed the respective mechanisms for the as-synthesized heterostructure NAs systems for each application with literature and experimental support. The overall research was performed at the lab scale.

ملخص الرسالة

الاسم الكامل: ابراهيم

عنوان الرسالة: أكاسيد المعادن الهجينة ذات المصفوفات النانوية : تصميمها، خصائصها ، وتطبيقات تحويل الطاقة

التخصص: الكيمياء

تاريخ الدرجة العلمية: ابريل 2018

توليد الطاقة من مصادر بديلة يعتبر مجال بحث قيد التطوير ليلاقي متطلبات الطاقة والبيئة المستدامة، بما ان حرق الوقود الاحفوري يسبب دمارا هائلا بسبب التلوث. لذلك الهدف الاساسي من بحث الدكتوراة هذا هو تطوير مواد ذو تركيب غيرمتجانس و مصفوفات نانوية هجينة لتطبيقات تحويل الطاقة. ولقد تم استكشاف تحديدا انقسام المائ الكهروضوئي لعدة مواد نانوية، التي تم تصميمها على قطب ضوئي كداعم ذاتي. المواد المحتملة المختاره لهذا الغرض تتضمن Au/In_2O_3 و$Ag/\alpha.Fe_2O_3/TiO_2$, RGO/ZnO, GaON/ZnO, RGO/ZnO/PVDF, Au/In_2O_3 NAs و$Ag/\alpha.Fe_2O_3/TiO_2$, تم تطوريها بتقنية الانود الكهروكيميائية المعدلة بينما Whereas RGO/ZnO, GaON/ZnO, RGO/ZnO/PVDF NAs تم تصنيعها بالطرق الكيميائية الرطبة المعززة بتقنية الصونوكيميائية. تم تطبيق عدة تقنيات تشخيص لاستكشاف الخواص الفيزوكيميائية. تم التحقق من الخواص الشكلية باستخدام المجهر الماسح الضوئي انبعاثي المجال، تم استخدام مطيافية الطاقة المتشتتة ومطيافية الاشعة السينية للفوتو الكترون لتحديد الحالة و الروابط الكيمايئية، التاكد من العناصر والتوزيع المتماثل للعناصر. تم اجراء تحليل حيود الأشعة السينية للتحقق من التبلر، الطور و ترتيب الوجوه للمواد النانوية. تم استخدام مطيافية الاشعة الحمراء و

رامان لدراسة الرواط الاهتزازية واوضاع فونون. من المفيد ايضا دراسة التلالؤ الضوئي و مطيافية الانتشار الانعكاسي للاشعة فوق البنفسجية-والاشعة المرئية لاستكشاف الخواص الضوئية الالكترونية للمواد النانوية مثل سلوك اتحاد الشحنة ل الكترون/الفجوة، مسافة الحزمة الصوئية و اماكن الحزمة. تم استخدام تقنيات كهروكيمائية مثل الفولتية الدورية، الفولتية الخطية ، الكرونوامبيرية و مطيافية المقاومة الالكترونية لدراسة اداء المواد النانوية لتطبيقات تجميع الطاقة على شكل كثافة تيار ضوئي (ملي امبير/ سم^2)، ثباتية، انتقال شحنة سعوي و كفاءة طاقة شمسية الى هيدروجين. بالاضافة الى ذلك تم اختبار RGO/ZnO/PVDF NAs المرن لتطبيقات البيزوكهربية عن طريق راسم الذبذبات و تقنيات ذات صلة. و اخيرا قمنا باقتراح ميكيانيكة للمواد النانوية المحضرة لكل تطبيق مع مسح ادبي وتجارب داعمة. ولقد تم كل هذا العمل البحثي على المستوى المعملي.

CHAPTER 1

INTRODUCTION

Renewable energy harvesting by using alternative sources is the emerging field of research due to its potential in the future energy industries and environmental sustainability. Fossil fuels still consider the primary fuel and the United States energy information administration (US-EIA) guesstimates in their report published in April 2017, that until late 2016, the primary energy sources comprised of coal 15 %, natural gas 29 % and petroleum 37 % nuclear electric power 9% amounting to approximately 90% share. The remaining 10% dedicated to renewable energy sources including energy from biomass, hydrothermal, geothermal and solar (Figure 1). Among these sources, solar energy harvesting is considering the most feasible way to generate energy due to its limited environmental hazards and abundant availability of the solar radiations on earth.

1.1 Renewable Energy on the Rise

In last few decades, immense interest developed in the field of renewable energy. Figure 2(a) indicates that in the early 1990s the renewable energy generation was approximately 30 quadrillions British unit thermal (BTU), which now stands at 70 quadrillions BTU and expected to jump at 130 quadrillions BTU approximately until 2014. Similarly, Figure 2(b) shows the research interest in the solar energy sector over the years. The data extracted from Scopus indicated that the number of research articles significantly

increased since 2000. These findings suggest that scientists are keen towards the development of renewable and solar energy devices to fulfill the future energy requirement.

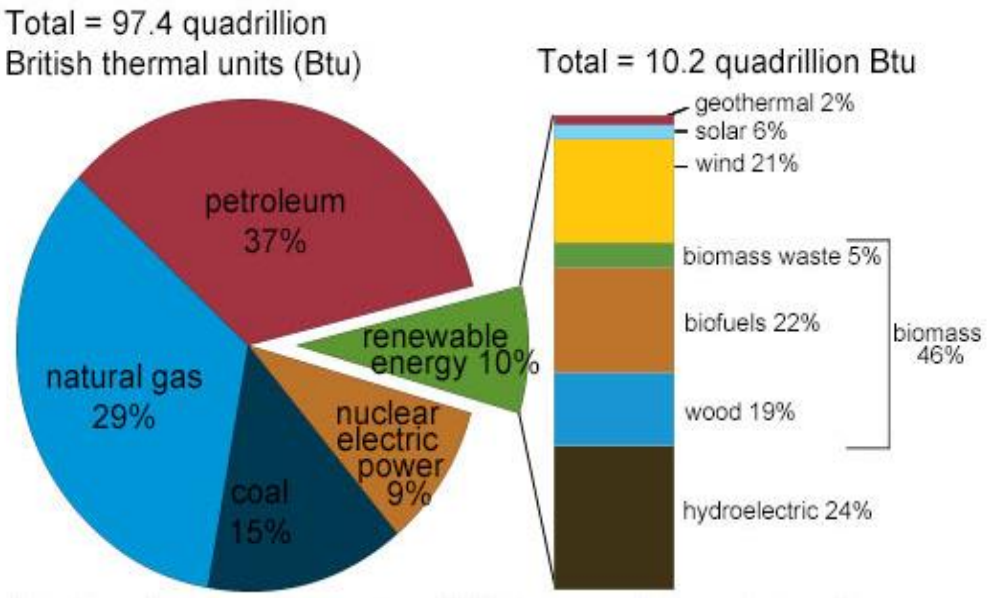

Figure 1: U.S. energy consumption by energy source for the year 2016 (Source: U.S. Energy Information Administration, Monthly Energy Review)

https://www.eia.gov/energyexplained/?page=us_energy_home, data retrieved on 02/12/2017

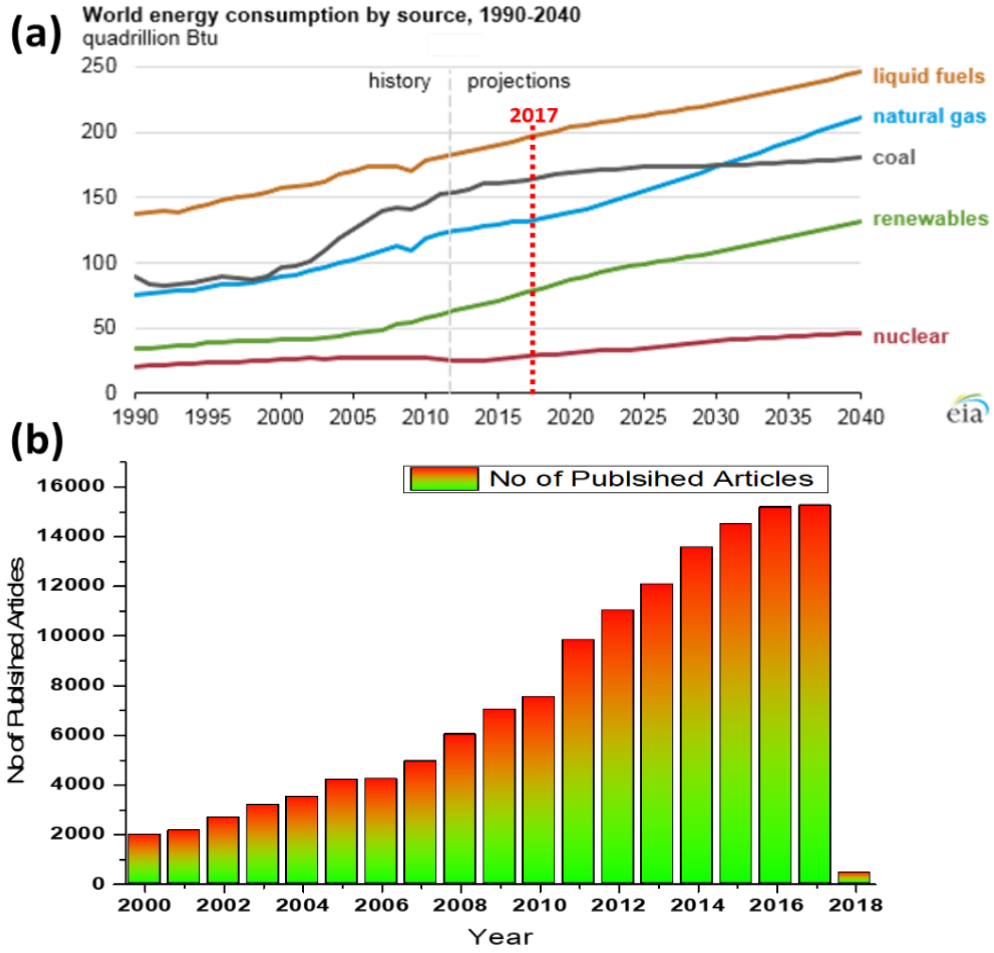

Figure 2: (a) Various energy sources consumption by the World: 1990-2014 (Source: U.S. Energy Information Administration, International Energy Outlook 2016), (b) Yearly publications using keyword solar energy (data extracted from Scopus 02/12/2017)

Industries have adopted certain protocols for energy harvesting such as energy generation from biomass, wind, hydrothermal and solar sources. Among these solar is considered more environmentally benign as it caused limited anthropogenic effects. Water and solar energy can be effectively used to generate energy in various ways. Both sources abundantly exist and therefore need to be utilized in the more proper way for energy applications. Water is composed of two potentially exceptional fuels i.e. hydrogen and oxygen. However, the splitting of water is commercially very challenging as it requires high energy both thermally and electrically. Depend on the nature of the catalyst the thermal water splitting needs high temperature ranges from 500 to 2000 ^{o}C. Additionally, there are a lot of chemical reactions involved and sophisticated reaction reactors are required, which can sustain this high amount of heat. Moreover, the heat generated in this process could contribute to environmental hazards. On the other hand, electrochemical water splitting also requires high voltage. The thermodynamic water splitting requires 1.23 V theoretical energy input. Therefore, researchers are now using solar-driven electrochemical approach to achieve hydrogen and oxygen fuel from water splitting.

1.2 Solar Energy: A great substitute to conventional energy sources

Sunlight offers a considerable alternative to fulfill the require global energy demands. By developing successful tools for solar energy harvesting, the lethal environmental impact can be encounter. Solar energy is readily available, inexhaustible and decentralized natural resource for the mankind and this world. There is as much as solar radiations reaching the earth, whose magnitude is averagely equivalent to the power of 130 million 500 MW power plants at each instant [1]. Additionally, the solar spectrum in Figure (3) shows that the spectrum is majorly occupied by the UV (7%), Visible (53%) and IR

region (34%) regions [2]. However, it is quite challenging to use this energy in a more appropriate manner like fossil fuels. Industries based on solar energy utilization is still in its initial stages and a lot of work has to be done to achieve the ultimate means by which we can store, carry and convert this energy efficiently. The researchers are trying to develop solar harvesting devices, which could have high efficiency and cost friendly.

1.2.1 Photoelectrochemical (PEC) Water Splitting

Enhanced photoelectrochemical (PEC) water splitting into usable hydrogen has already knocked the industrial doors, that not only provide green fuel in the forms of hydrogen and oxygen but also pollution free [3]. Jia et al. already achieved Solar to hydrogen efficiency of 30%, which is quite significant [4]. The main requirement for the accomplishment of PEC water splitting, we need viable and cheaper electric cell, which contain electrodes and suitable electrolyte, a solar source and a potentiated to provide artificial solar radiations and required potential, respectively. The working electrode is the one, where we need to deposit the engineered photoactive materials i.e. semiconductors, where water splitting take place on its interface.

Fujishima et al. initially described solar-driven water splitting via TiO_2 (worked as working electrode) [5]. After their discovery, a large number of research groups attracted to this field and utilized many approaches to split water in the visible regime of light. PEC water splitting photocells require semiconductor nanostructures that are gifted with (i) swift charge transfer at a semiconductor/electrolytic solution interface (ii) display longstanding stability and (iii) can competently captivate a large percentage of the solar spectrum, especially the visible region.

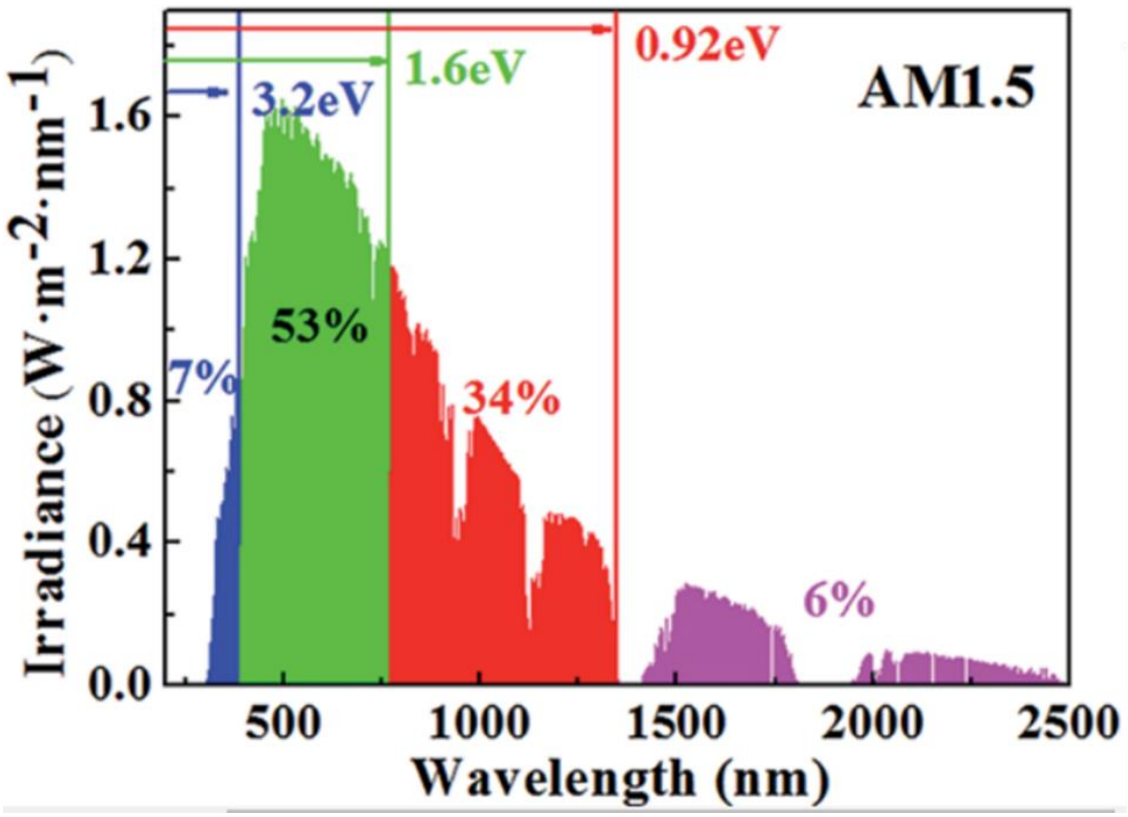

Figure 3: Solar spectrum and distribution of different regions; UV (blue), Visible (green), IR (red) and others (purple)

The water splitting leads into hydrogen (H_2) and oxygen (O_2) with the combined effect of solar light and current, and therefore called PEC water splitting. It is an arduous process and thermodynamic free energy change ($\Delta G°$) for one water molecule to split into the final product i.e. hydrogen and oxygen, is +237 kJ/mol. The positive $\Delta G°$ indicated that the reaction is nonspontaneous, and we have to supply this energy to the system. This energy can be converted to electron Volts (eV) by using Nernst equation (1) i.e. ~ 1.23 eV [6].

$$\Delta G° = - n F E° \quad (1.1)$$

Thus, $\Delta E°$ = 1.23 eV energy is required per electron transferred, which is very high. 1.23Ve can be converted to wavelength by simple mathematical calculations as follow (equation 2 and 3).

$$E° = h\nu = hc/\lambda \quad (1.2)$$

$$\lambda = hc/E° \quad (1.3)$$

$$\lambda = 1239.8 \text{ eV.nm} / 1.23 \text{ eV} = \sim 1008 \text{ nm}$$

Thus, for effective water splitting with solar light alone, ~1000 nm of energy is required, and the semiconductor should have the absorption capacity in this range. The water splitting reaction takes place as follow.

$2H_2O\ (I) \longrightarrow 4H^+ + 4e^- + O_{2\ (g)}$ Oxygen Evolution Reaction (OER) at 0.82 V

$4H^+ + 4e^- \longrightarrow 2H_2\ (g)$ Hydrogen Evolution Reaction (HER) at -0.41 V

$2H_2O \longrightarrow O_2 + 2H_2$ Overall Reaction (ΔG = +237 kJ/mol or 1.23 V)

OER and HER half reactions require a minimum of 1.23 V vs. NHE and complete water splitting of one water molecule [7]. The equations also indicated that HER requires a minimum of two e^-/holes (h^+) pairs to produce one molecule of hydrogen. These electrons came from OER half reaction step. Semiconductor materials are suitable for water splitting due to the fact that they possess tunable band gaps as compared to metals (with zero band gaps) and insulators (with very large band gaps).

The role of sunlight is significant, as these radiations produce electron/hole (e^-/h^+) pairs in the semiconductor material upon interaction. The general scheme for this process is provided in Figure 4(a). The three steps are essential for overall water splitting. (a) generation of the photoexcitons (e^-/h^+) pairs, (b) separation of the photoexcitons, (c) transfer of photoexcitons to the reaction site. A specialized 2- and 3-electrode electrochemical cell used for this purpose, supported by a light source and potentiostat (Figure 4b) [8].

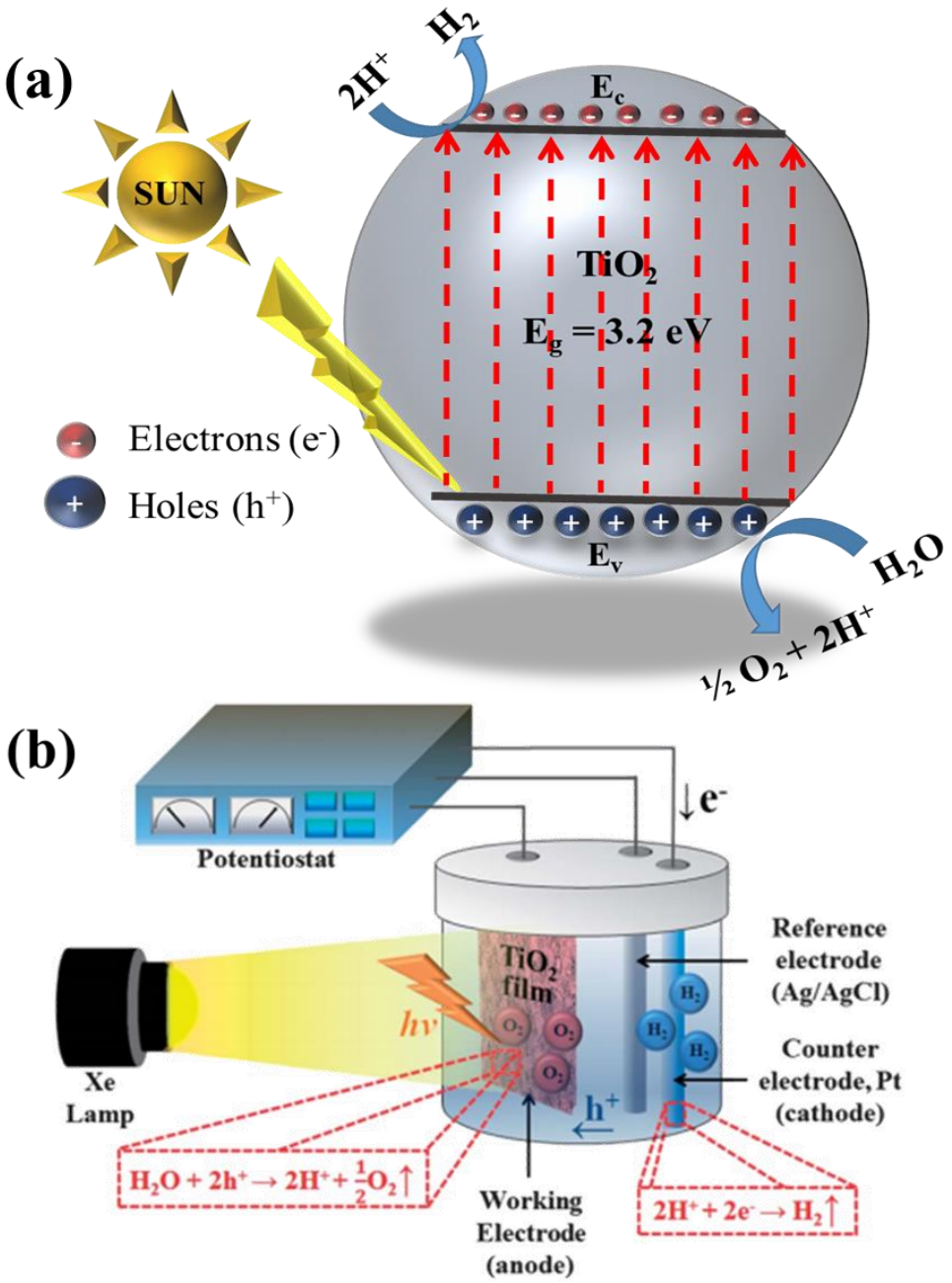

Figure 4: (a) Reported photoelectrochemical water splitting mechanism, (b) Photoelectrochemical water splitting setup

1.3 Piezoelectricity: The Future energy prospect

Piezoelectricity is a relatively older concept of generating an electric current from a suitable material by using mechanical energy. Thus, in simple words, the piezoelectric effect is the creation of electrical potential in response to applied mechanical force. This effect is entirely reversible. The device having the piezoelectric material is termed as "piezoelectric generator" [9]. Certain materials such as ceramics, crystals, and polymer nanocomposites can be used for fabrication of nanogenerators piezoelectrics. piezoelectric voltage and strain constant, mechanical quality, electromechanical coupling (***k***), and dielectric constant are few factors which play important role in the determination of high-quality piezoelectric behavior of the material [10]. Additional to these all factors, the storing capacity of the material substantially requires. Since the role of the energy harvester is to convert as much mechanical energy into electrical energy, it is important to select a material with high electromechanical coupling factor. The factor ***k*** is also an important parameter, as it determines the injected mechanical energy, which would be converted into electrical energy. Those materials having high ***k*** would convert the large portion of applied mechanical energy and vice versa. Equation 1.4 can be used for the determination of the overall piezoelectric capacity of the target material.

$$k_{31}^2 = \frac{d_{31}^2}{\varepsilon_{33}^T s_{11}^E} \qquad \textbf{(1.4)}$$

Where; k_{31}^2 is the electromechanical coupling factor, d_{31}^2 is the piezoelectric induced strain constant (induced polarization in "3" direction per unit stress applied in "1" direction), s_{11}^E is the elastic compliance and ε_{33}^T is the permittivity under constant stress.

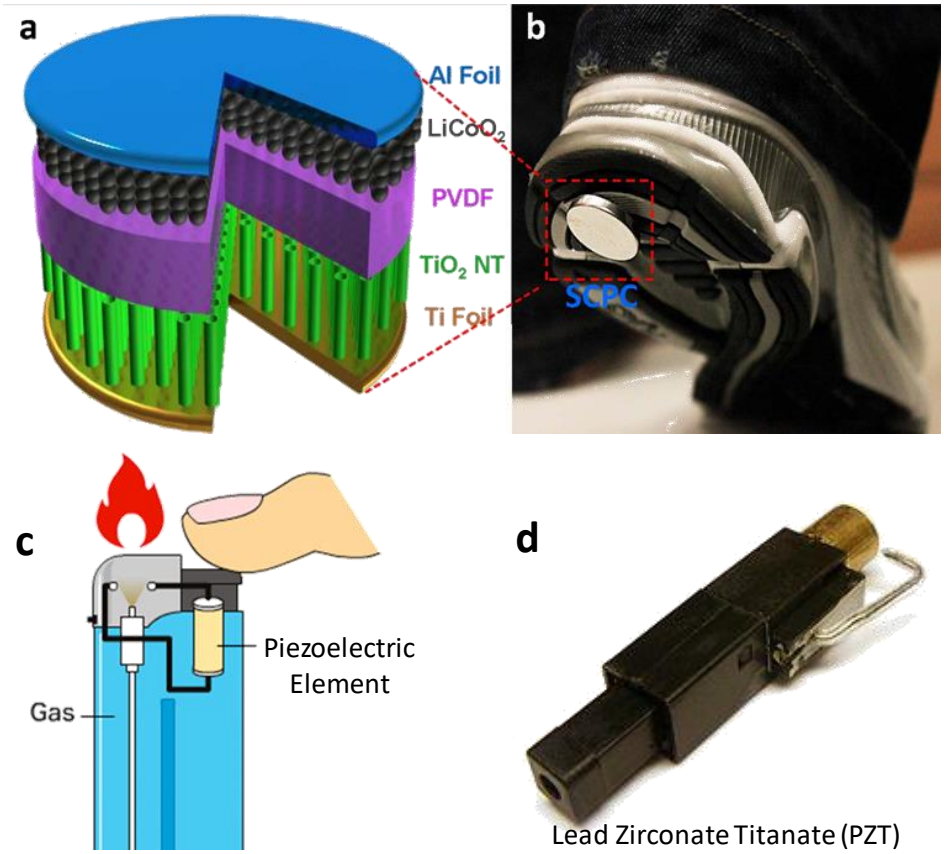

Figure 5: Piezoelectric devices

In order to extract the maximum amount of energy from the energy harvester, it is highly recommended to operate it near its resonance. Nevertheless, it is very difficult to match the frequency of the piezoelectric with the input frequency of the host material owing to volume constraint of the device. Figure 5 shows few examples of piezoelectric based materials.

1.4 Research Objectives

The primary theme of this proposed study was to synthesize aligned heterostructure NAs, which possess enhanced optical properties. These materials were further investigated for renewable energy harvesting applications. Photoelectrochemical (PEC) water splitting and piezoelectric properties of the materials investigated as proposed. While more concentration is given to the earlier application. The major objectives achieved are listed as follow.

1.4.1 Development of Materials

The purpose of this objective was to synthesize novel and shape control NAs materials for PEC water splitting and piezoelectric studies. We successfully developed different NAs i.e. (i) Fe_2O_3-TiO_2 (ii) ZnO/GaON (iii) ZnO-RGO, and (iv) Au-In_2O_3, by various synthetic techniques for photoinduced water splitting applications. We also developed modified ZnO/PVDF/RGO hybrid composite for piezoelectric studies.

1.4.2 Optimization of Reaction Conditions

Different reaction parameters such as the effect of time, temperature, the concentration of the precursors and other chemical reagents were optimized to achieve aligned NAs hybrid nanomaterials.

1.4.3 Characterizations of Hybrid Nanoarrays

Different physicochemical properties of the hybrid materials were investigated via various characterization techniques. We used FESEM and AFM for topographical studies. The XRD, XPS, Raman, and FTIR spectroscopies were utilized mainly for the determination of the structural properties. Finally, UV-Vis/DRS and PL techniques were employed to study the optical properties such as band gap calculations, optical absorptions, and band edge positions etc.

1.4.4 Water Splitting Assembly Setup and Measurements

To study the PEC water splitting, we make complete setup, consist of solar simulator, monochromator, electrochemical cell, and potentiostat. Prior to PEC water splitting measurements, proper training is conducted. We use the as-synthesized hybrid NAs as working electrode, while Platinum (Pt) and Saturated calomel electrode (SCE) acted as a counter and a reference electrode, respectively in a three-electrode cell. 0.5 M Na_2SO_4 electrolyte was used for transport of ions in the electrolytic cell.

1.4.5 Piezoelectric Device Engineering and Measurements

We also investigate the piezoelectric properties of RGO/ZnO/PVDF hybrid NAs in specially designed piezoelectric device. In addition to a multimeter, Oscilloscope was mainly used to measure the conversion of mechanical force to current (piezoelectricity).

CHAPTER 2

LITERATURE REVIEW

Renewable energy is evolving industry due to the fact that the fossil fuels are substantially consumed and caused significant anthropogenic effects with serious health hazards [11, 12]. Figure 6 shows some forms of environmental hazards caused by fossil fuel burning and processing. Due to these serious environmental and health implications, the scientists/researchers greatly motivated towards renewable sources in the last few decades. Important renewable energy forms included energy from biomass, water, wind, solar and mechanical (piezoelectrics). The solar energy is the most reputable candidate among these sources as it is an immortal and continuous source of energy as discussed in chapter 1. This energy can be converted to other forms of energies in various ways. Photoelectrochemical water splitting is one of those approaches, in which the solar energy is converted to electrical energy by using suitable photocatalyst and external bias (voltage).

2.1 Photoelectrochemical Water Splitting

Photoelectrochemical (PEC) alteration of energy obtained from solar spectrum into chemical forms is one of the major scientific challenges and is extensively pursued in research due to its promising environmental energy sustainability. Variety of materials are prone to solar light and they trap the solar radiations by absorbing it. Most of these photoactive materials are based on semiconductors [13], however, metal oxides and earth metals [14, 15], coordinate complexes [16, 17] and even conjugated polymers [18, 19] are also employed. Especially the semiconductors nanostructures preferred due to their --

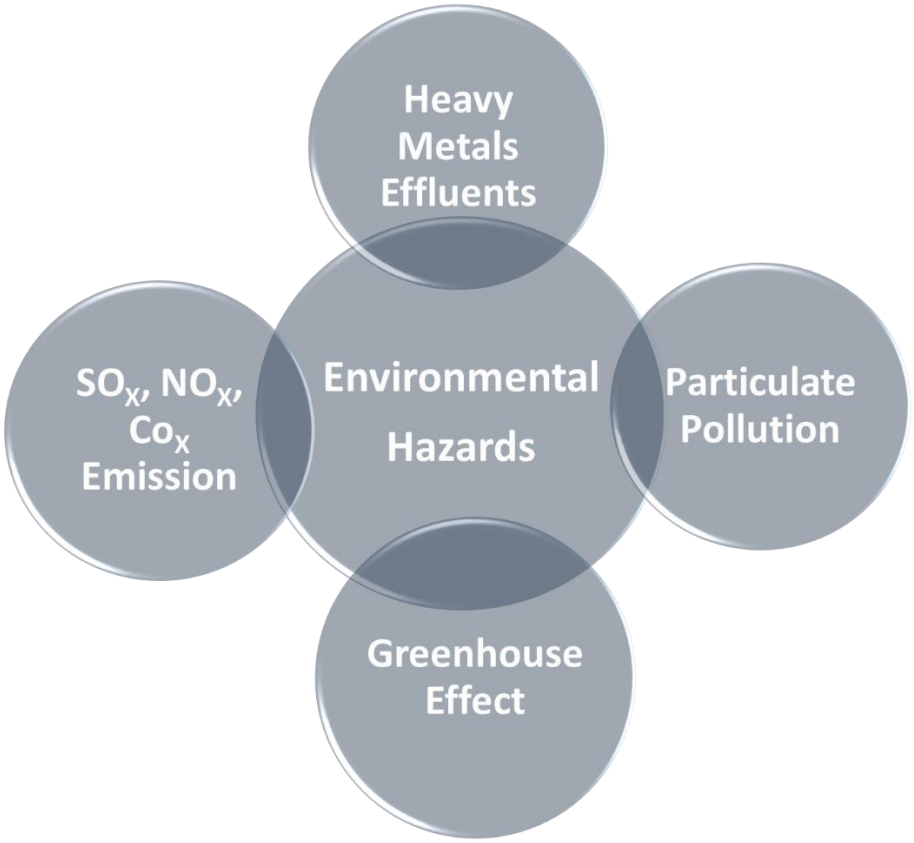

Figure 6: Environmental hazards caused by fossil fuel processing and burning

innate characteristics such as light absorption, desirable charge separation, and stability towards photocorrosion. Owing to exceptional optical properties and ease in synthesis, numerous metal oxide semiconductors e.g. ZnO nanorods (NRs) [20], TiO_2 nanotubes (NTs) and nanoparticles (NPs) [21–23], Ta_2O_5 [24], etc. have been thoroughly studied for solar-driven PEC water splitting. Most of these semiconductor nanomaterials have wide band gaps in their pristine form and therefore show limited PEC performance. The required band gap energy difference of valance and conductance band of the photoelectrode must be between 1.5–2.5 eV, where they absorb the maximum amount of visible light. In addition to the band gap, the photoelectrode should produce a large number of photogenerated charge carriers i.e. electron (e^-) and hole (h^+) pairs, show high chemical stability, have high corrosion resistance, and cost competitive [13]. Furthermore, the position of conduction (E_{CB}) and valence bands (E_{VB}) should be such that they aid the absorption of as much visible light as possible [25]. Approximately, 42–43% of the sunlight that reaches earth lies in the visible range i.e. $420 < \lambda < 700$ nm. Hence, photoelectrodes capable of absorbing radiation in the visible-light region due to lower band gap are of primary interest to the PEC research community [23]. Various approaches have been adopted to achieve these characteristics, which include metals [26] and nonmetals [27] doping, defects and oxygen vacancies creation [28], catalysis and co-catalysis, [29] using the surface plasmon resonance (SPR) of the well-known metals i.e. gold and silver [30], composite and heterostructure formation of two or more photoactive materials [20, 31, 32]. But still, the quest for efficient, robust and cost-effective catalyst is continued.

2.1.1 Semiconductor Oxides for PEC Water Splitting

As discussed earlier, a variety of oxides have been tested for PEC water splitting. Figure 7 showed important oxides with their band positions, which have been utilized for the cited purpose [7]. Three kinds of photocatalysts are distinct, depending on their optical band positions. These are:

(a) WO_3, Fe_2O_3, and $BiVO_4$ are suitable for water oxidation as their band position straddle with the 0.82V, which is the thermodynamic voltage value of water oxidation (0.82 V) vs normal hydrogen electrode (NHE) at pH = 7.

(b) The second category comprises of Si, Bi_2S_3, GaAs, Cu_2O, and GaP. The band position values of these materials straddle with the thermodynamic voltage value of water reduction (-0.41 V) vs normal hydrogen electrode (NHE) at pH = 7

(c) The final group of oxides includes CdSe, Ta_3N_5, TaON, CdS, C_3N_4 and SiC are suitable for overall water splitting as the conductance and valence bands are straddle with the water oxidation and reduction values.

Note: TiO_2 is not included in the list, though it is suitable for overall water splitting, but it is only active in visible region due to wide band gap [5].

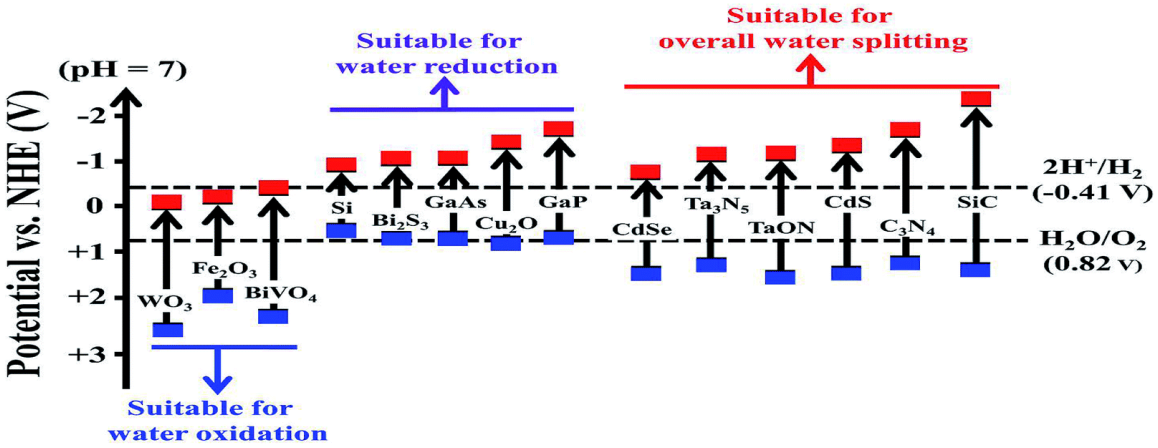

Figure 7: Band gap and band positions of various visible-light metal oxide photocatalysts

2.1.2 Reported Photoelectrochemical Water Splitting of Aligned Nanoarrays

From the initial experiment performed by Fujishima et al. [5], a wide range of materials has been utilized, while most of them showed PEC water splitting, some of them set the high limits of photocurrent density. Morphology also influenced the PEC water splitting performance of photoelectrode due to certain physicochemical properties. Alignment of NAs and size reduction of materials into the nanometer regime can advance device performance and lead to novel findings. For example, the size of transistors shrunken over the years, and more transistor can accommodate in a small silicon area, which ultimately enhanced the performance of these devices with an immense decrease in power consumption [12]. Certain size-dependent characteristics possessed by one dimensional (1D) nanomaterials included photon emission and absorption [13], [14] and quantized or ballistic transport properties, metal to insulator conversion in materials [15] etc. Besides the opportunity to investigate and evaluate novel physical properties of 1D materials, the controlled fabrication of high-quality nanowires (NWs) and their growth mechanisms has attracted tremendous attention. These material classes include metallic elements, oxides, nitrides, carbides, and sulphides [33] etc. Owing to such excellent optoelectric characteristics, 1D aligned NAs trialed by many research groups for PEC water splitting and other photocatalytic applications as well. The NAs are suitable for overall water splitting applications and therefore their PEC assisted OER and HER characteristics are reported in the literature. The ALD protocol was adopted for the synthesis of ZrO_2/ZrN NTAs. The Ultrathin Layers of ZrN was used to tune the photoactivity of Zirconia NTs for visible solar radiation mediated PEC water splitting

[34]. The nitridation effectively enhanced the visible light absorption capacity of the photoanodes and hence increase the overall PEC water splitting. The highest photocurrent density of ~ 1.25 was achieved for the optimized composition of the ZrO_2/ZrN NTAs nanocomposite with excellent interfacial charge transfer. The oxygen evolution reaction (OER) is a critical step in PEC water splitting to produce hydrogen. Metal supported aligned WO_3 NAs synthesized via porous alumina-assisted electrochemical anodization with various aligned morphologies [35]. These materials exhibited improved semiconducting properties due to aligned morphology as indicated by the foregoing discussion. They induce significant oxygen vacancies in WO_3, which is regarded as electron donors and thus leading to deviation from the expected Mott-Schottky plot. This indicated the formation of suboxide, which can be critical for photocatalytic applications. Additionally, the EIS measurements also showed several orders difference for air- and vacuum-annealed WO_3 NAs confirming the existing of the WO_3 and suboxide $WO_{2.9}$ phases, respectively, at the tops of the NRs. Table 1 showed reported photocurrent densities of some prominent photoactive nanomaterials.

Table 1: Reported photocurrent densities of some important aligned NAs photoelectrodes for PEC water splitting with %IPCE

Materials	**Aligned Nanostructures**	**Characteristics**	**Substrate Electrolyte pH**	**Photocurrent Density (mA/cm^2)**	**% IPCE**	**Ref**
Titania NAs based PEC materials	TiO_2 NTAs	Elongated tabular NAs facilitate charge transfer	FTO 1 M KOH (pH = 13.5)	20 mA/cm^2 at 0.50V under UV	10%	[36]
	Heterostructured TiO_2 Nanorod@ Nanobowl Arrays	hierarchical arrayed, the rutile/anatase phase junction, large surface area	FTO 1 M NaOH (pH = 13.6)	1.24 mA/cm^2 at 1.23 V	77%	[37]
	hyperbranched TiO_2	enhanced light absorption and increased contact surface area	FTO not given	1.21 mA/cm^2 at 1.23 V	77%	[38]
	TiO_2 NTs transferred on FTO	reduced interfacial resistance between the nanotube arrays and FTO substrate, oxygen vacancies	FTO not given	~2.0 mA/cm^2 at 1.23 V	90%	[39]
	TiO_2 NRs	Hydrogenated oxygen vacancies in the outer layer	FTO 1 M KOH (pH = 13.5)	1.17 mA/cm^2 at 1.23 V	60%	[40]
	TiO_2/CeO_2 core/shell heterojunction NAs	Heterojunction formation decrease the band gap and enhance the light absorption	FTO 1 M KOH (pH = 13.5)	5.30 mA/cm^2 at 1.23 V	7%	[41]
	Carbon layer silicon (C@ Si) NWs/TiO_2 core-	broad light absorption, efficient charge	FTO 1 M KOH (pH = 13.5)	5.97 mA/cm^2 at 1.00 V	68%	[42]

	shell	separation, fast interfacial charge transfer and redox properties				
	Hierarchical TiO_2–$CuInS_2$ core–shell NAs	Improved absorption efficiency and the appropriate gradient energy gap structure	FTO 1 M KOH (pH = 13.7)	19.07 mA/cm^2 at 0.71 V	23%	[43]
Zinc oxide NAs based PEC materials	ZnO nanopencils	unique structure with an abrupt shrinkage in diameter between the tip and the pencil-holder	FTO 0.5 M Na_2SO_4 (pH of 7.0)	~ 1.3 mA/cm^2 at 1.00 V	18%	[44]
	ZnO NWs	Alignment of NWs provided smooth charge transfer path	FTO 0.1 M KOH (pH = 13)	0.5 mA/cm^2 at 1.00 V	Not reported	[45]
	ZnO NWs/nanodiscs (NDs)	larger surface area due to hierarchical NDs structures	FTO 0.5 M Na_2SO_4 (pH of 6.5)	0.42 mA/cm^2 at 0.70 V	7%	[46]
	ZnO NWs with Ultrathin Titania Shells	TiO_2 coating helps in partial removal of surface trap states and minimizes the path for the minority carriers (photoholes)	FTO 0.1 M KOH (pH = 13)	0.7 mA/cm^2 at 1.00 V	≥ 80%	[45]
	Nitrogen doped ZnO NRs	Nitrogen doping decrease the band gap and enhance the charge	FTO 0.5 M $NaClO_4$ (pH of 7.0)	0.4 mA/cm^2 at 1.00 V	14.6%	[47]

		separation				
	Nitrogen and cobalt co-doped zinc oxide NWs	$(Zn_{0.95}Co_{0.05})O:N$ NWs have reduced band gap, good light absorption, high carrier density, improved charge separation	FTO 0.5 M Na_2SO_4 (pH of 7.0)	8.78 mA/cm^2 at 1.00 V	15%	[48]
	Reduced graphene oxide (RGO)/ZnO NWAs	RGO provide efficient support for electron transfer and enhance the light absorption	FTO 0.5 M Na_2SO_4 (pH of 7.0)	1.55 mA/cm^2 at 1.00 V	NA	[20]
	ZnO–ZnGaON NWAs	Conductive and high-crystalline oxynitride nanostructure with an anti-photocorrosive surface	FTO 0.5 M Na_2SO_4 (pH of 7.0)	1.50 mA/cm^2 at 0.80 V	NA	[49]
	ZnO/CdS NWAs	The 3D-branched nanostructure of ZnO NWAs improved roughness and an enhanced surface area,	FTO Na_2S aqueous Solution	3.58 mA/cm^2 at 0.00V	11.00 %	[50]
Tantalum based NAs materials	Ta_2O_5 NTAs and Ta_3N_5	Surface modification through cocatalysis and Nitridation to decrease the photocorrosion and charge recombination	FTO 1 M KOH (pH = 13.7)	5.90 mA/cm^2 at 1.23 V with CoPi cocatalyst 7.50 mA/cm^2 at 1.23 V with Ba doped CoPi cocatalyst	NA	[24]

	Tantalum nitride (TaN) NTs	Nitridation and Cocatalysis through Co-Pi+$Co(OH)_x$ enhanced the overall optoelectric properties	FTO 1 M KOH (pH = 13.7)	4.70 mA/cm^2 at 1.23 V	NA	[51]
	Carbon layer passivated p-Cu_2O/n-TaON heterojunction NRAs	improvements are due to a high built-in potential in the p–n heterojunction device that is protected from the electrolyte by being encapsulated in an ultrathin graphitic carbon sheath	FTO 0.5 M NaOH	3.06 mA/cm^2 at 1.23 V	59%	[52]
	Ta doped TiO_2/$BiVO_4$ NWs heterostructure	Type II band alignment necessary for favorable electron transfer	FTO Na_2SO_3	2.10 mA/cm^2 at 1.23 V	65%	[53]
Miscellaneous NAs materials	hexagonal nanoflower WO_3	Morphology of WO3 determined the photoactivity of the catalyst	FTO 1 M H_2SO_4	1.3 mA/cm^2 at 1.23 V	29%	[54]
	nanoblock WO_3			0.4 mA/cm^2 at 1.23 V	4%	
	WO_3/$BiVO_4$ NRAs	Core-shell formation between the components	Potassium phosphate buffer	6.72 mA/cm^2 at 1.23 V	<90%	[55]
	WO_3/$BiVO_4$ NWs	NWAs facilitate the charge transfer and the composite decrease the band gap with charge recombination	FTO 0.5 M Na_2SO_4 (pH of 7.0)	0.5 mA/cm^2 at 0.00 V	NA	[56]

	$WO_3/BiVO_4$ Core/ Shell NWs	Core/shell NWs achieve the highest product of light absorption and charge separation efficiencies	FTO 0.5 M Na_2SO_4 (pH of 7.0)	3.10 mA/cm^2 at 1.23 V	60%	[57]
	$WO_3/BiVO_4$ helix NAs	effective light scattering, improved charge separation and transportation, and an enlarged contact surface area	FTO 0.5 M K_2SO_4 (pH of 7.0)	5.35 mA/cm^2 at 1.23 V	> 90%	[58]
	Fe_2O_3 NAs	Arrays formation enhance the current density	FTO 1 M KOH (pH = 13.5)	1.56 mA/cm^2 at 1.23 V	9%	[59]
	P doped Fe_2O_3 NAs	phosphorus (P) improve the charge separation	FTO 1 M KOH (pH = 13.5)	2.00 mA/cm^2 at 1.23 V	28%	
	Aligned $CuInS_2$ (CIS) NRAs	CIS NRAs were decorated with CdS and ZnS coating,	FTO 0.5 M Na_2SO_4 (pH of 7.0)	-0.5 µA/cm^2 at 0.30 V	NA	[60]
	core-shell tandem junction n–p+-Si/n-WO3 microwire arrays	The tandem designing facilitates overall water splitting	FTO 1.0 M H_2SO_4	0.58 mA/cm^2 at 0.70 V	NA	[61]
	ZrO_2/ZrN NTAs	Presence of oxygen vacancies	Not given	1.25 mA/cm^2 at 1.00 V	NA	[34]
	GaN nano-pyramid arrays (NPAs)	High hole transfer efficacy due to pyramid shape	Si (111) not given	0.89 mA/cm^2 at 0.60 V under UV	46.50 %	[62]

2.2 Piezoelectric Materials

Piezoelectrics are unique materials that efficiently convert applied mechanical energy into electricity and vice versa. This phenomenon is traced back to early 1880s and coined by two famous physicists, Pierre and Jacques Curie [63]. They used piezoelectric crystals of topaz, quartz and Rochelle salt for the first time. It was hence realized that when mechanical stress is applied to these materials they could convert this energy into electric charge. Later, Gabriel and Lippmann deduced thermodynamically that these materials also exhibit significant strain in an electric field (applied). Finally, the Curie brothers experimentally confirmed the above effect with the proof of piezoelectric reversibility [64]. Over the years the piezoelectric materials have been used in a variety of devices or actuators. One of the early applications was the use of these materials in the ultrasonic submarine detector. These detectors were developed during the World War (I) [65]. A montage of extremely thin quartz crystals fastened between two steel plates, which worked as a transducer having a resonance frequency of 50 MHz.

1D nanomaterials are preferable for the fabrication of piezoelectric devices due to high value of ***k***, which arise from good elasticity and alignment. The elasticity enables the fabricated material to restore back to its original shape and hence increase the lifetime of piezogenerator. Various 1D shapes, such as NWs, NRs, and nanofibers are effectively employed. Zinc oxide [66], lead zirconate titanate [67], and gallium nitride and aluminum nitride [68, 69] are few examples. Zinc oxide is extensively explored due to its amazing 1D NRs structure and suitability towards piezoelectricity. Wang et al. initially demonstrated the conversion of mechanical energy into electrical from well-aligned 1D ZnO NWs. They determined that power generator mechanism depends on the

piezoelectric and semiconducting properties, in addition to Schottky barrier formation between ZnO and the metal contacts. ZnO is suitable due to three main reasons i.e. (i) it displays semiconducting and piezoelectric characteristics at the same time, (ii) It is relatively and having little toxicity, and (iii) It shows abundant configurations such as NWS, NRs, nanobows, nanorings etc. [66].

Elasticity is the most important factor, which enhances the piezoelectric performance of the material. Therefore, researchers are trying to grow the aligned structures over a flexible substrate. Conducting polymers are the most trustable materials for this purpose. PVDF is extensively employed by researchers for this purpose. PVDF offers inimitable advantages over ceramic and other polymer substrates, like flexibility, stability, inertness and toughness under sunlight, low density, and high voltage coefficient due to lower dielectric permittivity [70]. Recently, Thakur et al. developed β crystallite ZnO/PVDF thin films, where the ZnO NPs in PVDF matrix has improved the dielectric value, effectively. Additionally, it was found to be self-charged under light [71]. In a related study, cobalt doped ZnO/PVDF-hexafluoropropylene (PVDF-HFP) nanofibers were fabricated by sophisticated electrospinning method. The dielectric constant and output voltage of the pristine PVDF-HFP polymer are 8 and 0.12 V, respectively. Conversely, for PVDF-HFP/2 wt.% Co-ZnO nanofibers, the values were found to be 38 and 2.8 V, respectively [72]. These results suggest that the proper designing of PVDF and ZnO based piezoelectric can generate efficient piezoelectric energy.

CHAPTER 3

ELECTROCHEMICAL SYNTHESIS OF Ag/α-Fe_2O_3/TiO_2 NANOARRAYS AND THEIR PHOTOELECTROCHEMICAL WATER SPLITTING

3.1 Introduction

Solar radiation and heat from the sun have been harnessed using a range of ever-developing technologies, such as solar water heaters [73], photovoltaics [74], solar architecture [75], artificial photosynthesis [76], and water splitting [5, 13, 77–79]. The solar electromagnetic radiation can be used to generate energy from water splitting as initially reported by Fujishima and Honda [5]. Since then, extensive research has been performed using a variety of semiconductors and metals as photocatalysts or co-catalysts for photoelectrochemical (PEC) water splitting [32, 77, 80, 81]. Among these semiconductor materials, TiO_2 is a promising candidate because of its light absorption and scattering capacity, high photocorrosion resistance, large surface area and tunable aspect ratio [82].

Among the different types of TiO_2, 1D TiO_2 semiconductor materials have been widely studied due to their distinctive properties, such as a high surface area and good aspect ratio in addition to their fascinating nanoscale features, which are better than those of TiO_2 NPs. These features are generally required for photoexcitons to travel and be transferred along the axial path, which enhances their overall lifetime. These chemical properties, in addition to their chemical stability, make 1D TiO_2 nanotube arrays (NTAs) ideal building blocks for further nanoengineering of heterostructure materials for

enhanced photoelectrochemical (PEC) water-splitting applications [83]. Nevertheless, the major drawback of pristine TiO_2 NTAs is their poor response in the visible part of the solar spectrum because of their wide band gap of 3.2 eV. In addition, they have low electron mobility and a low affinity towards the oxygen evolution reaction (OER) for water splitting in the visible region [84]. TiO_2 NTAs have been combined with other semiconductors and plasmonic metals to overcome these limitations and enhance the PEC properties in the visible region [84–86]. Certain dopants have been utilized to increase the water-splitting efficiency of pristine TiO_2, but the dopants normally deteriorate the usual crystal structure, create extra energy states, which can lead to fast charge recombination, and decrease the extent of other alterations on the characteristics of the bulk material [87].

N-type Fe_2O_3 has been investigated for enhanced photocatalytic applications because of its low band gap (2.3 eV) and economical nature [88]. Sivula et al. provide insight in their review on the efficient use of hematite for photocatalytic applications [89]. Nonetheless, pristine Fe_2O_3 has some incongruities weaknesses, such as low conductivity, short diffusion length (10-20 nm) [90], and corrosion susceptibility [91].

Heterostructure engineering is one approach that can be used to overcome the issues related to pristine TiO_2 and Fe_2O_3 nanostructures. Heterostructures exhibit remarkable characteristics, and by varying the concentration of each component, their absorption spectrum and band gap can be tuned to the desired wavelength [7]. In recent years, several groups have investigated Fe_2O_3/TiO_2-based heterostructures, but the structures have some discernable limitations. For instance, Li et al. reported an atomic layer deposition (ALD)-based, two-step blend method for the synthesis of TiO_2 deposited on

hematite (Fe_2O_3) nanostructures [92]. Hematite was synthesized via a simple hydrothermal method but was followed by the expensive and intricate ALD of TiO_2. The final product was annealed at a high temperature, i.e., 650°C. Additionally, the incorporation of noble metals, such as Ag, Au, and Pt, efficiently increased the photocatalytic performance. Recently, Valenti *et al.* used plasmonic NPs to enhance the light absorption capacity of semiconductors for water-splitting applications; the enhanced light absorption capacity was attributed to the localized surface plasmon resonance (SPR) effect [30]. The enhancement mechanism via SPR involves four processes: (a) light concentration (LC), (b) light scattering (LS), (c) hot electron injection (HEI), and (d) plasmon-induced resonance energy transfer (PIRET). The first two processes (LC and LS) involve light trapping mechanisms, which increase the light absorption capacity above the optical band edge of the semiconductors, whereas the HEI and PIRET processes decrease the light absorption capacity below the optical band edge. Amongst the noble metals, Ag has been utilized for plasmonic applications because it is relatively inexpensive and exhibits intriguing catalytic/plasmonic properties [84]. In a related study, Hung et al. reported an Ag plasmonic effect on the overall PEC water-splitting properties of Fe_2O_3/TiO_2 heterostructures with low photocurrent density. This effect was probably due to the non-uniform morphology and polycrystalline nature of the structures, which influenced the kinetics of the PEC water-splitting reaction [84]. Hence, the synthesis methods play a pivotal role in successfully fabricating a nanoarchitecture with the desired morphology and tailored growth. Meanwhile, the electrochemical anodization technique is relatively new compared to traditional solvothermal methods [93] and can easily be coupled with sonochemical systems. This method results in uniform/controlled growth by

modulating various parameters. Moreover, it is more swift and can be performed at room temperature with minimal energy requirements [94]. Using this technique, Momeni *et al.* successfully synthesized TiO_2 NTAs and their various composites for photocatalytic and water-splitting applications with control shape and morphological features, which enhanced their photocatalytic efficiencies [78, 95, 96].

In this work, we report the first use of a pulse sonochemical-assisted single-step *in situ* electrochemical anodization technique to combine the expedient properties of TiO_2 and Fe_2O_3 for improved water-splitting activity. These heterostructures were fabricated at a relatively low voltage, and *in situ* electrochemical Ag pseudo-nanocubes were also decorated on the surface of the α-Fe_2O_3/TiO_2 NTAs to further enhance water splitting via the SPR phenomenon.

3.2 Methods and Materials

3.2.1 Synthesis of Ag/α-Fe_2O_3/TiO_2 heterostructure

In a simple experiment, 1 x 2 cm^2 titanium metal foil (0.05mm thick) (Sigma Aldrich) was cut, polished and washed with ethanol and acetone under moderate sonication to remove the native oxidized TiO_2 layer along with other impurities. TiO_2 NTAs were grown via the sonochemical-assisted electrochemical anodization technique. The Ti foil was used as the anode and platinum as the cathode in a two-electrode electrochemical cell with a ~1 cm distance between the two. A 0.5 wt% NaF solution in ethylene glycol supplemented with 5% DI water was used as the electrolyte. DI water assisted the dissolution of NaF in the organic solvent and decreased the viscosity of the solution [97], and ethylene glycol provided a mild etching environment to obtain more organized and uniform nanotubes because of its polar protic nature [98]. The anodization time and

voltage were 2 h and 20 V, respectively, for this step. After 2 h, 0.5 M $FeCl_3$ (Sigma Aldrich) was added as the Fe_2O_3 precursor, and sonication was continued in the pulse sequence mode. The pulses were delivered with a 30 s delay time. Pulse sonication increased the deposition rate [99]. The reaction time for the *in situ* Fe_2O_3 deposition was 30 min. Similarly, Ag was also deposited in the same manner using a 0.5 M $AgNO_3$ salt solution as the Ag precursor. The prepared photoanodes were slowly and carefully washed with DI water, dried in an oven, and finally calcined at 400°C to increase their crystallinity. The overall fabrication process is illustrated in Figure 8, which shows the stepwise *in situ* Ag/α-Fe_2O_3/TiO_2 heterostructure formation through repeated anodization reactions assisted by pulse ultrasonication.

3.2.2 Material Characterizations

a. Physicochemical Characterization

The morphological topography of Ag/α-Fe_2O_3/TiO_2 was investigated using a field emission scanning electron microscope (FESEM) to analyze the distribution and size of the NTAs. SEM micrographs were obtained using LYRA 3 Dual Beam instrument (Tescan) operated at an acceleration voltage of 20 kV. This instrument was also equipped with an energy dispersion spectrometer (EDX, Oxford Instruments), which was used to determine the elemental ratio and confirm the constituent elements. X-ray characterization was performed using a Rigaku X-ray Ultima IV diffractometer equipped with a Cu Kά (λ = 0.15406 nm) radiation source and operated from 2θ = 20° to 65° at a scan rate of 1 degree/min to determine the facet arrangement and crystalline phase of the Ag/α-Fe_2O_3/TiO_2 heterostructures. Fourier transform infrared (FT-IR) spectra from 600 to 2000 cm^{-1} were recorded on Thermo-Scientific FT-IR instruments. An ESCALAB

250Xi X-ray photoelectron spectrometer (XPS) microprobe device was utilized to study the oxidation details of the component elements in the Ag/α-Fe_2O_3/TiO_2 heterostructures. A Carry 5000 model was used to investigate sample optical properties. Absorption spectra were recorded from 200 nm to 800 nm at a scan rate of 200 nm/min. In addition, F(R) vs eV spectra from 1.5 to 4 eV were obtained to calculate the exact band gap using the Kubelka-Munk (KM) equation [81]. Photoluminescence (PL) spectra were recorded on a Horiba model fluorescence spectrometer (FluoroLog-3-2iHR) at an excitation wavelength of 300 nm using an S1-(R928) (SCD1) detector with a 450 W xenon lamp.

b. Photoelectrochemical Measurements

PEC water splitting was performed in a three-electrode PEC cell containing a 0.5 M Na_2SO_4 (Sigma Aldrich) electrolyte (pH 7.0). The TiO_2, α-Fe_2O_3/TiO_2 and Ag/α-Fe_2O_3/TiO_2 NTA substrates were used as the working electrodes and were controlled by an Autolab potentiostat. Platinum (Pt) and saturated calomel electrode (SCE) served as the counter and reference electrodes, respectively. All PEC measurements were recorded using NOVA software installed on a data collecting device under the controlled chopping of dark and light. A solar simulator (Oriel Sol-3A Newport) provided artificial solar light irradiation, and the power was calibrated using a silicon diode solar cell (Oriel-diode) and fixed at 100 mW/cm^2, which is equivalent to 1 SUN. The solar simulator was also equipped with AM-1.5 G and UV cutoff ($\lambda > 420$ nm) filters. The filters are important to control the wavelength of the simulated solar light on the substrate. For electronic impedance spectroscopy (EIS) measurements, we applied a forward bias set at the open circuit voltage (V_{OC}) with an alternating current (AC) amplitude of 10 mV, between the working (WE) and counter electrodes (CE) from 100 kHz to 100 mHz.

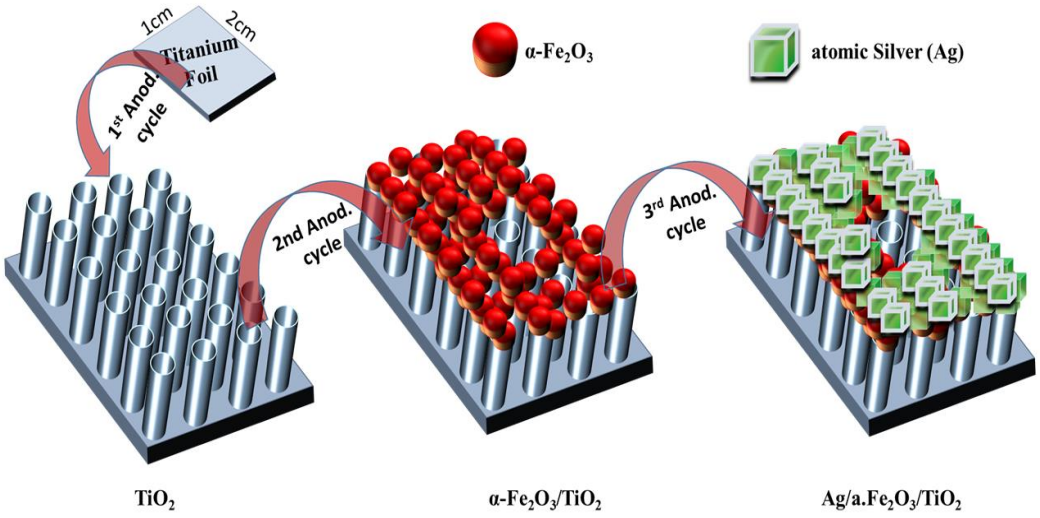

Figure 8: Graphical growth mechanism for the formation of the Ag/α-Fe_2O_3/TiO_2 heterostructure

3.3 Results and Discussion

3.3.1 Structural and optical properties

Figure 9 show low and high magnification FESEM micrographs of the anodized substrates. The TiO_2 NTAs exhibit a uniform distribution (Figures 9a-c), and diameters and lengths of ~40-50 and ~250-300 nm, respectively. The surface of the α-Fe_2O_3/TiO_2 NTAs was gently scratched at the edge to reveal the deposition and incorporation of Fe_2O_3. The nanotubes can be clearly seen under the aggregated Fe_2O_3 NPs in Figures 9(d,e). The inset in Figure 9(f) shows the cross-section of the α-Fe_2O_3/TiO_2 NTAs, which reveal the top layer of Fe_2O_3 on the TiO_2 NTAs. Low and high magnification SEM images (Figures 9g-i) of the Ag/α-Fe_2O_3/TiO_2 heterostructures show pseudo-nanocube shaped Ag nanocrystals (80-90 nm) thoroughly deposited on the surface of the Fe_2O_3/TiO_2 composite. In some locations, the TiO_2 nanotubes can be clearly seen under the Ag and are highlighted with circles.

Figure 10(a) presents the elemental mapping of the component atoms, which are evenly distributed throughout the heterostructure. Similarly, Figure 10(b) displays the EDX spectra obtained from the Ag/α-Fe_2O_3/TiO_2 heterostructure, which also confirm the presence of Ag, Fe, Ti and O in the heterostructure. These results indicated the formation of Ag/α-Fe_2O_3/TiO_2 NTAs.

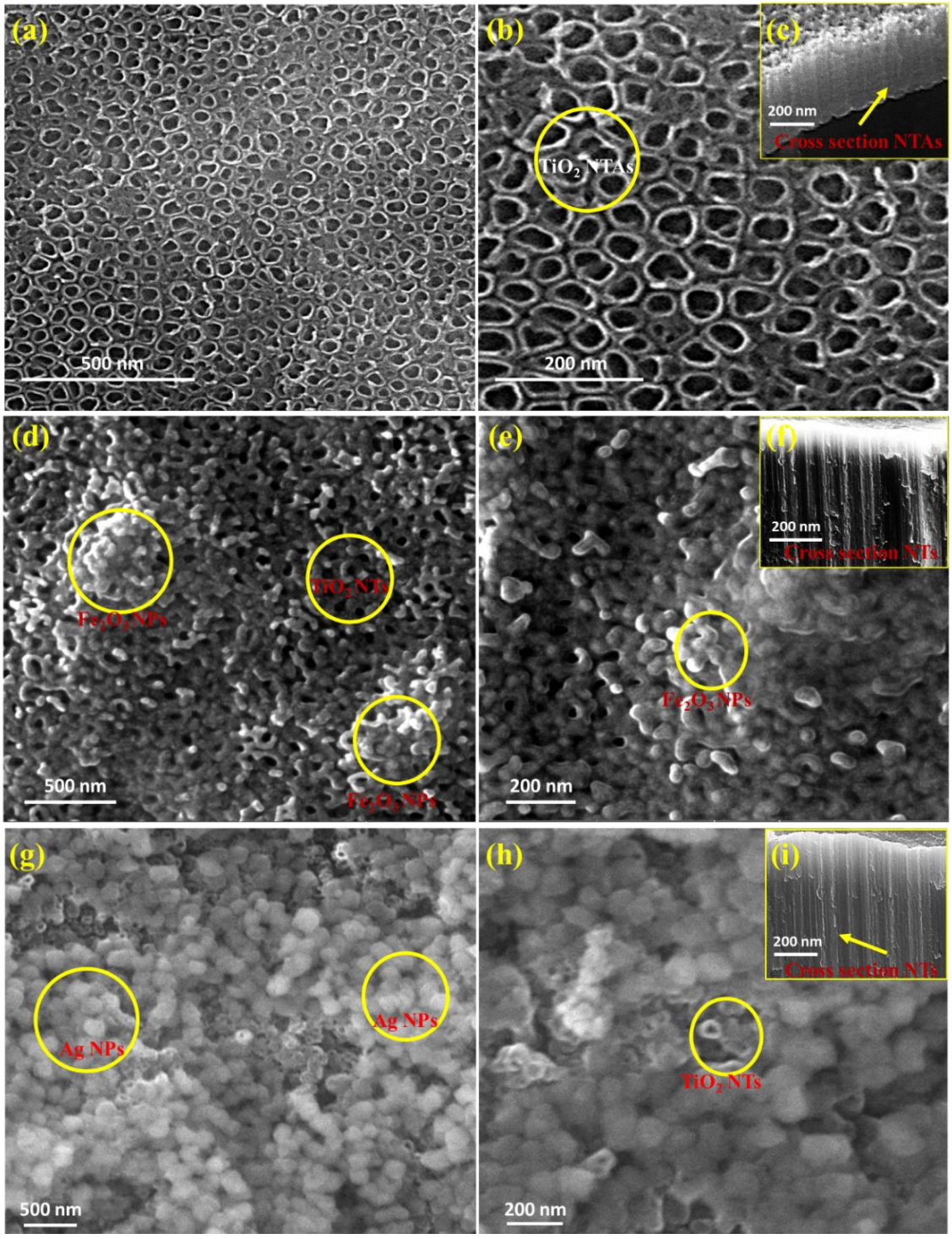

Figure 9: Low and high magnification FESEM images of anodized (a, b) pristine TiO_2 NAs, (c, d) α-Fe_2O_3/TiO_2, and (e, f) Ag/α-Fe_2O_3/TiO_2 heterostructures.

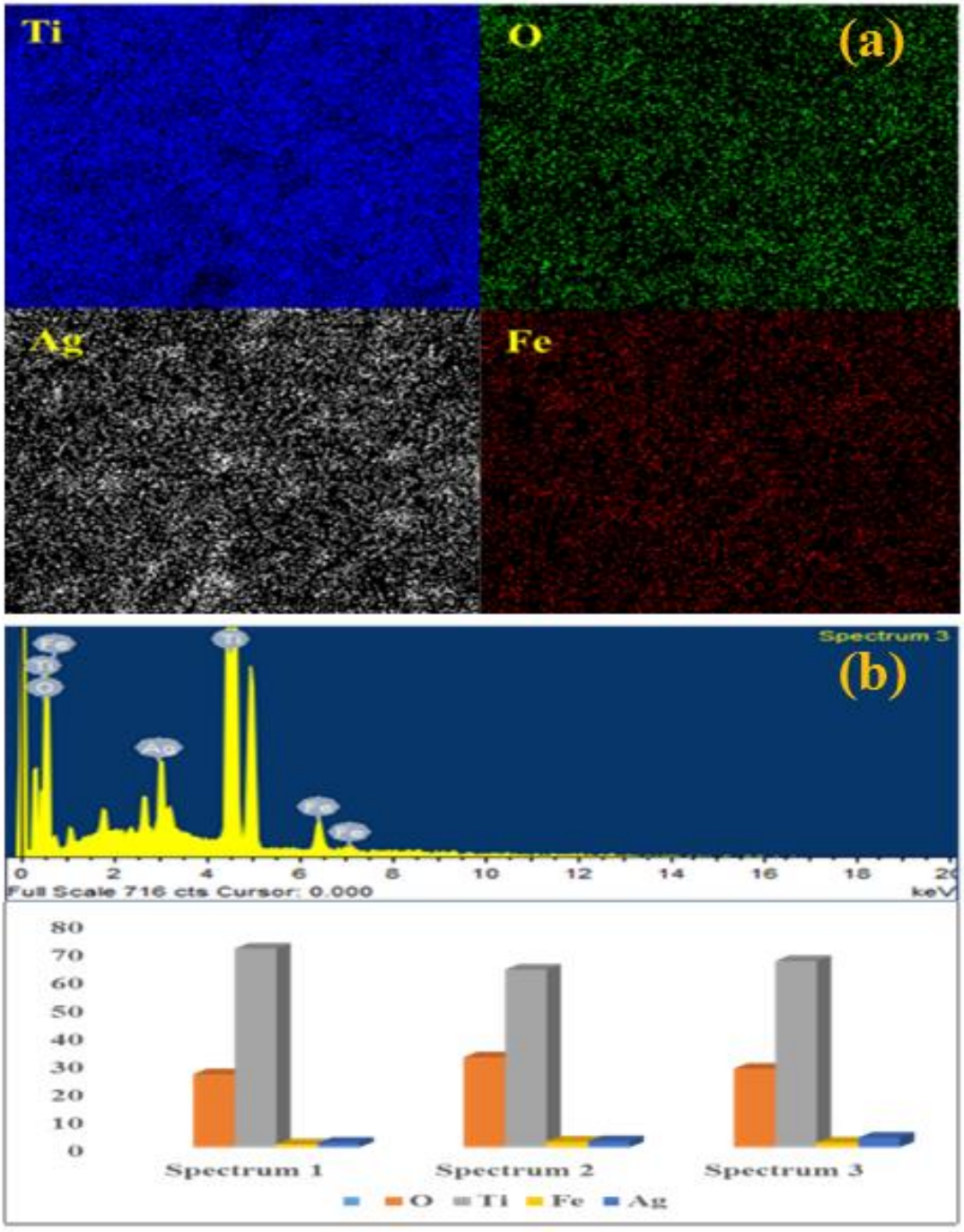

Figure 10: (a) Elemental mapping and (b) EDX spectrum of Ag/α-Fe_2O_3/TiO_2 heterostructures.

Figure 11(a) presents the stacked and annulated X-ray diffraction patterns obtained from pristine TiO_2, α-Fe_2O_3/TiO_2 and Ag/α-Fe_2O_3/TiO_2 heterostructures. The characteristic peaks in XRD pattern of TiO_2 at 25.07° (101), 37.65° (004), 47.81° (200), 53.94° (105), 54.81° (211), and 62.55° (204) matched the anatase crystalline phase [85]. In the case of α-Fe_2O_3/TiO_2, some additional peaks appeared in the XRD pattern at 23.00° (weak), 33.07° (strong), 36.35°, 46.13º (sharp) and 54.41° (strong), which corresponded to the (012), (104), (110), (024) and (116) diffraction facets, respectively, and were assigned to α-Fe_2O_3 phase after matching JCPDS 84-0311. After the deposition of Ag and Fe_2O_3 (pattern c in Figure 11a), the parent peaks of α-Fe_2O_3/TiO_2 slightly shifted towards a higher angle (~0.10°), possibly because of the strain caused by the Ag NPs, which might relax the unit cell of the parent crystal in case of heterostructure formation [100–102]. The additional peaks appeared at the diffraction pattern of Ag/α-Fe_2O_3/TiO_2 at 34.02°, 39.11°, and 43.01° are indexed as metallic Ag.

The FT-IR spectra for TiO_2 NT, α-Fe_2O_3/TiO_2 and Ag/α-Fe_2O_3/TiO_2 are provided in Figure 11(b) and comprehend the vibrational properties. It is evident that the intensity of the peaks increased due to the plasmonic behavior of Ag, with the shift in the case of Ag/α-Fe_2O_3/TiO_2 NTAs was negligible compared to the pristine and modified Fe_2O_3/TiO_2 heterostructures [103]. The peaks for TiO_2 exist in the Ag/α-Fe_2O_3/TiO_2 spectrum, which confirmed the presence of TiO_2 NTs. Starting from higher wavenumber, the peak appearing at 1610, 1598 and 1592 cm^{-1} in the spectra of TiO_2 and α-Fe_2O_3/TiO_2 can be assigned to H-O-H bending. The intensity of this peak increased with the *in situ* growth of Fe_2O_3 and Ag, and the growth is probably due to water molecules being incorporated into the crystal structure [92]. The broadband at 664 cm^{-1} in the TiO_2

spectrum shifted slightly to the right, 648 and 640 cm^{-1}, in the α-Fe_2O_3/TiO_2 and Ag/α-Fe_2O_3/TiO_2 spectra, respectively, with a significant decrease in the intensity due to the incorporation of Ag and Fe_2O_3 in the structures. This peak was assigned to Ti-O stretching vibrations [104]. In addition to the TiO_2 bands, new IR bands appeared in the heterostructure spectra, e.g., peaks at 726 and 720 cm^{-1} in the α-Fe_2O_3/TiO_2 and Ag/α-Fe_2O_3/TiO_2 spectra, which corresponded to the Fe-O vibrational stretches in these products, respectively. The impregnation of Ag was also evident based on the notable shift of the IR bands to the right in the case of Ag/α-Fe_2O_3/TiO_2 IR spectrum. The right shift provided significant evidence that the dense Ag atoms pushed away the lighter atoms, i.e., iron and titanium, in the parent crystal, which confirmed the formation of the heterostructure [105]. These results are in good agreement with the XRD patterns.

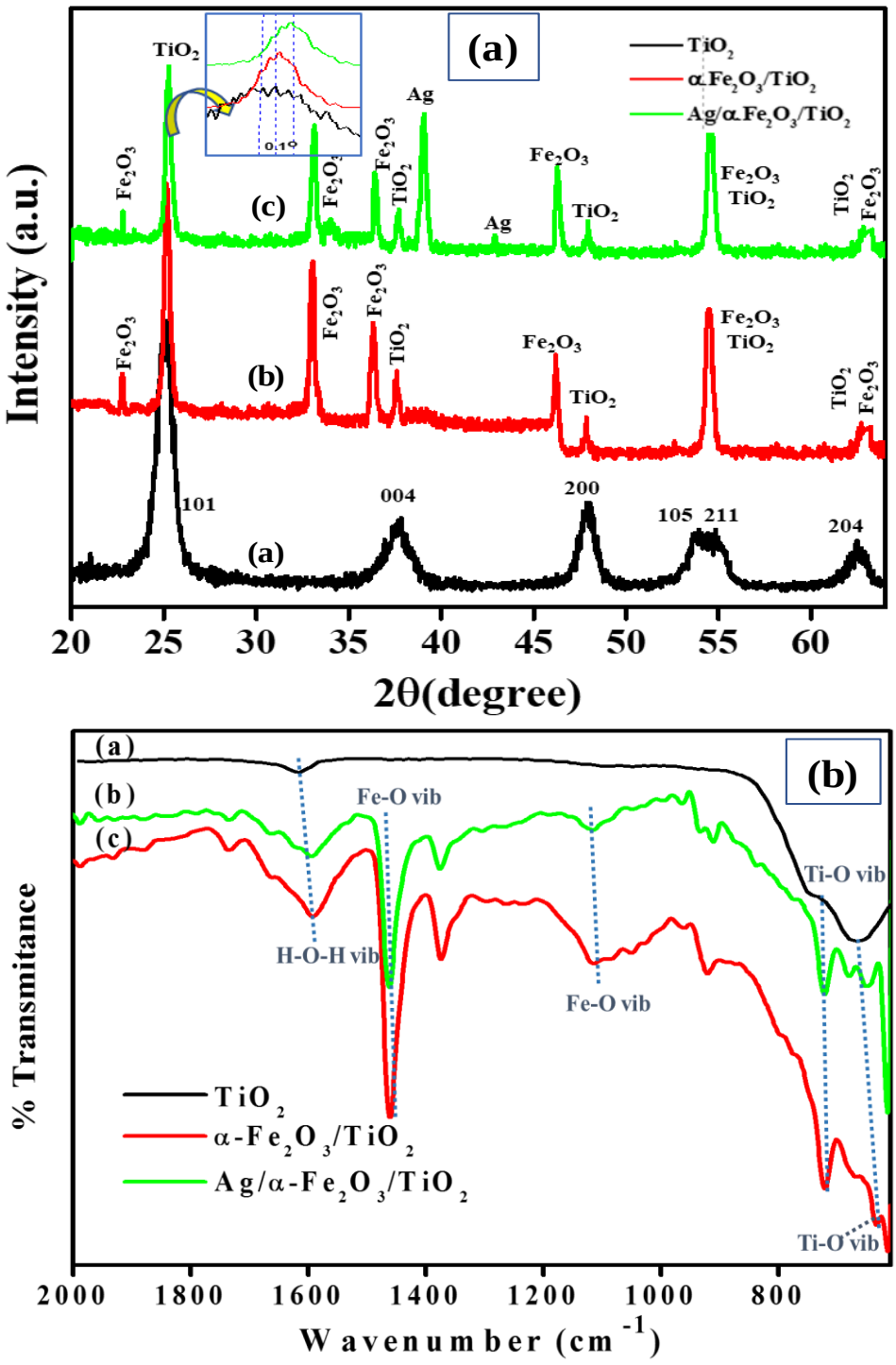

Figure 11: (a) XRD patterns, and (b) FT-IR spectra of pristine TiO_2, α-Fe_2O_3/TiO_2 and Ag/α-Fe_2O_3/TiO_2 photoanodes

XPS profiling was performed to determine the chemical states and presence of Ag and Fe_2O_3 in the TiO_2 structure, and the results are provided in Figures 12A and 12B. Figure 12A.(a) demonstrates the appearance of Ag peaks in the survey of Ag/α-Fe_2O_3/TiO_2 in low energy region. The spectrum also showed characteristic low-intensity peaks for Fe in the high energy regions after 700 eV. Both the regions are intentionally encircled to identify it from the rest. The Ag peak is absent in the case of α-Fe_2O_3/TiO_2 and TiO_2 samples. Another important observation is the intensity of the XPS spectra, which show great improvement in case of Ag/α-Fe_2O_3/TiO_2 heterojunctions as compared to other samples. This phenomenon clearly demonstrated by the high-resolution spectra of Ti and O (Figure 12A. (b,c). Additionally, there is a small shift of ~0.05-0.1 eV occurs towards higher binding energy in the XPS spectra of Ti and O which could be related to the successful heterojunction formation as also depicted by the XRD results. Another important feature of the XPS profile in case of oxygen is the appearance of broad shoulder (encircled) after the incorporation of Fe, which is further intensified in the case of Ag/α-Fe_2O_3/TiO_2 (Figure 12A. (c). This might suggest that the incorporation of Fe ions into the crystal lattice of TiO_2 influence the crystal properties. A similar observation is reported by Abazović et al. lately [104, 106]. Figure 12B. displays the high-resolution deconvoluted spectra obtained from the component element exist in Ag/α-Fe_2O_3/TiO_2 heterojunctions. Silver showed $3d_{5/2}$ and $3d_{3/2}$ spin-orbital splitting photoelectrons at the binding energies at 367.81 and 373.81 eV (Figure 12B. a), respectively. The doublet peak values are in good agreement with the Ag (0) state values thus suggesting that it is existing in a non-oxidized form [107]. The high-resolution deconvoluted spectra of Fe [2p] in Figure 12B. (b) depict a pseudo-doublet at (711.55 and 725.05 eV), with a

satellite peak at 720.36 eV. The deconvoluted peaks can be assigned to Fe (III) chemical states of iron in hematite, and correlate to Fe-O-Fe bonding. Figure 12B. (c) shows the XPS profile of Ti [2p], correspond to Ti (IV) states at (458.72 and 464.45 eV), with a very low concentration peak observed at 460.25, which signifies the existence of Ti-O-Fe bond. Similar results have been reported by Pham et al. [108]. The deconvoluted spectra of oxygen (O [1s]) in Figure 12B. (d) showed a singlet peak at 529.58 eV with a broad shoulder at 531.54 eV(encircle). The earlier peak suggested the existence of oxygen as O^{-2} in TiO_2 and Fe_2O_3, while the appearance of the shoulder signifies the existence of -OH due to the chemisorbed water species. The shoulder peak broadens and intensified in $Ag/\alpha\text{-}Fe_2O_3/TiO_2$, suggesting that Fe (III) induce some chemical changes in the TiO_2 lattice structure. Similar results are reported by Michael et al. in the case of Fe_2O_3-TiO_2-Au nanocomposites prepared by plasma-assisted method [109].

(A)

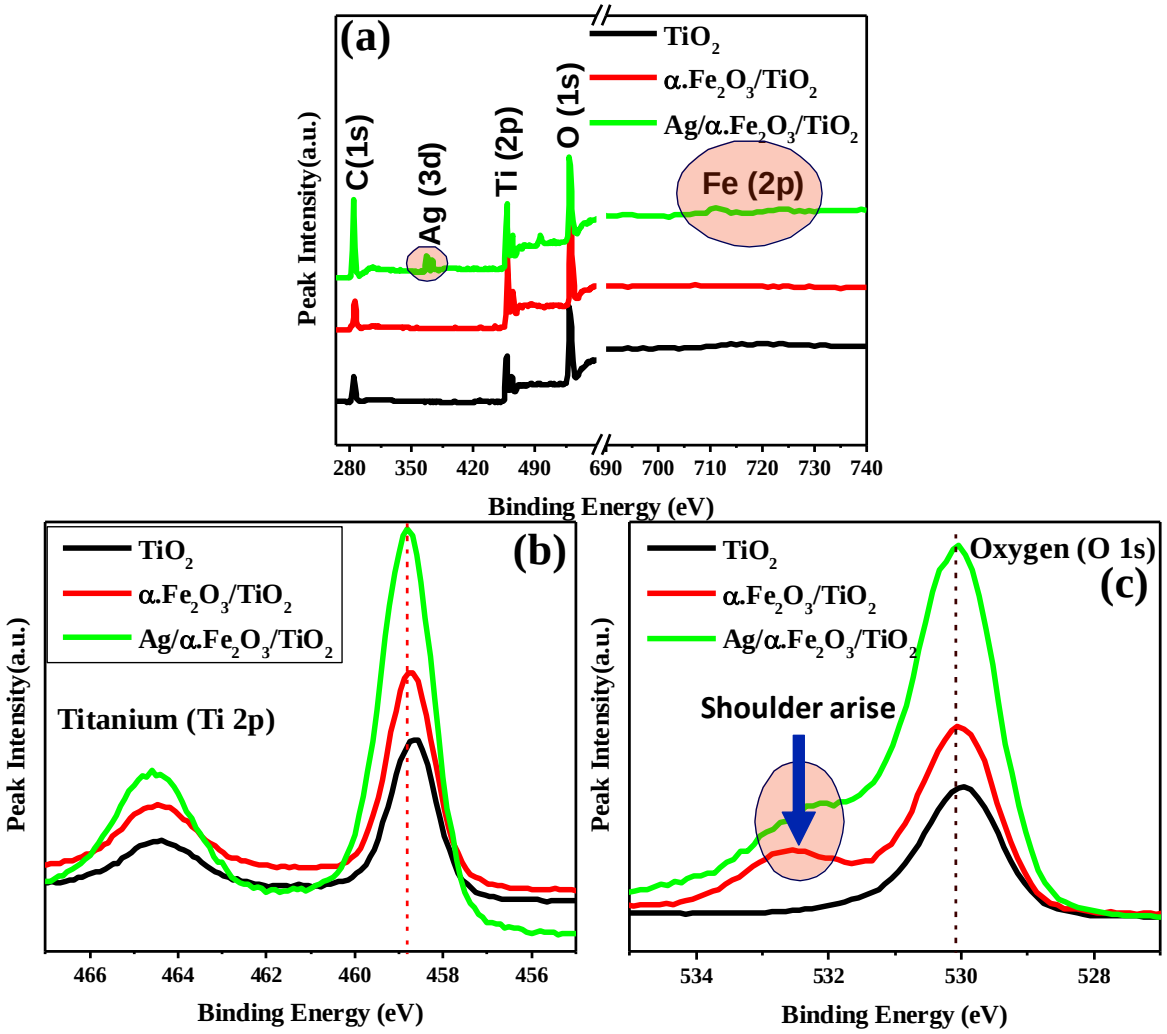
(a)
TiO2
α.Fe2O3/TiO2
Ag/α.Fe2O3/TiO2
C(1s)
Ag (3d)
Ti (2p)
O (1s)
Fe (2p)
Peak Intensity(a.u.)
280 350 420 490 690 700 710 720 730 740
Binding Energy (eV)
(b)
Titanium (Ti 2p)
466 464 462 460 458 456
Binding Energy (eV)
(c)
Oxygen (O 1s)
Shoulder arise
534 532 530 528
Binding Energy (eV)

(B)

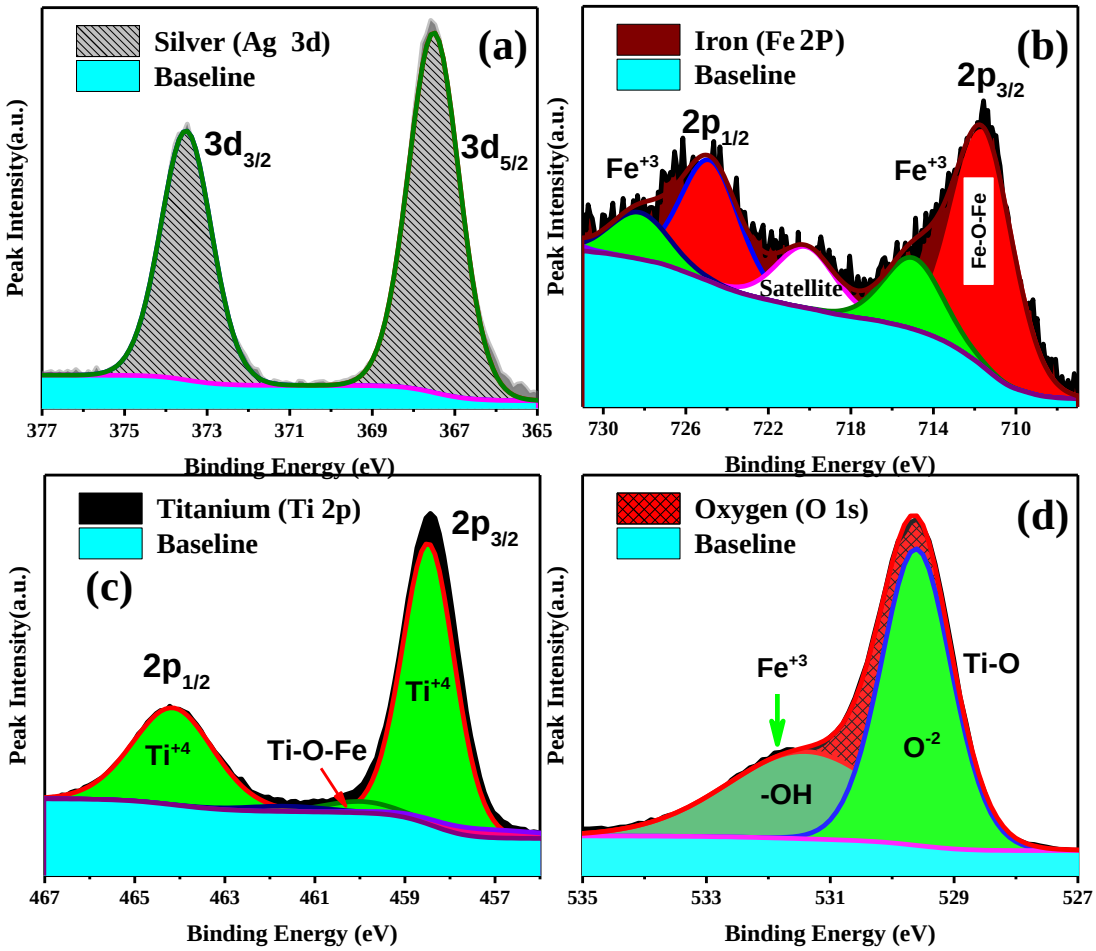

Figure 12: (a) Comparative XPS profiles of TiO_2, α-Fe_2O_3/TiO_2 and Ag/α-Fe_2O_3/TiO_2: (a) Surveys, (b) High resolution XPS spectra of Ti (2P), and (c) O (1s). B: XPS profiling of Ag/α-Fe_2O_3/TiO_2 heterostructures: (a) Ag (3d), (b) Fe (2p), (c) Ti (2p) and (d) O (1s).

To study the optical behavior of the photoanodes, diffuse reflectance spectroscopy (DRS) was performed. The spectra in Figure 13(a) indicated a shift towards higher wavelengths in the visible region of the spectrum after loading Fe_2O_3 and Ag onto pristine TiO_2 NTAs. The absorption increased in the order of TiO_2 (~386 nm) > Fe_2O_3/TiO_2 (~424 nm) > $Ag/\alpha\text{-}Fe_2O_3/TiO_2$ (~470 nm). The band gaps of these materials were determined using the same spectra. The absorption edge for the TiO_2 NTAs is at ~370 nm, which correlates to a band gap of ~3.22 eV. Similarly, for $\alpha\text{-}Fe_2O_3/TiO_2$, the absorption edge shifted to ~424 nm, which corresponds to a band gap of 2.95 eV. The Ag deposition further shifted the absorption edge to ~486 nm, which corresponds to a band gap of 2.64 eV. Additionally, the characteristic plasmonic Ag shoulder can be seen at ~420 nm on the absorption $Ag/\alpha\text{-}Fe_2O_3/TiO_2$ peak [110, 111]. electrochemical deposited Ag NPs increased the light absorption capacity of $Ag/\alpha\text{-}Fe_2O_3/TiO_2$ photoanodes by inducing SPR effect. This mechanism involves the following four types of processes namely (a) LC, (b) LS, (c) HEI, and (d) PIRET, as discussed above. Consequently, the absorption capability for the plasmonic product is enhanced as compared to pristine TiO_2 and $\alpha\text{-}Fe_2O_3/TiO_2$ nanostructures, which suggested that LC and LS processes are dominant. All the band gaps were calculated using the band gap "$\mathbf{E_g = hc/\lambda}$" equation [112]. The dramatic decrease in the band gap is useful for PEC applications because it allows these materials to efficiently absorb the visible part of the solar spectrum [86]. For water-splitting applications, the most suitable band gap is approximately 2 eV [113]. To confirm the band gap values, the KM equation was used [114], and the Tauc`s plots are provided in Figure 13(b). These plots present the band gap values in accordance with those obtained from the absorption spectra.

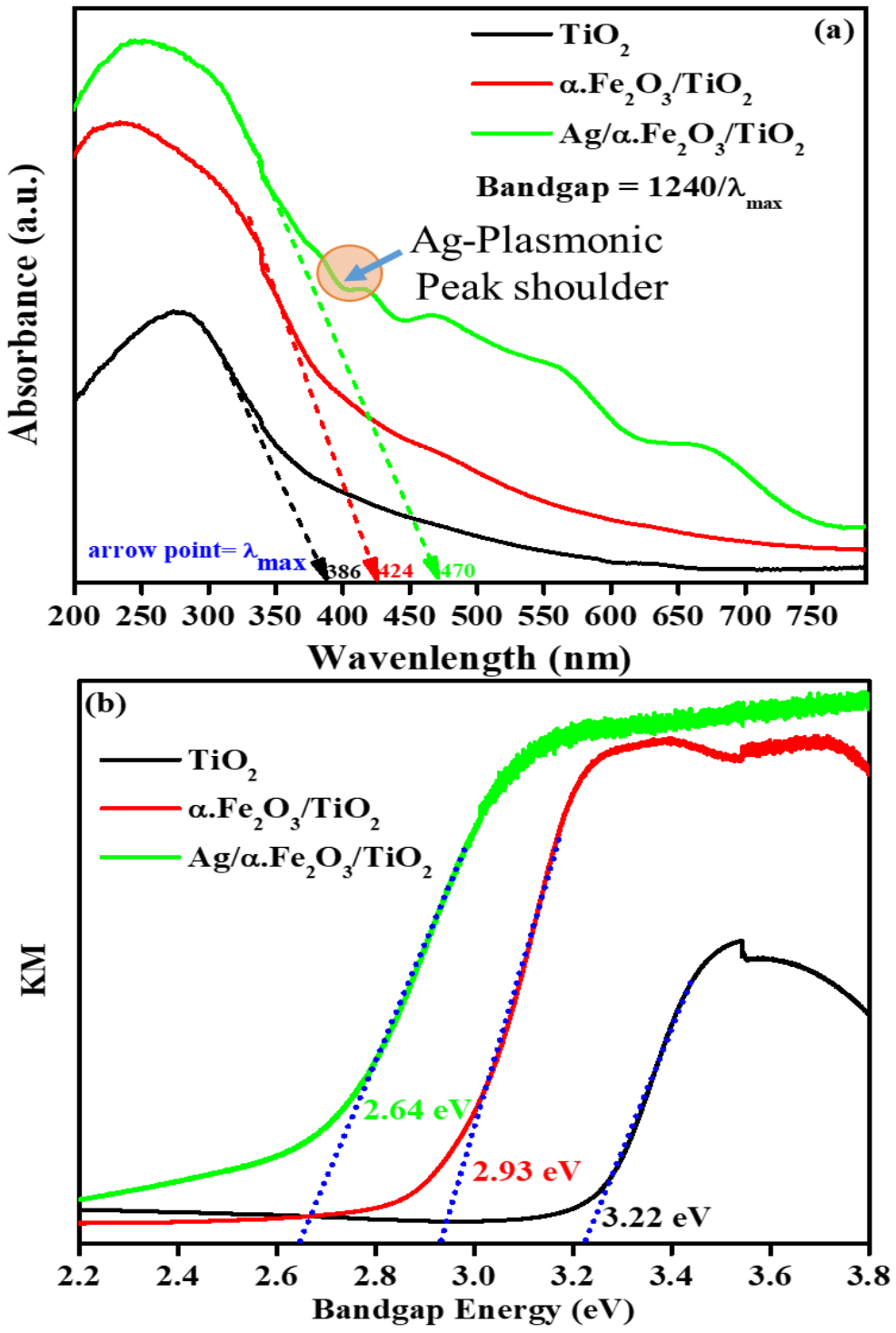

Figure 13: (a) DRS absorption and (b) KM vs. eV band gap spectra of pristine TiO_2, α-Fe_2O_3/TiO_2 and Ag/α-Fe_2O_3/TiO_2 photoanodes.

Furthermore, Figure 14 depicts photoluminescence (PL) spectra for TiO_2, α-Fe_2O_3/TiO_2, and Ag/α-Fe_2O_3/TiO_2 photoanodes. The enhanced PEC property of the later may occur because of the exceptional plasmonic and charge trapping properties of Ag, which enhanced the opposite charge separation as well. Moreover, the dramatic decrease in the PL intensity with the deposition of Ag can be correlated to the formation of locally Schottky junctions at the interface with rather much higher potential gradients, which resulted in higher PEC activity of the semiconductor oxide heterostructures. This leads to higher charge separation capacity of the excitons [84, 115].

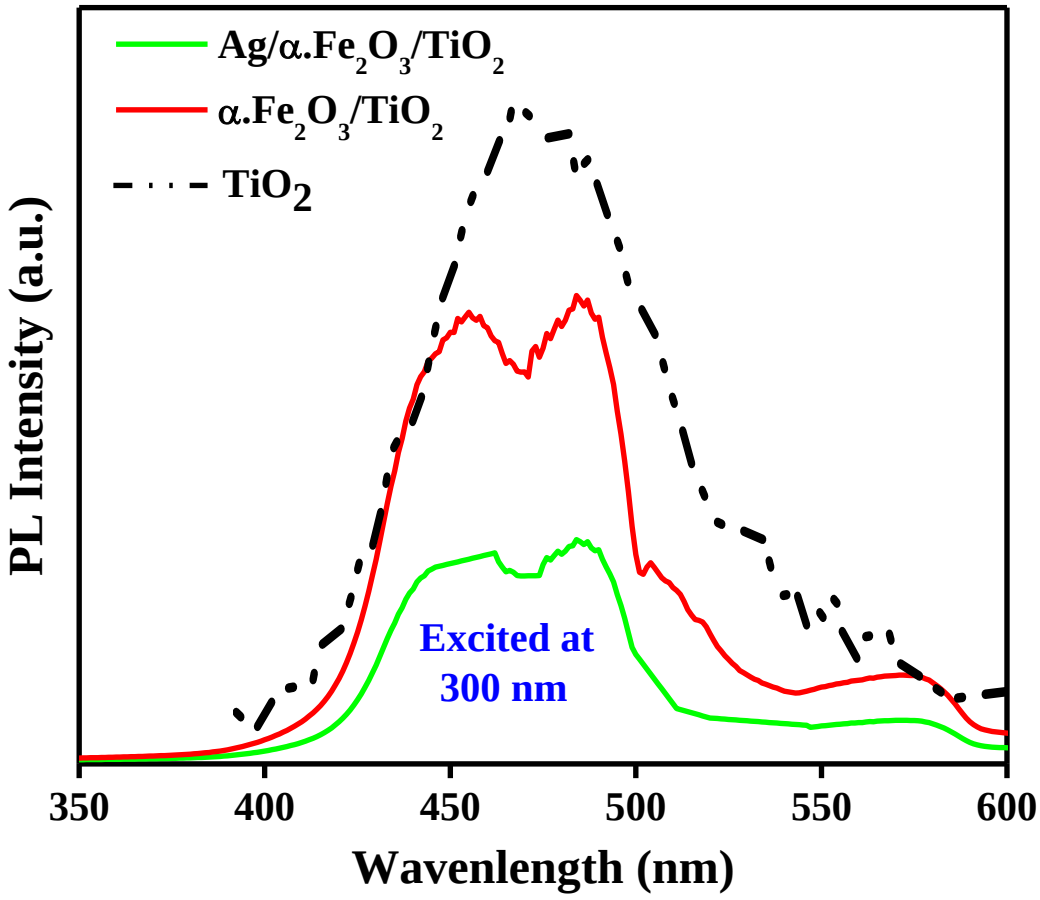

Figure 14: Room Temperature Photoluminescence (PL) spectra of TiO_2, α-Fe_2O_3/TiO_2 and Ag/α-Fe_2O_3/TiO_2.

3.3.2 Photoelectrochemical performance

The PEC performance of the TiO_2, α-Fe_2O_3/TiO_2 and Ag/α.Fe_2O_3/TiO_2 heterostructures was explored via cyclic voltammetry (CV), linear-sweep voltammetry (LSV) and chronoamperometry. Figure 15(a) presents the LSV measurements under regular ON/OFF solar illumination. In all cases, the dark current remained significantly lower. while under the simulated light, the current densities increased immensely with the voltage, which is indicated by the *I-V* spectra. The results revealed that the current density increased in the order of TiO_2 < α-Fe_2O_3/TiO_2 < Ag/ α-Fe_2O_3/TiO_2. The *I-V* spectra also revealed that up to 1.0 V, the current densities under light for the TiO_2 NTAs and α-Fe_2O_3/TiO_2 do not increase significantly. However, for Ag/α-Fe_2O_3/TiO_2, the photocurrent density showed an onset potential at 0.4 V and reached a plateau at 0.9 V. The early onset current elevation can be attributed to the plasmonic nature of Ag, which not only provided extra electrons but also imparted SPR properties to the photoanode [116]. For all the substrates, the photocurrent densities reached saturation at 1.5 V. However, the photocurrent densities observed at the thermodynamic potential (1.23 V) of the water oxidation reaction were ~0.54, ~1.05 and ~2.59 mA/cm^2 for TiO_2, α-Fe_2O_3/TiO_2 and Ag/α-Fe_2O_3/TiO_2, respectively. A significant dark current appeared above 1.23 V for the latter sample, which can be attributed to photocorrosion [117]. The *I-t* ON/OFF cycles indicated that during light chopping, the photocurrent reached a maximum value under illumination and diminished in the dark at 1.23 V. The photocurrent values under the light are almost on the same order as those obtained using LSV.

Figure 15(b) shows the long-term *I-t* stability curve obtained from photoanodes under light with an illumination period of 3600 s. For the Ag/α-Fe_2O_3/TiO_2 photoanode, the stability curve initially decreased from ~2.60 to ~2.50 mA/cm^2 and then remained stable until later. For α-Fe_2O_3/TiO_2, the stability curve initially remains relatively stable but showed a significant decrease after 2500 s, which can be attributed to the PEC corrosion of the α-Fe_2O_3/TiO_2 photoanode due to the susceptibility of the α-Fe_2O_3 NPs. As expected, TiO_2 showed considerable resilience and stability for most of the period.

Electronic impedance spectroscopy (EIS) was performed to investigate the interfacial charge transfer in pristine TiO_2, TiO_2/α-Fe_2O_3 and Ag/α-Fe_2O_3/TiO_2 photoanodes from the electrolyte to the surface of the electrode (point of reaction). All samples were analyzed under dark and simulated solar illumination with a DC voltage sweep across the working electrode. Nyquist plot spectra with representative semicircles are provided in Figure 15(c) for the labeled photoanodes. The resistance range decreased in the order of TiO_2 > α-Fe_2O_3/TiO_2 > Ag/α-Fe_2O_3/TiO_2 both in dark and light. Additionally, the respective sample shows lower impedance value under light as compared to dark, suggesting good charge transfer. The lowest impedance value in the latter case was attributed to the rapid interfacial charge transfer from the electrolyte bulk to the electrode surface; i.e., the overall conductance is the highest for the Ag/α-Fe_2O_3/TiO_2 photoanodes [92].

In order to explain the effects of α.Fe_2O_3 and Ag NPs on the electronic behavior of TiO_2 NTs, Mott–Schottky (MS) plots were obtained in the aqueous solution of Na_2SO_4 (0.5M) at 1 kHz frequency (Figure 15 d). The plots show positive slopes, which attributes that all photoanodes are n-type semiconductors i.e. electrons are the majority carriers.

Additionally, the slope of TiO_2 is greater and at more negative voltage than the rest, which replicates that $\alpha.Fe_2O_3/TiO_2$ and $Ag/\alpha.Fe_2O_3/TiO_2$ photoanodes possess higher electron donor density [118]. The slope lines touch the quasi-linear regions at -0.204 V, -0.179 V and -0,171 V on extrapolation, which are the flat band potentials (V_{fb}) of TiO_2, $\alpha.Fe_2O_3/TiO_2$ and $Ag/\alpha.Fe_2O_3/TiO_2$ NTAs, respectively. The remarkable shift of V_{fb} values in case of $\alpha.Fe_2O_3/TiO_2$ and $\alpha.Fe_2O_3/TiO_2$ NTAs suggest that the band bending took place with the incorporation of $\alpha.Fe_2O_3$ and Ag NPs in the TiO_2 NTs [118], which is essential for effective charge transfer between heterojunction as in the present study. The enhanced electrical conductivity can increase the lifetime of photoexcitons, giving rise to a decrease in the electron−hole recombination [119].

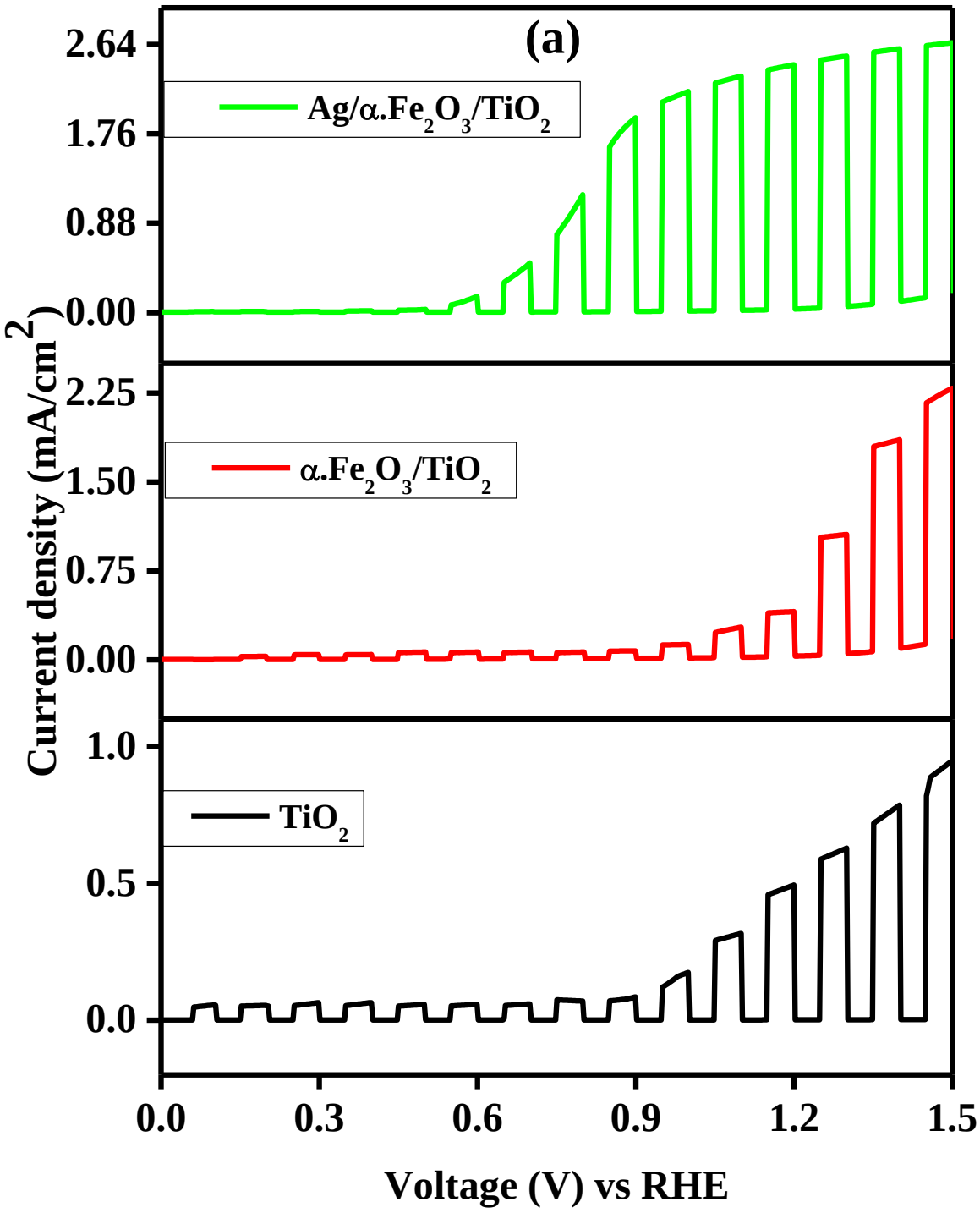
(a)
Ag/α.Fe2O3/TiO2
α.Fe2O3/TiO2
TiO2
2.64
1.76
0.88
0.00
2.25
1.50
0.75
0.00
1.0
0.5
0.0
0.0
0.3
0.6
0.9
1.2
1.5
Current density (mA/cm2)
Voltage (V) vs RHE

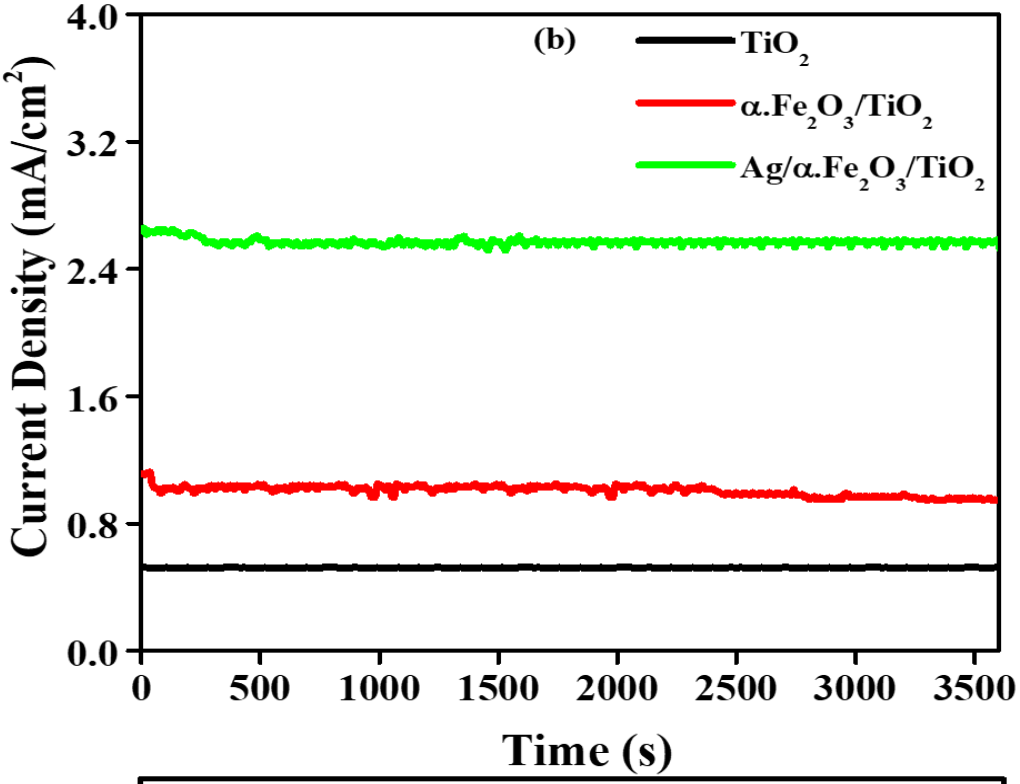
(b)
TiO2
α.Fe2O3/TiO2
Ag/α.Fe2O3/TiO2
Current Density (mA/cm2)
Time (s)
4.0
3.2
2.4
1.6
0.8
0.0
0
500
1000
1500
2000
2500
3000
3500

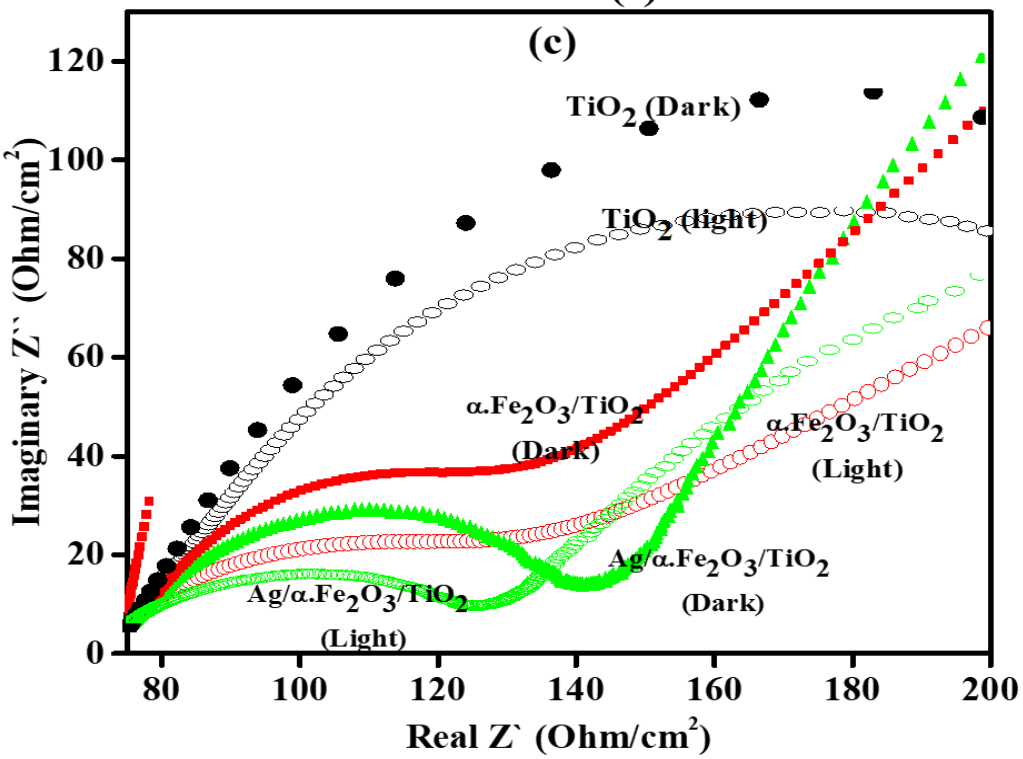
(c)
TiO2 (Dark)
TiO2 (light)
α.Fe2O3/TiO2
(Dark)
α.Fe2O3/TiO2
(Light)
Ag/α.Fe2O3/TiO2
(Dark)
Ag/α.Fe2O3/TiO2
(Light)
Imaginary Z`` (Ohm/cm2)
Real Z` (Ohm/cm2)
120
100
80
60
40
20
0
80
100
120
140
160
180
200

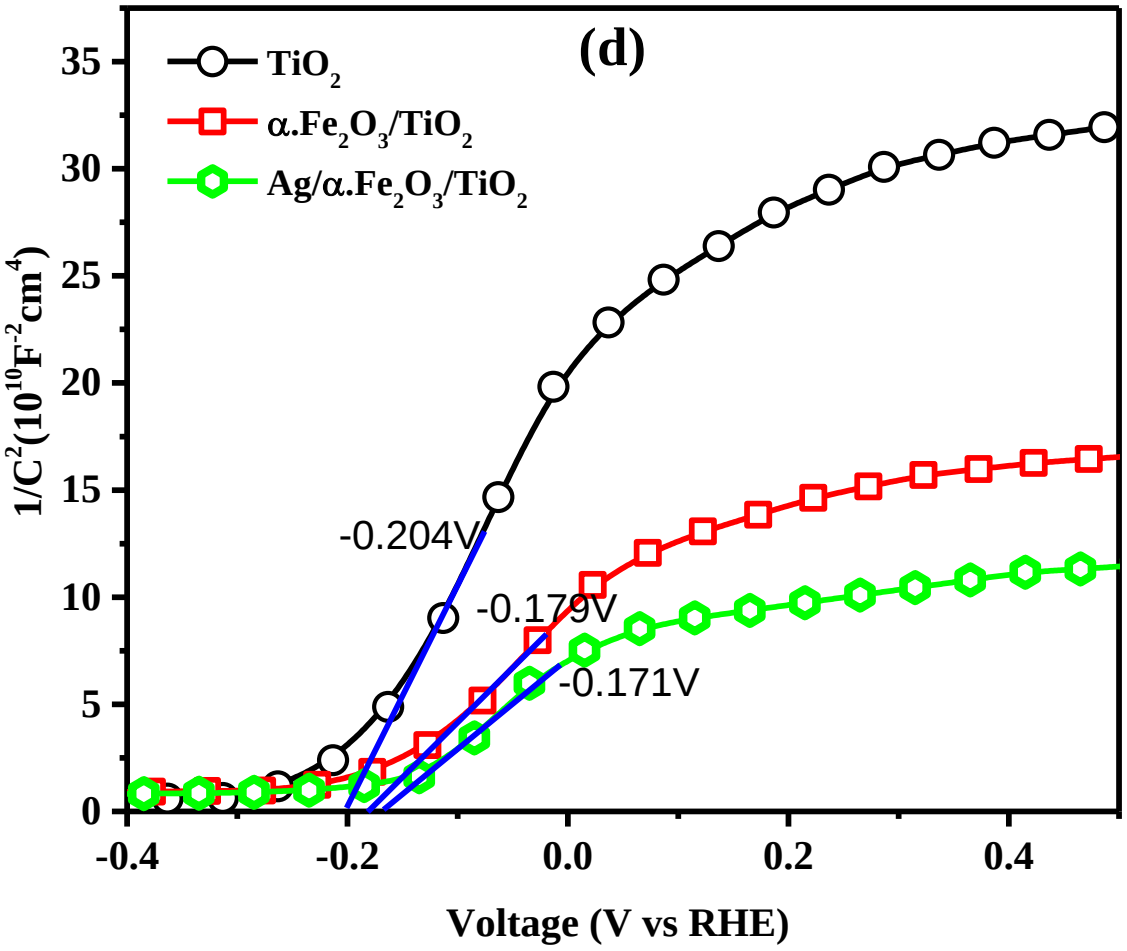

Figure 15: Photoelectrochemical measurements (a) chopped linear-sweep voltammograms (I-V), (b) chronoamperometric (I-t) stability curve and (c) electrochemical impedance spectroscopy (EIS) spectra under light and dark conditions. (d) effects of $\alpha.Fe_2O_3$ and Ag NPs on the electronic properties of TiO_2 NTs (Mott–Schottky plots)

The photocurrent densities achieved in this study are significant compared with those in the literature [84, 120, 121]. Table 2 provides comparative current densities obtained from the α-Fe_2O_3/TiO_2 and Ag/α-Fe_2O_3/TiO_2 nanostructures. The reported photocurrent values indicate that our material generates the highest current density, which suggests that the *in situ* electrochemical syntheses of α-Fe_2O_3/TiO_2 and Ag/α-Fe_2O_3/TiO_2 induces greater PEC characteristics in the materials because of the tailored growth of the aligned TiO_2 nanotubes and the efficient deposition of Fe_2O_3 and Ag. Further comparisons can be made with the results reported by Hung et al., who also synthesized Ag/Fe_2O_3/TiO_2 heterostructures via the more rigorous and time-consuming sol-gel method [84]. They reported a maximum photocurrent value of 5.0 x 10^{-7} A/cm^2, which is lower than the value obtained in the present work. The probable reason for their lower current could be due to the irregular morphology and lower resilience of the Fe_2O_3/TiO_2 hybrid formed via the traditional sol-gel technique. Similarly, Li et al. reported a high photocurrent density of 1.9 mA/cm^2 for TiO_2-coated hematite prepared using ALD at 1.23 V in a highly basic 1.0 M NaOH solution. It is well known that metal oxides are not particularly stable in more basic electrolytes. Moreover, their chronoamperometric results under solar light were significantly lower, and the plateau reached 0.5 mA/cm^2 as the stability decreased (Table 2). The possible reasons for the enhanced current density in our case are the better morphology and controlled deposition, which can play important roles in charge transfer, charge recombination, visible-light absorption and photoanode stability [122]. It has been reported that grain boundaries can inhibit charge transfer; thus, the morphology and structure play vital roles in the overall photocurrent density generation [123].

Table 2: Reported photocurrent densities for Fe_2O_3/TiO_2 nanostructures synthesized using different methods and with different morphologies

S.No	Nanostructure	Synthesis	Morphology	Photocurrent density (A/cm^2)	Ref
1	Fe_2O_3/TiO_2	Hydrothermal and ALD methods	Hematite NRs covered with ultrathin ALD TiO_2	1.90×10^{-3}	[92]
2	Fe_2O_3/TiO_2	Hydrothermal method	Tetragonal nanorod-shaped TiO_2 covered with Fe_2O_3 NPs	0.13×10^{-3}	[120]
3	Fe_2O_3/TiO_2	Hydrothermal method	Tetragonal nanorod-shaped TiO_2 covered with a dense Fe_2O_3 layer	1.8×10^{-3}	[121]
4	Fe_2O_3/TiO_2	Sol-gel method	Variable shaped TiO_2 and Fe_2O_3 NPs	1.0×10^{-7}	[84]
4`	Ag-Fe_2O_3/TiO_2	Sol-gel method	Variable shaped TiO_2 and Fe_2O_3 NPs	5.0×10^{-7}	[84]
5	Fe_2O_3/TiO_2	Pulse sonication-assisted electrochemical synthesis	NPs of Fe_2O_3 deposited on aligned TiO_2 nanotubes	1.0×10^{-3}	This study
5`	Ag/Fe_2O_3/TiO_2	Pulse sonication-assisted electrochemical synthesis	NPs deposited on aligned TiO_2 nanotubes	2.59×10^{-3}	This study

3.3.3 Proposed Mechanism for Water Splitting

A possible mechanistic view of the PEC response of the Ag/α-Fe_2O_3/TiO_2 photoanodes based on the available literature is shown in Figure 16 [124, 125]. The band gap of the TiO_2 NTAs is ~3.24 eV, which is not suitable for visible-light absorption, and they showed the lowest current (~0.54), even at 1.23 V. The addition of α-Fe_2O_3 and Ag significantly enhanced the current density of Ag α-Fe_2O_3/TiO_2. As predicted in Figure 16, the band gap of α-Fe_2O_3 is 2.3 eV, and, therefore, it can shift light absorption into the visible regime to substantially reduce the band gap, i.e., from 3.24 eV to 2.93 eV in our case. This effect resulted in greater absorption and ultimately more photocurrent generation from α-Fe_2O_3/TiO_2 [126]. Electrons might drift from the hematite to the conduction band (E_c) of TiO_2 because Ti^{3+} states were observed in the electron paramagnetic resonance (EPR) spectrum after irradiation, and the states formed via Ti^{4+} reduction by electrons from the E_c band of Fe_2O_3 [125, 127]. Based on this discussion, we assumed that the electrons are excited from the valence band (Ev) of Fe_2O_3 to different energy levels of E_c at λ = 424 nm. The lower energy photoelectrons recombine with the holes, and electrons with more energy than the E_c of TiO_2 drift and reduce H^+ ions to H_2 [125]. Moreover, the photogenerated holes will oxidize water into O_2. The OER is dominant over the hydrogen evolution reaction (HER) because the overall band position of Fe_2O_3/TiO_2 is below the hydrogen band position and a very high bias is required to generate hydrogen [7].

Similarly, for Ag/α-Fe_2O_3/TiO_2, Ag imparted its plasmonic and electron-donating properties to the overall system and further increased the current density and %IPCE value. The surface electrons in Ag are mainly responsible for this phenomenon because

they are readily available to holes (h^+) and decrease the recombination of excitons by providing electrons to the system. The surface electrons also oscillate with a certain frequency and induce the SPR effect [116], which increases the absorption capability of a material in the visible region and further enhances the water-splitting ability of the photoanode. Additionally, HER process is also dominated, which converted the hot electrons to harvest solar energy [111]. The PL spectra (Figure 14) of the electrochemically synthesized TiO_2, α-Fe_2O_3/TiO_2 and Ag/α-Fe_2O_3/TiO_2 photoanodes showed significant quenching in case of Ag/α-Fe_2O_3/TiO_2 in the emission bands. Sharp emission bands are normally attributed to the maximum recombination of excitons, i.e., electrons (e^-) and holes (h^+) [128]. Thus, the decrease in the PL intensity at ~440 – 480 nm in the heterostructure material signified that the e^-/h^+ recombination rate was comprehensively reduced. The EIS results further supported the proposed mechanism, as the Nyquist semicircular plots of resistance (Figure 15c) show significant decreases in the radii. The decrease in the impedance was related to the lower rate of recombination and higher interfacial charge transfer, as discussed above [125]. Mott–Schottky (MS) plots (Figure 15d), also show that incorporation of $\alpha.Fe_2O_3$ and Ag NPs in TiO_2 NTs, effectively increase electrons in the conduction bands as they are majority carriers. Additionally, the slope of $Ag/\alpha.Fe_2O_3/TiO_2$ photoanodes is lower and has low V_{fb} value of -0,171 V, suggesting effective charge transfer between heterojunction. The enhanced electrical conductivity can increase the lifetime of photoexcitons, giving rise to a decrease in the electron−hole recombination [119]. The lower recombination rate is always favorable for effective photocatalytic applications [105, 125]. The LSV and chronoamperometric results shown in Figures 15(a,b) clearly indicate that the highest

OER activity during water splitting occurred with the Ag/α-Fe_2O_3/TiO_2 photoanodes because the current density values are on the far positive ordinate of voltage for this material [129].

The overall results and proposed mechanism indicated that Fe_2O_3 deposition and Ag decoration significantly increased the conductance and current density of TiO_2 and the stability of the photoanode via efficient heterostructure formation, improved nanoarchitecture, and the dominant SPR phenomenon.

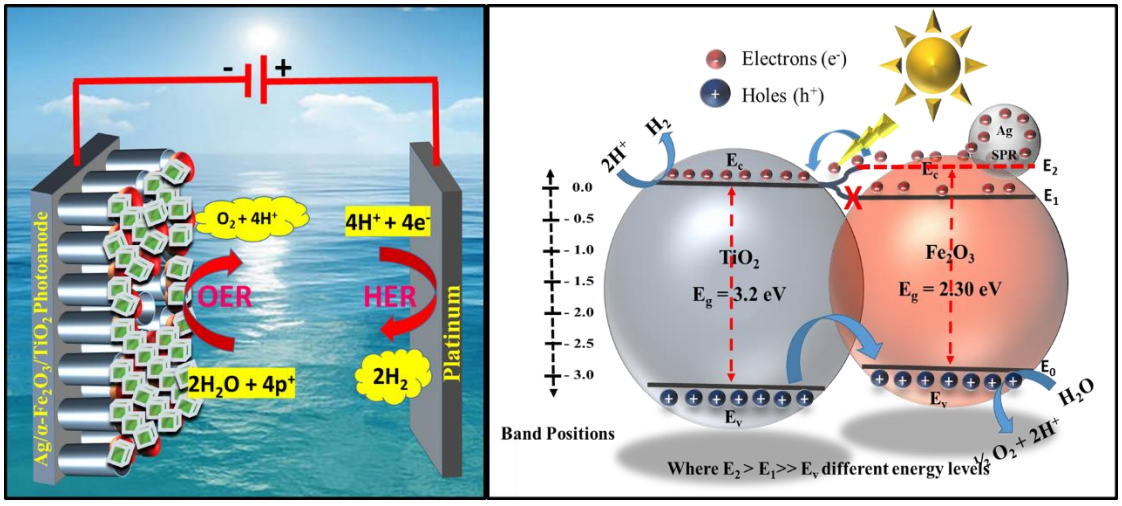

Figure 16: PEC water splitting and oxygen evolution reaction mechanisms over the Ag/α-Fe_2O_3/TiO_2 heterostructures

CHAPTER 4

ELECTROCHEMICAL SYNTHESIS OF INDIUM OXIDE (In_2O_3) NANOWIRES AND THEIR PHOTOELECTROCHEMICAL WATER SPLITTING

4.1 Introduction

Nanoarchitecting of various shaped materials is one of the best tools to control the optoelectronic characteristics of the nanomaterials for specific applications. Various nanoarchitectures have been widely reported by researchers such as nanotubes, NRs, nanobolts, nanowires (NWs), nanosheets, nanoflowers or other hierarchical NWs [66, 130–132]. Preparation of NWAs receives great interest from the researchers in recent years due to their tunable properties and efficient charge transfer characteristics due to longer pathway [131]. Different synthetic protocols have been adopted to control the morphology of nanomaterials such as surfactant assistant hydrothermal methods, sol-gel etc. The major problem with those methods is the purity and yield of the NPs. Normally it is very difficult to remove the surfactant components from the nanomaterial products due to their sticky nature [133]. Therefore, sophisticated methods should be practiced for the development of shape-controlled nanomaterials. Recently, many experts employed anodization technique for the preparation of nanoarchitectures [134–136]. In this method, the material (to be treated) served as an anode, while platinum acts as a cathode. Anodization method is found useful for the surface modification of valuable metals like Titanium, Tungsten, Tantalum etc. to produce controlled shape oxide NWs. As compared to other traditional metal oxide synthesis methods anodization is proved to be more

advantageous as by controlling limited parameters such as composition, pH of electrolytes and applied voltage etc., we can obtain nonmaterial products with high purity and single-phase morphology. As stated earlier, the NWs materials were found useful in photocatalytic and photoelectrochemical (PEC) applications due to the fact that these materials are suitable for charge transfer as they provide a longer pathway to charges and hence also reduce the recombination of electrons and holes. Likewise, the arrayed nanoarchitectures showed efficient visible solar driven PEC water splitting performance. Due to the need of environmentally friendly and regenerative sources of energy, water splitting is arising as a useful technique to be accompanied with the traditional sources of energy i.e. fossil fuels, hydrothermal, wind energy etc. Water splitting is preferable as water abundantly exists in the universe. The process has environmental fitting liability and extreme reproducibility. The scientists are trying to synthesize suitable materials for this purpose, which should be cheaper, nontoxic and highly efficient. The graphene-based nanomaterials are found useful in dye-sensitized based solar cells for energy generation [137] and PEC water splitting [138]. Lately, single dimensional (1D) earth abundant nanomaterials have been explored for PEC water splitting applications with significant photocurrent yields [139], yet the search for best materials is continued.

More recently, Indium oxide (In_2O_3) is an also considered to be one of the applicants for efficient PEC water splitting. It is an n-type semiconductor and has tunable band gap [140]. Due to remarkable optoelectronic properties, In_2O_3 has utilized widely used in different areas like transistors [141] and biosensing [142, 143], gas sensing [144, 145], hydrogenation catalysis of CO_2 [146] and energy harvesting [147]. Moreover, the band gap of this material can be tuned for photocatalytic applications. Xu et al. fabricated

In_2O_3/In_2S_3/Ag nanocubes on the FTO substrate using electrodeposition method. This material showed photocurrent density of 8.75 mA cm^{-2}, which is more than 4-folds of the photocurrent density of pure In_2O_3. The good efficiency of the composite was correlated to the efficient charge separation of excitons and plasmonic effect of Ag [115]. Many other methods have been reported for the synthesis of indium oxide, but those methods have some or more discrepancies. For example, the well-established hydrothermal synthesis methods have been employed for In_2O_3 preparation by many researchers, but the reaction time and temperature are the two major concerns. Also, the sample may contain impurities due to shifting from one crucible to other during sampling. More importantly, there is no report published on the growth of aligned NAs via electrochemical anodization methods to the best of our knowledge. Therefore, in this article, we are going to report a facile one-step electrochemical anodization technique for the preparation of In_2O_3 NWs at controlled morphology. This article represents the first attempt to use anodization method for In_2O_3 NWs synthesis to the best of our knowledge. The advantage of anodization technique is to obtain highly pure single phase In_2O_3 NWs, with more uniform morphology. Furthermore, the anodization was performed at a relatively low voltage at room temperature for short intervals of time, which is highly productive, reproducible and cheaper from energy and time consumption point of view. The localized surface plasmon resonance (LSPR) effect of gold, which enhances the solar absorption in the visible region, will be explored. The LSPR is significantly influenced by the size, shape and loading concentration of NPs [148].

4.2 Methods and Materials

4.2.1 Synthesis of In_2O_3 and Au/In_2O_3

The experiment was carried out at different voltages, by using PeakTech® DC power supply model 6005D, with 30V supply capability. Pure Indium metallic sheet (0.30mm x 100mm x 100mm) is purchased from Nilaco Corporation Tokyo and 0.5x1 cm^2 pieces were used as anodes during anodization. Analytical grade NaF (Mol wt = 41.99 g/mol) was obtained from Sigma Aldrich, which acted as an etching agent for NWAs formation. Ethylene Glycol (99.8% purity) is used as a major component in solution and is also purchased from Sigma Aldrich. The optimized concentration of the solution was obtained after various successful attempts and the final ratio of the solvent components was adjusted at 95% ethylene glycol 5% DI water. The DI water significantly enhances the solubility of the electrolyte in the ethylene glycol. The anodization was carried out in 0.5 M NaF and larger portion of ethylene glycol solvent to provide less aggressive environment due to highly malleable nature of the In_2O_3 metallic substrate. In case of strong electrolytes, the Indium surface is very unstable, and hence completely deteriorated. The anodization is performed at various time intervals and voltages to achieve the optimize reaction time and voltage for well uniform and homogenous In_2O_3 NWs growth. The optimized reaction conditions determined to be 4 hrs and 10 V, respectively. All the experiments were performed at room temperature. After anodization, the treated Indium metallic foil sonicated for 15 s with DI water to remove the debris and then allowed to dry in the open air.

4.2.2 Material Characterizations

a. Physicochemical Characterizations

The X-ray characterization was carried out by the help of Rigaku X-ray diffractometer with CuKά radiation from $2\theta = 20^0$ to 70^0 with scan rate 2 degrees/min, to find out the facet arrangement and crystallinity of the formed NWs shape. The morphological study was performed by using the field emission scanning electron microscope (FESEM) to analyze the distribution and size of the achieved In_2O_3 NWs. The LYRA 3 Dual Beam (Tescan) SEM instrument operated at an acceleration voltage of 20 kV is used to get SEM micrographs. FESEM is also equipped with energy dispersion spectroscopy (EDX, Oxford Instruments), which is used for determination of the elemental ratio and confirmation of gold, indium and oxygen elements. Raman spectrum was recorded from 50 to 1000 cm-1 with the help of LabRAM HR high-resolution Raman spectrometer (HoribaJobin Yvon), which used He–Ne laser (Red 632 nm) with a D1 equipped filter at room temperature. The X-Ray ESCALAB 250Xi X-ray Photoelectron Spectrometer (XPS) Microprobe device was used to study the chemical nature of the component elements in the Au-In_2O_3 NWs. Avantage software was utilized for peaks deconvolution. Carry 5000 model was used to measure the ultraviolet/visible-diffuse reflectance spectrum (UV/Vis-DRS) of as-synthesized substrates sample from 200 nm to 800 nm at scan rate 50 nm/min. The tauc plots were obtained by plotting F(R) vs eV and then use the Kubelka-Munk function [149]. The photoluminescence emission spectrum was recorded by fluorescence spectrometer (FluoroLog-3-2iHR) Horiba model at 300nm excited wavelength by using S1-(R928) (SCD1) detector with a 450W xenon lamp.

b. Photoelectrochemical Measurements

PEC water splitting was performed in a three-electrode PEC cell containing a 0.5 M Na_2SO_4 (Sigma Aldrich) electrolyte (pH 7.0). The as-grown In_2O_3 and Au/In_2O_3 NWs substrates were used as the working electrodes and were controlled by a more sophisticated Autolab potentiostat in a three-electrode cell. Platinum (Pt) and saturated calomel electrode (SCE) served as the counter and reference electrodes, respectively. A solar simulator (Oriel Sol-3A Newport) provided artificial solar light irradiation, and the power was calibrated using a silicon diode solar cell (Oriel-diode) and fixed at 100 mW/cm^2, which is equivalent to 1 SUN. The solar simulator was also equipped with AM-1.5 G and UV cutoff ($\lambda > 420$ nm) filters. For electronic impedance spectroscopy (EIS) measurements, we applied a forward bias set at the open circuit voltage (V_{OC}) with an alternating current (AC) amplitude of 10 mV, between the working (WE) and counter electrodes (CE). The frequency range for EIS was fixed from 100 kHz to 100 mHz. All PEC results were adjusted against RHE by Nernst equation [150] i.e.

$$\mathbf{E_{RHE} = E_{(SCE)} + 0.059\ pH + E^{o}_{(SCE)}} \qquad \mathbf{(4.1)}$$

4.3 Results and Discussion

The morphological features of In_2O_3 and Au-In_2O_3 NWAs are given in Figures 17(a,b). The FESEM micrographs of anodized In_2O_3 NWs taken at low and high magnification indicated the uniform 1D growth of In_2O_3 NWs over the surface of the metallic Indium foil. The thickness of the individual wire is about 30-40 nm. Dense NWAs can be clearly seen in the given images. There are no visible morphological changes recorded after the deposition of gold as shown in Figures 17(c,d). The existence of gold in Au/In_2O_3 NWAs is confirmed by the EDX spectrum in Figures 18(a,b).

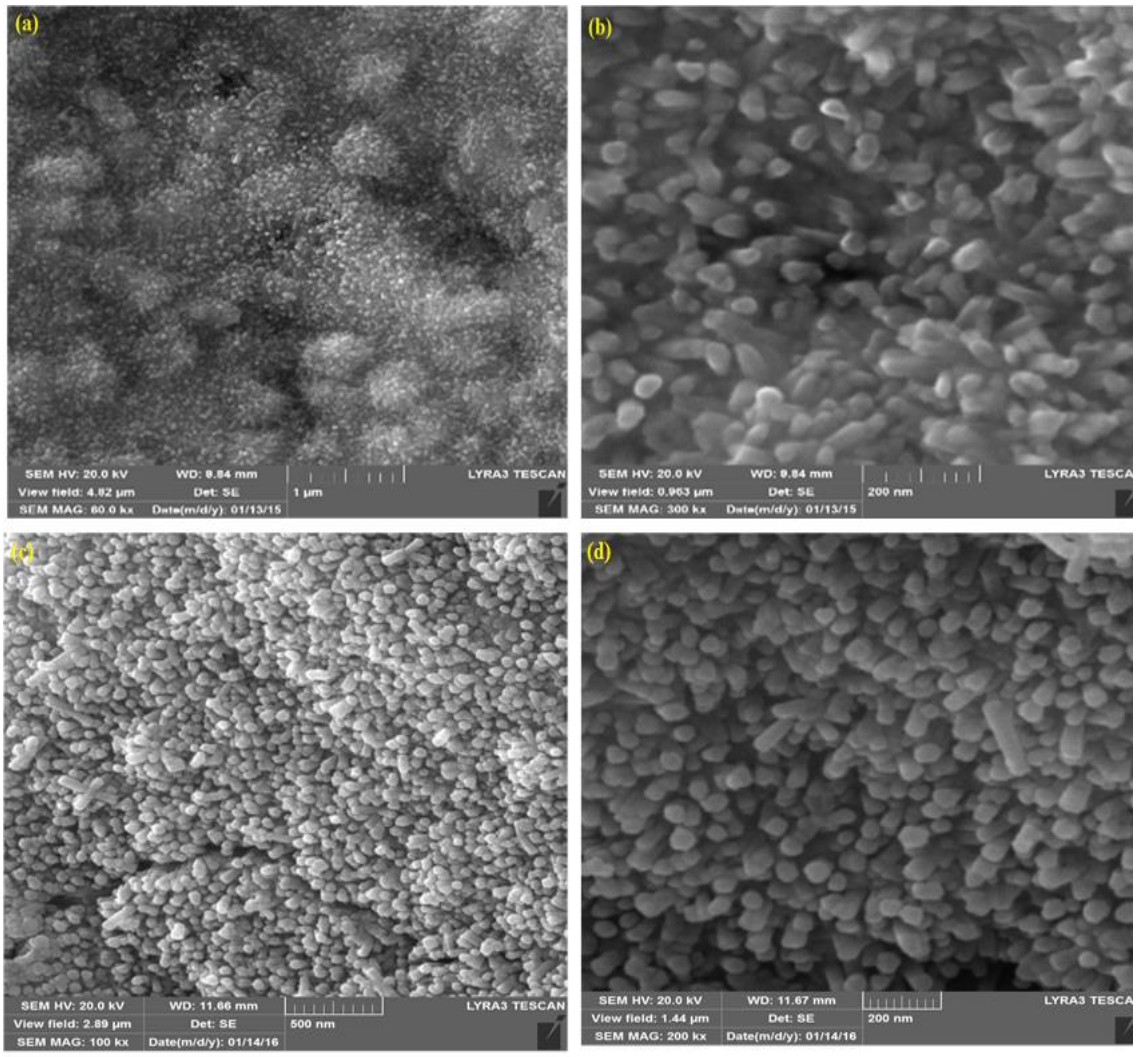

Figure 17: Various magnifications SEM micrographs of (a)-(c) In_2O_3, and (d) Au/In_2O_3 NWs

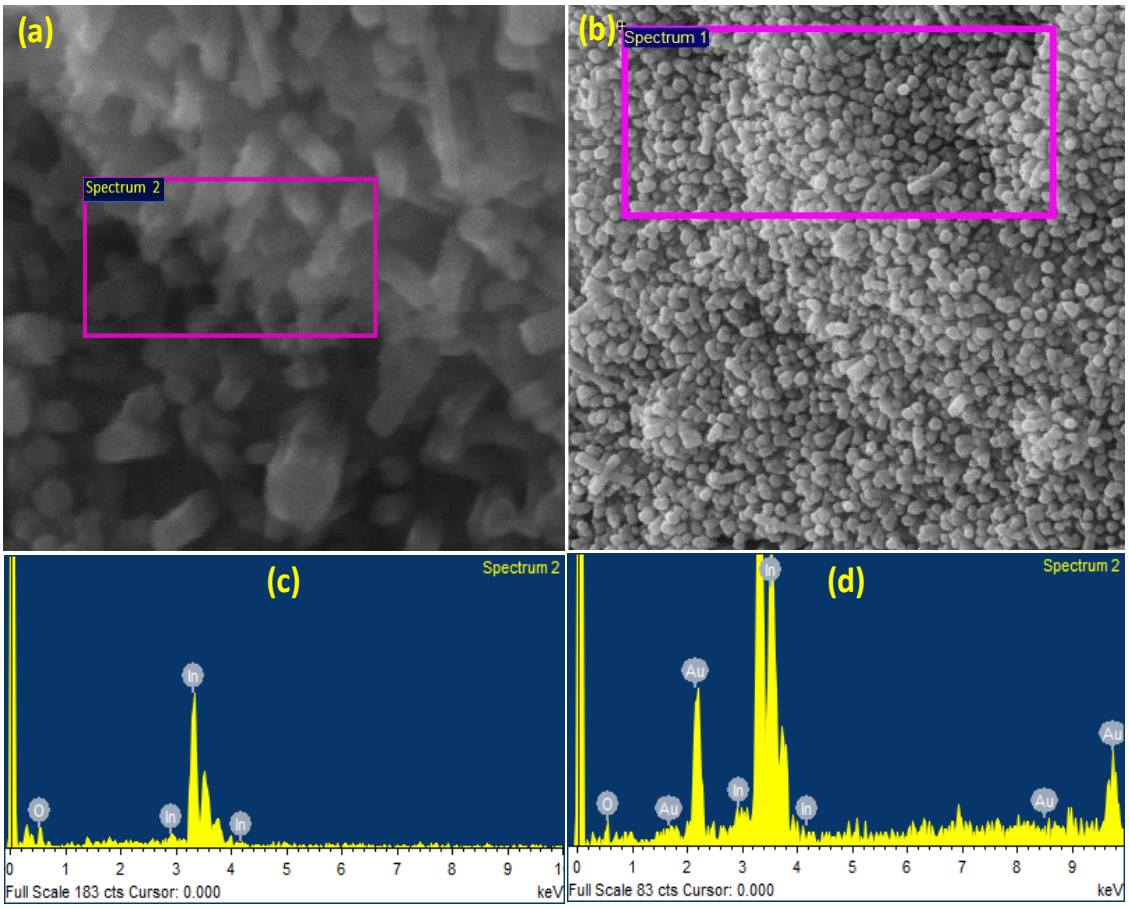

Figure 18: EDX spectra of (a, c) In_2O_3 NWs, and (b, d) Au-In_2O_3 NWs

The crystallinity and phase purity of anodized In_2O_3 and Au/In_2O_3 NWs was determined by X-ray diffractometer (XRD). The XRD patterns are provided in Figure 19. All the characteristic patterns are indexed and well matched with the available literature [145, 151]. A characteristic dominant (222) facet oriented at $2\theta = \sim 30^o$ indicates the formation of cubic phase of In_2O_3. The rough average size from this peak is calculated to be ~ 30 nm, by using Debye-Scherrer equation [81, 152]. Other cubic In_2O_3. characteristic XRD patterns are observed at $2\theta = 23^o, 38^o, 44^o, 47.5^o, 53^o, 63^o$. These peaks can be indexed to the (211), (411), (332), (431), (611) and (622) crystal planes of the cubic crystal In_2O_3. The peaks are matched with JCPDS card # 06-0416. The extra peaks for gold arise in the Au-In_2O_3 XRD pattern as well, which are also indexed as red stars. The calculated lattice values for both samples are 10.112 A^0 for a, b and c planes. The sharp XRD peaks also indicated the high crystalline shape of the as-engineered NWs.

The high resolution deconvoluted XPS spectra obtained from the characteristic binding energy regions of the specific element to understand the chemical states of each element. As shown in Figure 20(a), we observed the characteristic doublet Indium peak in at 444.66 and 452.27 for In_2O_3, which is slightly shifted (+0.11 eV) for gold-coated In_2O_3 and the doublet is. The doublets appeared due to the spin-orbital splitting of Indium 3d orbitals into $3d_{5/2}$ and $3d_{3/2}$ spin states. The similar doublet is observed in case of Au/In_2O_3 (Figure 20c). However, the $3d_{5/2}$ and $3d_{3/2}$ peaks are shifted +0.11 eV towards high binding energies and appeared at 444.75 and 452.36 eV, respectively. This energy shift can be attributed to the different chemical environment after the deposition of Au. The oxygen (1s) shows a single peak for both samples in Figures 20(b,d), respectively. in the case of In_2O_3, the deconvolution of this peak gives two sub binding energy peaks at

528.83 and 529.72 eV, which are attributed to the deficient oxygen and In-O bonding, respectively [153]. The comparison of O (1s) peaks in both samples suggest that the oxygen-deficient species increased as the peak area widens due to Au incorporation and temperature treatment. These results suggest that significant oxygen vacancies created on the surface of the pure In_2O_3 in addition to slight high energy shift. The characteristic Au(4f) doublet is observed at the binding energies values of 84.11 and 87.93 eV for Au/In_2O_3 due to incorporated gold NPs. These values predict that gold has maintained its zero oxidation state in the composite [154].

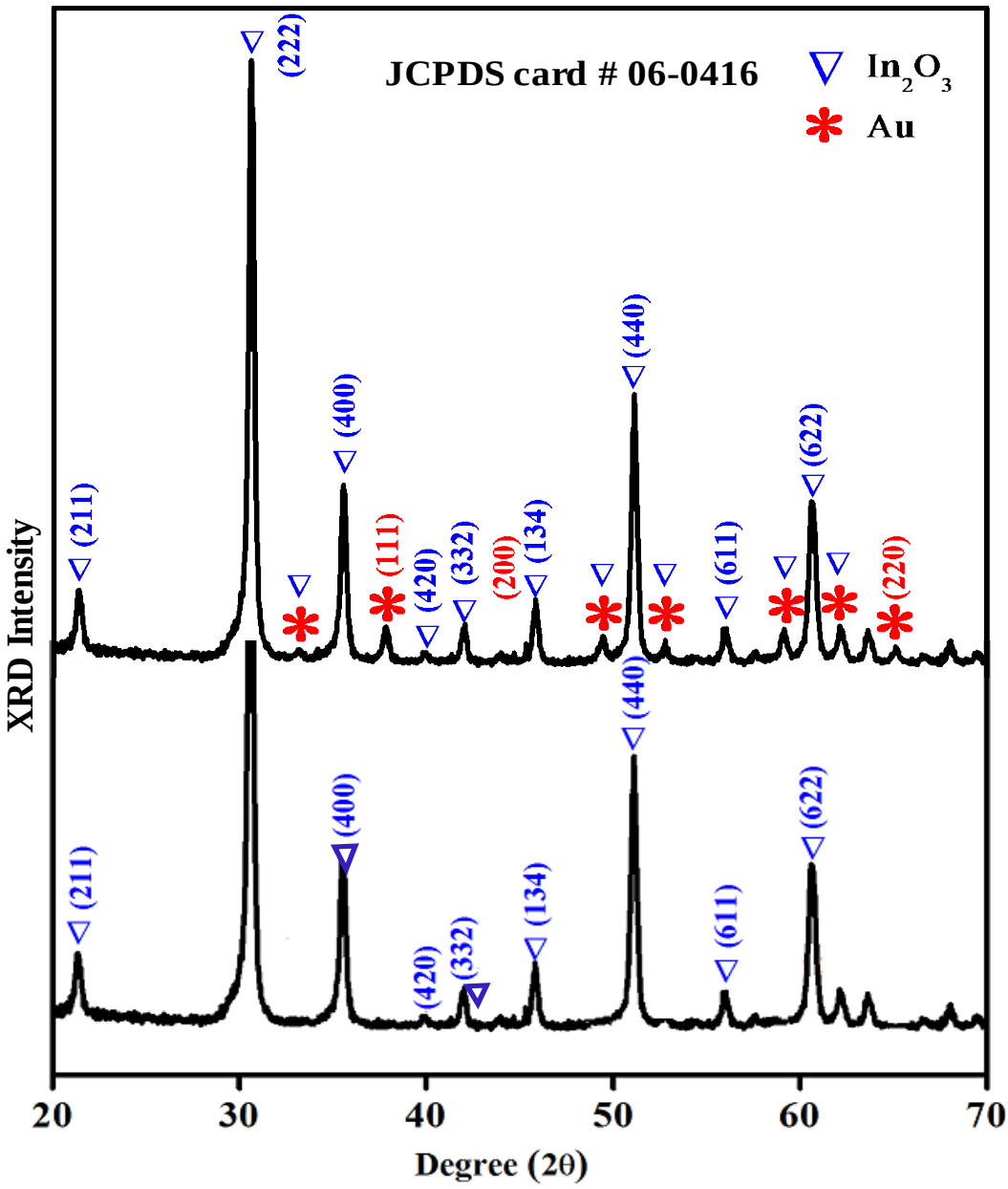

Figure 19: Indexed XRD patterns spectra of In_2O_3 and Au-In_2O_3 NWs

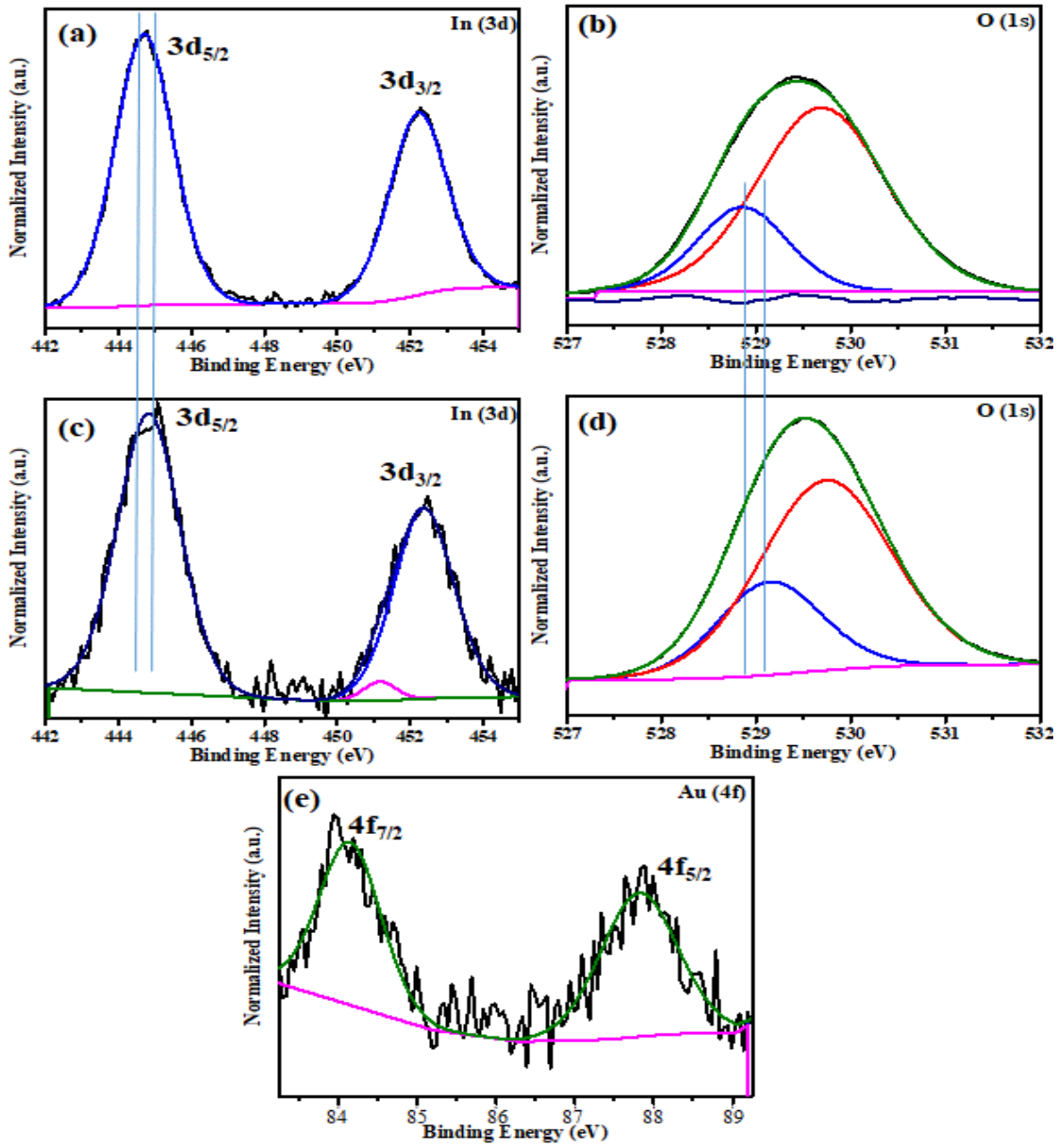

Figure 20: XPS analysis of (a,b) In_2O_3, and (c-e) Au/In_2O_3 NWs i.e. (a), (c) Indium (b) (d) Oxygen and (e) Gold

Figure 21 depicts room temperature vibrational Raman spectrum for Au-In_2O_3 NWs. The spectrum is showing characteristic peaks in the lower vibrational region from 50 to 700 cm^{-1}. It is widely known that the cubic crystal structure of In_2O_3 relates to the I^3_a, T^1_h space group [25]. For such space groups, the most Raman active symmetries are Ag, Eg, and Tg, while remaining Tu vibrations are IR active. The In_2O_3 Raman spectrum shows the expected phonons at 79 (medium), 129.5 (very strong), 189 (weak), 210 (weak), 307 (strong) cm^{-1}, followed by weak peaks at 363.5, 413, 493 cm^{-1} and a medium peak at 628 cm^{-1}. These are fingerprint peaks for In_2O_3 as reported in the literature [25, 26]. Presence of intense phonons in the Raman spectra of In_2O_3 NWs is associated with the excitation of the Ag, Eg, and Tg vibrational modes and also indicated the good crystallinity of the samples as also revealed from the XRD pattern [26]. Some unassigned peaks were also observed at ~ 210, 420 and 880 cm^{-1}, which can be attributed to gold-coated effect and we assigned them as Au-In_2O_3 peaks in figure 21.

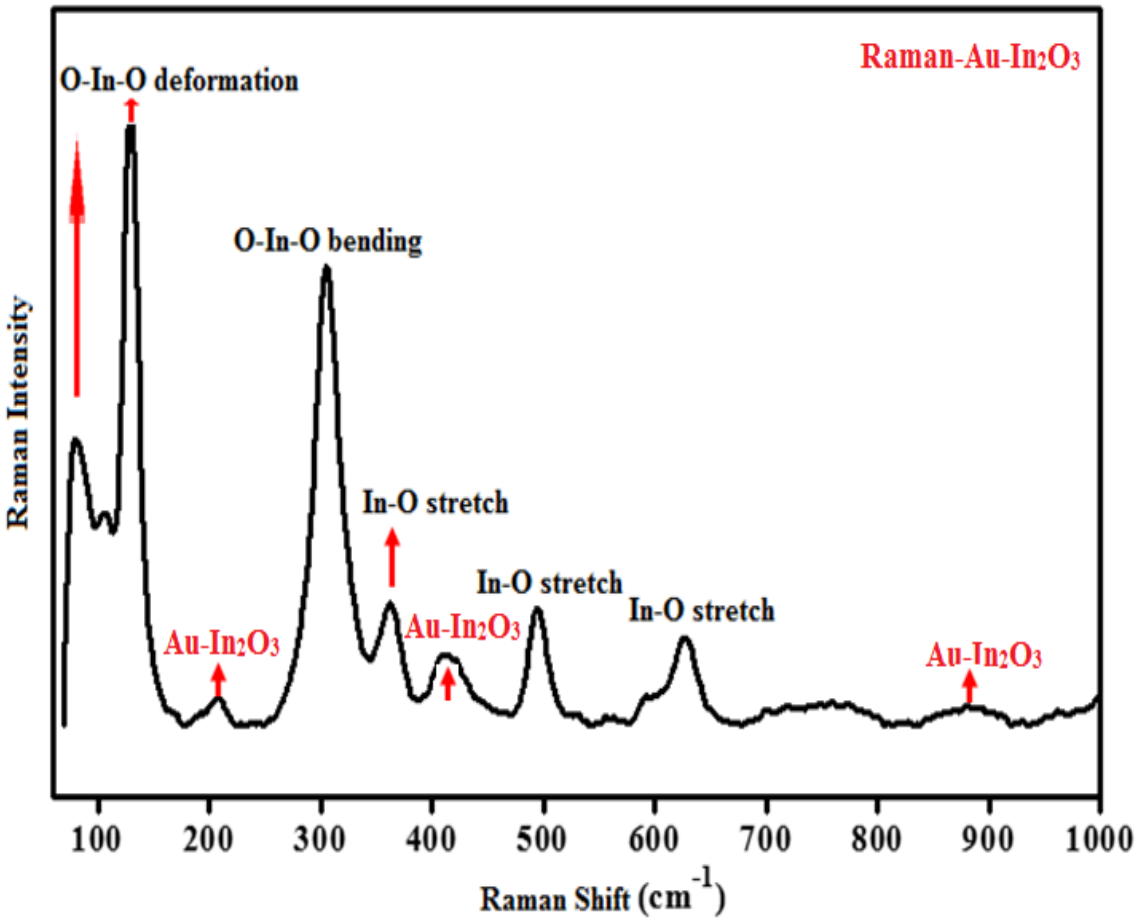

Figure 21: Labelled Raman spectrum taken from Au/In_2O_3 NWs

The UV spectrum is recorded at a slower rate scan rate of 50 nm/min from 200 to 800 nm. Figure 22(a) represented the absorption peaks for pure and gold modified In_2O_3. It can be depicted that the Au/In_2O_3 shows high absorption peak as compared to pristine In_2O_3 sample due to the effect of gold. Additionally, a broad plasmonic band of gold can be seen in the visible range around ~530 nm, caused by the localized surface plasmon resonance (LSPR) effect of surface gold electrons [116]. This LSPR is arising from the overall oscillations caused by the surface hot electron upon simulated solar irradiation of the Visible lamp [148]. The LSPR peak for pure gold is reported at 520 nm, while in case of Au/In_2O_3, the same peak is observed at a higher wavelength i.e. 535 nm (encircled area in Figure 22). The significant red shit is ascribed to the deviation in the reflective index (increase) of the composite sample., which reflect the light with different intensity and angles. These results are consistent with reported $Au@In_2O_3$ core-shell NPs study performed by Chava et al [155]. Moreover, the In_2O_3 peak also shows slight red shift after gold incorporation. Kubelka-Munk (KM) function utilized for the calculations of band gaps. The KM function i.e. $(\alpha h\nu)^n \propto h\nu - E_g$ can be utilized for direct and indirect band gap materials with a slight variation of transition process value (n) i.e. n = ½ for indirect and n = 2 for direct band gap materials. E_g, α, ν and h represent the band gap, absorption coefficient, frequency of light and plunk`s constants. Figure 22(b) (inset) shows the band gap calculations for both materials and as expected the band gap for Au-In_2O_3 is 2.90 eV, which is 0.23eV lesser than the pure In_2O_3 (3.13 eV). This decrease in the band gap has fruitful consequences, as lower band gap favors good photocatalytic behavior of the material [28]. Figure 22(c) indicated the PL spectrum, which further support LSPR effect, narrowing band gap and good efficiency of the prepared materials

in photocatalysis [115]. The PL emission spectra obtained at 270 nm excitation for both materials. The intensity at 388 nm decreased with a negligible red shift in case of gold coated In_2O_3.The PL peak suppression directly suppresses the charge recombination. We derived a conclusion that gold metal greatly suppressed the recombination of the carriers and eased the parting and carriage of photogenerated carrier species, thus leads to the fact that Au-In_2O_3 can be used as an effective material for PEC water splitting application.

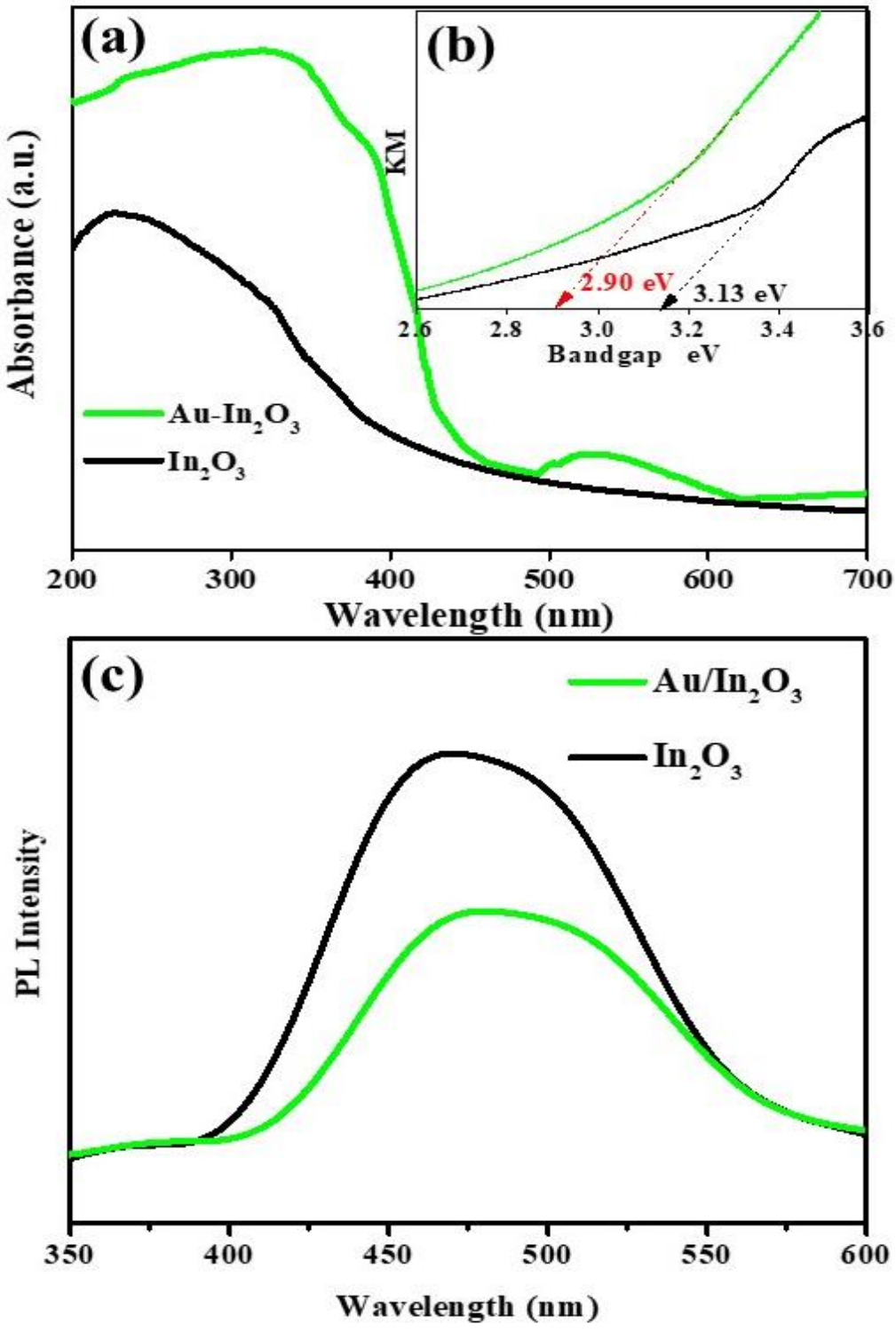

Figure 22: Optoelectronic properties of In_2O_3 and Au-In_2O_3 NWs by (a) UV-VIS absorption spectra, (b) Tauc`s plots and (c) PL spectra (excited at 270 nm)

4.3.1 Growth Mechanism

We investigate the mechanism of formation and growth of In_2O_3 NWs on indium metallic surface in 0.5 NaF electrolyte contain ethylene glycol and DI water solution. Initially, the cleaned surface of Indium metal is vigorously etched by the fluoride ions (F^-) present in the electrolytic solution. This leads to intense bubble formation around the substrate. After 4 to 6 minutes bubbles production considerably reduced, and the current is also stabilized. This indicates the formation of oxide passive layer due to In_2O_3 or $In(OH)_3$, which is termed as passivation [156, 157]. After passivation, the thickness of oxide layer increases gradually, and it leads to the formation of NWs. This mechanism is based on periodic bond chain (PBC) theory [158], which stated that each atom tends to attain the minimum energy state in the crystal. The dominant [2,2,2] peaks in XRD at 31^0 showed that each Indium and oxygen atom in Indium oxide tends to remain at the corner of the cube to minimize their energy. It also indicated that [2,2,2] is the most suitable facet for In_2O_3 NWs growth. In case of anodization, various factors can be taken into account to predict the mechanism of the In_2O_3 growth. The possible sequence of reactions can be given as follow.

$$\mathbf{In \rightarrow In^{3+}} \qquad \mathbf{(I)}$$

$$\mathbf{2In^{3+} + 3H_2O \rightarrow In_2O_3 + 6H^+} \qquad \mathbf{(II)}$$

$$\mathbf{In_2O_3 + 6H^+ + 6F^- \rightarrow [InF_6]^{3-} + 3H_2O} \qquad \mathbf{(III)}$$

In the first step, the current treatment oxidized the surface indium ions (In^{3+}), followed by solvation and conversion to oxide form. Finally, In_2O_3 is etched by fluoride ions and form $[InF_6]^{3-}$ complex. The process is continued until the available In^{3+} consume and surface

passivation occur. A schematic presentation of with SEM images provided in Figure 23 at different interval of time.

4.3.2 Photoelectrochemical Water Splitting Measurements

The PEC performance of the In_2O_3 and Au/In_2O_3 NWs explores by employing electrochemical techniques supported by the simulated solar light. Figure 24(a) represents the linear sweep voltammogram (LSV) obtained in dark and light. The dark current is significantly low until 1.2V, after which the increase is caused by the dominant electrochemical processes at a higher voltage, where oxidation is supported by electrochemical reaction rather than solar light [159]. The photocurrent under light shows onset potential of 0.63 V for In_2O_3 and Au/In_2O_3 photoanodes, respectively. However, the positive slope is larger for the later, suggesting more photocurrent generation. The photocurrent acquired saturation at 1.12 V, followed by a relatively straighter line. It is evident from the *I-V* spectra that the photocurrent density of Au/In_2O_3 NWs is significantly enhanced after incorporation of gold. The photocurrent enhancement can be attributed to the plasmonic nature of Au, which not only provided extra electrons but also imparted SPR properties to the photoanode [116]. Conversely, the pure In_2O_3 NWs shows relatively lower photocurrent density due to the wider band gap and less light absorption capacity. Figure 24(b) provided the stability and periodic chopped light photocurrent measurements. The long-term stability under illumination for an extensive period of 2000 s shows no reasonable photocurrent decay. The photocurrent slightly drops initially upon illumination, followed by brief stable photocurrent curves under continuous illumination.

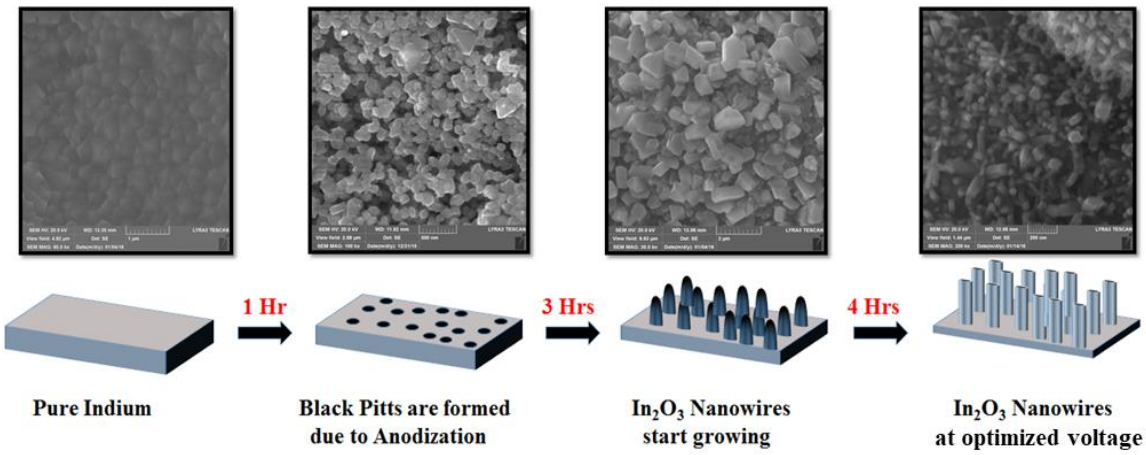

Figure 23: SEM supported growth of In_2O_3 NWs at various intervals of time

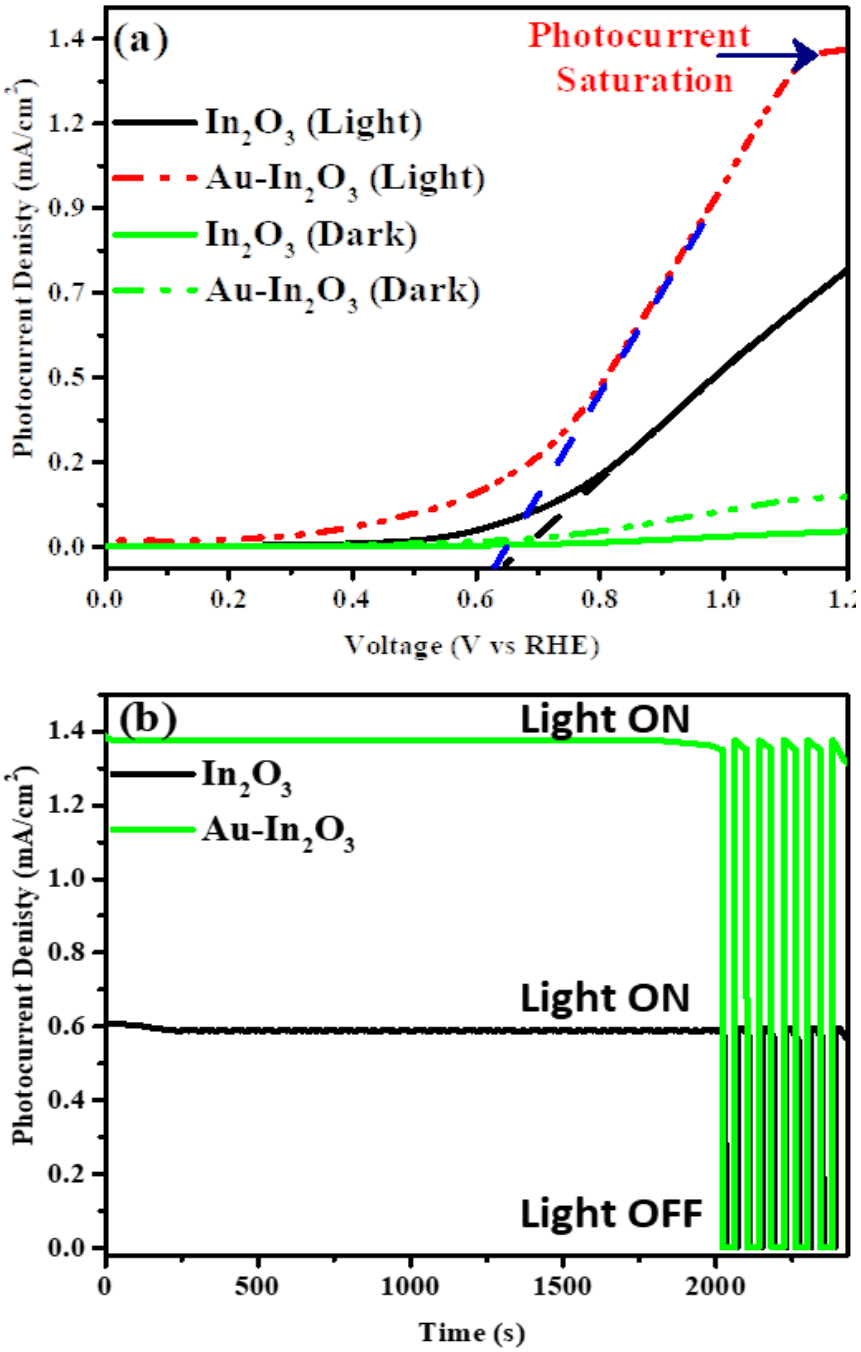

Figure 24: Photoelectrochemical water splitting performance of In_2O_3 and Au-In_2O_3 NWs (a) *I-V* voltammograms under light and dark, and (b) The time-dependent *(I-t)* photocurrent spectra obtained at 1.2 V under periodic ON/OFF Light mode.

Stability curve is followed by the periodic photocurrent region under successive light and dark cycles with ~ 40 s intervals, which show the photocurrent reached a maximum value of 0.59 and 1.39 mA/cm^2 under illumination (almost double fold increase) for In_2O_3 and Au/In_2O_3 photoanodes at 1.20 V. The photocurrent immediately diminished to the base value under the dark period. The photocurrent values under the light are almost in the same order as those obtained using LSV. The regular periodic photocurrent suggests that the samples are relatively stable towards photocorrosion. Therefore, these results confirm the resilience and stability of In_2O_3 and Au/In_2O_3 NWs under light during PEC water splitting.

4.3.3 Mechanism of PEC water splitting

The Electronic impedance spectroscopy (EIS) and Mott–Schottky (MS) plots ware utilized to investigate the interfacial charge transfer and chemical band positions of the In_2O_3 and Au/In_2O_3 photoanodes. In case of EIS, the samples were analyzed under dark and simulated solar illumination with a DC voltage sweep across the working electrode. Nyquist plot spectra with representative semicircles are provided in Figure 25(a) for the labeled photoanodes. The radii of semicircle arc minimized after Au deposition, suggesting lower impedance value under light for Au/In_2O_3 NWs [92]. These results suggesting that the charge transfer capacity is significantly enhanced. The electronic behavior is explored by Mott–Schottky (MS) plots in an aqueous solution of Na_2SO_4 (0.5M) at 1 kHz frequency (Figure 25b). All the plots show positive slopes, which attributes that all photoanodes are n-type semiconductors i.e. electrons are the majority carriers. Additionally, the slope of Au/In_2O_3 is greater and at more negative voltage than the In_2O_3 NWs, which replicate that Au/In_2O_3 NWs possess higher electron donor density

[118]. The slope line touches the quasi-linear regions at -0.201 V and -0.173 V on extrapolation, which indicated their flat-band potentials (V_{fb}), respectively. The remarkable shift of V_{fb} values in case of Au/In_2O_3 NWs suggest that the band bending took place with the incorporation of Au [118], which is essential for effective charge transfer between heterojunction as in the present study. On the basis of foregoing discussion, it can be assumed that the visible light induces electrons/holes generation in Au/In_2O_3 NWs, these electrons transferred to the conductance band of In_2O_3 NWs, and thereby perform the water reduction. The holes (h^+) area readily consumed and converted into oxygen in the valence band (Figure 25c). These results suggest that Indium based photoanodes can be an efficient applicant for the future energy harvesting applications if the best possible combination with other materials is realized.

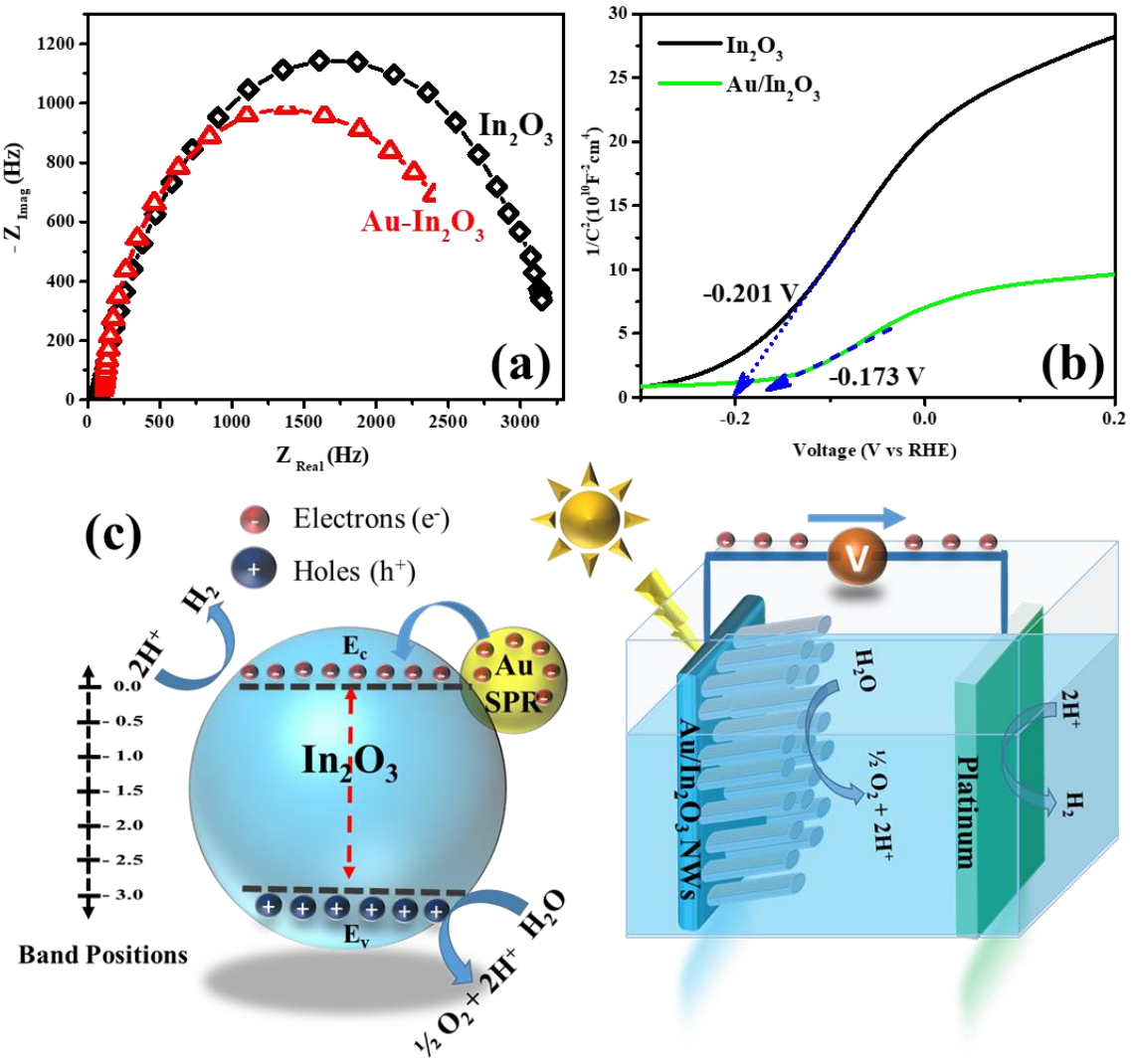

Figure 25: Nyquist (EIS) and Mott-Schottky (MS) supported photoelectrochemical water splitting mechanism (a) EIS plot under light, (b) MS spectra under light, and (c) PEC water splitting scheme for Au/In_2O_3 photoanodes

CHAPTER 5

FABRICATION OF GaON/ZnO NANOARCHITECTURE PHOTOANODE AND THEIR PHOTOELECTROCHEMICAL WATER SPLITTING

5.1 Introduction

Solar radiations considered proficient renewable energy substitute for fossil fuels, which can effectively accomplish the obligation of energy worldwide with minimal environmental threats. In this regard, PEC water splitting is regarded as a promising solution to produce H_2, a renewable energy carrier, from ample and green resources of water and abundant sunlight. In principle, the semiconductor photoelectrodes captured sunlight photons to generate photoexcitons i.e. electrons (e^-) and holes (h^+) in their conduction (CB) and valence bands (VB). The photoexcitons have sufficient energy to initiate the Red-Ox reactions to split water into H_2 and O_2 gases. Fujishima and Honda accomplished the overall water splitting via TiO_2 photocatalyst with ultraviolet radiations [5]. This explores the new dimension of research towards metals, semiconductors, and even organic conjugated systems to accomplish more output of the process in the visible solar regime [77, 86, 115]. However, the fundamental issue relates to PEC technique is the fabrication of efficient and stable PEC water splitting systems. Additionally, certain factors poison PEC water splitting catalyst and hence decrease the overall efficiency of the energy transfer process, such as limited light absorption, insufficient generation of photoexcitons (e^- and h^+) and their separation, and limited water Red-Ox reactions. Therefore, researchers adopted certain approaches to overcome these problems, which

included tandem cell fabrication, hybrid/composite structure formations, nitrogen doping and photoelectrode`s surface decoration with stable, cheap and efficient co-catalysts such as Ag and Au due to their improved water red-ox reaction kinetics [13, 160–162]. Even though these protocols improve the PEC water splitting significantly, further exertions should be devoted to make the fabrication cost-effective. Generally, those solar junction cells are considered efficient in which the photoelectrode split water without the assistance of co-catalyst and robust to photocorrosion. This depends on the growth of high-performance photoactive materials.

ZnO is a cost-effective alternative to TiO_2, having n-type semiconductor characteristic with indirect band gap (3.37 eV). Moreover, ZnO showed improved photocurrent densities than TiO_2 as revealed from their comparative study by Hernández *et al.* [163] It is good photocatalyst for oxygen evolution reaction (OER) as their band edge straddle the water oxidation potential level. However, due to high recombination rate of their excitons, the quantum yield is unsatisfactory [164], which makes its commercialization challenging in pristine form. Therefore, significant attempts have been made to enhance the photo-efficiency of this material through doping [165] or making their heterostructures or composites [20, 166] with suitable band gap materials. The photocatalytic properties of pristine semiconductors can be increased by loading appropriate noble metal co-catalysts and transition-metal oxides. As an example, GaN:ZnO has been tested for overall PEC water splitting, owing to virtuous visible light absorption and photocorrosion resistance characteristics [167]. 5 wt % RuO_2 loading to GaN:ZnO further enhanced the photocatalytic activity of the overall catalytic system. Additionally, suitable band edge alignments with the thermodynamic OER and hydrogen

evolution reaction (HER) energy bands enable this material for overall PEC water splitting. Continued effort in the modified synthesis of these materials has led to long lifetime PEC water splitting under visible solar light with the aid of $Rh_{2-y}Cr_yO_3$ co-catalysts [168], yet high-efficiency not achieved due to undesirable recombination between (e^-) and (h^+) till date. The synthesis of high-quality ZnO:GaN is expected to be a promising approach to overcome the charge recombination and suppression of the electron diffusion toward the ZnO:GaN/electrolyte interface. Furthermore, nitridation and assembly of these materials into a conductive electrode such as ITO, FTO etc. enable external electric field to further enhance the charge separation [169]. Gallium oxynitride (GaON) can be impending and suitable additive to ZnO for this purpose. It is nitrogen and oxygen-rich, and showed improved optical properties, depending on the amount of doped nitrogen [77, 170]. Lately, Delaunay and Domen et al. fabricated ZnO-ZnGaON photoanode composite by more challenging chemical vapor deposition (CVD) method at relatively high temperature i.e. 600 ^oC. They achieve good photocurrent efficiency of ~ 1.5 mA/cm^2 [49]. More recently, we reported a simple solvothermal synthesis and photoelectrochemical water splitting properties of GaON nanosheets [77]. However, the photocurrent density was relatively lower for pristine GaON. Therefore, in this work we designed simple and novel GaON/ZnO composite for much improved PEC water splitting performance. The incorporation of nitrogen is carried out and mild temperature, unlike high-temperature ammonia treatment which requires complex safety measures.[14] In such heterogeneous systems, the composite materials provide additional reaction sites, thus promoting/accelerating photocatalytic reactions [171]. The incorporated materials usually have complex structures, which are difficult to be defined experimentally. In this

context, first-principles density functional theory (DFT) calculations are known to be an effective tool to study the structural, physical and chemical properties of such nanoarchitecture systems and to get the fundamental understanding of the mechanisms of photocatalytic reactions [172]. To complement our experimental results on GaON/ZnO heterostructures, we have conducted DFT calculations for a model system consisting of Zn_3O_3 cluster loaded on (111) surface of GaON. We found that Zn_3O_3 model provides efficient reaction sites and enhances the dissociative adsorption energy of water molecules. The DFT results support the experimental PEC water splitting process in GaON/ZnO nanoarchitecture.

5.2 Materials and Methods

5.2.1 Synthesis of GaON/ZnO NAs heterojunctions

The raw materials i.e. GaON nanosheets and ZnO NRs were synthesized by established synthetic routes [77, 173]. One pot GaON/ZnO NRAs synthesis is achieved by mixing optimized concentrations of GaON nanosheets and ZnO NRs by weight (5:95) in a beaker containing 50 mL DI water through regular sonication for 1hr. The uniform mixture was then transferred to Teflon vessel with vertically suspended, freshly washed 2x2 cm^2 FTO glass (purchased from Sigma Aldrich). The purpose of suspended FTO with reaction mixture is to deposit the as-synthesized GaON/ZnO NRAs directly over its uncovered conducting surface to achieve the efficient ZnO alignment, which boasts their photocatalytic properties. The Teflon was sealed in the autoclave and kept at 80 ^oC for 6 hrs in the synthetic oven. The temperature was increased at the ramping rate of 5 ^oC/min to avoid vigorous heating and to achieve uniform reaction rate. The uniform firm thin film of GaON/ZnO NRAs were deposited on the FTO glass within the autoclave at

elevated pressure. The autoclave was removed from the oven and was cool down at room temperature. The GaON/ZnO deposited FTO electrode removed from autoclave, washed gently with DI water and kept at 100 ^{o}C for more drying for 2 hrs. For the comparison purpose, we also fabricate ZnO/FTO and GaON/FTO photoelectrodes by the same approach. Figure 26 provides the schematic adaptation of the cited procedure.

5.2.2 Material Characterizations

a. Physicochemical Characterizations

The crystallinity of GaON/ZnO NRAs has been examined with the help of Mini-X-ray Diffraction (Mini-XRD) with Cu Ka X-ray radiation source (k = 0.15406 nm). The morphology and composition have been identified by field emission scanning electron microscopy (FESEM) (Tescan Lyra-3)) and energy dispersion X-ray spectroscopy (EDX) equipped with FESEM, respectively. further structure information was obtained via Infrared (FT-IR) spectroscopy (measured at room temperature with Thermo-Fisher device) from 600-1200 cm^{-1} region. The XPS analysis performed via V.G. Scientific ESCALAB Mk(II) spectrometer using a non-monochromatic Al source (Kα, 1486.6 eV). The output power was adjusted at 130 W. Before starting, the binding energy (eV) of the device was calibrated with standard reference lines (Cu 2p3/2 = 932.67 eV, Cu 3p3/2 = 74.9 eV and Au 4f7/2 = 83.98 eV). The permitted energy of the electron analyzer was fixed at 10 eV. The energy resolution was about 1.0 eV. Diffuse Reflectance Spectroscopy (DRS) (HORIBA) and Photoluminescence (PL) spectroscopies were utilized for study the most important optical properties of the pristine ZnO and GaON and their nanoarchitecture deposited FTO material. Origin Pro-8 was used to draw all the graphs and labels.

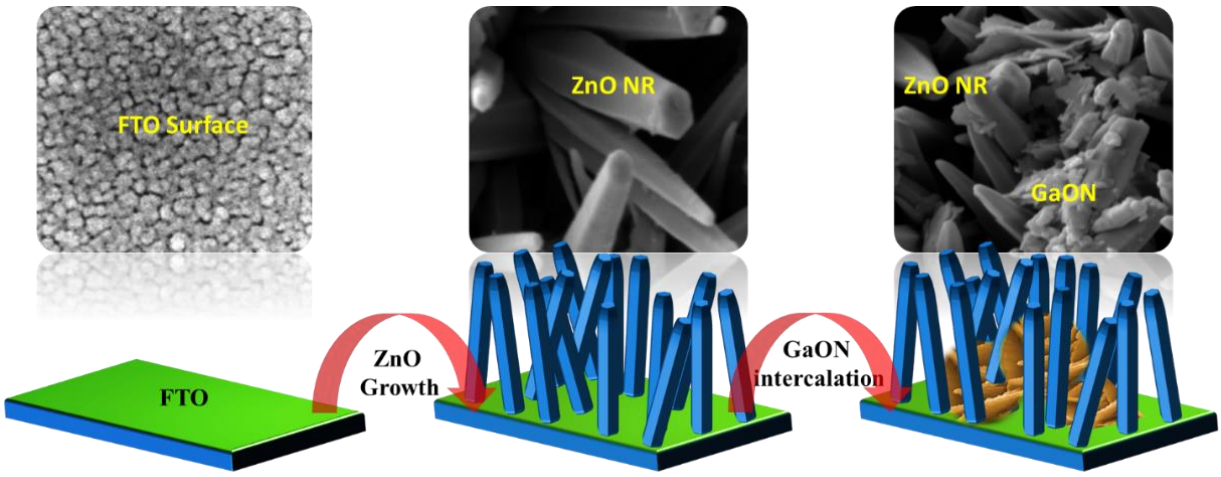

Figure 26: Schematic for the formation of GaON/ZnO NRAs

b. Photoelectrochemical Measurements

The photoelectrochemical water splitting performance was examined in three electrodes photochemical cell supported by potentiostat (Autolab) and solar simulator (ORIEL SOL-3A). The intensity of the artificial light source is calibrated with standard silicon diode (ORIEL) photodevice and tuned at 1 SUN (100 mW/cm^2) power. The solar simulator is provided with 1.5 A.M and UV cutoff wavelength (<420 nm) filters. Three electrode cell contained Platinum (Pt) as a counter electrode, Secondary Calomel Electrode (SCE) as a reference electrode and GaON, ZnO and GaON/ZnO NRAs as working electrode (alternatively). 0.5 M sodium sulfate (Na_2SO_4) solution in DI water was used as an electrolyte for photocurrent density measurements. 0.05 V/s scan rate was maintained for Linear Sweep Voltammetry (LSV) between 1.5 V to -1.5V. The chronoamperometric study was performed at the chopping ON/OFF rate of ~ 60 s/cycle.

c. DFT Calculations

DFT calculations conducted using the generalized gradient approximation of Perdew-Burke-Ernzerhof for the exchange-correlation energy [174]. The Brillouin zone sampling was done using 12 × 12 × 12 Monkhorst-Pack k-point sampling for the unit cell of GaON (see Figure 27a). For the slab geometries (Figures 27b,c) 12 × 12 × 1 k-points are used due to the presence of vacuum spacing more than 10 Å perpendicular to the slabs. The electrostatic potential is determined on a real-space grid with mesh cutoff energy of 150 Ry and double-zeta-polarized basis sets of numerical orbitals are used to describe the atoms. van der Waals interactions are introduced by Grimme's empirical dispersion correction [175]. The convergence criterion was 0.01 eV/ Å for Hellman-Feynman forces. The adsorption energy of a water molecule is defined as

$$E_{ads} = E_{GaON/(GaON+ZnO)+H2O} - E_{GaON/(GaON+ZnO)} - E_{H2O}, \qquad (5.1)$$

where $E_{GaON/(GaON+ZnO)+H2O}$ is the total energy of GaON/(GaON+ZnO) slab with an adsorbed water molecule, $E_{GaON/(GaON+ZnO)}$ is the total energy of GaON/(GaON+ZnO) slab and E_{H2O} is the total energy of isolated water molecule. All calculations are conducted using the computational package Atomistix toolkit [Distributed by QuantumWise company, Copenhagen, Denmark. http://www.quantumwise.com].

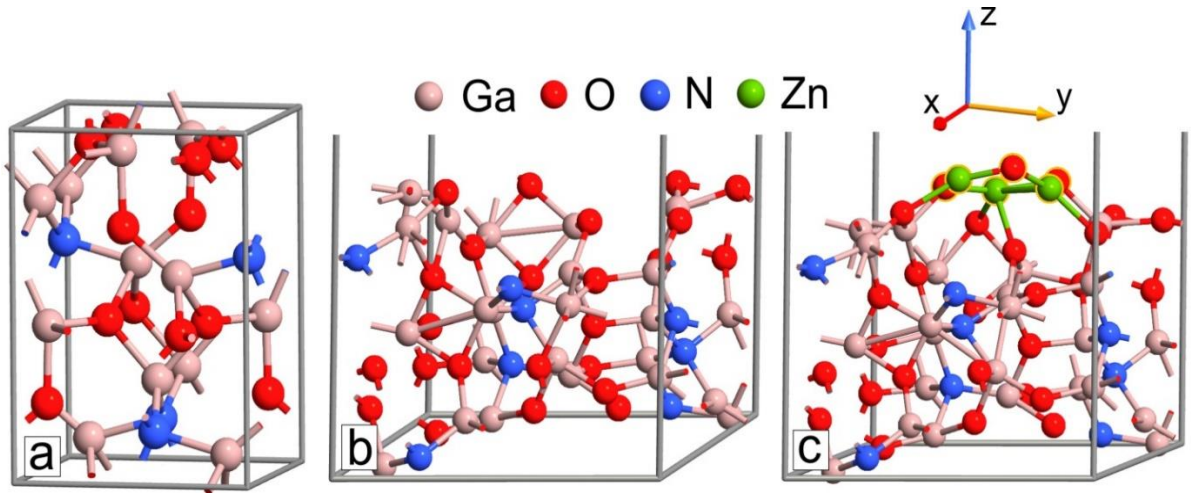

Figure 27: (a) Optimized unit cell of GaON. (b-c) slab geometries with O-rich (111) surface orientation without (b) and with Z_3O_2 cluster (c, highlighted).

5.3 Results and Discussion

5.3.1 Structural and Optical Properties

The XRD analysis was useful to determine the crystalline phase of the final product, as crystallinity and phase distinctly affect the overall performance of the photoelectrodes [176]. Figure 28. represents the stacked XRD patterns for GaON, ZnO and GaON/ZnO NRAs, respectively. The XRD 2θ values for FTO have been subtracted from all results to obtain real XRD patterns for ZnO, GAON and GaON/ZnO NRAs. Characteristic intense XRD peak [2 2 2] for ZnO is observed at 2θ = ~34^{o} in pristine as well as in GaON/ZnO nanoarchitecture XRD pattern with slightly lower intensity [105]. In addition, other peaks for ZnO also appear in the nanoarchitecture spectrum at almost same level as pristine ZnO. Bunch of peaks for GaON can be seen in the GaON/ZnO nanoarchitecture XRD spectrum from 33^{0} to 43^{0}. Some additional peaks are also observed in the nanoarchitecture spectrum, especially at the far end of the XRD spectrum at 44.76^{o}, 59^{o}, 67^{o} and 69.48^{o}. These peaks were not observed in ZnO nor in GaON spectrum either and therefore assigned to GaON/ZnO NRAs formation.

SEM micro details were obtained for GaON and GaON/ZnO NRAs. Figures 29(a,b) represent the low and high magnification SEM images for GaON nanosheets. The nanoflowers sheets morphology with variable size and channels like appearance is observed for GaON. Moreover, Figures 29(c,d) show the GaON/ZnO nanoarchitecture NRAs distribution at lower and higher resolution. The images demonstrate clear mixing of the two materials at the nanoscale level. The ZnO NRs can be seen in bulging out form, from GaON nanosheets in the micrographs in intercalating pattern.

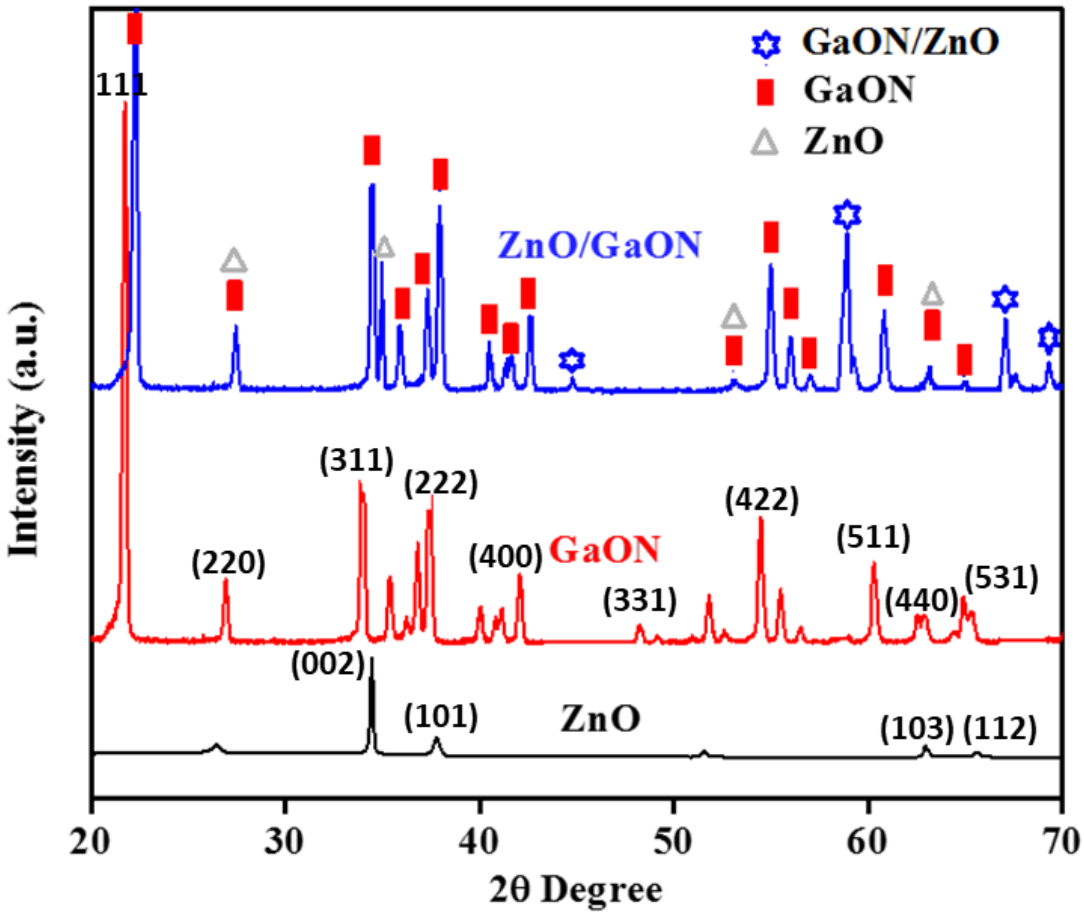

Figure 28: XRD patterns for ZnO, GaON and GaON/ZnO NRAs

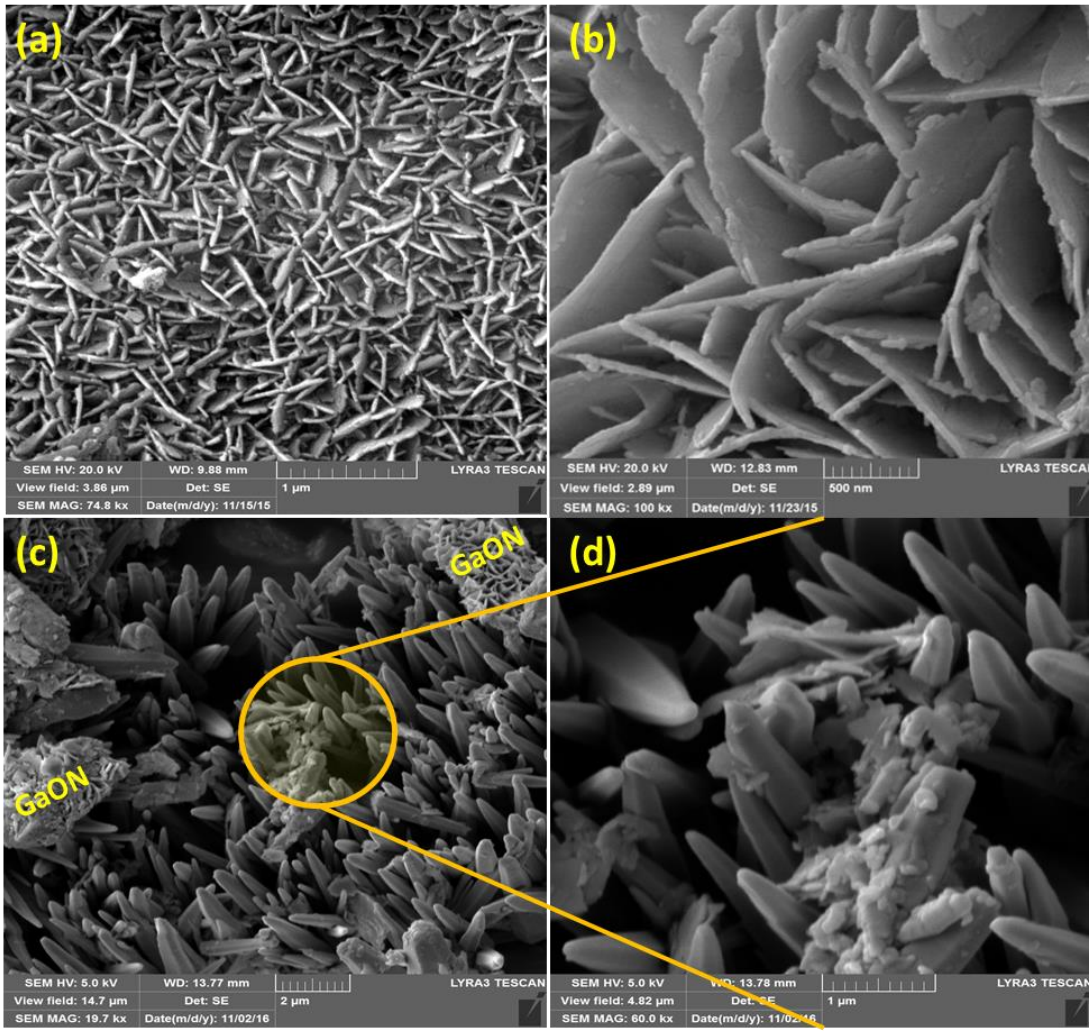

Figure 29: (a,b) low and high magnification FESEM images of GaON nanosheets, (c,d) Low and high magnification FESEM images of GaON/ZnO nanoarchitecture NRAs.

The nitrogen ratio is the most important entity in GaON and it is clearly detected by the EDX and elemental mapping in Figure 30. These results also provide further details about the nanoarchitecture formation of GaON nanosheets and ZnO NRs. EDX spectrum in Figure 30(a) displayed known peaks for Zn, Ga, O, and N. The Quantitative ratio indicated that nitrogen existed in significant amount (~ 3%) in the final product. Mapping results in Figures 30(b-e) support the EDX results and mapped area showed significant distribution of nitrogen entities in the nanoarchitecture. Nitrogen-doped materials are extensively studied for water splitting applications [177]. Keeping the nitrogen quantity intact in the nanoarchitecture product was the most challenging job in this study and we performed various experiments to get the optimized conditions at which the nitrogen remained in the nanoarchitecture as revealed further by the XPS analysis.

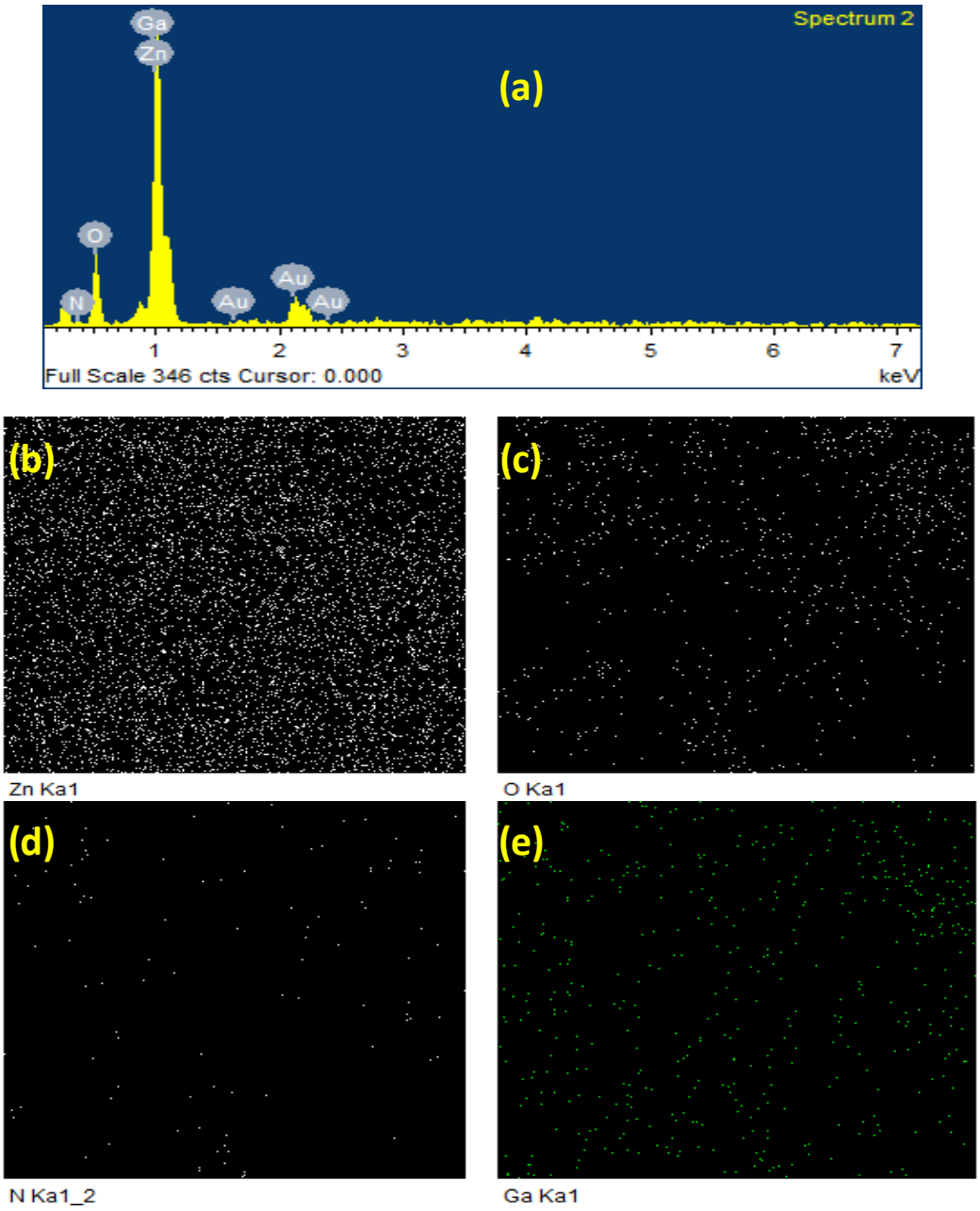

Figure 30: (a) EDX analysis and (b)-(e) Elemental Mapping of GaON/ZnO NRAs

XPS profiling was carried out to explore the nature of bonding and to detect the existence of nitrogen in the GaON/ZnO NRAs product. The core level fitted/deconvoluted XPS spectra (blue lines) of the elemental components of GaON/ZnO NRAs indicated in Figures 31(a-e). Figure 31(a) shows broader fitted XPS binding energy peak for nitrogen (1s) lies from 390 to 402 eV. The fitted peaks covered three sub-peaks, which can be assigned to Ga-O (394.6 eV), Ga-N (397.5 eV) and Ga-O-N (399.9 eV) bonding after comparing with the available literature [167, 178]. The characteristic oxygen (1s) XPS peak is observed at 528-535 eV and deconvolution showed two sub-peaks. These peaks may be assigned to Zn-O (530.66 eV) and Ga-O-N (532.3 eV) bonds (Figure 31b) [179]. The observed Zn ($2p_{1/2}$) and ($2p_{3/2}$) distinctive binding peaks at 1022 and 1045 eV is revealed in Figure 31©. These peaks corroborate that the Zn exists in the Zn^{+2} state in GaON/ZnO nanoarchitecture, thus the oxidation state of Zn remains unchanged [180]. The Gallium elemental XPS peaks for Ga (3d) and ($2p_{3/2}$) observed in 16-24 eV and 1012-1022 eV regions, respectively (see Figures 31d and e). The peaks resolved into three sub-peaks i.e., The red and green highlighted area under the are assigned to Ga-N and Ga-O bonding respectively. The black highlighted peaks represent some the traces of unreacted Ga metal.

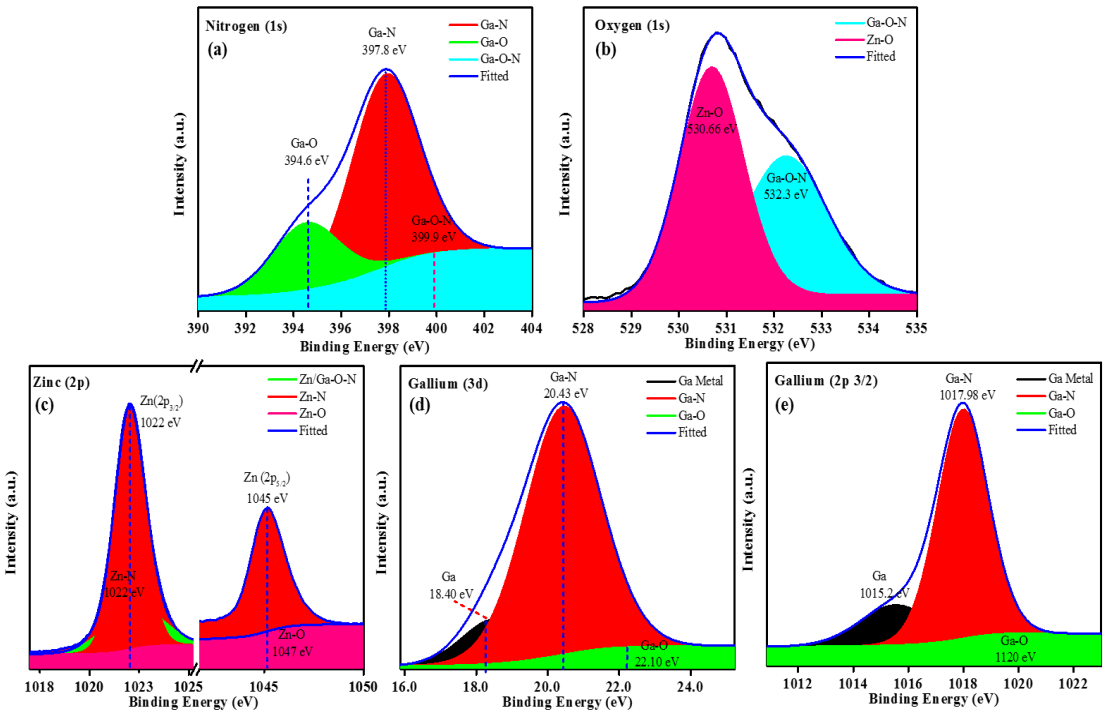

Figure 31: XPS deconvoluted elemental Spectra of GaON/ZnO NRAs

The comparative FT-IR results can be helpful to see the variation in the vibrational properties of final materials from pristine GaON nanosheets and ZnO NRs. These variations could be useful to conclude about the GaON/ZnO NRAs formation. The stacked IR spectra provided in Figure 32 for GaON, ZnO and GaON/ZnO NRAs, respectively. The peaks appeared in ZnO spectrum at 925 cm^{-1} and 883 cm^{-1} is reported for Zn-O vibrational stretching due to Zn-O lattice. These peaks are slightly shifted towards higher frequencies in GaON/ZnO NRAs spectrum to 921 cm^{-1} and 880 cm^{-1}. This significant shift can be related to the formation of some new bonds in the GaON/ZnO NRAs [105]. By looking to the indexed values in GaON/ZnO spectrum, it can be shown that the spectral vibrational peaks of GaON are also appeared at the slightly shifted position from their original GaON spectrum by 3-5 cm^{-1} at 1098, 985, 858, 745 and a broadened peak around 665 cm^{-1}. This again provided strong evidence about the nanoarchitecture formation. The photoactive GaON/ZnO NRAs spectrum also showed some new peaks, which are appeared due to the mixing of GaON and ZnO vibrational modes. These peaks are existed at 1025, 921, 811 and 690 cm^{-1} and assigned to GaON/ZnO NRAs composite.

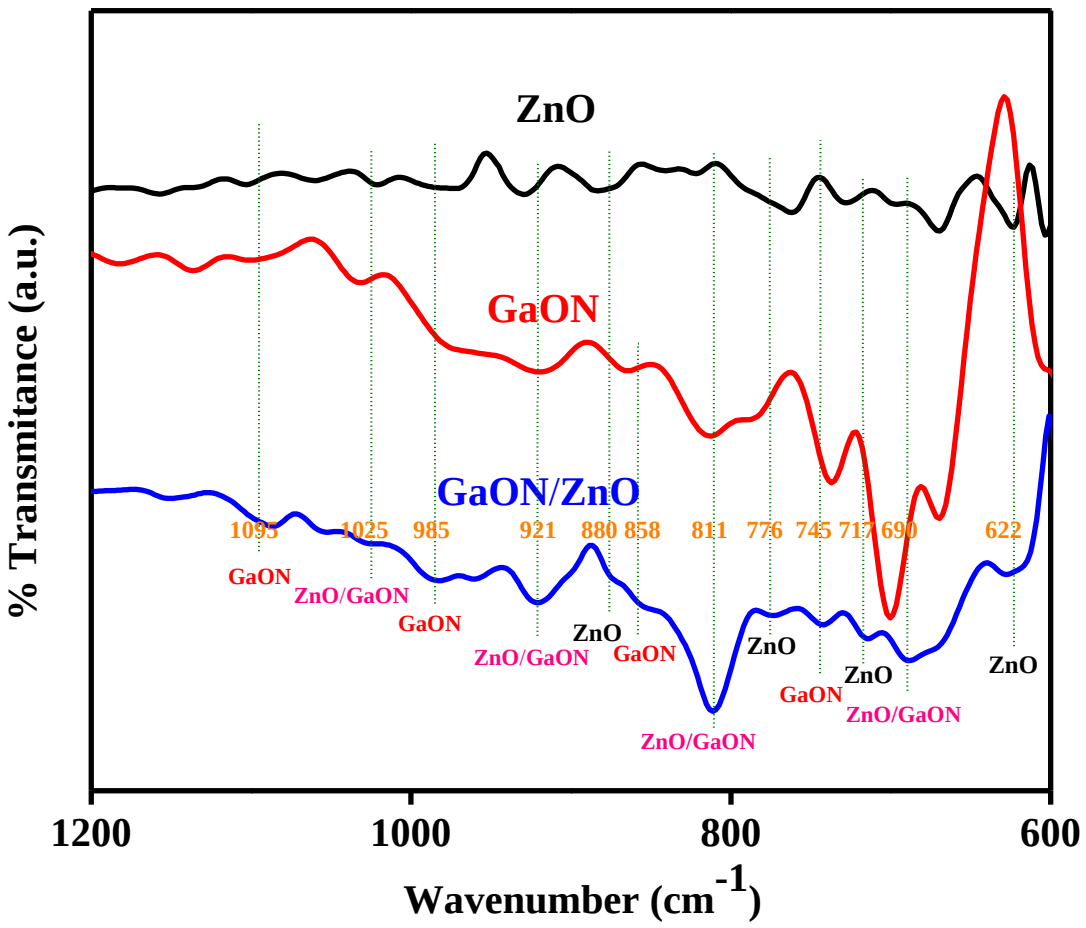

Figure 32: FT-IR vibrational spectral comparison of ZnO, GaON and GaON/ZnO NRAs

The optical properties in terms of absorption and photoluminescence are very for PEC water splitting [181–183] studies. UV/Vis-DRS spectra in Figure 33(a) showed the effect of GaON on ZnO absorption edge. The ZnO spectrum indicated the redshift towards higher wavelength in the visible region with GaON loading. The approximate absorption edges for ZnO, GaON and GaON/ZnO found at 408, 465 and 530 nm, which corresponded to 3.26, 2.58 and 2.01 eV band gap, respectively (Figure 33b inset) by using Kubelka-Munk equation [104]. The dramatic decrease in band gap is very useful for photocatalytic applications, as these materials can efficiently absorb the visible electromagnetic radiation [184]. For water-splitting reaction, the appropriate band gap is determined to be around 2 eV [113]. The decrease in the band gap can be attributed to the intermixing of the band gap levels of higher band gap ZnO (3.24eV) and lower band gap GaON (2.01 eV). Both materials advanced their valance and conductance band in the GaON/ZnO nanoarchitecture product [185]. The lowest band gap i.e. 2.58 eV in case of GaON/ZnO NRAs is suitable for photocatalytic applications as discussed above and therefore we further test this material for photoelectrochemical water splitting studies.

The photoluminescence (PL) spectra for ZnO and GaON/ZnO NRAs are indicated in Figure 33(c) which distinctly showed substantial quenching of the ZnO by an almost double fold in their nanoarchitecture with GaON, with wavelength shift from 383 nm to 406 nm. The PL quenching has a direct effect on the overall lifetime of excitons and recombination rates, and hence the spectrum showed an improved lifetime for GaON/ZnO NRAs excitons as compared to pristine ZnO. The shift towards high wavelength indicated that GaON effectively embedded in the structure and therefore affect the overall optical properties [186].

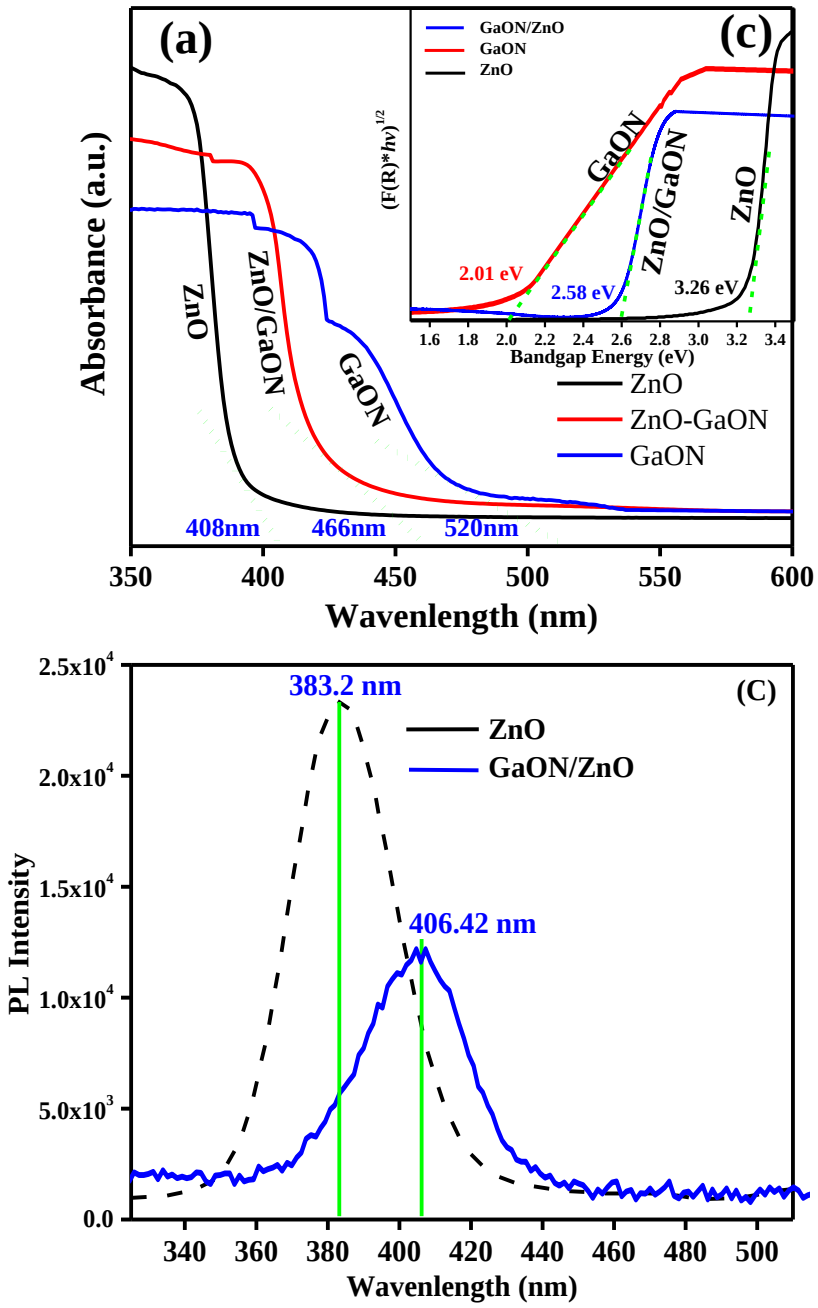

Figure 33: Optical properties of ZnO, GaON and GaON/ZnO NRAs: (a) DRS absorption spectra, (b) band gap measurement spectra (inset) and (c) Photoluminescence (PL) Spectra

5.3.2 Photoelectrochemical Water Splitting Performance

The photoelectrochemical results were collected in the form of LSV and chronoamperometry graphs. Figure 34(a) presented the LSV results, which clearly indicated no significant dark current at first instant as indicated by the dotted lines. Under electromagnetic illumination, the current densities jumped considerably as indicated by the solid lines. As the voltage increase, the current density values are also increased accordingly. A significant elevation in current density can be observed for GaON/ZnO NRAs at onset potential 0.6V as compare to pristine GaON and ZnO and reach to saturation at 1.1 V. The comparative photocurrent value for pristine GaON, pristine ZnO and GaON/ZnO NRAs are measured to be ~ 0.2, 0.45 and 1.2 mA/cm^2, respectively at 1.2V bias potential. Thus, it clearly showed that GaON improved the photocurrent of ZnO from 0.45 to 1.2 mA/cm^2, which is more than 2-folds increase under the light. Figure 34(b) showed the periodic chronoamperometric photocurrent results of GaON, ZnO and GaON/ZnO NRAs at 1.0V bias voltage under light and dark. The light was provided for ~60s, which was followed by the dark interval of ~60s. The results are in accordance with the LSV results and a significant increase in current densities are observed for all materials under the light. The GaON/ZnO nanoarchitecture materials showed the maximum jumped at 0.95 – 1.0 mA/cm2 in almost all cycles, which is about 2.4 times higher than ZnO (~0.42 mA) and several times higher than GaON (0.018 mA). These results also reveal that even after that many cycles, the nanoarchitecture material showed good stability. Figure 34(c) represents the stability measurement for our materials. The stability line remained almost stable after several minutes and the current density for GaON/ZnO NRAs only dropped from 0.97 to 0.96 mA/cm^2.

Nyquist plot (Figure 34d) was recorded to examine the charge transfer resistance for ZnO, GaON and GaON/ZnO NRAs at the interface. All materials showed the characteristic semicircular resistance curve, indicating that they all are feasible for charge transfer [187, 188]. The radii of the semicircular curves, which represent the electron transfer resistance at the interface of the electrode and deposited layers, decrease in the order of ZnO NRs > GaON nanosheets > GaON/ZnO NRAs. Thus, from the EIS Nyquist plots it clearly determined that the faster interfacial charge transfer is possible in case of GaON/ZnO NRAs, and therefore it showed much enhanced photoactive behavior than pristine ZnO NRs and GaON nanosheets as revealed by LSV and chronoamperometry. Table 3. provided the comparison of synthetic methods and photocurrent densities obtained from PEC water splitting by using various Gallium (Ga) based photocatalysts. It can be concluded that pristine gallium oxide (Ga_2O_3), gallium nitride (GaN) and gallium oxynitride (GaON) showed comparatively lower current densities as compared to their nanocomposites. Similarly, $BiVO_4/GaO_xN_{1-x}$, which was prepared by a sol-gel spin coating technique, also showed reasonably lower photocurrent density of at 0.37 mA/cm^2 at 1.23 V. The ZnO based GaN/ZnO showed significant photocurrent density of 0.9 – 1.2 mA/cm^2. Nevertheless, the nitridation was performed by thermal treatment of GaN/ZnO NPs under harsh NH_3 environment, over relatively more expensive TiO_2 substrate.

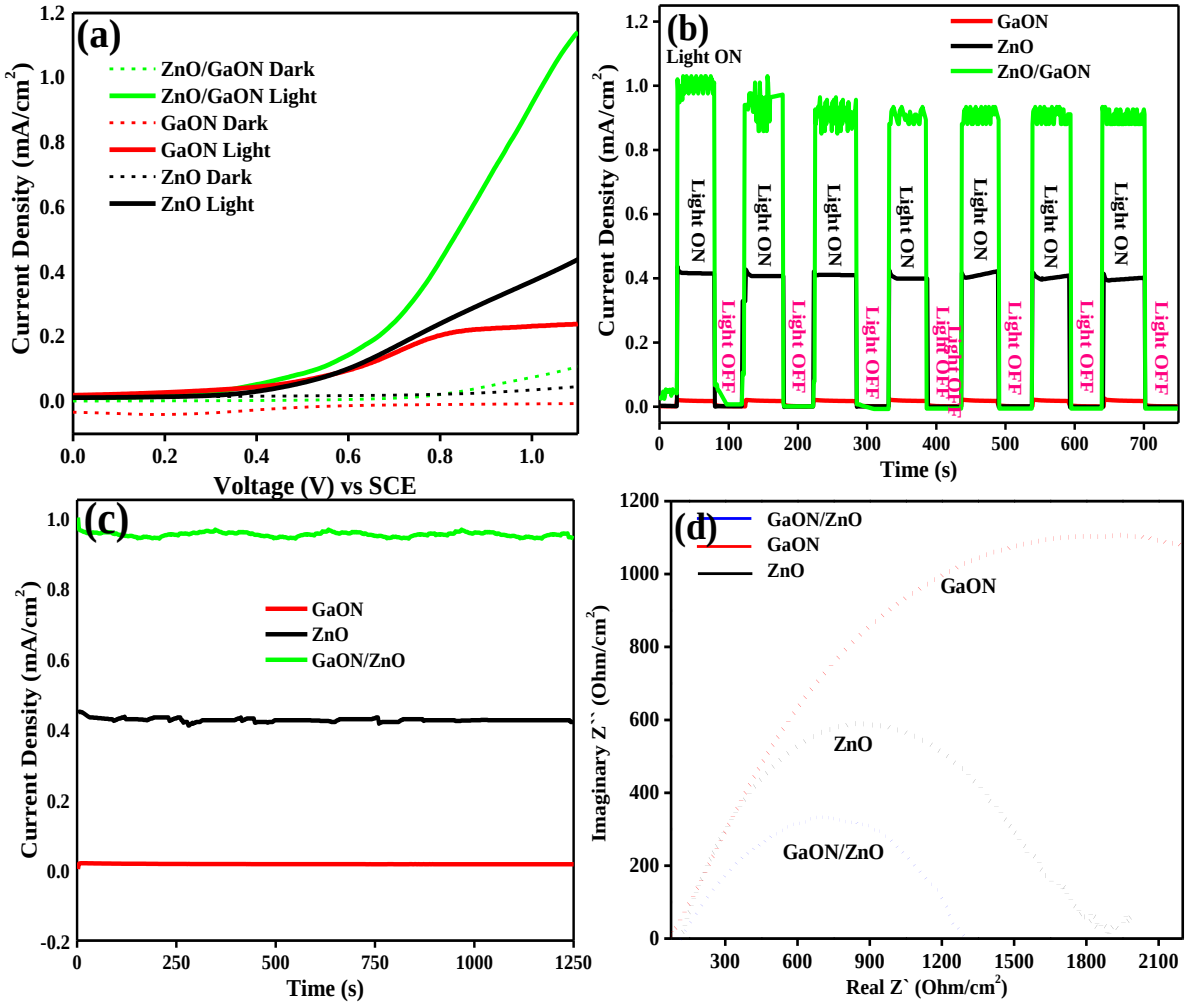

Figure 34: Photoelectrochemical (PEC) measurements for ZnO, GaON and GaON/ZnO NRAs: (a) linear-sweep voltammograms (LSV) under light and dark (b) amperometric $I - t$ curves at an applied potential of 1.23 V vs SCE under with 40 s ON/OFF cycle (c) I-t stability curve under luminescence (d) EIS Nyquist plot spectra under luminescence.

Table 3: Comparative photoelectrochemical water splitting performance of Gallium based photocatalysts in terms of photocurrent density

Materials	Synthesis method	Electrolytes	Applied Voltage (V)	Photocurrent Density (I)	Ref.
1. β-Ga_2O_3 NPs	RF Sputtering	1 M NaCl	0.2 V vs Ag/AgCl	0.002 mA/cm^2	[189]
2. Flat Porous GaN	Thermal Ammonia Treatment	0.5M Na_2SO_4	1.23 V vs Ag/AgCl	0.20 mA/cm^2	[190]
3. GaON Nanosheets	Hydrothermal Method	0.5M Na_2SO_4	0.60 V vs SCE	0.28 mA/cm^2	[77]
4. $BiVO_4/GaO_xN_{1-x}$	Sol-Gel Spin Coating	0.5M K_3PO_4	1.23 V vs Ag/AgCl	0.37 mA/cm^2	[191]
5. GaN/ZnO NPs	Thermal Ammonia Treatment	0.5M K_3PO_4	1.23 V vs SCE	0.9-1.2 mA/cm^2	[192]
6. GaON/ZnO NTAs	Chemical Mixing	0.5M Na_2SO_4	1.23 V vs SCE	1.2 mA/cm^2	**This work**

5.3.3 Mechanism of Photoelectrochemical Water Splitting

DFT can be helpful to propose the possible water splitting and charge transfer mechanism in GaON/ZnO NRAs (Figure 35). An earlier study indicated the valence band (VB) of ZnO lie well below the ideal OER conduction level of water splitting and therefore showed less significant water splitting [193]. On the other hand, GaON is a good photoactive material for HER [77]. We assumed that in GaON/ZnO these energy bands to a certain extent, that the water splitting efficacy increase. During this contact, the band structure of GaON/ZnO NRAs reconfigured, as the band bending take place from GaON to ZnO and drifting of electron started from the former towards later. In addition to band bending, the valence band of ZnO shifts upward, due to intermixing of their orbitals with GaON nanosheets in the GaON/ZnO NRAs. The shifting of energy levels continues until the Fermi levels achieve a new equilibrium. Upon photon irradiation from the solar simulator, photoexcitons are generated in the valance and conduction band. The negative electron (e^-) lift behind positive holes (h^+) in the valence band and jumped to the conduction band. These electrons drift from GaON though bending sites to ZnO surface from where it transfers to counter electrode through an external circuit. These electrons are readily available for reduction reaction to form hydrogen from water. On the other hand, the holes (h^+) in the VB bands of GaON migrate to the VB of ZnO in a similar fashion and consume by the water molecules for OER. As indicated by the Nyquist plot in Figure 34(d), these photogenerated exciton pairs (h^+ and e^-) are effectively separated from each other and therefore, contribute in the PEC water splitting reaction. The PL spectrum also supported this phenomenon, as it showed dramatic quenching, which can be correlated with the enhancement of the lifetime of photogenerated charges.

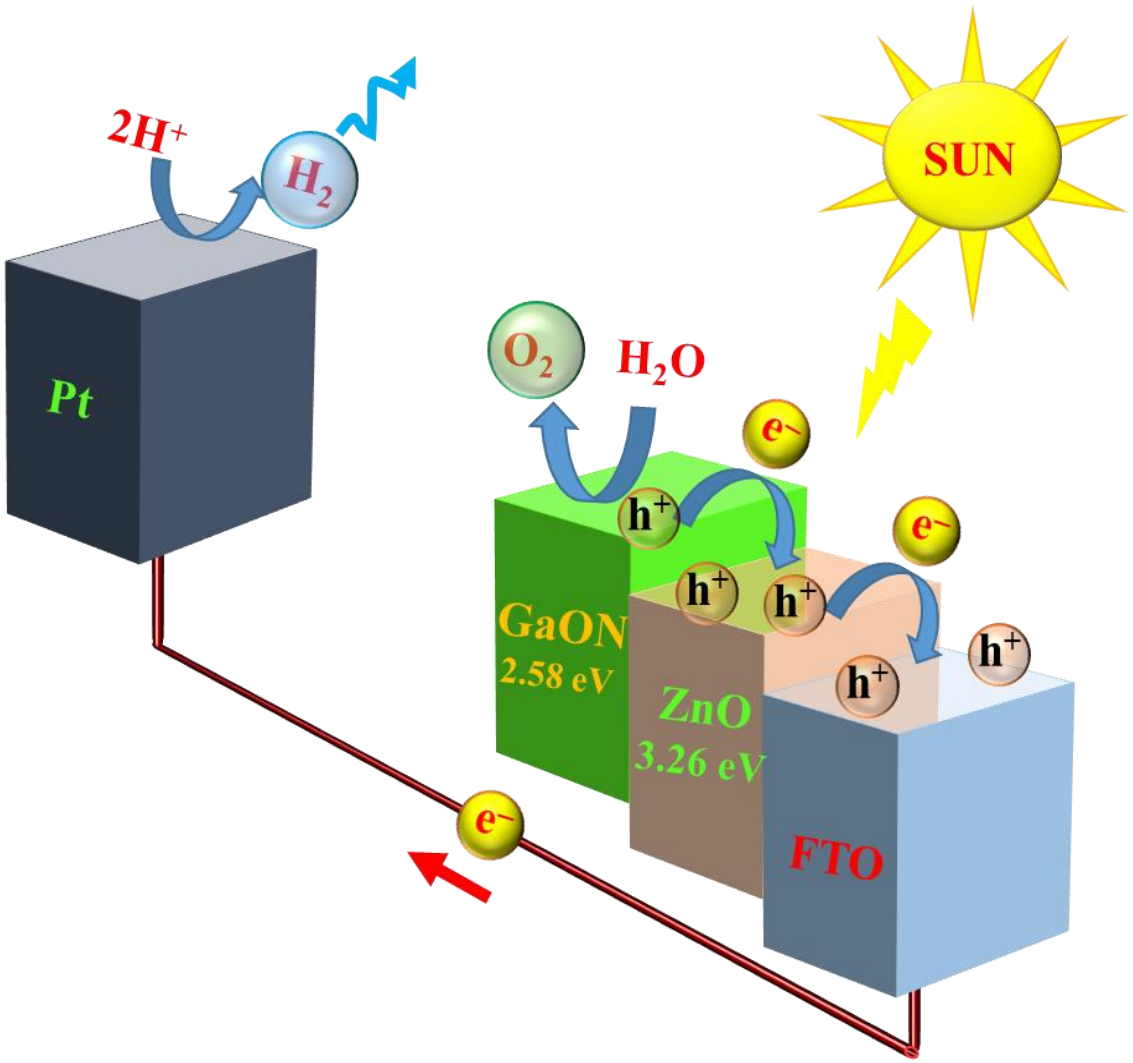

Figure 35: The Photoelectrochemical (PEC) water splitting mechanism over photoactive GaON/ZnO NRAs

5.3.4 DFT based Theoretical Water Splitting Correlation

For theoretical water splitting calculations, we considered spinel structure (*Imm*2, no. 44) gallium oxynitride (Ga_3O_3N) with lattice parameters a, b=5.8534Å and c=8.2780 Å [194]. Only atomic positions are relaxed during the structural optimization. After optimization, we have created a slab geometry with O-rich (111) surface orientation, which was found to be the lowest energy surface in the experiments (see Figure 27b).

In order to study the water adsorption on the considered systems, we introduced a single water molecule in the vacuum region at the distance 5 Å above the surface. Structural optimizations are conducted for 8 different initial locations of the water molecule using LBFGS optimizer method [195]. Some atoms at the bottom of the slab were kept fixed during the simulations. The adsorption occurs through the formation of Ga-O or Zn-O bonds. Black columns in Figure 36 show the adsorption energies E_{ads} of the water molecule on the (111) surface of GaON. The water molecule is chemisorbed with adsorption energy less than 2 eV with the formation of the Ga-O bond (see Figure 36b). We also obtained dissociation of the water molecule during the structural optimization (Figures 36c,d), which gives the adsorption energies more than 4 eV. One hydrogen atom of the water molecule is transferred to neighboring O or N atoms. Interestingly, the water molecule dissociates into one hydroxyl and one hydrogen in the GaON+Zn_3O_3 nanoarchitecture system whenever the water molecule is adsorbed on the Zn_3O_3 cluster (see Figures 36e,f). Consequently, the adsorption energies become more than 4 eV (see red columns in Figure 36). Molecular adsorption is found in this system only when the water molecule interacts with the Ga toms (Figure 36g). Thus, Zn_3O_3 cluster plays an important role as a catalytic center for the water splitting process.

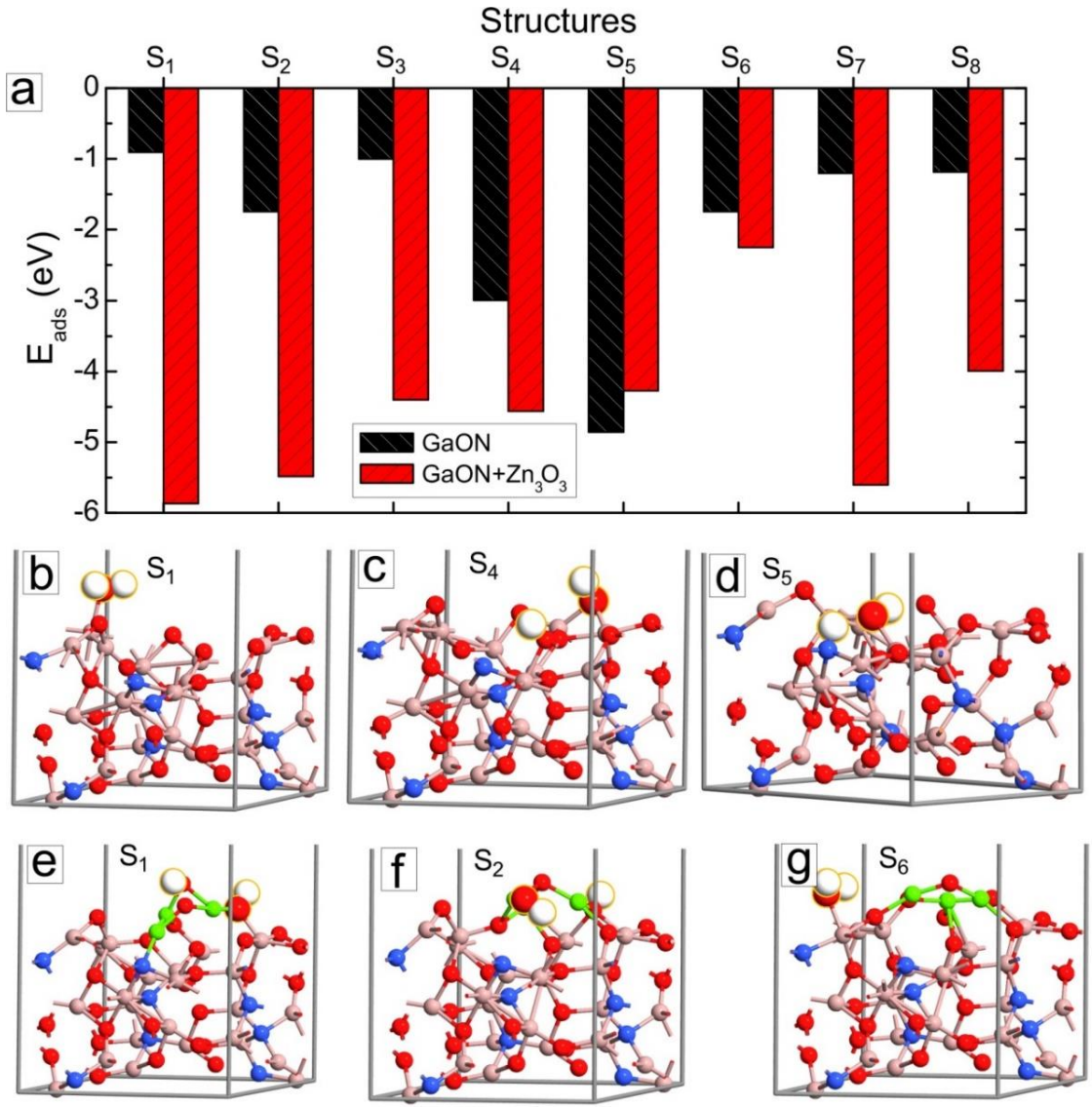

Figure 36: (a) Adsorption energies of water molecule on O-rich (111) surface of GaON and GaON+Z_3O_3 heterostructure, (b-g) Optimized structures of water molecules (larger balls) on the surface of GaON (b-d) and GaON+Z_3O_3 (e-g).

CHAPTER 6

SONICATION ASSISTED SYNTHESIS OF REDUCED GRAPHENE OXIDE (RGO)/ZnO NANOWIRE ARRAYS FOR PHOTOELECTROCHEMICAL WATER OXIDATION

6.1 Introduction

Atomic layers of RGO has been the attracted incredible interest due to their fascinating properties in many industrial and commercial electronic devices, chemical sensors, optical devices, energy storage, and composite materials [196–201]. On the other hand, one-dimensional (1D) metal oxide nanostructures, such as nanobelts, NWs, NRs, and nanoneedles represents significant type of tiniest dimension nanomaterials for smooth transport of electron and excitons and expected as building blocks for advanced functional nanoelectronics and nanosystems [202–205]. Among various metal oxide semiconductors, Zinc oxide (ZnO) is extensively investigated due to its fascinating electronic, optical, catalytic, photoelectrochemical, sensing and photovoltaic properties [173, 200, 206, 207].

However recently more attention has been devoted to the formation of hybrid nanostructured nanomaterials, composed of interactively both inorganic and organic components, with multiple functionalities and enhanced catalytic properties compared to single component materials [173, 208, 209]. This inimitable class of hybrid nanostructured materials cannot only maintain significant features of both components but also offers the potential to engineer the significant properties of the hybrid materials by the combining their functional components. The distinguished properties of ZnO

utilized in hybrid materials to get better outcomes. Among, different types of hybrid materials, semiconductor RGO/ZnO nanostructures emerging as distinctive class of materials, where RGO enhanced bulk properties of pristine ZnO and provides supportive electrical, optical and catalytic properties [200]. Recently various groups have successfully engineered RGO/ZnO hybrid materials for different applications [210–216]. The physiochemical properties of hybrid materials greatly influenced the synthetic approach. Therefore, an adaptation of suitable synthetic technique can be helpful to achieve a desired product with enhanced characteristics and properties. Among the various synthetic techniques, the sonochemical assisted method has emerged as a powerful tool to fabricate different semiconductor materials with unique morphologies [217]. The eminent acoustic cavitation phenomenon arose from ultrasonic waves, in which energy is transferred to the solution, responsible for the formation of miniscule bubbles. Later, these bubbles collapse and harvest temporary micro-level hot spots. This phenomenon is highly exothermic and elevates the solution temperature and pressure as much as ~5000 K and ~1800 atm with a cooling rate of 109 K/s, respectively [218–220]. This high temperature and pressure accelerate the physical intermixing of the hybrid materials.

In this work, we have efficiently synthesized hybrid RGO/ZnO NWAs nanoarchitectures on FTO substrate by low temperature hydrothermal and pulse sonication deposition technique. Detailed structural characterization of ZnO and RGO/ZnO NWAs investigated by FESEM, EDX, XRD, and Raman techniques. The optical properties studied by UV-Vis spectroscopy and photoresponse measurement of pristine and hybrid ZnO NWAs carried out by photoelectrochemical (PEC) techniques.

6.2 Methods and Materials

6.2.1 Synthesis of ZnO NWAs

ZnO NWAs were directly grown over the surface of FTO, placed in the reaction mixture. For the synthesis of ZnO NWAs, analytical grade zinc nitrate hexahydrate [Zn $(NO_3)_2 \cdot 6H_2O$] (Sigma Aldrich) and hexamethylenetetramine [HMTA; $C_6H_{12}N_4$] (Sigma Aldrich) were used as reagents without further purification. In a typical reaction, the mixture of 0.1 M aqueous solution of Zn $(NO_3)_2 \cdot 6H_2O$ and HMTA were mixed and transferred into hydrothermal vessel and kept in a synthetic oven at 85 ^oC for 4 hours. The ZnO/FTO glass substrate immersed upside down in the hydrothermal vessel. The pH of the solution is maintained at 6. After the successful growth of ZnO NWAs on FTO substrate, the system was cooled to the room temperature slowly and the ZnO deposited substrate is rinsed with DI water and then dried at room temperature for 2 hrs. To achieve high crystalline product the ZnO deposited FTO substrate calcined at 400 ^oC for optimum time.

6.2.2 Ultrasonic Impregnation of RGO in ZnO NWAs

In order to design RGO/ZnO NWAs nanohybrid architecture, initially, the RGO prepared by modified hummer method, well dispersed in ethanol (2 wt %) to make a suspension [221]. The suspension sonicated until obtained well-dispersed RGO solution. The as-prepared ZnO NWAs on FTO substrate introduced to the homogenous RGO dispersed suspension and pulse sonication technique employed for proper interaction of RGO in the nanogaps of ZnO NWAs. The sequence of pulse kept at 15 seconds ON and 15 seconds OFF. This sequence followed for 10 complete ON/OFF pulse cycles. Due to this vigorous vibrational energy treatment through sonication, it was assumed that the RGO dispersed

in ZnO NWAs, which was later confirmed by their physicochemical characterizations. This intercalation of the RGO into the ZnO NWAs framework strongly depended on the time and amplitude of ultrasonic treatment.

6.2.3 Material Characterizations

c. Physicochemical Characterizations

The surface morphology of the hybrid composite examined by field emission scanning electron microscope (FESEM). Chemical composition investigated by the energy dispersion spectroscopy (EDX). The crystalline phase of RGO/ZnO NWAs were explored by X-ray powder diffraction (XRD) with Cu Kα X-ray radiation (λ=0.15406 nm). Raman spectra of the hybrid composite were recorded with a LabRAM HR high-resolution Raman spectrometer (Horiba–Jobin Yvon) using a He–Ne laser (λ=632.8 nm) with D1 filter to reveal their structural properties. The optical properties measured with UV/Vis spectrophotometer at room temperature within the wavelength range 300–800 nm.

d. Photoelectrochemical Measurements

The PEC water splitting experiments were carried out in 0.5 M sodium sulfate (Na_2SO_4) (Sigma Aldrich) electrolyte in DI water. The photocurrent response was measured in a standard three-electrode configuration cell, where RGO/ZnO NWAs was used as working electrode, platinum foil as a counter electrode and Ag/AgCl as reference electrode respectively. The potential and current of the photo-electrode controlled by a potentiostat (Autolab). The samples were illuminated by an artificial sunlight simulator (Oriel Newport) equipped with xenon lamp to simulate AM 1.5 illumination (100 mW/cm^2).

However, only the visible portion of the light spectrum used by filtering the UV portion by the help of UV Cut-off filter i.e. the visible portion of solar light directed at the working electrode.

6.3 Results and Discussion

6.3.1 Growth Mechanism

Figures 37(a-d) provided a schematic pathway for the formation of RGO/ZnO heterostructure NWAs. In the initial step, the reaction between ZnO precursor and HMTA leads to uniform distribution of ZnO seeds on the FTO conducting surface. These seeds served as nucleating sites for ZnO NWAs growth in specific directions. HMTA plays pivotal roles in this reaction. First, it provides OH^- ions to achieve the precipitation reaction by the help of thermal degradation [222]. Secondly, HMTA also acts as a pH buffer and provides basic environment by releasing OH^- ions through decomposition in hydrothermal reaction, the rate of which is inverse to the pH of the solution [223]. Thirdly, HMTA direct only (001) epitaxial growth, by attacking on the nonpolar facets of the ZnO NWs and averts excess Zn^{2+} ions to these sites [32]. Thus, HMTA directed the seed distribution and redirect the ZnO NWAs growth in specific dimension in the following steps. Figure 37(d) shows the schematic of intercalated RGO in ZnO NWAs gaps after pulse sonication treatment of 10 cycles.

Figure 38 shows XRD pattern of ZnO NWAs grown on FTO substrate. All the peaks (100), (002), (101), (102) and (110) of XRD spectrum revealed purely wurtzite hexagonal phase of ZnO. Moreover, XRD peaks (designated by a star) were referred to FTO substrate. The FTO substrate almost covered by ZnO thick film, thus their characteristic peaks are mostly disappeared or faded.

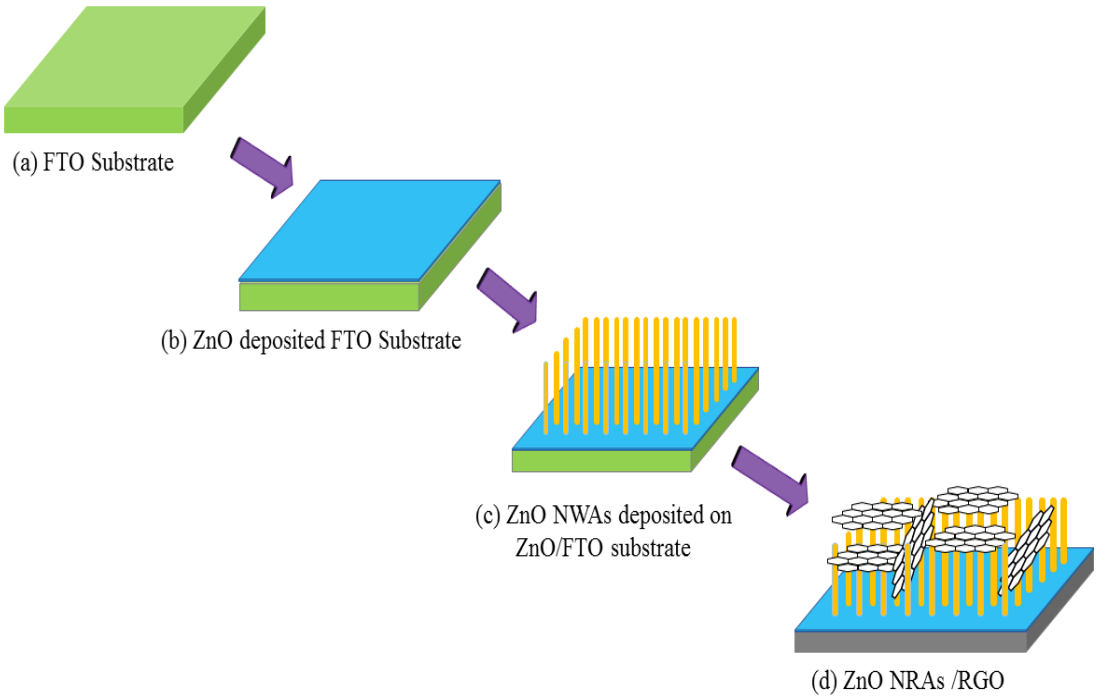

Figure 37: Schematic diagram for the formation of RGO/ZnO NWAs heterostructures on FTO substrate

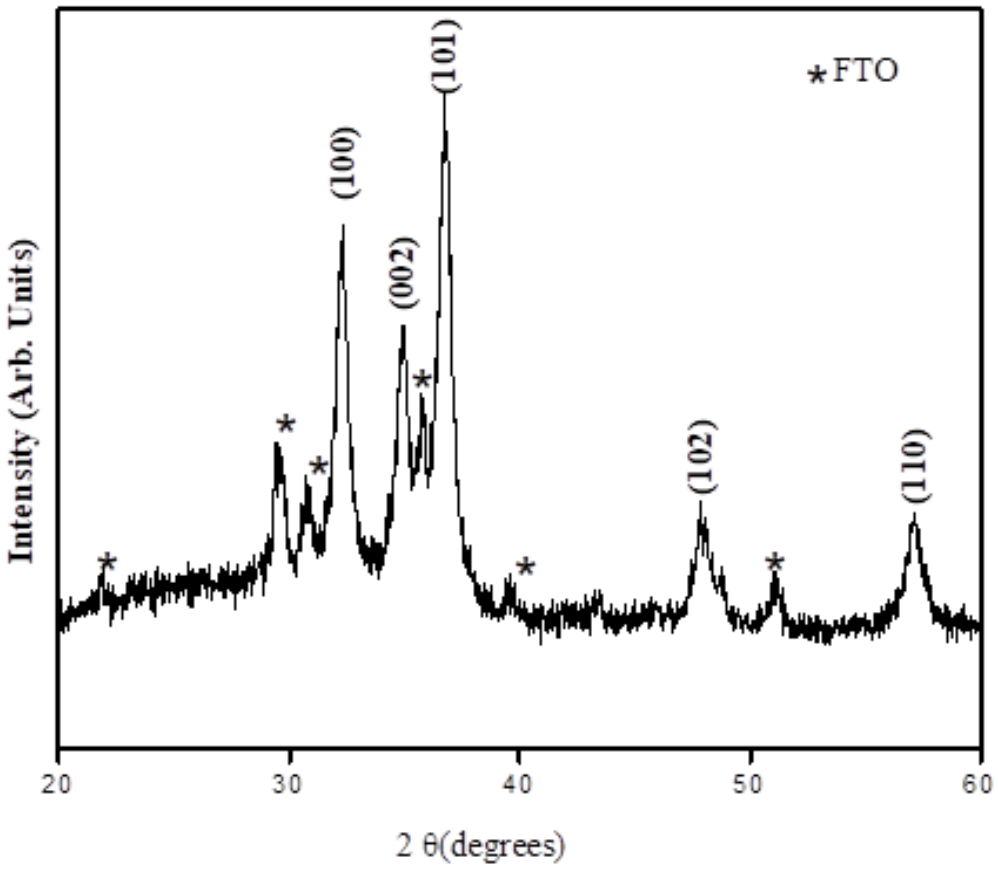

Figure 38: XRD analysis of ZnO NWAs

Figures 39(a,b) show low and high magnification micrographs of ZnO NWAs grown on the FTO substrate after initial hydrothermal treatment. The diameter of each nanowire is about 60-80 nm and their length up to 1.5 μm respectively. ZnO NWAs are uniform in their size, well ordered and partially oriented on the substrate. The high-magnification SEM image showed NWAs are not densely packed but have smaller nanogaps between them, which can be important for incorporation or intercalation of RGO monodispersed layers. Figures 39(c,d) show top view FESEM micrographs of RGO/ZnO NWAs heterostructure. These micrographs reveal effective intercalation or stacking of RGO on the surface of ZnO NWAs. High magnified micrographs (Figure 39d) revealed that the ZnO NWAs embedded within RGO monolayers and their tips can be seen within those layers upon keen observation, suggesting their successful intercalation. ZnO exhibited tapering features and their diameter and length is about 80-150 nm and 1-2 μm respectively. It is important to note that ZnO arrays used for composite have large aspect-ratio due to thick ZnO seed film of about 200 nm. ZnO NAs with smaller dimensions does not stand pulse sonication and gets detached from the substrate eventually. The EDX spectrum in Figure 40 showed peaks for Zn, O, C, Si, Sn and In elements. Presence of Zn, C, and O with elemental ratios > 20% (% EDX is provided in supplementary materials) ensure the formation of RGO/ZnO NWAs heterostructures, while the rest elemental peaks are appeared due to the constituents of FTO coated glass.

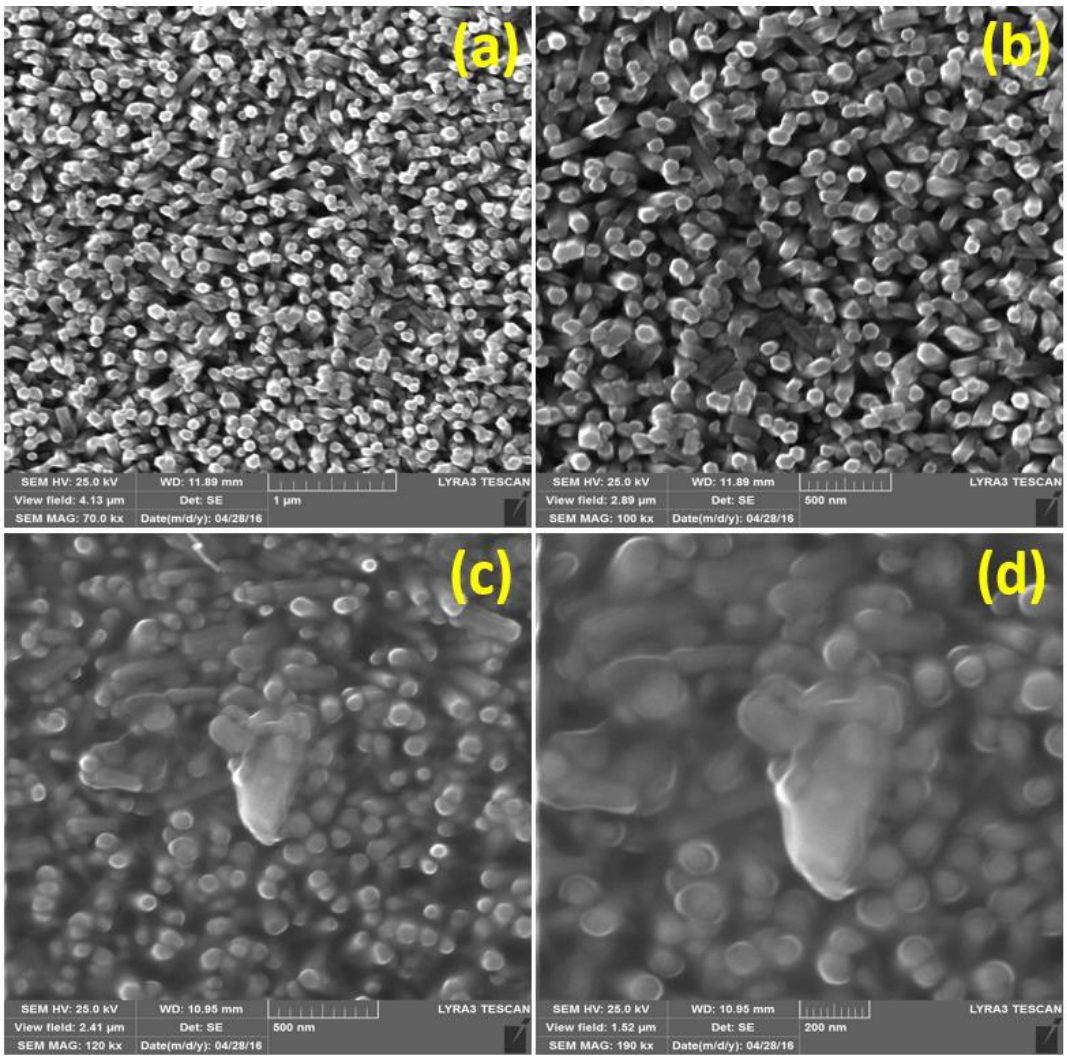

Figure 39: FESEM images of ZnO and RGO/ZnO NWAs arrays grown on FTO glass substrate. (a) and (b) showing low and high magnification micrographs of pristine ZnO NWAs, (c) and (d) showing low and high magnification micrographs of RGO/ZnO NWAs

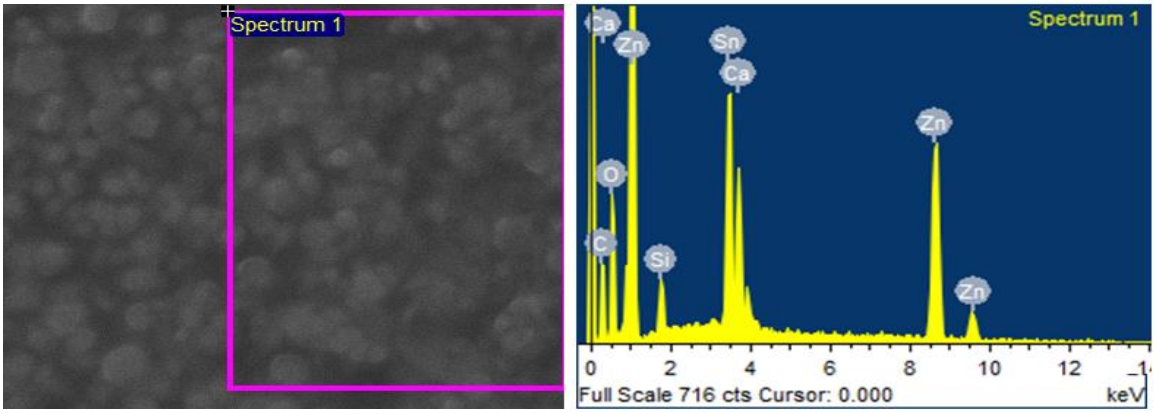

Figure 40: EDX spectrum of RGO/ZnO NWAs heterostructures on FTO glass substrate

Raman spectrum provided in Figure 41 to comprehend RGO/ZnO NWAs heterostructure formation. Figure 41(a) shows the Raman spectrum of the RGO. The sample showed distinct Raman peaks at 1338 and 1580-1584 cm^{-1}, corresponding to the defects (D) and graphitic (G) (~1582 cm^{-1} in graphite) [224]. The ratio of D and G band is very low i.e. 1.29, which is attributed to the disorders, structural defects and formation of small sp^2 domains during reduction [225]. Figure 41(b) represents Raman analysis of RGO/ZnO NWAs on FTO glass substrate. Apart from Si (Due to glass substrate) peaks, two major peaks 447, 590 and 1110 cm^{-1} were seen in the Raman spectrum of hybrid materials in addition to D and G peaks for RGO. These peaks assigned as E_1 E_2 and A_1 Raman active phonons and they are characteristic for ZnO nanomaterials. Moreover, the D, G peaks shifting in the hybrid product, which is attributed to defects and strained caused by interaction between RGO and ZnO NWAs [226]. Pulse sonication intercalation of RGO may also attribute to the defects and ultimately to the shift of these peaks slightly shifted to lower wavenumbers. The background noise in Raman spectrum is due to the contribution of FTO constituents. Which are also vulnerable to add their vibrational contribution to the spectrum.

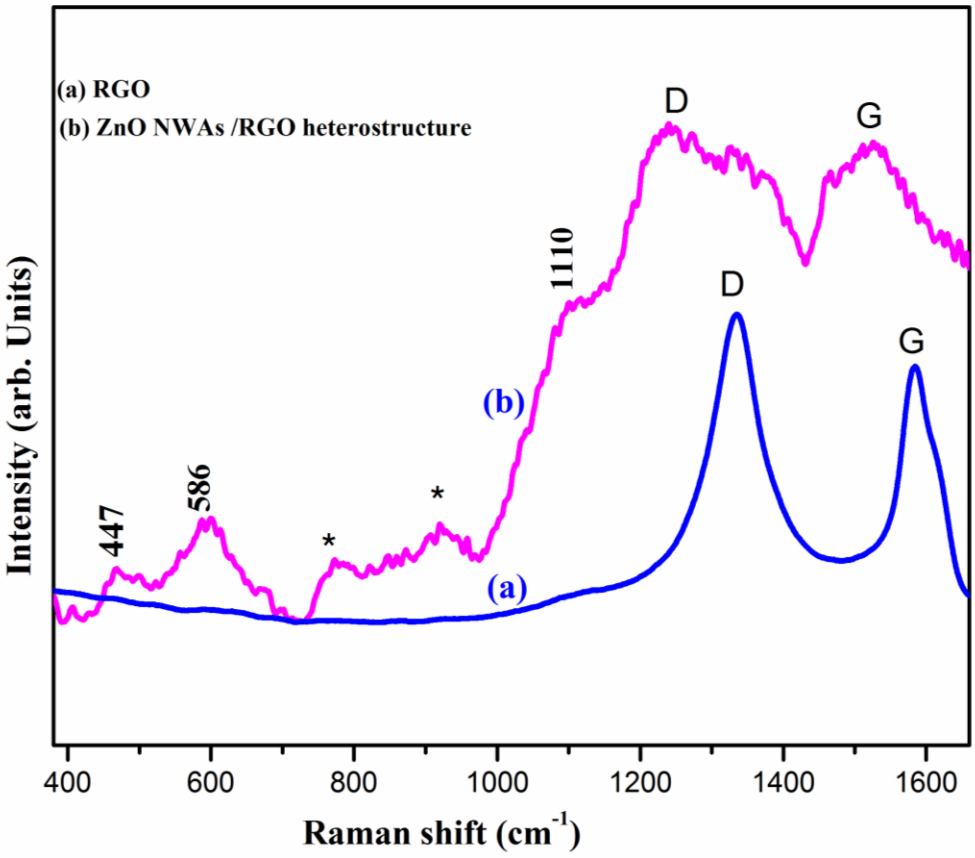

Figure 41: Raman spectrum of RGO and RGO/ZnO NWAs heterostructure

The UV–Vis absorption spectrum of the RGO/ZnO NWAs shown in Figure 42. It is worthwhile to mention that Srikant and Clarke [227] used diverse techniques to examine the optical band gap of ZnO single crystals and established that the room temperature band gap of ZnO was 3.3 eV, however, the lower values could be associated to the presence of a valence band-donor transitions [228]. Additionally, the absorbance spectra reported in the literature are typically wide-ranging because of the influence of innumerable defects to the absorbance [228]. In our case, the absorption spectrum for ZnO has a narrow peak near the band edge in the exciton absorption region at about ~365 nm, which corresponds to ~3.38 eV band gap. For pristine RGO two distinct peaks were observed at 233 nm and 300 nm which are ascribed to $\pi \rightarrow \pi^*$ transition of aromatic C–C bonds, and $n \rightarrow \pi^*$ transition of C═O bonds. However, in case of RGO/ZnO composite formation, the absorption edge appears at ~ 410 nm (band gap ~3.0 eV) as the RGO/ZnO experienced redshift. Similarly, the absorption peak of RGO also appears almost at a similar position as for pure RGO in the composite spectrum. As expected the composite absorption peak quenched, which is due to the variation in the optical behavior of the RGO/ZnO NWAs product after the addition of RGO multi sheets. These results also provide strong evidence to support the formation of RGO/ZnO NWAs heterostructures.

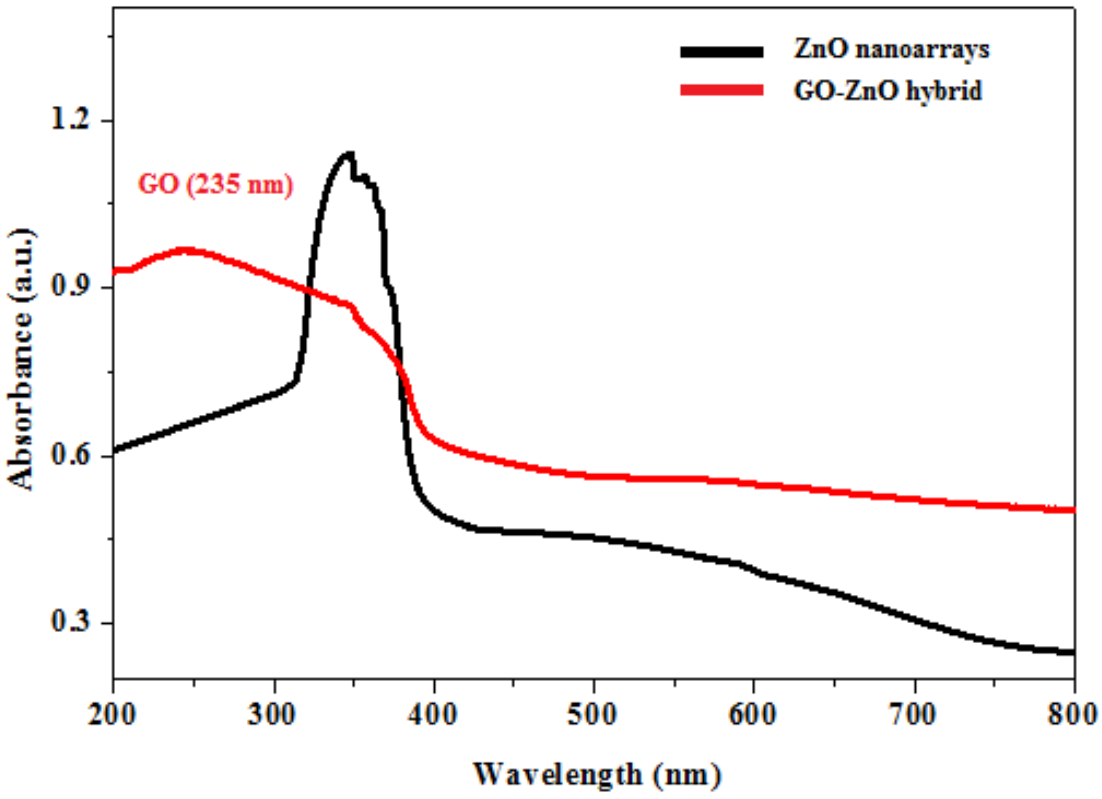

Figure 42: UV visible spectrum of ZnO, RGO and RGO/ZnO NWAs heterostructures

6.3.2 Photoelectrochemical Properties of RGO/ZnO NWAs

Linear Sweep Voltammetry (LSV) and Chronoamperometry techniques used to investigate the photoelectrochemical properties of the nanoarchitecture. Pristine ZnO and RGO/ZnO NWAs heterostructures grown over FTO substrate used as working electrodes in this study. FTO substrate used due to their conducting ability as a working electrode. The voltage sweep range was kept from -1 V to 1 V and the results are provided in Figure 43(A). In absence of luminescence of solar light, no significant photocurrent observed for any material. This observation indicated that materials are inactive in absence of light. Though, insignificant current density is observed at high voltage even in dark due to over potential energy. Noteworthy photocurrent response is observed for pristine ZnO NWAs-based devices under visible light illumination through solar simulator, which reached to a maximum value of ~ 0.25 mA/cm^2 at 0.5 V and remain steady until 1.0 V. Significant increase and amelioration observed for RGO intercalated ZnO NWAs as the voltage assisted photocurrent density continuously increase and reach to maximum value of ~2.4 mA/cm^2 at 0.8 V. The LSV measurement showing positive photocurrent densities for all materials under solar visible light luminescence, which indicated the oxygen evolution reaction (OER) is rather dominant for our materials at provided voltage range. Figure 43(B) indicated the chronoamperometric response of ZnO and RGO/ZnO NWAs at a bias voltage 0.25V with and without solar illumination. The momentary photocurrent responses were obtained from pristine ZnO and RGO/ZnO NWAs during repeated ON/OFF visible light illumination cycles, where the ON/OFF time interval was kept constant. The lowest bias

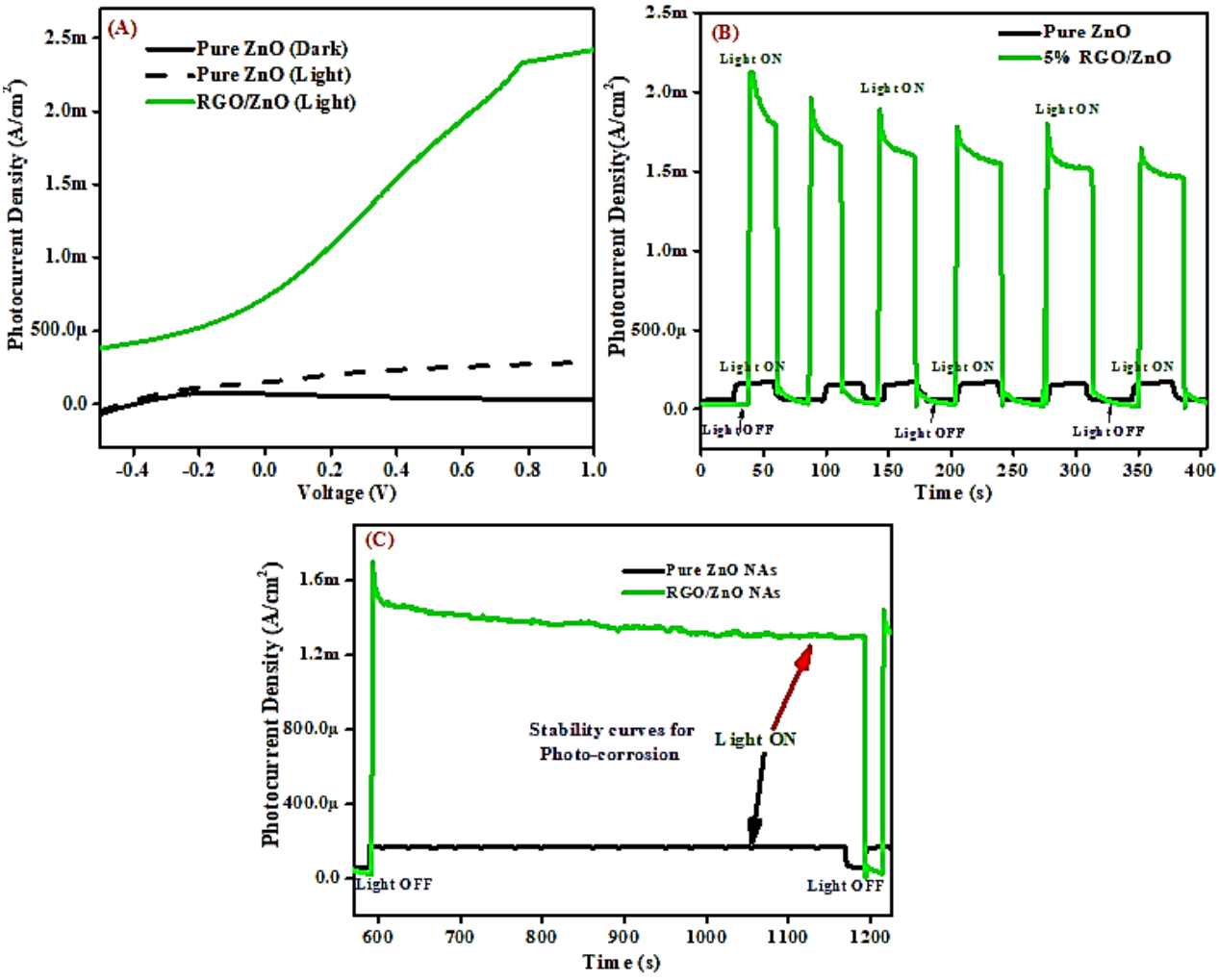

Figure 43: Photoelectrochemical (LSV) properties of RGO/ZnO NWAs electrodes: (A) Linear Sweep Voltammograms (LSV) collected with a scan rate of 0.05 mV/s in dark and under illumination; (B) Periodic $I-t$ curves at bias potential of 0.25V under illumination with regular light ON/OFF cycles. (C) $I-t$ stability curves demonstration

voltage deliberately provided to see the maximum photoresponse of the material with minimum voltage support. Results showed that in dark both materials are negligibly active but under illumination, these materials become active due to the generation of excitons, as

it absorbs visible light energy to knocked electrons from their valence band (VB) to conduction band (CB). However, in case of pristine ZnO the current density is lower, and its maximum value is recorded at ~0.15 mA/cm^2. As expected, for RGO modified ZnO NWAs the value of current density is jumped to ~1.55 mA/cm^2, which is ~10-fold increase in current density after incorporating RGO in ZnO. These results are quite impressive as compared to available literature as indicated in Table 4. It can be seen that researcher mainly used the solvothermal method. Larger photocurrent density of 1.52 mA/cm^2 has been reported by Chandrasekaran at high voltage (1.45 V) for triangle shaped GO/ZnO nanomaterials. The large photocurrent for these materials related to the oxygen vacancies and defects in the crystal phase [229]. Yusoff et al. decorated core-shell Fe_3O_4/ZnO over RGO by solvothermal method and determined that the photocurrent density increased with the contents of RGO. They measured photocurrent density of 0.85 mA/cm^2 at a relatively high voltage of 1.23V [230]. In related study Xu et al. anchored ZnO over RGO by conventional hydrothermal and ion exchange technique [231]. They achieved <0.5 mA/cm^2 current density for RGO/ZnO, which is very lower as compared to our work [231]. The comparative results suggested that sonochemical intercalation of RGO completely alter the physiochemical properties of RGO/ZnO NWAs and enhanced the optical properties to a greater extent. The total ideal percent solar to hydrogen (STH

%) efficiency under steady-state conditions by ignoring all side process can be calculated by following equation [232].

$$\underbrace{\mathrm{STH}(\%) = 0.123 \times J_{ph}(\mathrm{Am}^{-2}) = 1.23 \times J_{ph}(\mathrm{mA\ cm}^{-2})}_{\text{for AM1.5}_g\text{ solar irradiation}} \quad \textbf{(6.1)}$$

Thus, in our case, the ideal calculated STH (%) for pristine ZnO is ~ 0.18% and for RGO/ZnO is ~ 1.91%. This dramatic increase in current density attributed to various reasons like lowering of the band gap of ZnO, efficient charge separation between valence band (VB) and conductance band (CB), the strong electronic nature of graphene, charge transfer enhancement of electrode and good light trapping ability of RGO/ZnO NWAs working electrode. Figure 43(C) revealed the photocorrosion stability graph for ZnO and RGO/ZnO NWAs. The results are satisfactory as even after 1200 seconds (s), the current density level under illumination retained in the range of ~ 1.4 mA/cm^2 for RGO/ZnO NWAs. The efficiency of the photoanode decreased from 1.55 mA/cm^2 to 1.4 mA/cm^2, which corresponds to 9.67% efficiency loss after 1200 s.

Table 4: Comparative photoelectrochemical water splitting performance of different ZnO architectures in terms of photocurrent density

S/No	Nanomaterials structure	Synthesis method	Characteristics	Photocurrent density	Ref.
1	graphene oxide/ZnO triangles	Solvothermal method	Oxygen vacancies and defects	1.52 mA/cm^2 at 1.45 V in 0.1 M NaOH solution	[229]
2	Core-shell Fe_3O_4-ZnO NPs decorated on RGO	Solvothermal method	With graphene contents, current density increased	0.85 mA/cm^2 at 1.23 V in 0.1 M KOH solution	[230]
3	ZnO/graphene heterostructure	Ionic liquid assisted solvothermal synthesis	p-n junction interface formation between graphene and ZnO.	0.015 mA/cm^2 at 0.3 V in 1M NaOH solution	[233]
4	RGO/ZnO hybrid NAs	Pulse Sonochemical assisted solvothermal method	The impregnation of RGO sheets in ZnO NAs and efficient charge transfer	1.55 mA/cm^2 at 1.00 V in 0.5 M Na_2SO_4 solution	This work

6.3.3 Mechanism of Photoelectrochemical Water Oxidation

We suggested the possible charge separation mechanism in Figure 44. Due to the formation of RGO/ZnO composite, photogenerated electrons from the conduction band of the ZnO might prolix along Zn-O-C bonds on the surface of the RGO, which are trapped by H^+ on the surface of RGO resulting into the formation of hydrogen. The holes are readily available for water oxidation reaction to generate oxygen at the working electrode i.e. RGO/ZnO NWAs [234]. The photoinduced holes favorably improve the separation of electrons and holes, and hence decrease the recombination of charge carriers [235]. In this reaction process, the rate of the interfacial charge transfer from ZnO NWAs to RGO is a crucial aspect of minimizing the recombination of electrons and holes and enhancing the overall photoelectrochemical properties of the materials. Thus, in general, the enhancement of photocurrent of RGO/ZnO NWAs composite attributed to better separation proficiency of photo-induced electron-hole pair and lower recombination rate due to the considerable interaction of ZnO NWAs and RGO on the surface [236].

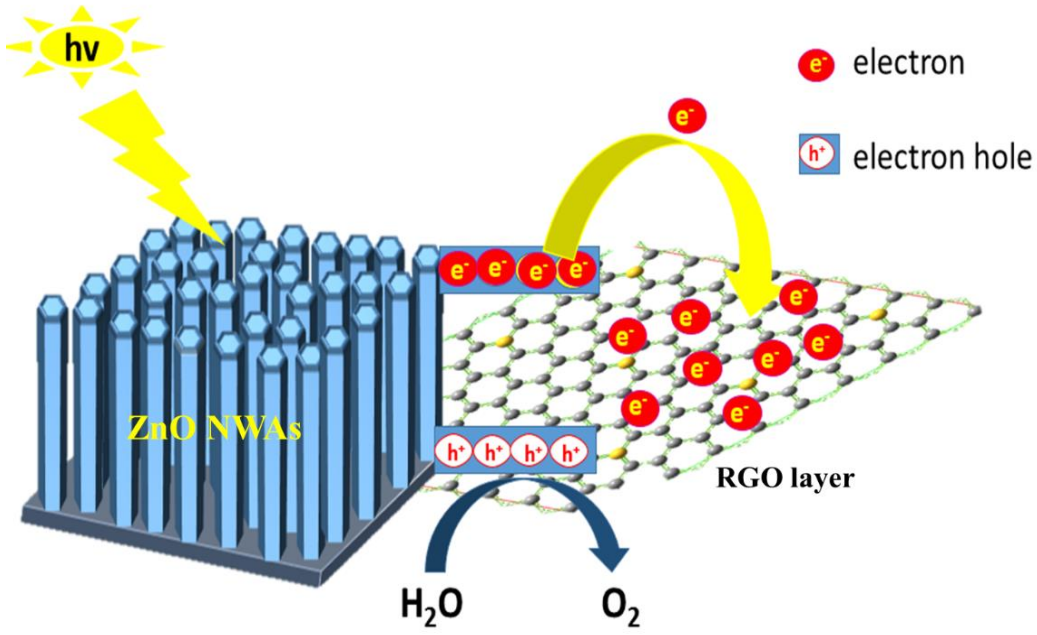

Figure 44: Schematic illustration of PEC water splitting over RGO/ZnO NWAs heterostructures

CHAPTER 7

FABRICATION OF FLEXIBLE PVDF SUPPORTED I-rGO/ZnO NANORODS AND THEIR PIEZOELECTRIC BEHAVIOR

7.1 Introduction

Presently, graphene-based heterostructures have engrossed significant attention for engineering numerous purposeful electrical devices owing to their unique and long lasting conducting characteristics. These include high electron mobility, which induces conductivity in these materials, high flexibility, stable mechanical and chemical properties, larger surface area, and more importantly transparency in the visible range of solar light [214]. Graphene can efficiently transform to reduced graphene oxide (rGO) and graphene oxide (GO) counterparts by adopting various protocols and hence can be used for various applications in that form [237, 238]. GO and rGO/semiconductor based nanohybrids have acknowledged substantial consideration for use in various optoelectric devices like optoelectronics [200, 239], photosensors [240], photocatalysis [241–243], and photoelectrochemical (PEC) water splitting [229, 244, 245] applications. Graphene moieties can be combined with various semiconductors oxide for optoelectronic applications. One of such combination is comprised of graphene and ZnO. ZnO is an n-type semiconductor oxide with a wider band gap of ~ 3.40 eV. The band gap of ZnO can be tuned by mixing it with a suitable nanomaterial. Additionally, it has high exciton binding energy (~ 60 meV) [213]. Like rGO, these unique characteristics make ZnO suitable for various optoelectrical applications [130, 246]. Additionally, the facile

designing of ZnO-based hybrid nanostructures with numerous morphologies has enabled them efficient building blocks for various engineering nano-devices [67, 204].

Synergetic mixing of rGO nanosheets and ZnO NRAs would be a very critical way to boost the physiochemical characteristics of the final material. Consequently, various researchers have been exploring the physicochemical characteristics of graphene/ZnO based nanomaterials i.e. GO and rGO/ZnO NRA hybrid structures by adopting various protocols. These include wet chemistry techniques like sol-gel method, seeded solution growth methods as well as dry chemical techniques such as physical and chemical vapor deposition (PVD and CVD) methods. The graphene/ZnO NRAs have been accomplished by mixing CVD-grown graphene with ZnO. The graphene was transported from the external substrate surface to build the final fusion structure [247]. In the case of GO and rGO, the composites are normally suffered from deprived electrical conductivity. This behavior is normal as the GO developed surface defects and hence the reduction progressions are mandatory during the experimental pathway [248]. In various cases the intercalation of ZnO NRAs and rGO is not successfully achieved due to incomplete intermixing as the required energy is not provided to the system or the rGO nanosheets do not sustain their durability in the hybrid system. Thus, a facile protocol is required to achieve highly arranged and intercalated rGO/ZnO NRAs hybrid system. Lately, researcher explores the piezoelectric characteristics of ZnO NRAs due to their potential piezo and semiconducting nature [66]. The piezoelectric property of the material is the generation of electric current under the action of external power i.e. electrical or mechanical and vice versa. The ZnO NRAs can be grown on a suitable conducting substrate for efficient piezoelectric performance.

In this case, we explore a modified pulse sonication strategy to form rGO/ZnO NRAs hybrid nanostructure. The well-aligned ZnO NRAs were grown over the surface of flexible conducting polymer Polyvinylidene fluoride (PVDF), and the rGO was intercalated through pulse sonication technique in wt% ratios of 1%, 3%, and 5%. Captivating on this approach, the PVDF can be easily recycled after the fabrication of the rGO/ZnO NRAs nanocomposite. Taking the advantage of flexibility, the PVDF supported rGO/ZnO hybrid was used in the piezo nanogenerator.

7.2 Methods and Materials

7.2.1 Synthesis of flexible PVDF films

The flexible PVDF films of uniform thickness (~1µm) were prepared via solution casting method. In a simple experiment 20 wt%, PVDF powder (Sigma Aldrich, mol wt = 100000) were mixed with N, N dimethylformamide (Sigma Aldrich) in 100 mL solution. This solution is stirred and ultrasonicated for 2 h, respectively. The homogenous translucent thick solution is obtained, which is then transfer to a leveled smooth glass surface and allow to mold at room temperature. Elastic and flexible films obtained as shown in Figure 46. These films were used as conducting supports for rGO/ZnO NRAs within piezoelectric nanogenerator fabrication.

7.2.2 Synthesis of PVDF supported ZnO NRAs

3x5 cm^2 of elastic PVDF substrates were thoroughly cleaned with DI water and ethanol to remove the surface residues. The ZnO grains were sputtered over these wafers by Direct Current (DC) magnetron sputtering, by means of a 4” zinc oxide (99.999%) ceramic target [249, 250]. After placing substrates within the vacuum chamber of the magnetron sputtering, the chamber is subjected to a very high vacuum of the magnitude

of $\leq 10^{-6}$ Torr by using strong turbopump. The distance between zinc ceramic target and PVDF substrate was maintained. Argon (Ar) and oxygen (O_2) were employed as sputtering gases. The process pressure is maintained at $\leq 10^{-3}$ Torr, while the DC power is kept at 80W. The percentage gas flow ratio of oxygen and argon kept at 10 : 90, respectively, with deposition time 45 min. The ZnO seeds were successfully deposited over PVDF as shown in Figure 45. To grow ZnO NRAs, these substrates were immersed in the aqueous solution of equimolar analytical grade zinc nitrate hexahydrate [$Zn(NO_3)_2 \cdot 6H_2O$] (Sigma Aldrich) and hexamethylenetetramine [HMTA; $C_6H_{12}N_4$] (Sigma Aldrich) in the hydrothermal vessel at 85ºC for 4 hrs. The pH of the solution maintained at 6. The hydrothermal vessel provided enough pressure for ZnO NRs to penetrate within the PVDF matrix. The ZnO/PVDF substrates were cooled slowly and rinsed with DI water followed by drying at room temperature.

7.2.3 Fabrication of I-rGO/ZnO/PVDF nanogenerators

For the successful intercalation of PVDF supported ZnO NRAs within rGO nanosheets is achieved by pulse sonication approach. GO was synthesized via reported modified Hummer technique, which is then reduced to rGO [238, 240]. 1, 3 and 5 wt % rGO nanosheets were inserted within the PVDF supported ZnO NRs via nontraditional pulse ultrasonication. The pulse was kept at 10 s ON/OFF cycle to avoid the detachment of ZnO NRs from the PVDF substrate. This treatment was done for 12 complete cycles for each substrate. These substrates were labeled as 1%-I-rGO/ZnO/PVDF, 3%-I-rGO/ZnO/PVDF, and 5%-I-rGO/ZnO/PVDF.

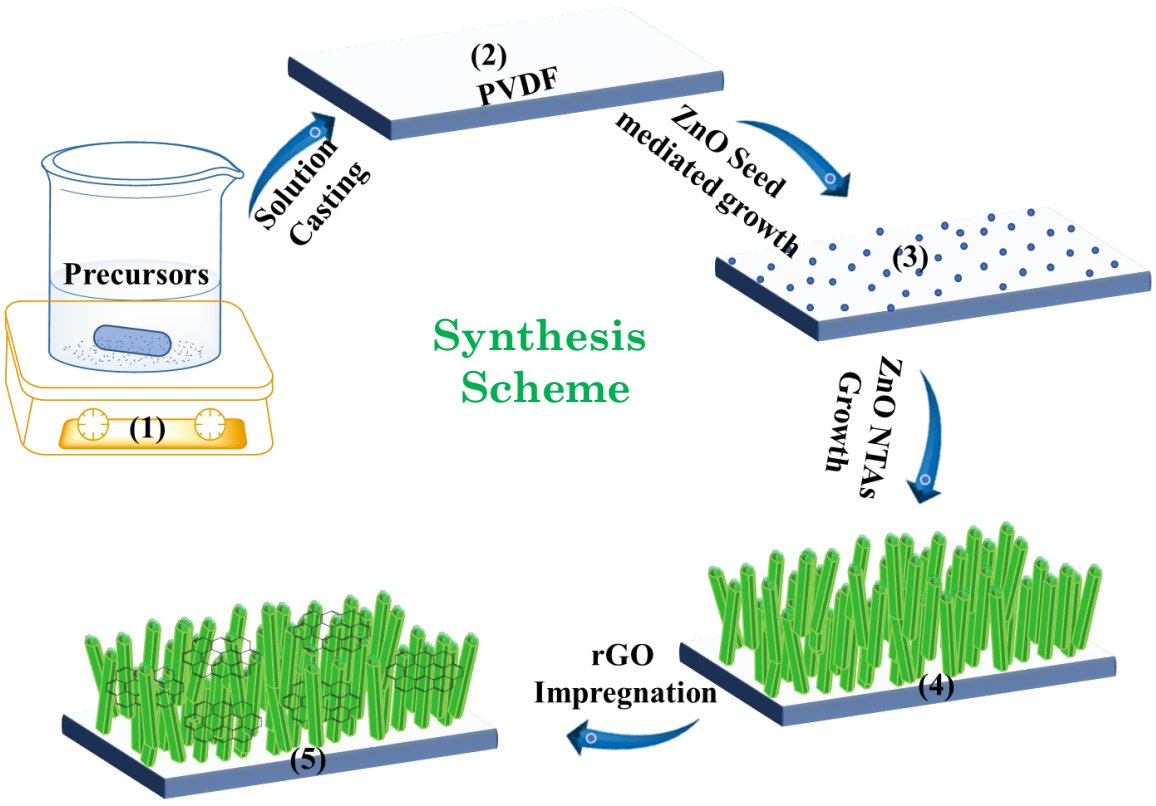

Figure 45: Schematic presentation of the assembling of I-rGO/ZnO/PVDF NRAs hybrid structure using a stepwise sputtering, hydrothermal and pulse sonication technique

7.2.4 Material Characterizations

The morphological features were examined using atomic force microscopy (AFM) and field emission scanning electron microscope (FESEM-Tescan Lyra-3) armed with energy dispersion spectroscopic (EDS) detector and operated at 20 kV acceleration voltage. The elemental confirmation and chemical composition were explored using EDS detector. The crystalline phases of the NRAs were scrutinized by X-rays powder diffraction (XRD) technique provided with Cupper Kα X-rays radiation (λ=0.15406nm) source. During XRD measurement, the scan rate was kept at 2^{o}/min by varying the angle (2θ) from 5^{o} to 70^{o}. The intercalation of rGO with ZnO NRAs, Raman spectra recorded via iHR320 Horiba Spectrometer by using ~532 nm LASER. The optoelectronic characteristics of the hybrid NRAs were examined via UV-Vis/DRS and photoluminescence (PL) spectra were recorded using FluoroLog-3 modular system with 450W Xenon lamp in the UV/Vis range. The electrical nature of the I-rGO/ZnO NRAs hybrid was detected by a source meter (Keithley 2010). The piezoelectric behavior was studied by using the handmade controller device and Tektronix 2215 60mhz oscilloscope (Figure 46).

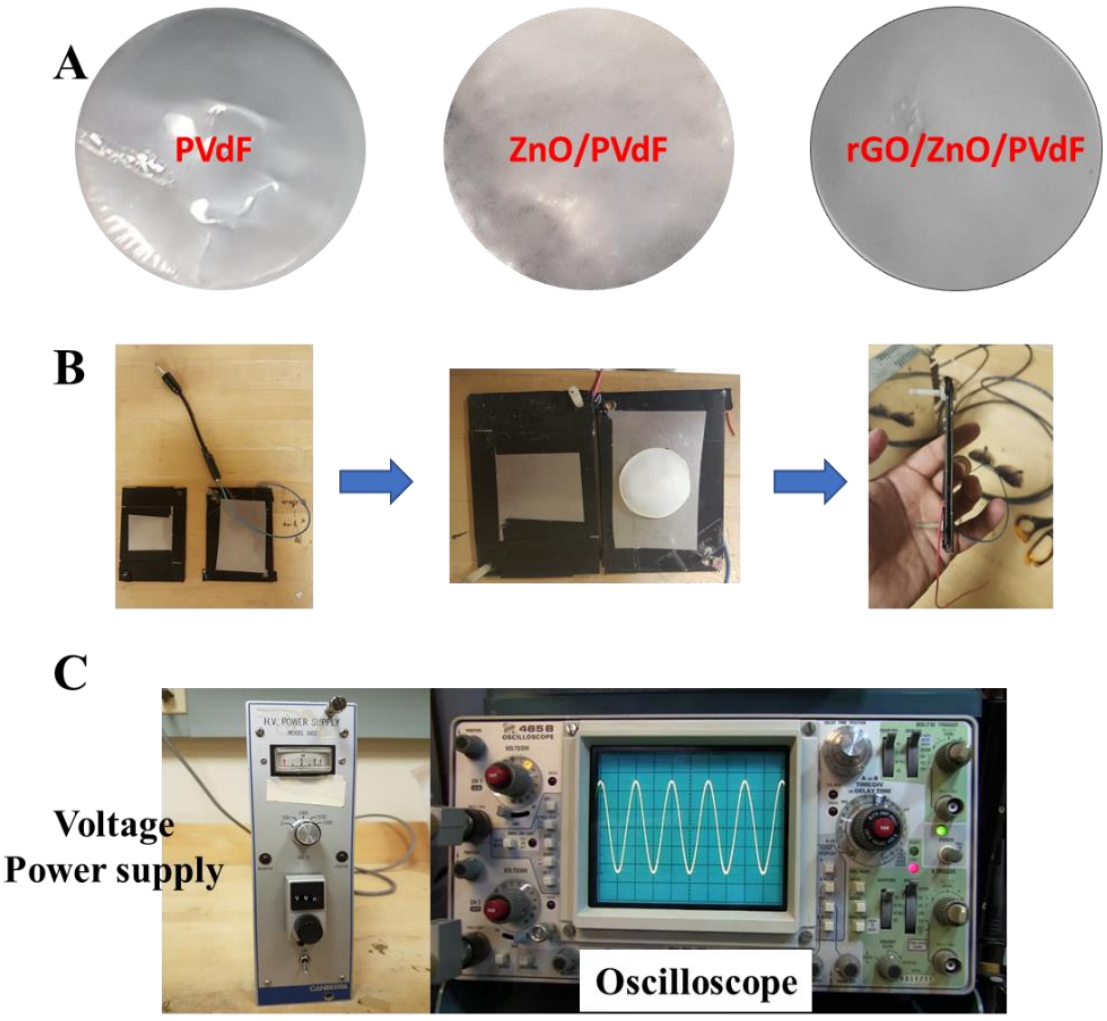

Figure 46: A. Piezo samples, B. The assembling of the piezogenerator device, and C. The power and piezo output recording devices

7.3 Results and Discussion

The stepwise growth of ZnO is also confirmed with the help of FESEM images. Figure 47(a) shows the SEM image of bare PVDF and there is no NPs or other impurities observed except the PVDF matrix. The ZnO seeds can be seen in Figure 47b) on the PVDF surface, which adsorbed after initial seeding. SEM micrographs of ZnO NRAs/PVDF and the rGO/ZnO/PVDF NRA hybrid structure is shown in Figure 47(c-g). As given in Figures 47(c,d), one dimensional epitaxial quasi-aligned ZnO NRs are grown over PVDF surface uniformly. The high magnification micrographs show the closer ZnO NRA with small spaces. Moreover, Figures 47(e,f) show the intercalated rGO layers within the ZnO NRAs, while Figure 47(f), showing the magnified rGO layer, in which the ZnO are embedded. The ZnO morphologies over PVDF wafer are same before and after the intercalation of rGO. The rGO layers provide mechanical strength to ZnO NRAs at atomic level owing to their strong mechanical properties [210].

To examine the optical characteristics of I-rGO/ZnO NRAs over PVDF substrate, PL spectra were taken, as revealed in Figure 48. The emission photoluminescence (PL) spectra of ZnO sample display two important bands i.e. a tiny sharp band at ~370 nm (UV) and a strong broadband at ~600 nm (visible). These emission bands are the characteristic PL bands of ZnO NRAs and arise from deep level related emissions [213]. The PL spectra of PVDF also provide for comparison, which indicates no PL emission. The intercalation of rGO significantly decreases the PL intensity of ZnO with a small right shift of ~ 5nm. This decrease can be attributed to the improvement of the optical properties as reported elsewhere [214, 251]. Due to the improved electrical conductance

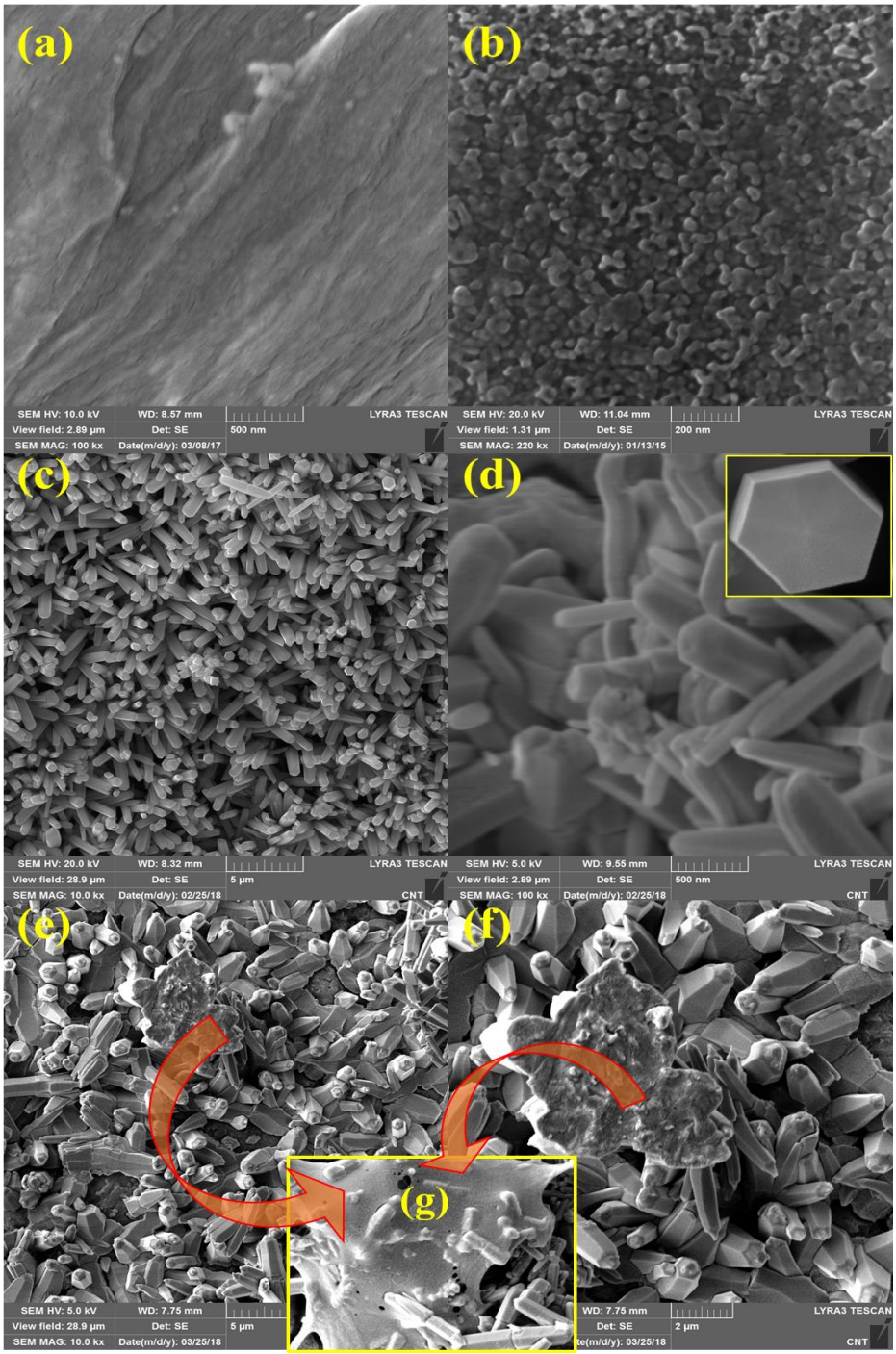

Figure 47: FE-SEM images (a)PVDF Film, (b) ZnO seeds over PVDF, (c) low and high resolution (d) ZnO NRAs after growth, and (e-g) I-rGO/ZnO NRAs over PVDF substrate.

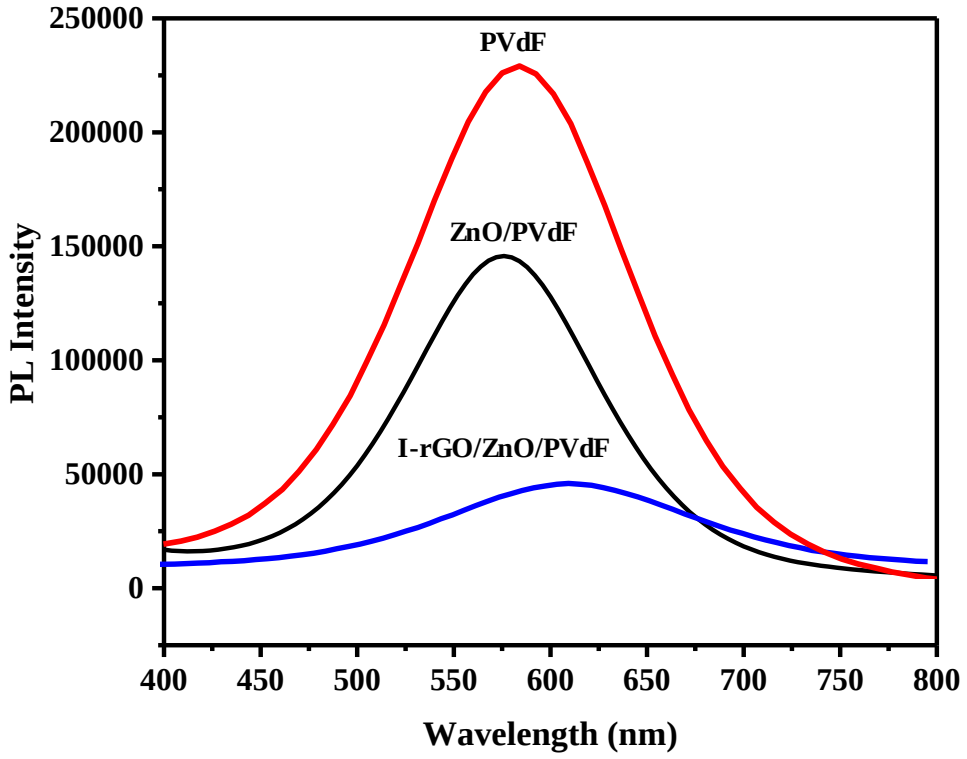

Figure 48: The emission photoluminescence spectra of ZnO/PVDF and I-rGO/ZnO/PVDF NRAs, measured at room temperature

of graphene, it provides an efficient pathway for carrier charge transfer, and hence improve the photogenerated electron-hole pairs lifetime. Thus, the extreme quenching is caused by intercalation of rGO nanosheets to ZnO NRs. The exceedingly mobile π-orbital electrons of rGO are the key to enhancing these characteristics. In addition to that, the overall conductive properties of the composite are also elevated due to the presence of sp^2 atoms in rGO [251].

The Raman spectrum of rGO displays distinctive doublet D and G Raman band in Figure 49. Due to reduction, the characteristic D/G band ratio changes significantly and they are at ~1.0:0.8 ratio. The Raman spectra of composite show ZnO NRAs (from 100 to 800 cm^{-1}), the D and G bands of rGO at 1346 and 1585 cm^{-1} with a slight shift from the vibrational values of pristine rGO. The as-grown ZnO NRAs mainly characteristic two peaks at ~339 and a strong single peak at ~440 cm^{-1} and assigned to the E^{high}_2 mode. The E^{high}_2 peak suggested that the ZnO NRAs are highly crystalline. Similar the optical modes (LO) are observed at 572, 1150 and 2450 cm^{-1}. The vibrational energies of ZnO experienced a significant shift of ~10 $cm^{-1}$with the intercalation of rGO [252]. For any hexagonal system, the shift can be calculated by equation 7.1 [253].

$$\Delta\omega = \left[b - a\left(\frac{C_{33}}{C_{13}}\right)\right]\varepsilon_{cc} \qquad \textbf{(7.1)}$$

Where $\varepsilon_{cc,}$ E^{high}_2 and ($\Delta\omega$) show strain along *c*-direction, peak position shift energy and peak position, respectively [253]. Similarly, *a* and *b* are showing the potential parameters of phonon deformation, while C_{13} and C_{33} displaying elastic constants. These results suggest that the strain state of ZnO was altered expressively by the biaxial compressive stress. This stress is acceptable due to the elastomeric properties of PVDF,

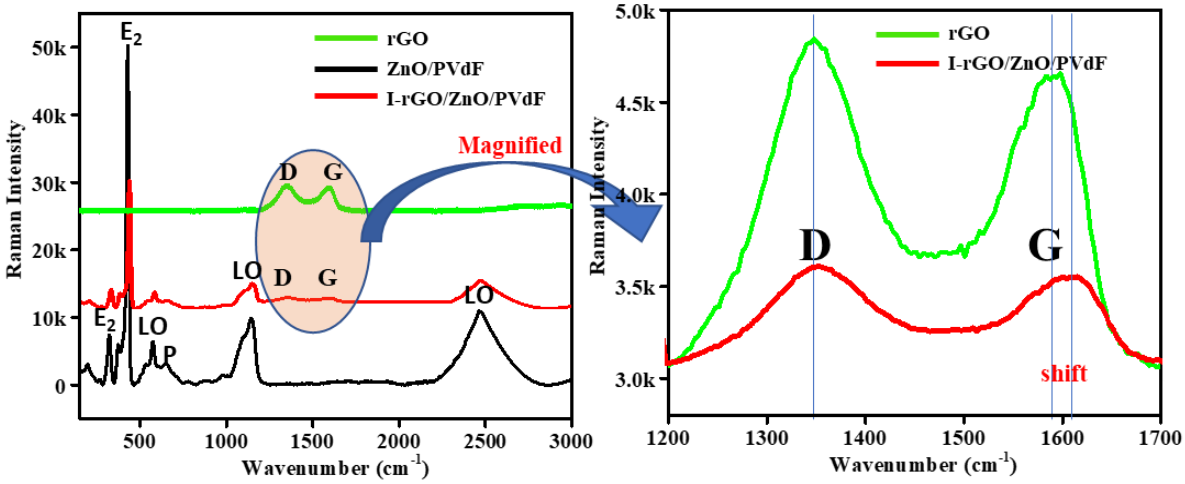

Figure 49: Room temperature Raman spectra of PVDF, ZnO/PVDF NRAs and the I-rGO/ZnO/PVDF.

which provided support for ZnO NRs. This modification in the ZnO NRAs strain state after rGO intercalation is steady with the PL spectral results (discussed above).

To further confirm the electrical conductance behavior of I-rGO-ZnO/PVDF NRAs and its rationality for piezo device applications, we performed the current-voltage (*I–V*) analysis and the spectra are supplied in Figure 50. The electrical characteristics of the ZnO /PVDF NRAs with and without I-rGO layer suggested that there is no significant current observed for the ZnO/PVDF NRAs, however, a significant current flow is observed for the I-rGO intercalated ZnO/PVDF NRAs sample. These comparative results suggest that the I-rGO layer significantly enhanced the charge conduction within I-rGO/ZnO/PVDF NRAs.

The as-fabricated flexible ZnO/PVDF and I-rGO/ZnO/PVDF NRA were further tested in piezoelectric energy actuator as shown in Figure 46(B). Figure 51 shows the piezoelectric output potential measurements of the ZnO/PVDF and I-rGO/ZnO/PVDF based piezoelectric nanogenerator. The controlled mechanical force was supplied by using cylindrical rod having 10 g mass and 10 mm diameter and, was used for applying mechanical force. The cylindrical rod was adjusted at certain heights to provide 10, 15 and 20 N of force to the piezogenerators containing the synthesized materials. The voltage output was measured with the help of oscilloscope. For each sample, the voltage window of oscilloscope adjusted accordingly. The ZnO oxide based piezoelectric nanogenerators in Figure 51(a) displayed a stable output voltage (V_{out}) for each sample. It can be realized that for ZnO/PVDF the maximum V_{out} is 1.8V. The gradual increase of rGO intercalation significantly enhanced the V_{out} value to 3.8V for 5% I-rGO/ZnO/PVDF nanogenerators. We also studied the effect of different loads on the performance of I-

rGO/ZnO/PVDF nanogenerators (Figure 51b). It can be seen that the V_{out} increased incrementally from ~3 to ~4 V with the increase in the load (10→15→20 N) by adjusting the distance between the 5% I-rGO/ZnO/PVDF piezo-nanogenerator and striking cylinder. Thus, it can be concluded that the piezoelectric nanogenerator generated V_{out} linearly increased as the mechanical load increases in accordance with the following equation [254].

$$V = \frac{dL}{\varepsilon_r \varepsilon_0 A} F \quad \textbf{(7.1)}$$

where V (output voltage), F (load), d (piezoelectric constant), ε_r (relative dielectric constant), ε_0 (vacuum dielectric constant), A (cross-section), and L (length), of the piezo nanogenerators used in the study, respectively. The I-rGO/ZnO/PVDF showed characteristic piezoelectric behavior like already reported study [255]. These results also suggested that flexible ZnO based nanogenerators can be a good candidate for advanced piezoelectric materials.

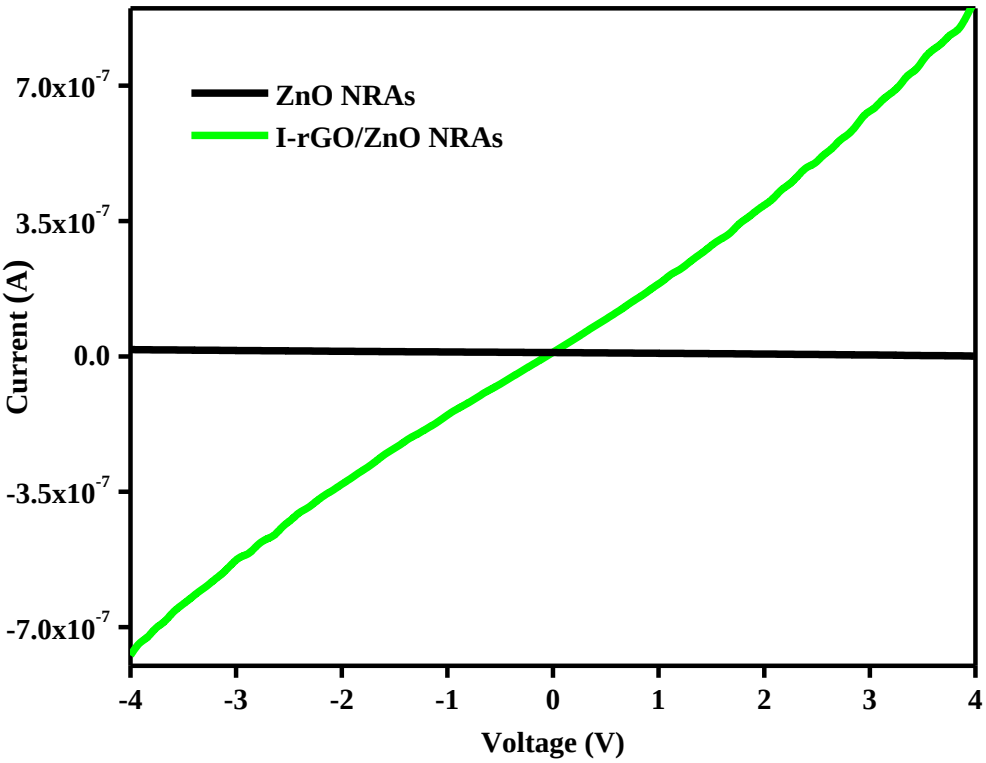

Figure 50: The I–V measurements of ZnO/PVDF NRAs and I-rGO/ZnO/PVDF NRA.

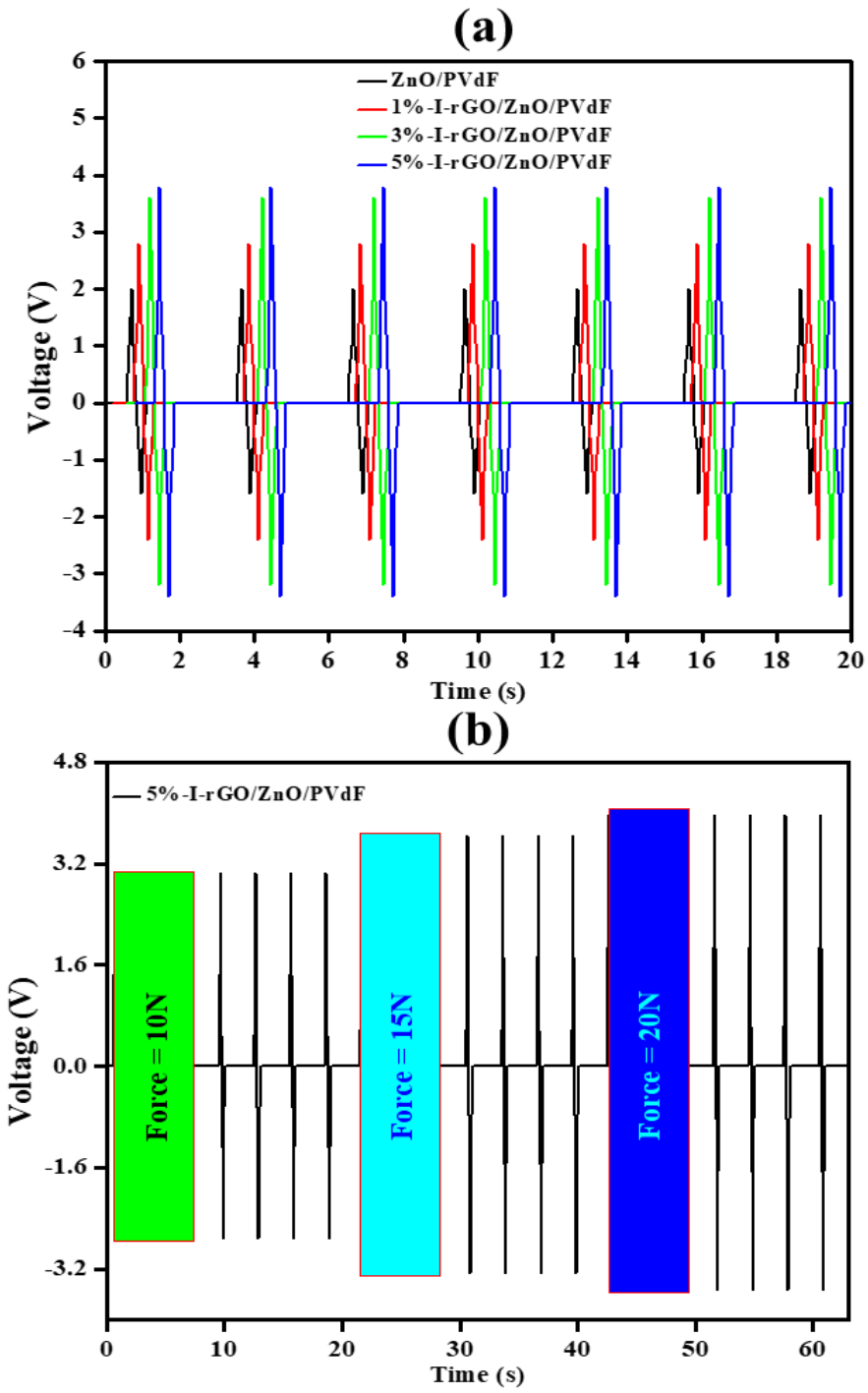

Figure 51: (a) Polarized Piezoelectric output voltage output for 1, 3 and 5 % I-rGO/ZnO/PVDF -based piezoelectric nanogenerator (b) Output voltage with a variation of the input mechanical force.

7.3.1 Mechanism of Piezoelectric Devices

Each crystalline structure materials have several charge units (q). The dipoles of these units are randomly arranged. This random orientation leads to the negligible dipole and hence the material possesses very limited piezoelectric behavior. Therefore, to enhance the piezoelectric performance of the material, it is always advised to perform poling prior to use it for testing. The poling can be done by applying external bias using the power supply. The charges start reorientation and poled in specific order to minimize the system energy [1,2]. Figure 52(A). is showing the poling process within the piezo material.

We performed the poling of PVdF, ZnO/PVdF, and rGO/ZnO/PVdF NAs with the help of high voltage power supply. The purpose of high voltage is to keep the poled charges intact even after removal of the external bias [2]. The NRs structures are usually suitable for polling due to efficient charge distribution at their surface. This makes them efficient for piezoelectric applications. Figure 52(B). provides the schematic of the stated mechanism by which the rGO/ZnO/PVdF nanogenerators showed the piezo behavior.

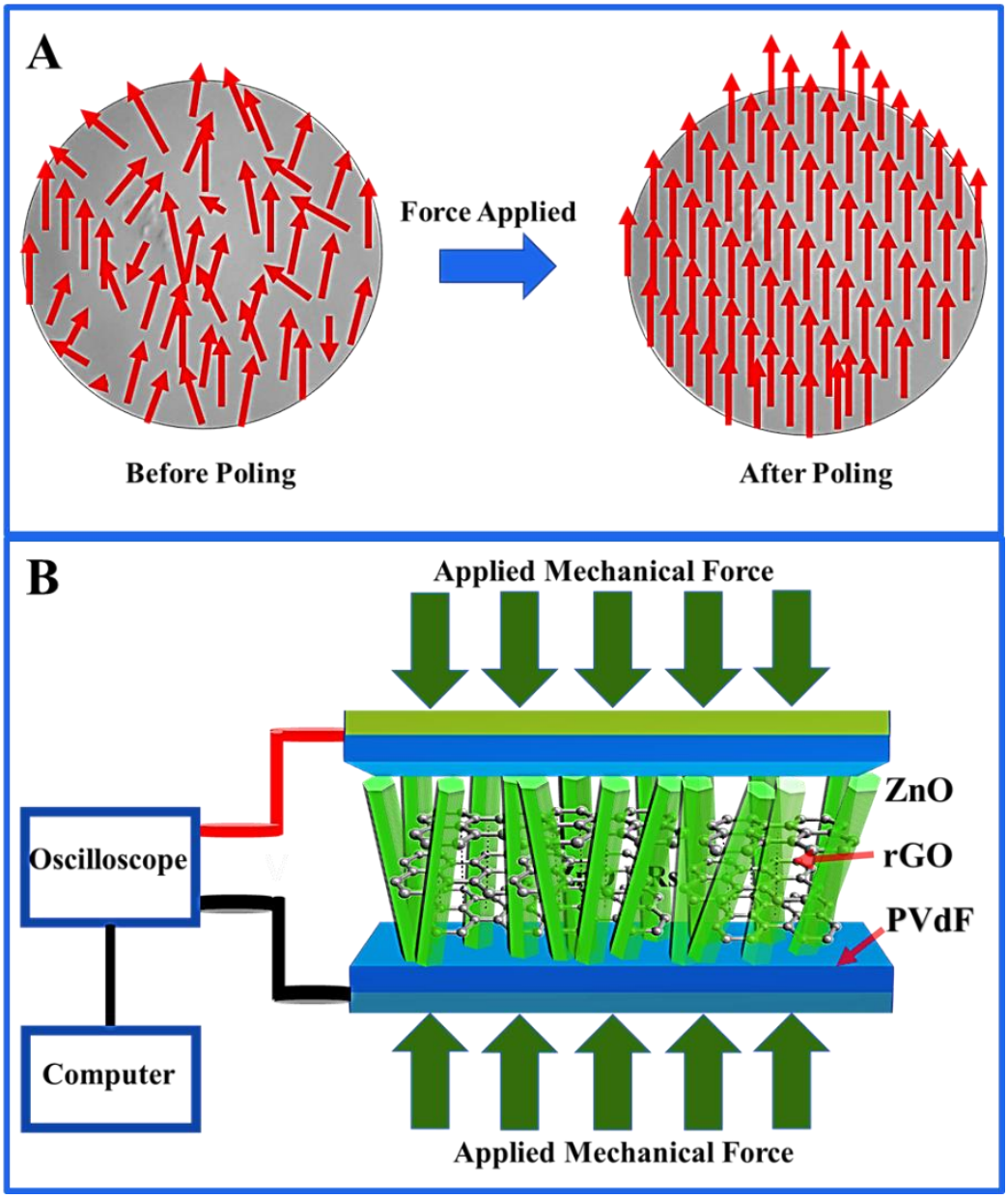

Figure 52: A. Poling mechanism of charges, B. Piezoelectric current generation by ZnO NRs

CHAPTER 8

CONCLUSIONS AND FUTURE RECOMMENDATIONS

We have reported various hybrid NAs for renewable energy harvesting applications. Some of the main conclusions are provided as follow.

Firstly, we successfully synthesized heterostructure photoanodes composed of Ag, Fe_2O_3 and TiO_2 NTAs through a pulse sonochemical-assisted *in situ* electrochemical anodization protocol. The as-synthesized photoanodes were investigated using different characterization techniques. FESEM, EDX, and elemental mapping confirmed the presence of Ag, Fe, Ti and O elements in the Ag/α-Fe_2O_3/TiO_2 NAs. XRD established the existence of the anatase and alpha phases for the TiO_2 NTAs and Fe_2O_3, respectively. The IR spectra exhibited characteristic vibrational bands and a right shift due to the heavier Ag atoms being incorporated into the crystal lattices of the heterostructures. The DRS spectra indicated a shift in the absorption band towards the visible region from 380 to 485 nm for Ag/α-Fe_2O_3/TiO_2. The PEC results indicated 2.5- and 5-fold increases in the current density for the α-Fe_2O_3/TiO_2 (1.05 mA/cm^2) and Ag/α-Fe_2O_3/TiO_2 (2.59 mA/cm^2) photoanodes, respectively, compared to the pristine TiO_2. The EIS Nyquist plots showed the lowest resistance for Ag/α-Fe_2O_3/TiO_2, which signified the feasibility of interfacial charge transfer in these materials. These results confirmed that heterostructure materials can be synthesized via simple anodization techniques with well-controlled shape and morphology for efficient photocatalytic applications.

Secondly, the first attempt to grow single dimensional (1D) Au/In_2O_3 NWs through electrochemical anodization on the Indium substrate is presented. Highly dense, uniform NWs of 30-40 nm thickness is grown. The XRD patterns disclosed that Au/In_2O_3 NWs existed in highly crystalline cubic phase with (222) peak at 31^0 is the dominant facet growth, while the deconvoluted XPS results established that Au is presented in zero oxidation state. The Raman spectrum indicated peaks between 100 to 700 cm^{-1} for In-O stretching and bending modes, which are characteristic of In_2O_3. The optical band gap was reduced from 3.13 eV to 2.90 eV in case of Au/In_2O_3 NWs with sufficient charge recombination suppression. The PEC water splitting measurements indicate significant photocurrent values of 0.58 and 1.39 mA/cm^2 at 1.2 V (vs RHE) for In_2O_3, Au/In_2O_3 NWs photoanodes, with good stability against photocorrosion. The EIS and Mott–Schottky results indicated that there is significant charge transfer and band bending took place in Au/In_2O_3 NWs.

Thirdly, GaON/ZnO composite photoelectrode is successfully achieved by simple solvothermal method over FTO in a single step. The morphological study through SEM indicated ZnO NRs embedded in GaON nanosheets. The EDX, Mapping, and XPS confirm the elemental details and existence of nitrogen in the overall nanoarchitecture. XRD and Raman spectrum showed slight right shift due to the replacement of Zinc by heavier Gallium atom in the crystal and formation of GaON/ZnO nanoarchitecture. The optical study via DRS and PL confirmed the decrease in the band gap ZnO from 3.26 to 2.58 eV and significant quenching in the case of GaON/ZnO NRAs, which can be attributed to significant visible light absorption and the decrease in the photogenerated exciton recombination rate, respectively. The photoelectrochemical results indicated that

the current density is enhanced up to 2.4 folds in the GaON/ZnO nanoarchitecture at 1.0 V bias and the maximum current density of 1.2 mA/cm^2 is achieved at 1.2V. The Nyquist plot showed the decrease in the resistance of GaON/ZnO NRAs, which can be correlated with enhancement of charge transfer through the interface. The conducted DFT calculations on water adsorption on GaON and GaON+Zn_3O_3 nanoarchitecture surfaces indicated that the catalytic performance of the system increases significantly due to the presence of the Zn_3O_3 cluster. Our simulation results are in line with the experiment. Nanoarchitecture materials can be targeted for successful and much-improved water splitting applications, due to their robust physiochemical properties as compared to pristine materials.

Fourthly, RGO/ZnO NWAs heterostructures were grown on FTO glass substrates by wet chemistry followed by pulse sonication technique at relatively lower temperature. FESEM micrographs demonstrated that multiple RGO layers have been effectively inserted between the ZnO nanowire arrays (NWAs). The diameter of each ZnO nanowire ~40-60 nm and length about 1.5 μm was observed. Furthermore, the existence of RGO layers was determined by EDX and Raman spectroscopy. Raman spectrum exhibited D, G peaks and ZnO (E_2) modes at 437 cm^{-1}, confirmed the formation of RGO/ZnO hybrid structure on FTO substrate. Under solar illumination, water was oxidized on the surface of RGO/ZnO NWAs heterostructure photoelectrode with significantly improved performance as compared to the ZnO NWAs. The photoelectrochemical performance of photo-electrode suggested that insertion of RGO layers in between ZnO NWAs enhanced the performance up to 10 folds from 0.14 mA/cm^2 to 1.55 mA/cm^2 correspond to ~ 1.91 ideal STH % efficiency.

Finally, we have successfully established a stepwise fabrication of I-rGO/ZnO/PVDF nanogenerators with the help of sonochemical assisted wet chemistry. The morphological results in FESEM revealed the successful intercalation of rGO and ZnO NRAs. The Raman and IR spectra also showed significant shift due to the strain caused by the intercalation of rGO within the ZnO NRAs. The PL spectra also revealed shifting of emission spectra towards the visible region in case of I-rGO/ZnO/PVDF NRAs. The electrical conductance behavior of the rGO/ZnO NRA showed improved current flow, due to the strong conductance nature of rGO. The ZnO/PVDF and I-rGO/ZnO/PVDF piezoelectric nanogenerators demonstrated piezo behavior and produce a voltage in the response to mechanical load. These nanogenerators showed stable V_{out} of 1.8 and 4V, respective. It was also revealed that the load proportionally increased the piezo current by varying the applied force. with alternating current output characteristics. These results are expected to offer a feasible way to practice flexible PVDF based nanogenerators for more advanced applications.

As for the future is concerned there is still immense amount of effort required to design nanomaterials with characteristics properties, which could fulfil the industrial requirement by having great reproducibility, stability and most importantly cost-effective.

REFERENCES

1. Walter, M.G., Warren, E.L., McKone, J.R., Boettcher, S.W., Mi, Q., Santori, E.A., Lewis, N.S.: Solar water splitting cells. Chem. Rev. 110, 6446–73 (2010). doi:10.1021/cr1002326
2. Wu, Z., Wang, W., Cao, Y., He, J., Luo, Q., Bhutto, W.A., Li, S., Kang, J.: A beyond near-infrared response in a wide-bandgap ZnO/ZnSe coaxial nanowire solar cell by pseudomorphic layers. J. Mater. Chem. A. 2, 14571 (2014). doi:10.1039/C4TA02971B
3. Hydrogen on the rise. Nat. Energy. 1, 16127 (2016). doi:10.1038/nenergy.2016.127
4. Jia, J., Seitz, L.C., Benck, J.D., Huo, Y., Chen, Y., Ng, J.W.D., Bilir, T., Harris, J.S., Jaramillo, T.F.: Solar water splitting by photovoltaic-electrolysis with a solar-to-hydrogen efficiency over 30%. Nat. Commun. 7, 13237 (2016). doi:10.1038/ncomms13237
5. Fujishima, A., Honda, K.: Electrochemical Photolysis of Water at a Semiconductor Electrode. Nature. 238, 37–38 (1972). doi:10.1038/238037a0
6. Feiner, A.-S., McEvoy, A.J.: The Nernst Equation. J. Chem. Educ. 71, 493-494 (1994). doi:10.1021/ed071p493
7. Li, X., Yu, J., Low, J., Fang, Y., Xiao, J., Chen, X.: Engineering heterogeneous semiconductors for solar water splitting. J. Mater. Chem. A. 3, 2485–2534 (2015). doi:10.1039/C4TA04461D
8. Latthe, S.S., An, S., Jin, S., Yoon, S.S.: High energy electron beam irradiated TiO_2

photoanodes for improved water splitting. J. Mater. Chem. A. 1, 13567-13575 (2013). doi:10.1039/c3ta13481d

9. Wang, Z., Pan, X., He, Y., Hu, Y., Gu, H., Wang, Y., Wang, Z., Pan, X., He, Y., Hu, Y., Gu, H., Wang, Y.: Piezoelectric Nanowires in Energy Harvesting Applications. Adv. Mater. Sci. Eng. 2015, 1–21 (2015). doi:10.1155/2015/165631
10. Munn, R.W.: Theory of piezoelectricity, electrostriction, and pyroelectricity in molecular crystals. J. Chem. Phys. 132, 104512 (2010). doi:10.1063/1.3340405
11. Berner, R.A.: The long-term carbon cycle, fossil fuels and atmospheric composition. Nature. 426, 323–326 (2003). doi:10.1038/nature02131
12. Bach, W.: Fossil fuel resources and their impacts on environment and climate. Int. J. Hydrogen Energy. 6, 185–201 (1981). doi:10.1016/0360-3199(81)90007-0
13. Hisatomi, T., Kubota, J., Domen, K.: Recent advances in semiconductors for photocatalytic and photoelectrochemical water splitting. Chem. Soc. Rev. 43, 7520–7535 (2014). doi:10.1039/C3CS60378D
14. Rettie, A.J.E., Chemelewski, W.D., Emin, D., Mullins, C.B.: Unravelling Small-Polaron Transport in Metal Oxide Photoelectrodes. J. Phys. Chem. Lett. 7, 471–479 (2016). doi:10.1021/acs.jpclett.5b02143
15. Yan, Q., Li, G., Newhouse, P.F., Yu, J., Persson, K.A., Gregoire, J.M., Neaton, J.B.: $Mn_2V_2O_7$: An Earth Abundant Light Absorber for Solar Water Splitting. Adv. Energy Mater. 5, 1401840 (2015). doi:10.1002/aenm.201401840
16. Kaufhold, S., Petermann, L., Staehle, R., Rau, S.: Transition metal complexes with N-heterocyclic carbene ligands: From organometallic hydrogenation reactions toward water splitting. Coord. Chem. Rev. 304, 73–87 (2015).

doi:10.1016/j.ccr.2014.12.004

17. Winter, A., Newkome, G.R., Schubert, U.S.: Catalytic Applications of Terpyridines and their Transition Metal Complexes. ChemCatChem. 3, 1384–1406 (2011). doi:10.1002/cctc.201100118

18. Zheng, Y., Lin, L., Wang, B., Wang, X.: Graphitic Carbon Nitride Polymers toward Sustainable Photoredox Catalysis. Angew. Chemie Int. Ed. 54, 12868–12884 (2015). doi:10.1002/anie.201501788

19. Tilley, S.D., Cornuz, M., Sivula, K., Grätzel, M.: Light-Induced Water Splitting with Hematite: Improved Nanostructure and Iridium Oxide Catalysis. Angew. Chemie Int. Ed. 49, 6405–6408 (2010). doi:10.1002/anie.201003110

20. Khan, I., Ibrahim, A.A.M., Sohail, M., Qurashi, A.: Sonochemical assisted synthesis of RGO/ZnO nanowire arrays for photoelectrochemical water splitting. Ultrason. Sonochem. 37, 669–675 (2017). doi:10.1016/j.ultsonch.2017.02.029

21. Shen, L., Xing, Z., Zou, J., Li, Z., Wu, X., Zhang, Y., Zhu, Q., Yang, S., Zhou, W.: Black TiO_2 nanobelts/g-C_3N_4 nanosheets Laminated Heterojunctions with Efficient Visible-Light-Driven Photocatalytic Performance. Sci. Rep. 7, 41978 (2017). doi:10.1038/srep41978

22. Ge, M., Li, Q., Cao, C., Huang, J., Li, S., Zhang, S., Chen, Z., Zhang, K., Al-Deyab, S.S., Lai, Y.: Water Splitting: One-dimensional TiO_2 Nanotube Photocatalysts for Solar Water Splitting. Adv. Sci. 4, (2017). doi:10.1002/advs.201770005

23. Shan, L., He, L., Suriyaprakash, J., Yang, L.: Photoelectrochemical (PEC) water splitting of BiOI{001} nanosheets synthesized by a simple chemical

transformation. J. Alloys Compd. 665, 158–164 (2016). doi:10.1016/j.jallcom.2016.01.008

24. Su, Z., Grigorescu, S., Wang, L., Lee, K., Schmuki, P.: Fast fabrication of Ta_2O_5 nanotube arrays and their conversion to Ta_3N_5 for efficient solar driven water splitting. Electrochem. commun. 50, 15–19 (2015). doi:10.1016/j.elecom.2014.10.017

25. Standing, A., Assali, S., Gao, L., Verheijen, M.A., van Dam, D., Cui, Y., Notten, P.H.L., Haverkort, J.E.M., Bakkers, E.P.A.M.: Efficient water reduction with gallium phosphide nanowires. Nat. Commun. 6, 7824 (2015). doi:10.1038/ncomms8824

26. Inoue, Y.: Effects of Metal-Ion Doping, Removal and Exchange on Photocatalytic Activity of Metal Oxides and Nitrides for Overall Water Splitting. In: On Solar Hydrogen & Nanotechnology. pp. 559–588. John Wiley & Sons, Ltd, Chichester, UK

27. Hou, Y., Wen, Z., Cui, S., Ci, S., Mao, S., Chen, J.: An Advanced Nitrogen-Doped Graphene/Cobalt-Embedded Porous Carbon Polyhedron Hybrid for Efficient Catalysis of Oxygen Reduction and Water Splitting. Adv. Funct. Mater. 25, 872–882 (2015). doi:10.1002/adfm.201403657

28. Gan, J., Lu, X., Wu, J., Xie, S., Zhai, T., Yu, M., Zhang, Z., Mao, Y., Wang, S.C.I., Shen, Y., Tong, Y.: Oxygen vacancies promoting photoelectrochemical performance of In2O3 nanocubes. Sci. Rep. 3, 1021 (2013). doi:10.1038/srep01021

29. Luo, S.-P., Mejía, E., Friedrich, A., Pazidis, A., Junge, H., Surkus, A.E., Jackstell,

R., Denurra, S., Gladiali, S., Lochbrunner, S., Beller, M.: Photocatalytic Water Reduction with Copper-Based Photosensitizers: A Noble-Metal-Free System. Angew. Chemie Int. Ed. 52, 419–423 (2013). doi:10.1002/anie.201205915

30. Valenti, M., Jonsson, M.P., Biskos, G., Schmidt-Ott, A., Smith, W.A.: Plasmonic nanoparticle-semiconductor composites for efficient solar water splitting. J. Mater. Chem. A. 4, 17891–17912 (2016). doi:10.1039/C6TA06405A

31. Kim, M., Joshi, B., Yoon, H., Ohm, T.Y., Kim, K., Al-Deyab, S.S., Yoon, S.S.: Electrosprayed copper hexaoxodivanadate (CuV_2O_6) and pyrovanadate ($Cu_2V_2O_7$) photoanodes for efficient solar water splitting. J. Alloys Compd. 708, 444–450 (2017). doi:10.1016/j.jallcom.2017.02.302

32. Khan, I., Abdalla, A., Qurashi, A.: Synthesis of hierarchical WO_3 and Bi_2O_3 /WO_3 nanocomposite for solar-driven water splitting applications. Int. J. Hydrogen Energy. 42, 3431–3439 (2017). doi:10.1016/j.ijhydene.2016.11.105

33. Barth, S., Hernandez-Ramirez, F., Holmes, J.D., Romano-Rodriguez, A.: Synthesis and applications of one-dimensional semiconductors. Prog. Mater. Sci. 55, 563–627 (2010). doi:10.1016/j.pmatsci.2010.02.001

34. Amer, A.W., El-Sayed, M.A., Allam, N.K.: Tuning The Photoactivity of Zirconia Nanotubes-Based Photoanodes via Ultrathin Layers of ZrN: An Effective Approach toward Visible-Light Water Splitting. J. Phys. Chem. C. 120, 7025–7032 (2016). doi:10.1021/acs.jpcc.6b01144

35. Mozalev, A., Bendova, M., Gispert-Guirado, F., Pytlicek, Z., Llobet, E.: Metal-substrate-supported tungsten-oxide nanoarrays via porous-alumina-assisted anodization: from nanocolumns to nanocapsules and nanotubes. J. Mater. Chem.

A. 4, 8219–8232 (2016). doi:10.1039/C6TA02027E

36. Allam, N.K., El-Sayed, M.A.: Photoelectrochemical Water Oxidation Characteristics of Anodically Fabricated TiO_2 Nanotube Arrays: Structural and Optical Properties. J. Phys. Chem. C. 114, 12024–12029 (2010). doi:10.1021/jp1037014

37. Gamarra, J.K., Solano, C., Piñeres, I., Gómez, H., Mass, J., Montenegro, D.N.: Systematic study of inorganic functionalization of ZnO nanorods by Sol-Gel method. J. Phys. Conf. Ser. 786, 12022 (2017). doi:10.1088/1742-6596/786/1/012022

38. Pan, Z., Qiu, Y., Yang, J., Liu, M., Zhou, L., Xu, Y., Sheng, L., Zhao, X., Zhang, Y.: Synthesis of three-dimensional hyperbranched TiO_2 nanowire arrays with significantly enhanced photoelectrochemical hydrogen production. J. Mater. Chem. A. 3, 4004–4009 (2015). doi:10.1039/C4TA06498D

39. Cho, I.S., Choi, J., Zhang, K., Kim, S.J., Jeong, M.J., Cai, L., Park, T., Zheng, X., Park, J.H.: Highly Efficient Solar Water Splitting from Transferred TiO_2 Nanotube Arrays. Nano Lett. 15, 5709–5715 (2015). doi:10.1021/acs.nanolett.5b01406

40. Sun, B., Shi, T., Tan, X., Liu, Z., Wu, Y., Liao, G.: Titanium Dioxide Nanorods with Hydrogenated Oxygen Vacancies for Enhanced Solar Water Splitting. J. Nanosci. Nanotechnol. 16, 6148–6154 (2016). doi:10.1166/jnn.2016.11036

41. Han, C., Yan, L., Zhao, W., Liu, Z.: TiO_2/CeO_2 core/shell heterojunction nanoarrays for highly efficient photoelectrochemical water splitting. Int. J. Hydrogen Energy. 42, 12276–12283 (2017). doi:10.1016/j.ijhydene.2017.03.068

42. Devarapalli, R.R., Debgupta, J., Pillai, V.K., Shelke, M. V., Yang, P.:

C@SiNW/TiO_2 Core-Shell Nanoarrays with Sandwiched Carbon Passivation Layer as High Efficiency Photoelectrode for Water Splitting. Sci. Rep. 4, 737–743 (2014). doi:10.1038/srep04897

43. Guo, K., Liu, Z., Han, J., Liu, Z., Li, Y., Wang, B., Cui, T., Zhou, C.: Hierarchical TiO_2–$CuInS_2$ core–shell nanoarrays for photoelectrochemical water splitting. Phys. Chem. Chem. Phys. Phys. Chem. Chem. Phys. 16, 16204–16213 (1620). doi:10.1039/c4cp01971g

44. Lv, R., Wang, T., Su, F., Zhang, P., Li, C., Gong, J.: Facile synthesis of ZnO nanopencil arrays for photoelectrochemical water splitting. Nano Energy. 7, 143–150 (2014). doi:10.1016/j.nanoen.2014.04.020

45. Liu, M., Nam, C.Y., Black, C.T., Kamcev, J., Zhang, L.: Enhancing Water Splitting Activity and Chemical Stability of Zinc Oxide Nanowire Photoanodes with Ultrathin Titania Shells. J. Phys. Chem. C. 117, 13396–13402 (2013). doi:10.1021/jp404032p

46. Chen, H., Wei, Z., Yan, K., Bai, Y., Zhu, Z., Zhang, T., Yang, S.: Epitaxial Growth of ZnO Nanodisks with Large Exposed Polar Facets on Nanowire Arrays for Promoting Photoelectrochemical Water Splitting. Small. 10, 4760–4769 (2014). doi:10.1002/smll.201401298

47. Yang, X., Wolcott, A., Wang, G., Sobo, A., Fitzmorris, R.C., Qian, F., Zhang, J.Z., Li, Y.: Nitrogen-doped ZnO nanowire arrays for photoelectrochemical water splitting. Nano Lett. 9, 2331–2336 (2009). doi:10.1021/nl900772q

48. Patel, P.P., Hanumantha, P.J., Velikokhatnyi, O.I., Datta, M.K., Hong, D., Gattu, B., Poston, J.A., Manivannan, A., Kumta, P.N.: Nitrogen and cobalt co-doped zinc

oxide nanowires-Viable photoanodes for hydrogen generation via photoelectrochemical water splitting. J. Power Sources. 299, 11–24 (2015). doi:10.1016/j.jpowsour.2015.08.027

49. Zhong, M., Ma, Y., Oleynikov, P., Domen, K., Delaunay, J.-J.: A conductive ZnO–ZnGaON nanowire-array-on-a-film photoanode for stable and efficient sunlight water splitting. Energy Environ. Sci. 7, 1693 (2014). doi:10.1039/c3ee43806f

50. Bai, Z., Yan, X., Li, Y., Kang, Z., Cao, S., Zhang, Y.: 3D-Branched ZnO/CdS Nanowire Arrays for Solar Water Splitting and the Service Safety Research. Adv. Energy Mater. 6, 1501459 (2016). doi:10.1002/aenm.201501459

51. Grigorescu, S., So, S., Yoo, J.E., Mazare, A., Hahn, R., Schmuki, P.: Open top anodic Ta_3N_5 nanotubes for higher solar water splitting efficiency. Electrochim. Acta. 182, 803–808 (2015). doi:10.1016/j.electacta.2015.09.159

52. Hou, J., Yang, C., Cheng, H., Jiao, S., Takeda, O., Zhu, H.: High-performance p-Cu $_2$ O/n-TaON heterojunction nanorod photoanodes passivated with an ultrathin carbon sheath for photoelectrochemical water splitting. Energy Environ. Sci. 7, 3758–3768 (2014). doi:10.1039/C4EE02403F

53. Resasco, J., Zhang, H., Kornienko, N., Becknell, N., Lee, H., Guo, J., Briseno, A.L., Yang, P.: $TiO_2/BiVO_4$ Nanowire Heterostructure Photoanodes Based on Type II Band Alignment. ACS Cent. Sci. 2, 80–88 (2016). doi:10.1021/acscentsci.5b00402

54. Wang, N., Wang, D., Li, M., Shi, J., Li, C.: Photoelectrochemical water oxidation on photoanodes fabricated with hexagonal nanoflower and nanoblock WO_3.

Nanoscale. 6, 2061 (2014). doi:10.1039/c3nr05601e

55. Pihosh, Y., Turkevych, I., Mawatari, K., Uemura, J., Kazoe, Y., Kosar, S., Makita, K., Sugaya, T., Matsui, T., Fujita, D., Tosa, M., Kondo, M., Kitamori, T.: Photocatalytic generation of hydrogen by core-shell WO_3/$BiVO_4$ nanorods with ultimate water splitting efficiency. Sci. Rep. 5, 11141 (2015). doi:10.1038/srep11141

56. Iqbal, N., Khan, I., Yamani, Z.H.A., Qurashi, A.: A facile one-step strategy for in-situ fabrication of WO_3-$BiVO_4$ nanoarrays for solar-driven photoelectrochemical water splitting applications. Sol. Energy. 144, 604–611 (2017). doi:10.1016/j.solener.2017.01.057

57. Rao, P.M., Cai, L., Liu, C., Cho, I.S., Lee, C.H., Weisse, J.M., Yang, P., Zheng, X.: Simultaneously Efficient Light Absorption and Charge Separation in WO_3/$BiVO_4$ Core/Shell Nanowire Photoanode for Photoelectrochemical Water Oxidation. Nano Lett. 14, 1099–1105 (2014). doi:10.1021/nl500022z

58. Shi, X., Choi, I.Y., Zhang, K., Kwon, J., Kim, D.Y., Lee, J.K., Oh, S.H., Kim, J.K., Park, J.H.: Efficient photoelectrochemical hydrogen production from bismuth vanadate-decorated tungsten trioxide helix nanostructures. Nat. Commun. 5, 4775 (2014). doi:10.1038/ncomms5775

59. Luo, Z., Li, C., Liu, S., Wang, T., Gong, J.: Gradient doping of phosphorus in Fe_2O_3 nanoarray photoanodes for enhanced charge separation. Chem. Sci. 8, 91–100 (2017). doi:10.1039/C6SC03707K

60. Yang, W., Oh, Y., Kim, J., Kim, H., Shin, H., Moon, J.: Photoelectrochemical Properties of Vertically Aligned CuInS2 Nanorod Arrays Prepared via Template-

Assisted Growth and Transfer. ACS Appl. Mater. Interfaces. 8, 425–431 (2016). doi:10.1021/acsami.5b09241

61. Shaner, M.R., Fountaine, K.T., Ardo, S., Coridan, R.H., Atwater, H.A., Lewis, N.S.: Photoelectrochemistry of core–shell tandem junction n–p^+-Si/n-WO_3 microwire array photoelectrodes. Energy Environ. Sci. 7, 779–790 (2014). doi:10.1039/C3EE43048K

62. Hou, Y., Yu, X., Syed, Z.A., Shen, S., Bai, J., Wang, T.: GaN nano-pyramid arrays as an efficient photoelectrode for solar water splitting. Nanotechnology. 27, 455401 (2016). doi:10.1088/0957-4484/27/45/455401

63. Curie, J., Curie, P.: Development, via compression, of electric polarization in hemihedral crystals with inclined faces. Bull. la Soc. Minerol. Fr. 3, 90–93 (1880)

64. Curie, J., Curie, P.: Contractions and expansions produced by voltages in hemihedral crystals with inclined faces. Comptes Rendus. 93, 1137–1140 (1881)

65. Mokrý, P.: 100 years of piezoelectric materials in acoustics: From a sonar to active metasurfaces. Presented at the (2016)

66. Wang, Z.L., Song, J.: Piezoelectric nanogenerators based on zinc oxide nanowire arrays. Science. 312, 242–6 (2006). doi:10.1126/science.1124005

67. Dakua, I., Afzulpurkar, N.: Piezoelectric Energy Generation and Harvesting at the Nano-Scale : Materials and Devices. Nanomater. Nanotechnol. 3, 1–16 (2013). doi:10.5772/56941

68. Lueng, C.M., Chan, H.L.W., Surya, C., Choy, C.L.: Piezoelectric coefficient of aluminum nitride and gallium nitride. J. Appl. Phys. 88, 5360–5363 (2000). doi:10.1063/1.1317244

69. Agrawal, R., Espinosa, H.D.: Giant Piezoelectric Size Effects in Zinc Oxide and Gallium Nitride Nanowires. A First Principles Investigation. Nano Lett. 11, 786–790 (2011). doi:10.1021/nl104004d

70. Jain, A., K. J., P., Sharma, A.K., Jain, A., P.N, R.: Dielectric and piezoelectric properties of PVDF/PZT composites: A review. Polym. Eng. Sci. 55, 1589–1616 (2015). doi:10.1002/pen.24088

71. Thakur, P., Kool, A., Hoque, N.A., Bagchi, B., Khatun, F., Biswas, P., Brahma, D., Roy, S., Banerjee, S., Das, S.: Superior performances of in situ synthesized ZnO/PVDF thin film based self-poled piezoelectric nanogenerator and self-charged photo-power bank with high durability. Nano Energy. 44, 456–467 (2018). doi:10.1016/J.NANOEN.2017.11.065

72. Parangusan, H., Ponnamma, D., Al-Maadeed, M.A.A.: Stretchable Electrospun PVDF-HFP/Co-ZnO Nanofibers as Piezoelectric Nanogenerators. Sci. Rep. 8, 754 (2018). doi:10.1038/s41598-017-19082-3

73. Devarajan, Y., Munuswamy, D.B.: Analysis on the Influence of Nanoparticles of Alumina, Copper Oxide, and Zirconium Oxide on the Performance of a Flat-Plate Solar Water Heater. Energy & Fuels. 30, 9908–9913 (2016). doi:10.1021/acs.energyfuels.6b02264

74. Grey, J.: Organic photovoltaics: Strong absorption in stiff polymers. Nat. Mater. 15, 705 (2016). doi:10.1038/nmat4666

75. Chang, J., Lin, Z., Zhu, H., Isikgor, F.H., Xu, Q.H., Zhang, C., Hao, Y., Ouyang, J.: Enhancing the photovoltaic performance of planar heterojunction perovskite solar cells by doping the perovskite layer with alkali metal ions. J. Mater. Chem.

A. 4, 16546–16552 (2016). doi:10.1039/C6TA06851K

76. Zhang, Z., Long, J., Yang, L., Chen, W., Dai, W., Fu, X., Wang, X.: Organic semiconductor for artificial photosynthesis: water splitting into hydrogen by a bioinspired $C_3N_3S_3$ polymer under visible light irradiation. Chem. Sci. 2, 1826–1830 (2011). doi:10.1039/C1SC00257K

77. Iqbal, N., Khan, I., Yamani, Z.H., Qurashi, A.: Sonochemical Assisted Solvothermal Synthesis of Gallium Oxynitride Nanosheets and their Solar-Driven Photoelectrochemical Water-Splitting Applications. Sci. Rep. 6, 32319 (2016). doi:10.1038/srep32319

78. Momeni, M.M., Ghayeb, Y.: Cobalt modified tungsten–titania nanotube composite photoanodes for photoelectrochemical solar water splitting. J. Mater. Sci. Mater. Electron. 27, 3318–3327 (2016). doi:10.1007/s10854-015-4161-2

79. Momeni, M.M., Ghayeb, Y.: Visible light-driven photoelectrochemical water splitting on ZnO–TiO2 heterogeneous nanotube photoanodes. J. Appl. Electrochem. 45, 557–566 (2015). doi:10.1007/s10800-015-0836-x

80. Butchosa, C., Guiglion, P., Zwijnenburg, M.A.: Carbon Nitride Photocatalysts for Water Splitting: A Computational Perspective. J. Phys. Chem. C. 118, 24833–24842 (2014). doi:10.1021/jp507372n

81. Khan, I., Ali, S., Mansha, M., Qurashi, A.: Sonochemical assisted hydrothermal synthesis of pseudo-flower shaped Bismuth vanadate ($BiVO_4$) and their solar-driven water splitting application. Ultrason. Sonochem. 36, 386–392 (2017). doi:10.1016/j.ultsonch.2016.12.014

82. Kobosko, S.M., Jara, D.H., Kamat, P. V.: $AgInS_2$–ZnS Quantum Dots: Excited

State Interactions with TiO_2 and Photovoltaic Performance. ACS Appl. Mater. Interfaces. 9, 33379–33388 (2017). doi:10.1021/acsami.6b14604

83. Ge, M., Cao, C., Huang, J., Li, S., Chen, Z., Zhang, K.-Q., Al-Deyab, S.S., Lai, Y.: A review of one-dimensional TiO_2 nanostructured materials for environmental and energy applications. J. Mater. Chem. A. 4, 6772–6801 (2016). doi:10.1039/C5TA09323F

84. Hung, W., Chien, T., Tseng, C.: Enhanced Photocatalytic Water Splitting by Plasmonic TiO_2–Fe_2O_3 Cocatalyst under Visible Light Irradiation. J. Phys. Chem. C. 118, 12676–12681 (2014). doi:10.1021/jp5033965

85. Su, G., Li, Q., Lu, H., Zhang, L., Huang, L., Yan, L., Zheng, M.: Thermal catalytic oxidation of octachloronaphthalene over anatase TiO_2 nanomaterial and its hypothesized mechanism. Sci. Rep. 5, 17800 (2015). doi:10.1038/srep17800

86. Avasare, V., Zhang, Z., Avasare, D., Khan, I., Qurashi, A.: Room-temperature synthesis of TiO_2 nanospheres and their solar driven photoelectrochemical hydrogen production. Int. J. Energy Res. 39, 1714–1719 (2015). doi:10.1002/er.3372

87. Neufeld, O., Toroker, M.C.: Platinum-Doped α-Fe_2O_3 for Enhanced Water Splitting Efficiency: A DFT^+ U Study. J. Phys. Chem. C. 119, 5836–5847 (2015). doi:10.1021/jp512002f

88. Momeni, M.M., Ghayeb, Y., Mohammadi, F.: Fe_2O_3 nanotube films prepared by anodisation as visible light photocatalytic. Surf. Eng. 31, 452–457 (2015). doi:10.1179/1743294414Y.0000000425

89. Sivula, K., Le Formal, F., Grätzel, M., Le Formal, F., Grätzel, M.: Solar Water

Splitting: Progress Using Hematite (α- Fe_2O_3) Photoelectrodes. ChemSusChem. 4, 432–449 (2011). doi:10.1002/cssc.201000416

90. Liao, P., Toroker, M.C., Carter, E.A.: Electron Transport in Pure and Doped Hematite. Nano Lett. 11, 1775–1781 (2011). doi:10.1021/nl200356n

91. Chen, M., Zhao, E., Yan, Q., Hu, Z., Xiao, X., Chen, D.: The Effect of Crystal Face of Fe_2O_3 on the Electrochemical Performance for Lithium-ion Batteries. Sci. Rep. 6, 29381 (2016). doi:10.1038/srep29381

92. Li, X., Bassi, P.S., Boix, P.P., Fang, Y., Wong, L.H.: Revealing the Role of TiO_2 Surface Treatment of Hematite Nanorods Photoanodes for Solar Water Splitting. ACS Appl. Mater. Interfaces. 7, 16960–16966 (2015). doi:10.1021/acsami.5b01394

93. Sivula, K., Grätzel, M.: CHAPTER 4. Tandem Photoelectrochemical Cells for Water Splitting. Presented at the (2013)

94. Zhang, J., Liu, Z., Liu, Z.: Novel WO_3/Sb_2S_3 Heterojunction Photocatalyst Based on WO_3 of Different Morphologies for Enhanced Efficiency in Photoelectrochemical Water Splitting. ACS Appl. Mater. Interfaces. 8, 9684–9691 (2016). doi:10.1021/acsami.6b00429

95. Momeni, M.M., Hakimian, M., Kazempour, A.: Preparation and characterisation of manganese–TiO_2 nanocomposites for solar water splitting. Surf. Eng. 32, 514–519 (2016). doi:10.1179/1743294415Y.0000000073

96. MOMENI, M.M.: Dye-sensitized solar cell and photocatalytic performance of nanocomposite photocatalyst prepared by electrochemical anodization. Bull. Mater. Sci. 39, 1389–1395 (2016). doi:10.1007/s12034-016-1280-1

97. Trimble, H.M., Frazer, G.E.: Solubility of Ethylene Glycol. Ind. Eng. Chem. 21, 1063–1065 (1929). doi:10.1021/ie50239a022

98. Huffman, B.A., Poltash, M.L., Hughey, C.A.: Effect of Polar Protic and Polar Aprotic Solvents on Negative-Ion Electrospray Ionization and Chromatographic Separation of Small Acidic Molecules. Anal. Chem. 84, 9942–9950 (2012). doi:10.1021/ac302397b

99. Grigioni, I., Stamplecoskie, K.G., Selli, E., Kamat, P. V: Dynamics of Photogenerated Charge Carriers in WO_3/$BiVO_4$ Heterojunction Photoanodes. J. Phys. Chem. C. 119, 20792–20800 (2015). doi:10.1021/acs.jpcc.5b05128

100. Ramana, E.V., Mahajan, A., Graça, M.P.F., Srinivas, A., Valente, M.A.: Ferroelectric and magnetic properties of magnetoelectric $(Na_{0.5}Bi_{0.5})TiO_3$–$BiFeO_3$ synthesized by acetic acid assisted sol–gel method. J. Eur. Ceram. Soc. 34, 4201–4211 (2014). doi:10.1016/j.jeurceramsoc.2014.06.027

101. Manzoor, U., Kim, D.K., Islam, M., Bhatti, A.S.: Removal of Micrometer Size Morphological Defects and Enhancement of Ultraviolet Emission by Thermal Treatment of Ga-Doped ZnO Nanostructures. PLoS One. 9, e86418 (2014). doi:10.1371/journal.pone.0086418

102. Gondal, M.A., Rashid, S.G., Dastageer, M.A., Zubair, S.M., Ali, M.A., Lienhard, J.H., McKinley, G.H., Varanasi, K.K.: Sol–Gel Synthesis of Au/Cu-TiO_2 Nanocomposite and Their Morphological and Optical Properties. IEEE Photonics J. 5, 2201908–2201908 (2013). doi:10.1109/JPHOT.2013.2262674

103. Amiot, C.L., Xu, S., Liang, S., Pan, L., Zhao, J.X.: Near-Infrared Fluorescent Materials for Sensing of Biological Targets. Sensors. 8, 3082–3105 (2008).

doi:10.3390/s8053082

104. Beranek, R., Kisch, H.: Tuning the optical and photoelectrochemical properties of surface-modified TiO_2. Photochem. Photobiol. Sci. 7, 40–48 (2008). doi:10.1039/B711658F

105. Pant, H.R., Pant, B., Sharma, R.K., Amarjargal, A., Kim, H.J., Park, C.H., Tijing, L.D., Kim, C.S.: Antibacterial and photocatalytic properties of Ag/TiO_2/ZnO nano-flowers prepared by facile one-pot hydrothermal process. Ceram. Int. 39, 1503–1510 (2013). doi:10.1016/j.ceramint.2012.07.097

106. Abazović, N.D., Mirenghi, L., Janković, I.A., Bibić, N., Šojić, D. V., Abramović, B.F., Čomor, M.I.: Synthesis and Characterization of Rutile TiO_2 Nanopowders Doped with Iron Ions. Nanoscale Res. Lett. 4, 518–525 (2009). doi:10.1007/s11671-009-9274-1

107. Zhang, J., Li, Y., Zhang, Y., Chen, M., Wang, L., Zhang, C., He, H.: Effect of Support on the Activity of Ag-based Catalysts for Formaldehyde Oxidation. Sci. Rep. 5, 12950 (2015). doi:10.1038/srep12950

108. Pham, M.H., Dinh, C.T., Vuong, G.T., Ta, N.D., Do, T.O.: Visible light induced hydrogen generation using a hollow photocatalyst with two cocatalysts separated on two surface sides. Phys. Chem. Chem. Phys. Phys. Chem. Chem. Phys. 16, 5937–5941 (2014). doi:10.1039/c3cp54629b

109. Warwick, M.E.A., Carraro, G., Toniato, E., Gasparotto, A., Maccato, C., Barreca, D.: XPS analysis of Fe_2O_3-TiO_2-Au nanocomposites prepared by a plasma-assisted route. Surf. Sci. Spectra. 23, 61–69 (2016). doi:10.1116/1.4954387

110. Mirzaei, A., Janghorban, K., Hashemi, B., Bonavita, A., Bonyani, M., Leonardi,

S., Neri, G.: Synthesis, Characterization and Gas Sensing Properties of Ag@α-Fe_2O_3 Core–Shell Nanocomposites. Nanomaterials. 5, 737–749 (2015). doi:10.3390/nano5020737

111. Lee, H., Lee, Y.K., Hwang, E., Park, J.Y.: Enhanced Surface Plasmon Effect of Ag/TiO_2 Nanodiodes on Internal Photoemission. J. Phys. Chem. C. 118, 5650–5656 (2014). doi:10.1021/jp409894b

112. Pudukudy, M., Yaakob, Z.: Facile Synthesis of Quasi Spherical ZnO Nanoparticles with Excellent Photocatalytic Activity. J. Clust. Sci. 26, 1187–1201 (2015). doi:10.1007/s10876-014-0806-1

113. Nozik, A.J.: CHAPTER 13. Novel Approaches to Water Splitting by Solar Photons. RSC Publishers (2013)

114. Lee, J.W., Son, D.Y., Ahn, T.K., Shin, H.W., Kim, I.Y., Hwang, S.J., Ko, M.J., Sul, S., Han, H., Park, N.-G.: Quantum-Dot-Sensitized Solar Cell with Unprecedentedly High Photocurrent. Sci. Rep. 3, 6873–6889 (2013). doi:10.1038/srep01050

115. Xu, R., Li, H., Zhang, W., Yang, Z., Liu, G., Xu, Z., Shao, H., Qiao, G.: The fabrication of In_2O_3/In_2S_3/Ag nanocubes for efficient photoelectrochemical water splitting. Phys. Chem. Chem. Phys. 18, 2710–7 (2016). doi:10.1039/c5cp05833c

116. Linic, S., Christopher, P., Ingram, D.B.: Plasmonic-metal nanostructures for efficient conversion of solar to chemical energy. Nat. Mater. 10, 911–21 (2011). doi:10.1038/nmat3151

117. Tamirat, A.G., Su, W.N., Dubale, A.A., Chen, H.M., Hwang, B.J.: Photoelectrochemical water splitting at low applied potential using a NiOOH

coated codoped (Sn, Zr) α- Fe_2O_3 photoanode. J. Mater. Chem. A. 3, 5949–5961 (2015). doi:10.1039/C4TA06915C

118. Shen, S., Zhou, J., Dong, C.L., Hu, Y., Tseng, E.N., Guo, P., Guo, L., Mao, S.S.: Surface Engineered Doping of Hematite Nanorod Arrays for Improved Photoelectrochemical Water Splitting. Sci. Rep. 4, 6627. doi:10.1038/srep06627

119. Meng, X.Y., Qin, G.W., Li, S., Wen, X.H., Ren, Y.P., Pei, W.L., Zuo, L.: Enhanced photoelectrochemical activity for Cu and Ti doped hematite: The first principles calculations. Appl. Phys. Lett. 98, 112104 (2011). doi:10.1063/1.3567766

120. Guo, C., Zhang, R., Wang, B., Qu, Y.: Visible-light-driven Fe_2O_3 nanoparticles/TiO_2 array photoelectrode and its photoelectrochemical property. Res. Chem. Intermed. 42, 7935–7946 (2016). doi:10.1007/s11164-016-2570-3

121. Song, X.-M., Zhou, X., Yuan, C., Zhang, Y., Tong, Q., Li, Y., Cui, L., Liu, D., Zhang, W.: One-dimensional Fe_2O_3/TiO_2 photoelectrode and investigation of its photoelectric properties in photoelectrochemical cell. Appl. Surf. Sci. 397, 112–118 (2017). doi:10.1016/j.apsusc.2016.11.143

122. D'Elia, D., Beauger, C., Hochepied, J.F., Rigacci, A., Berger, M.H., Keller, N., Keller-Spitzer, V., Suzuki, Y., Valmalette, J.-C., Benabdesselam, M., Achard, P.: Impact of three different TiO_2 morphologies on hydrogen evolution by methanol assisted water splitting: Nanoparticles, nanotubes and aerogels. Int. J. Hydrogen Energy. 36, 14360–14373 (2011). doi:10.1016/j.ijhydene.2011.08.007

123. Pinaud, B.A., Vesborg, P.C.K., Jaramillo, T.F.: Effect of Film Morphology and Thickness on Charge Transport in Ta_3N_5/Ta Photoanodes for Solar Water

Splitting. J. Phys. Chem. C. 116, 15918–15924 (2012). doi:10.1021/jp3041742

124. Tang, J., Durrant, J.R., Klug, D.R.: Mechanism of Photocatalytic Water Splitting in TiO_2 Reaction of Water with Photoholes, Importance of Charge Carrier Dynamics , and Evidence for Four-Hole Chemistry. 127, 13885–13891 (2008)

125. Luan, P., Xie, M., Liu, D., Fu, X., Jing, L.: Effective charge separation in the rutile TiO2 nanorod-coupled α-Fe_2O_3 with exceptionally high visible activities. Sci. Rep. 4, 6180. doi:10.1038/srep06180

126. Hussein, A.K.: Applications of nanotechnology in renewable energies-A comprehensive overview and understanding. Renew. Sustain. Energy Rev. 42, 460–476 (2015). doi:10.1016/j.rser.2014.10.027

127. Luan, P., Xie, M., Fu, X., Qu, Y., Sun, X., Jing, L.: Improved photoactivity of TiO_2–Fe_2O_3 nanocomposites for visible-light water splitting after phosphate bridging and its mechanism. Phys. Chem. Chem. Phys. 17, 5043–5050 (2015). doi:10.1039/C4CP04631E

128. J. Yang, J. Zheng, H. Zhai, X. Yang, L. Yang, Y. Liu, J. Lang, M. Gao: Orented growth of ZnO nanostructures on different substrates via hydrothermal method. J. Alloy. Com- pounds. 489, 51–55 (2010)

129. Wang, D., Bassi, P., Qi, H., Zhao, X., Gurudayal, Wong, L., Xu, R., Sritharan, T., Chen, Z.: Improved Charge Separation in WO_3/$CuWO_4$ Composite Photoanodes for Photoelectrochemical Water Oxidation. Materials. 9, 348 (2016). doi:10.3390/ma9050348

130. Khan, I., Qurashi, A., Berdiyorov, G., Iqbal, N., Fuji, K., Yamani, Z.H.: Single-step strategy for the fabrication of GaON/ZnO nanoarchitectured photoanode their

experimental and computational photoelectrochemical water splitting. Nano Energy. 44, 23–33 (2018). doi:10.1016/j.nanoen.2017.11.050

131. Zhang, F., Qi, L.: Recent Progress in Self-Supported Metal Oxide Nanoarray Electrodes for Advanced Lithium-Ion Batteries. Adv. Sci. 3, 1600049 (2016). doi:10.1002/advs.201600049

132. An, K., Somorjai, G.A.: Size and Shape Control of Metal Nanoparticles for Reaction Selectivity in Catalysis. ChemCatChem. 4, 1512–1524 (2012). doi:10.1002/cctc.201200229

133. Cargnello, M., Chen, C., Diroll, B.T., Doan-Nguyen, V.V.T., Gorte, R.J., Murray, C.B.: Efficient Removal of Organic Ligands from Supported Nanocrystals by Fast Thermal Annealing Enables Catalytic Studies on Well-Defined Active Phases. J. Am. Chem. Soc. 137, 6906–6911 (2015). doi:10.1021/jacs.5b03333

134. Altomare, M., Pozzi, M., Allieta, M., Bettini, L.G., Selli, E.: H_2 and O_2 photocatalytic production on TiO_2 nanotube arrays: Effect of the anodization time on structural features and photoactivity. Appl. Catal. B Environ. 136–137, 81–88 (2013). doi:10.1016/j.apcatb.2013.01.054

135. Li, Y., Nagato, K., Delaunay, J.-J., Kubota, J., Domen, K.: Fabrication of highly ordered Ta_2O_5 and Ta_3N_5 nanorod arrays by nanoimprinting and through-mask anodization. Nanotechnology. 25, 14013 (2014). doi:10.1088/0957-4484/25/1/014013

136. Allam, N.K., Deyab, N.M., Abdel Ghany, N.: Ternary Ti–Mo–Ni mixed oxide nanotube arrays as photoanode materials for efficient solar hydrogen production. Phys. Chem. Chem. Phys. 15, 12274 (2013). doi:10.1039/c3cp52076e

137. Roy-Mayhew, J.D., Aksay, I.A.: Graphene Materials and Their Use in Dye-Sensitized Solar Cells. Chem. Rev. 114, 6323–6348 (2014). doi:10.1021/cr400412a

138. Xiang, Q., Yu, J.: Graphene-Based Photocatalysts for Hydrogen Generation. J. Phys. Chem. Lett. 4, 753–759 (2013). doi:10.1021/jz302048d

139. Li, J., Zheng, G.: One-Dimensional Earth-Abundant Nanomaterials for Water-Splitting Electrocatalysts. Adv. Sci. 4, 1600380 (2017). doi:10.1002/advs.201600380

140. Suzuki, T., Watanabe, H., Ueno, T., Oaki, Y., Imai, H.: Significant Increase in Band Gap and Emission Efficiency of In_2O_3 Quantum Dots by Size-Tuning around 1 nm in Supermicroporous Silicas. Langmuir. 33, 3014–3017 (2017). doi:10.1021/acs.langmuir.6b04181

141. Nayak, P.K., Hedhili, M.N., Cha, D., Alshareef, H.N.: High performance In_2O_3 thin film transistors using chemically derived aluminum oxide dielectric. Appl. Phys. Lett. 103, 33518 (2013). doi:10.1063/1.4816060

142. Qurashi, A., Rather, J.A., Yamazaki, T., Sohail, M., De Wael, K., Merzougui, B., Hakeem, A.S.: Swift electrochemical detection of paraben an endocrine disruptor by In_2O_3 nanobricks. Sensors Actuators B Chem. 221, 167–171 (2015). doi:10.1016/J.SNB.2015.06.026

143. Curreli, M., Li, C., Sun, Y., Lei, B., Gundersen, M.A., Thompson, M.E., Zhou, C.: Selective Functionalization of In_2O_3 Nanowire Mat Devices for Biosensing Applications. J. Am. Chem. Soc. 127, 6922–6923 (2005). doi:10.1021/ja0503478

144. Mansha, M., Qurashi, A., Ullah, N., Bakare, F.O., Khan, I., Yamani, Z.H.:

Synthesis of In_2O_3/graphene heterostructure and their hydrogen gas sensing properties. Ceram. Int. 42, 11490 (2016). doi:10.1016/j.ceramint.2016.04.035

145. Xing, R., Xu, L., Song, J., Zhou, C., Li, Q., Liu, D., Wei Song, H.: Preparation and Gas Sensing Properties of In_2O_3/Au Nanorods for Detection of Volatile Organic Compounds in Exhaled Breath. Sci. Rep. 5, 10717 (2015). doi:10.1038/srep10717

146. Sun, K., Fan, Z., Ye, J., Yan, J., Ge, Q., Li, Y., He, W., Yang, W., Liu, C.: Hydrogenation of CO_2 to methanol over In_2O_3 catalyst. J. CO_2 Util. 12, 1–6 (2015). doi:10.1016/J.JCOU.2015.09.002

147. Koumoto, K., Funahashi, R., Guilmeau, E., Miyazaki, Y., Weidenkaff, A., Wang, Y., Wan, C.: Thermoelectric Ceramics for Energy Harvesting. J. Am. Ceram. Soc. 96, 1–23 (2013). doi:10.1111/jace.12076

148. Yonezawa, T., Matsune, H., Kunitake, T.: Layered Nanocomposite of Close-Packed Gold Nanoparticles and TiO_2 Gel Layers. Chem. Mater. 11, 33–35 (1999). doi:10.1021/cm980687a

149. Ali, S., Khan, I., Khan, S.A., Sohail, M., Yamani, Z.H., Morsy, M.A., Qamaruddin, M.: Plasmon aided $(BiVO_4)_x$–$(TiO_2)_{1-x}$ ternary nanocomposites for efficient solar water splitting. Sol. Energy. 155, 770–780 (2017). doi:10.1016/j.solener.2017.07.031

150. Wang, L., Lee, C.Y., Schmuki, P.: Solar water splitting: preserving the beneficial small feature size in porous α-Fe_2O_3 photoelectrodes during annealing. J. Mater. Chem. A. 1, 212–215 (2013). doi:10.1039/C2TA00431C

151. Guo, P., Pan, H.: Selectivity of Ti-doped In_2O_3 ceramics as an ammonia sensor. Sensors Actuators B Chem. 114, 762–767 (2006). doi:10.1016/j.snb.2005.07.040

152. Borchert, H., Shevchenko, E. V., Robert, A., Mekis, I., Kornowski, A., Grübel, G., Weller, H.: Determination of Nanocrystal Sizes: A Comparison of TEM, SAXS, and XRD Studies of Highly Monodisperse $CoPt_3$ Particles. Langmuir. 21, 1931–1936 (2005). doi:10.1021/la0477183

153. Chen, C., Chen, D., Jiao, X., Chen, S.: In_2O_3 Nanocrystals with a Tunable Size in the Range of 4−10 nm: One-Step Synthesis, Characterization, and Optical Properties. J. Phys. Chem. C. 111, 18039–18043 (2007). doi:10.1021/jp076117s

154. Huo, Z., Tsung, C., Huang, W., Zhang, X., Yang, P.: Sub-Two Nanometer Single Crystal Au Nanowires. Nano Lett. 8, 2041–2044 (2008). doi:10.1021/nl8013549

155. Chava, R.K., Oh, S.Y., Yu, Y.T.: Enhanced H_2 gas sensing properties of Au@ In_2O_3 core–shell hybrid metal–semiconductor heteronanostructures. CrystEngComm. 18, 3655–3666 (2016). doi:10.1039/C6CE00352D

156. Popova, T.I., Simonova, N.A.: The passivation of indium in aqueous solutions. Bull. Acad. Sci. USSR Div. Chem. Sci. 12, 1086–1089 (1963). doi:10.1007/BF00849661

157. Le, Y., Shao, Y., Xiao, X., Xu, X., Zhang, S.: Indium–Tin–Oxide Thin-Film Transistors With In Situ Anodized Ta_2O_5 Passivation Layer. IEEE Electron Device Lett. 37, 603–606 (2016). doi:10.1109/LED.2016.2548785

158. Hartman, P., Chan, H.K.H.: Application of the Periodic Bond Chain (PBC) Theory and Attachment Energy Consideration to Derive the Crystal Morphology of Hexamethylmelamine. Pharm. Res.10,1052(1993). doi:10.1023/A:1018927109487

159. Yi, Y., Weinberg, G., Prenzel, M., Greiner, M., Heumann, S., Becker, S., Schlögl, R.: Electrochemical corrosion of a glassy carbon electrode. Catal. Today. 295, 32–

40 (2017). doi:10.1016/J.CATTOD.2017.07.013

160. Esiner, S., van Pruissen, G.W.P., Wienk, M.M., Janssen, R.A.J., P van Pruissen, G.W., Wienk ab, M.M., J Janssen, R.A., van Pruissen, G.W.P., Wienk, M.M., Janssen, R.A.J.: Optimized light-driven electrochemical water splitting with tandem polymer solar cells. J. Mater. Chem. A. 4, 5107–5114 (2016). doi:10.1039/C5TA10459A

161. Veikko, U., Zhang, X., Peng, T., Cai, P., Cheng, G.: The synthesis and characterization of dinuclear ruthenium sensitizers and their applications in photocatalytic hydrogen production. Spectrochim. Acta Part A Mol. Biomol. Spectrosc. 105, 539–544 (2013). doi:10.1016/j.saa.2012.12.061

162. Nguyen Van, C., Do, T.H., Chen, J.W., Tzeng, W.Y., Tsai, K.A., Song, H., Liu, H.J., Lin, Y.C., Chen, Y.C., Wu, C.L., Luo, C.W., Chou, W.C., Huang, R., Hsu, Y.J., Chu, Y.H.: WO_3 mesocrystal-assisted photoelectrochemical activity of BiVO4. NPG Asia Mater. 9, e357 (2017). doi:10.1038/am.2017.15

163. Hernández, S., Hidalgo, D., Sacco, A., Chiodoni, A., Lamberti, A., Cauda, V., Tresso, E., Saracco, G.: Comparison of photocatalytic and transport properties of TiO_2 and ZnO nanostructures for solar-driven water splitting. Phys. Chem. Chem. Phys. 17, 7775–7786 (2015). doi:10.1039/C4CP05857G

164. Liu, Z.Q., Kuang, P.Y., Wei, R.B., Li, N., Chen, Y.B., Su, Y.Z.: BiOBr nanoplate-wrapped ZnO nanorod arrays for high performance photoelectrocatalytic application. RSC Adv. 6, 16122–16130 (2016). doi:10.1039/C5RA27310B

165. Choi, H.J., Choi, S.J., Choo, S., Kim, I.D., Lee, H.: Hierarchical ZnO Nanowires-loaded Sb-doped SnO_2-ZnO Micrograting Pattern via Direct Imprinting-assisted

Hydrothermal Growth and Its Selective Detection of Acetone Molecules. Sci. Rep. 6, 18731 (2016). doi:10.1038/srep18731

166. Lee, J., Yong, K.: Combining the lotus leaf effect with artificial photosynthesis: regeneration of underwater superhydrophobicity of hierarchical ZnO/Si surfaces by solar water splitting. NPG Asia Mater. 7, e201 (2015). doi:10.1038/am.2015.74

167. Maeda, K., Takata, T., Hara, M., Saito, N., Inoue, Y., Kobayashi, H., Domen, K.: GaN:ZnO Solid Solution as a Photocatalyst for Visible-Light-Driven Overall Water Splitting. J. Am. Chem. Soc. 127, 8286–8287 (2005). doi:10.1021/ja0518777

168. Ohno, T., Bai, L., Hisatomi, T., Maeda, K., Domen, K.: Photocatalytic Water Splitting Using Modified GaN:ZnO Solid Solution under Visible Light: Long-Time Operation and Regeneration of Activity. J. Am. Chem. Soc. 134, 8254–8259 (2012). doi:10.1021/ja302479f

169. Yu, S., Liu, B., Wang, Q., Gao, Y., Shi, Y., Feng, X., An, X., Liu, L., Zhang, J.: Ionic Liquid Assisted Chemical Strategy to TiO_2 Hollow Nanocube Assemblies with Surface-Fluorination and Nitridation and High Energy Crystal Facet Exposure for Enhanced Photocatalysis. ACS Appl. Mater. Interfaces. 6, 10283–10295 (2014). doi:10.1021/am5016809

170. Hu, C.-C., Teng, H.: Gallium Oxynitride Photocatalysts Synthesized from $Ga(OH)_3$ for Water Splitting under Visible Light Irradiation. J. Phys. Chem. C. 114, 20100–20106 (2010). doi:10.1021/jp1070083

171. Zong, X., Yan, H., Wu, G., Ma, G., Wen, F., Wang, L., Li, C.: Enhancement of Photocatalytic H_2 Evolution on CdS by Loading MoS_2 as Cocatalyst under Visible

Light Irradiation. J. Am. Chem. Soc.130, 7176 (2008). doi:10.1021/ja8007825

172. Setvin, M., Aschauer, U., Scheiber, P., Li, Y.F., Hou, W., Schmid, M., Selloni, A., Diebold, U.: Reaction of O_2 with Subsurface Oxygen Vacancies on TiO_2 Anatase (101). Science (80-.). 341, 988–991 (2013). doi:10.1126/science.1239879

173. Qurashi, A., Faiz, M., Tabet, N., Alam, M.W.: Low temperature synthesis of hexagonal ZnO nanorods and their hydrogen sensing properties. Superlattices Microstruct. 50, 173–180 (2011). doi:10.1016/j.spmi.2011.05.014

174. Perdew, J.P., Burke, K., Ernzerhof, M.: Generalized Gradient Approximation Made Simple. Phys. Rev. Lett. 77, 3865–3868 (1996). doi:10.1103/PhysRevLett.77.3865

175. Grimme, S.: Semiempirical GGA-type density functional constructed with a long-range dispersion correction. J. Comput. Chem. 27, 1787–1799 (2006). doi:10.1002/jcc.20495

176. Chua, C.S., Ansovini, D., Lee, C.J.J., Teng, Y.T., Ong, L.T., Chi, D., Hor, T.S.A., Raja, R., Lim, Y.-F.: The effect of crystallinity on photocatalytic performance of Co_3O_4 water-splitting cocatalysts. Phys. Chem. Chem. Phys. 18, 5172–5178 (2016). doi:10.1039/C5CP07589K

177. Chen, C.J.K., Shen, Y.P., Chen, H.M., Chen, C.J.K., Chan, T.S., Lee, J., Liu, R.: Quantum-Dot-Sensitized Nitrogen-Doped ZnO for Efficient Photoelectrochemical Water Splitting. Eur. J. Inorg. Chem. 2014, 773–779 (2014). doi:10.1002/ejic.201301310

178. Wang, Z., Huang, B., Yu, L., Dai, Y., Wang, P., Qin, X., Zhang, X., Wei, J., Zhan, J., Jing, X., Liu, H., Whangbo, M.-H.: Enhanced Ferromagnetism and Tunable

Saturation Magnetization of Mn/C-Codoped GaN Nanostructures Synthesized by Carbothermal Nitridation. J. Am. Chem. Soc. 130, 16366–16373 (2008). doi:10.1021/ja807030v

179. Wei, W., Qin, Z., Fan, S., Li, Z., Shi, K., Zhu, Q., Zhang, G.: Valence band offset of β-Ga_2O_3/wurtzite GaN heterostructure measured by X-ray photoelectron spectroscopy. Nanoscale Res. Lett. 7, 562 (2012). doi:10.1186/1556-276X-7-562

180. Wilkins, S.J., Paskova, T., Ivanisevic, A.: Modified surface chemistry, potential, and optical properties of polar gallium nitride via long chained phosphonic acids. Appl. Surf. Sci. 327, 498–503 (2015). doi:10.1016/j.apsusc.2014.11.179

181. Yan, H., Wang, X., Yao, M., Yao, X.: Band structure design of semiconductors for enhanced photocatalytic activity: The case of TiO_2. Prog. Nat. Sci. Mater. Int. 23, 402–407 (2013). doi:10.1016/j.pnsc.2013.06.002

182. Tachikawa, T., Ochi, T., Kobori, Y.: Crystal-Face-Dependent Charge Dynamics on a $BiVO_4$ Photocatalyst Revealed by Single-Particle Spectroelectrochemistry. ACS Catal. 6, 2250–2256 (2016). doi:10.1021/acscatal.6b00234

183. Khan, I., Qurashi, A.: Shape Controlled Synthesis of Copper Vanadate Platelet Nanostructures, Their Optical Band Edges, and Solar-Driven Water Splitting Properties. Sci. Rep. 7, 14370 (2017). doi:10.1038/s41598-017-14111-7

184. Shah, M.W., Zhu, Y., Fan, X., Zhao, J., Li, Y.: Facile Synthesis of Defective TiO_{2-x} Nanocrystals with High Surface Area and Tailoring Bandgap for Visible-light Photocatalysis. Nat. Publ. Gr. 1–8 (2015). doi:10.1038/srep15804

185. Domen, K.M.: Particulate Oxynitrides for Photocatalytic Water Splitting Under Visible Light. 109–131 (2013)

186. Park, J.H., Mandal, A., Kang, S., Chatterjee, U., Kim, J.S., Park, B.G., Kim, M.D., Jeong, K.U., Lee, C.R.: Hydrogen Generation using non-polar coaxial InGaN/GaN Multiple Quantum Well Structure Formed on Hollow n-GaN Nanowires. Sci. Rep. 6, 31996 (2016). doi:10.1038/srep31996

187. Lai, Y.H., Lin, C.Y., Chen, H.W., Chen, J.G., Kung, C.-W., Vittal, R., Ho, K.C.: Fabrication of a ZnO film with a mosaic structure for a high efficient dye-sensitized solar cell. J. Mater. Chem. 20, 9379 (2010). doi:10.1039/c0jm01787f

188. Zirak, M., Zhao, M., Moradlou, O., Samadi, M., Sarikhani, N., Wang, Q., Zhang, H.L., Moshfegh, A.Z.: Controlled engineering of WS_2 nanosheets–CdS nanoparticle heterojunction with enhanced photoelectrochemical activity. Sol. Energy Mater. Sol. Cells. 141, 260–269 (2015). doi:10.1016/j.solmat.2015.05.051

189. Chang, S.J., Wu, Y.L., Weng, W.Y., Lin, Y.H., Hsieh, W.K., Sheu, J.K., Hsu, C.L.: Ga_2O_3 Films for Photoelectrochemical Hydrogen Generation. J. Electrochem. Soc. 161, H508–H511 (2014). doi:10.1149/2.0471409jes

190. Kim, H.J., Park, J., Ye, B.U., Yoo, C.J., Lee, J.L.L., Ryu, S.-W.W., Lee, H., Choi, K.J., Baik, J.M.: Parallel Aligned Mesopore Arrays in Pyramidal-Shaped Gallium Nitride and Their Photocatalytic Applications. ACS Appl. Mater. Interfaces. 8, 18201–18207 (2016). doi:10.1021/acsami.6b05500

191. Kang, B.K., Han, G.S., Baek, J.H., Lee, D.G., Song, Y.H., Kwon, S. Bin, Cho, I.S., Jung, H.S., Yoon, D.H.: Nanodome Structured $BiVO_4/GaO_xN_{1-x}$ Photoanode for Solar Water Oxidation. Adv. Mater. Interfaces. 4, 1700323 (2017). doi:10.1002/admi.201700323

192. Wang, Z., Han, J., Li, Z., Li, M., Wang, H., Zong, X., Li, C.: Moisture-Assisted

Preparation of Compact GaN:ZnO Photoanode Toward Efficient Photoelectrochemical Water Oxidation. Adv. Energy Mater. 6, 1600864 (2016). doi:10.1002/aenm.201600864

193. Tamirat, A.G., Rick, J., Dubale, A.A., Su, W.-N., Hwang, B.J.: Using hematite for photoelectrochemical water splitting: a review of current progress and challenges. Nanoscale Horiz. 1, 243–267 (2016). doi:10.1039/C5NH00098J

194. Boyko, T.D., Zvoriste, C.E., Kinski, I., Riedel, R., Hering, S., Huppertz, H., Moewes, A.: Anion ordering in spinel-type gallium oxonitride. Phys. Rev. B. 84, 85203 (2011). doi:10.1103/PhysRevB.84.085203

195. Liu, D.C., Nocedal, J.: On the limited memory BFGS method for large scale optimization. Math. Program. 45, 503–528 (1989). doi:10.1007/BF01589116

196. Bonaccorso, F., Sun, Z., Hasan, T., Ferrari, A.C.: Graphene photonics and optoelectronics. Nat. Photonics. 4, 611–622 (2010). doi:10.1038/nphoton.2010.186

197. Dikin, D.A., Stankovich, S., Zimney, E.J., Piner, R.D., Dommett, G.H.B., Evmenenko, G., Nguyen, S.T., Ruoff, R.S.: Preparation and characterization of graphene oxide paper. Nature. 448, 457–460 (2007). doi:10.1038/nature06016

198. Ke, Q., Wang, J.: Graphene-based materials for supercapacitor electrodes – A review. J. Mater. 2, 37–54 (2016). doi:10.1016/j.jmat.2016.01.001

199. Meric, I., Han, M.Y., Young, A.F., Ozyilmaz, B., Kim, P., Shepard, K.L.: Current saturation in zero-bandgap, top-gated graphene field-effect transistors. Nat. Nanotechnol. 3, 654–659 (2008). doi:10.1038/nnano.2008.268

200. Qurashi, A., Subrahmanyam, K.S., Kumar, P.: Nanofiller graphene–ZnO hybrid nanoarchitecture: optical, electrical and optoelectronic investigation. J. Mater.

Chem. C. 3, 11959–11964 (2015). doi:10.1039/C5TC02729B

201. Yazyev, O. V., Katsnelson, M.I.: Magnetic Correlations at Graphene Edges: Basis for Novel Spintronics Devices. Phys. Rev. Lett. 100, 47209 (2008). doi:10.1103/PhysRevLett.100.047209

202. Pan, Z.W.: Nanobelts of Semiconducting Oxides. Science (80-.). 291, 1947–1949 (2001). doi:10.1126/science.1058120

203. Annanouch, F.E., Haddi, Z., Vallejos, S., Umek, P., Guttmann, P., Bittencourt, C., Llobet, E.: Aerosol-Assisted CVD-Grown WO_3 Nanoneedles Decorated with Copper Oxide Nanoparticles for the Selective and Humidity-Resilient Detection of H_2S. ACS Appl. Mater. Interfaces. 7, 6842–6851 (2015). doi:10.1021/acsami.5b00411

204. Huang, H., Liang, B., Liu, Z., Wang, X., Chen, D., Shen, G.: Metal oxide nanowire transistors. J. Mater. Chem. 22, 13428 (2012). doi:10.1039/c2jm31679j

205. Mohapatra, J., Mitra, A., Tyagi, H., Bahadur, D., Aslam, M.: Iron oxide nanorods as high-performance magnetic resonance imaging contrast agents. Nanoscale. 7, 9174–9184 (2015). doi:10.1039/C5NR00055F

206. Xu, S., Wang, Z.L.: One-dimensional ZnO nanostructures: Solution growth and functional properties. Nano Res. 4, 1013–1098 (2011). doi:10.1007/s12274-011-0160-7

207. Han, J., Liu, Z., Guo, K., Wang, B., Zhang, X., Hong, T.: High-efficiency photoelectrochemical electrodes based on $ZnIn_2S_4$ sensitized ZnO nanotube arrays. Appl. Catal. B Environ. 163, 179–188 (2015). doi:10.1016/j.apcatb.2014.07.040

208. Srivastava, M., Singh, J., Kuila, T., Layek, R.K., Kim, N.H., Lee, J.H.: Recent

advances in graphene and its metal-oxide hybrid nanostructures for lithium-ion batteries. Nanoscale. 7, 4820–4868 (2015). doi:10.1039/C4NR07068B

209. Williams, G., Kamat, P.V.: Graphene−Semiconductor Nanocomposites: Excited-State Interactions between ZnO Nanoparticles and Graphene Oxide. Langmuir. 25, 13869–13873 (2009). doi:10.1021/la900905h

210. Huang, K., Li, Y.H., Lin, S., Liang, C., Wang, H., Ye, C.X., Wang, Y.J., Zhang, R., Fan, D.Y., Yang, H.J., Wang, Y.G., Lei, M.: A facile route to reduced graphene oxide–zinc oxide nanorod composites with enhanced photocatalytic activity. Powder Technol. 257, 113–119 (2014). doi:10.1016/j.powtec.2014.02.047

211. Haldorai, Y., Voit, W., Shim, J.-J.: Nano ZnO@reduced graphene oxide composite for high performance supercapacitor: Green synthesis in supercritical fluid. Electrochim. Acta. 120, 65–72 (2014). doi:10.1016/j.electacta.2013.12.063

212. Jaleh, B., Jabbari, A.: Evaluation of reduced graphene oxide/ZnO effect on properties of PVDF nanocomposite films. Appl. Surf. Sci. 320, 339–347 (2014). doi:10.1016/j.apsusc.2014.09.030

213. Baitimirova, M., Viter, R., Andzane, J., van der Lee, A., Voiry, D., Iatsunskyi, I., Coy, E., Mikoliunaite, L., Tumenas, S., Załęski, K., Balevicius, Z., Baleviciute, I., Ramanaviciene, A., Ramanavicius, A., Jurga, S., Erts, D., Bechelany, M.: Tuning of Structural and Optical Properties of Graphene/ZnO Nanolaminates. J. Phys. Chem. C. 120, 23716–23725 (2016). doi:10.1021/acs.jpcc.6b07221

214. Nam, G.H., Baek, S.H., Cho, C.H., Park, I.K.: A flexible and transparent graphene/ZnO nanorod hybrid structure fabricated by exfoliating a graphite substrate. Nanoscale. 6, 11653–11658 (2014). doi:10.1039/C4NR02318H

215. Yue, H.Y., Huang, S., Chang, J., Heo, C., Yao, F., Adhikari, S., Gunes, F., Liu, L.C., Lee, T.H., Oh, E.S., Li, B., Zhang, J.J., Huy, T.Q., Luan, N. Van, Lee, Y.H.: ZnO Nanowire Arrays on 3D Hierachical Graphene Foam: Biomarker Detection of Parkinson's Disease. ACS Nano. 8, 1639–1646 (2014). doi:10.1021/nn405961p

216. Qurashi, A., Alhaffar, M., Yamani, Z.H.: Hierarchical ZnO/zeolite nanostructures: synthesis, growth mechanism and hydrogen detection. RSC Adv. 5, 22570–22577 (2015). doi:10.1039/C4RA15497E

217. ullah, H., Khan, I., Yamani, Z.H., Qurashi, A.: Sonochemical-driven ultrafast facile synthesis of SnO_2 nanoparticles: Growth mechanism structural electrical and hydrogen gas sensing properties. Ultrason. Sonochem. 34, 484–490 (2017). doi:10.1016/j.ultsonch.2016.06.025

218. Tzanakis, I., Lebon, G.S.B., Eskin, D.G., Pericleous, K.A.: Characterizing the cavitation development and acoustic spectrum in various liquids. Ultrason. Sonochem. 34, 651–662 (2017). doi:10.1016/j.ultsonch.2016.06.034

219. Jiang, L., Ge, H., Liu, F., Chen, D.: Investigations on dynamics of interacting cavitation bubbles in strong acoustic fields. Ultrason. Sonochem. 34, 90–97 (2017). doi:10.1016/j.ultsonch.2016.05.017

220. Shang, M., Wang, W., Zhou, L., Sun, S., Yin, W.: Nanosized $BiVO_4$ with high visible-light-induced photocatalytic activity: Ultrasonic-assisted synthesis and protective effect of surfactant. J. Hazard. Mater. 172, 338–344 (2009). doi:10.1016/j.jhazmat.2009.07.017

221. Chen, Y.L., Hu, Z.A., Chang, Y.Q., Wang, H.W., Zhang, Z.Y., Yang, Y.Y., Wu, H.Y.: Zinc Oxide/Reduced Graphene Oxide Composites and Electrochemical

Capacitance Enhanced by Homogeneous Incorporation of Reduced Graphene Oxide Sheets in Zinc Oxide Matrix. J. Phys. Chem. C. 115, 2563–2571 (2011). doi:10.1021/jp109597n

222. Ashfold, M.N.R., Doherty, R.P., Ndifor-Angwafor, N.G., Riley, D.J., Sun, Y.: The kinetics of the hydrothermal growth of ZnO nanostructures. Thin Solid Films. 515, 8679–8683 (2007). doi:10.1016/j.tsf.2007.03.122

223. Govender, K., Boyle, D.S., Kenway, P.B., O'Brien, P.: Understanding the factors that govern the deposition and morphology of thin films of ZnO from aqueous solution. J. Mater. Chem. 14, 2575–2591 (2004). doi:10.1039/B404784B

224. Pham, V.H., Cuong, T.V., Nguyen-Phan, T.D., Pham, H.D., Kim, E.J., Hur, S.H., Shin, E.W., Kim, S., Chung, J.S.: One-step synthesis of superior dispersion of chemically converted graphene in organic solvents. Chem. Commun. 46, 4375 (2010). doi:10.1039/c0cc00363h

225. Cuong, T.V., Pham, V.H., Tran, Q.T., Hahn, S.H., Chung, J.S., Shin, E.W., Kim, E.J.: Photoluminescence and Raman studies of graphene thin films prepared by reduction of graphene oxide. Mater. Lett. 64, 399–401 (2010). doi:10.1016/j.matlet.2009.11.029

226. Wang, G., Li, Z., Li, M., Liao, J., Chen, C., Lv, S., Shi, C.: Enhanced field-emission of silver nanoparticle–graphene oxide decorated ZnO nanowire arrays. Phys. Chem. Chem. Phys. 17, 31822–31829 (2015). doi:10.1039/C5CP05036G

227. Srikant, V., Clarke, D.R.: On the optical band gap of zinc oxide. J. Appl. Phys. 83, 5447 (1998). doi:10.1063/1.367375

228. Luo, Q.P., Yu, X.Y., Lei, B.X., Chen, H.Y., Kuang, D.B., Su, C.Y.: Reduced

Graphene Oxide-Hierarchical ZnO Hollow Sphere Composites with Enhanced Photocurrent and Photocatalytic Activity. J. Phys. Chem. C. 116, 8111–8117 (2012). doi:10.1021/jp2113329

229. Chandrasekaran, S., Chung, J.S., Kim, E.J., Hur, S.H.: Exploring complex structural evolution of graphene oxide/ZnO triangles and its impact on photoelectrochemical water splitting. Chem. Eng. J. 290, 465–476 (2016). doi:10.1016/j.cej.2016.01.029

230. Yusoff, N., Kumar, S.V., Pandikumar, A., Huang, N.M., Marlinda, A.R., An'amt, M.N.: Core-shell Fe_3O_4-ZnO nanoparticles decorated on reduced graphene oxide for enhanced photoelectrochemical water splitting. Ceram. Int. 41, 5117–5128 (2015). doi:10.1016/j.ceramint.2014.12.084

231. Xu, J., Sang, H., Wang, X., Wang, K.: Facile synthesis and photocatalytic properties of ZnO core/ZnS–CdS solid solution shell nanorods grown vertically on reductive graphene oxide. Dalt. Trans. 44, 9528–9537 (2015). doi:10.1039/C5DT00293A

232. Vayssieres, L.: On Solar Hydrogen and Nanotechnology. John Wiley & Sons (2010)

233. Min, Y., Zhang, K., Chen, L., Chen, Y., Zhang, Y.: Ionic liquid assisting synthesis of ZnO/graphene heterostructure photocatalysts with tunable photoresponse properties. Diam. Relat. Mater. 26, 32–38 (2012). doi:10.1016/j.diamond.2012.04.003

234. Zou, R., He, G., Xu, K., Liu, Q., Zhang, Z., Hu, J.: ZnO nanorods on reduced graphene sheets with excellent field emission, gas sensor and photocatalytic

properties. J. Mater. Chem. A. 1, 8445 (2013). doi:10.1039/c3ta11490b

235. Bhirud, A., Sathaye, S., Waichal, R., Park, C.-J., Kale, B.: In situ preparation of N–ZnO/graphene nanocomposites: excellent candidate as a photocatalyst for enhanced solar hydrogen generation and high performance supercapacitor electrode. J. Mater. Chem. A. 3, 17050–17063 (2015). doi:10.1039/C5TA03955J

236. Yu, Z.B., Xie, Y.P., Liu, G., Lu, G.Q. (Max), Ma, X.L., Cheng, H.-M.: Self-assembled CdS/Au/ZnO heterostructure induced by surface polar charges for efficient photocatalytic hydrogen evolution. J. Mater. Chem. A. 1, 2773 (2013). doi:10.1039/c3ta01476b

237. Chen, D., Feng, H., Li, J.: Graphene Oxide: Preparation, Functionalization, and Electrochemical Applications. Chem. Rev. 112, 6027–6053 (2012). doi:10.1021/cr300115g

238. Yu, H., Zhang, B., Bulin, C., Li, R., Xing, R.: High-efficient Synthesis of Graphene Oxide Based on Improved Hummers Method. Sci. Rep. 6, 36143 (2016). doi:10.1038/srep36143

239. Liu, Y., Wang, F., Wang, X., Wang, X., Flahaut, E., Liu, X., Li, Y., Wang, X., Xu, Y., Shi, Y., Zhang, R.: Planar carbon nanotube-graphene hybrid films for high-performance broadband photodetectors. Nat. Commun. 6, 8589 (2015). doi:10.1038/ncomms9589

240. Shelke, N.T., Karche, B.R.: Ultraviolet photosensor based on few layered reduced graphene oxide nanosheets. Appl. Surf. Sci. 418, 374–379 (2017). doi:10.1016/j.apsusc.2016.12.150

241. Yeh, T.F., Teng, C.Y., Chen, L.C., Chen, S.J., Teng, H.: Graphene oxide-based

nanomaterials for efficient photoenergy conversion. J. Mater. Chem. A. 4, 2014–2048 (2016). doi:10.1039/C5TA07780J

242. Yeh, T.F., Chen, S.J., Teng, H.: Synergistic effect of oxygen and nitrogen functionalities for graphene-based quantum dots used in photocatalytic H_2 production from water decomposition. Nano Energy. 12, 476–485 (2015). doi:10.1016/j.nanoen.2015.01.021

243. Tang, W., Chase, D.B., Sparks, D.L., Rabolt, J.F.: Selective and Quantitative Detection of Trace Amounts of Mercury(II) Ion (Hg^{2+}) and Copper(II) Ion (Cu^{2+}) Using Surface-Enhanced Raman Scattering (SERS). Appl. Spectrosc. 69, 843–849 (2015). doi:10.1366/14-07815

244. Georgakilas, V., Tiwari, J.N., Kemp, K.C., Perman, J.A., Bourlinos, A.B., Kim, K.S., Zboril, R.: Noncovalent Functionalization of Graphene and Graphene Oxide for Energy Materials, Biosensing, Catalytic, and Biomedical Applications. Chem. Rev. 116, 5464–5519 (2016). doi:10.1021/acs.chemrev.5b00620

245. Adeli, B., Taghipour, F.: Reduced Graphene Oxide Composite of Gallium Zinc Oxynitride Photocatalyst with Improved Activity for Overall Water Splitting. Chem. Eng. Technol. 39, 142–148 (2016). doi:10.1002/ceat.201500239

246. Ahsanulhaq, Q., Kim, J.H., Lee, J.S., Hahn, Y.B.: Electrical and gas sensing properties of ZnO nanorod arrays directly grown on a four-probe electrode system. Electrochem. commun. 12, 475–478 (2010). doi:10.1016/j.elecom.2010.01.023

247. Choi, D., Choi, M.Y., Choi, W.M., Shin, H.J., Park, H.K., Seo, J.S., Park, J., Yoon, S.M., Chae, S.J., Lee, Y.H., Kim, S.W., Choi, J.Y., Lee, S.Y., Kim, J.M.: Fully Rollable Transparent Nanogenerators Based on Graphene Electrodes. Adv.

Mater. 22, 2187–2192 (2010). doi:10.1002/adma.200903815

248. Yin, Z., Wu, S., Zhou, X., Huang, X., Zhang, Q., Boey, F., Zhang, H.: Electrochemical Deposition of ZnO Nanorods on Transparent Reduced Graphene Oxide Electrodes for Hybrid Solar Cells. Small. 6, 307–312 (2010). doi:10.1002/smll.200901968

249. Damiani, L.R., Mansano, R.D.: Zinc oxide thin films deposited by magnetron sputtering with various oxygen/argon concentrations. J. Phys. Conf. Ser. 370, 12019 (2012). doi:10.1088/1742-6596/370/1/012019

250. Hoon, J.W., Chan, K.Y., Krishnasamy, J., Tou, T.Y., Knipp, D.: Direct current magnetron sputter-deposited ZnO thin films. Appl. Surf. Sci. 257, 2508–2515 (2011). doi:10.1016/j.apsusc.2010.10.012

251. Abdolhosseinzadeh, S., Asgharzadeh, H., Sadighikia, S., Khataee, A.: UV-assisted synthesis of reduced graphene oxide–ZnO nanorod composites immobilized on Zn foil with enhanced photocatalytic performance. Res. Chem. Intermed. 42, 4479–4496 (2016). doi:10.1007/s11164-015-2291-z

252. Wang, L., Wu, Y., Chen, F., Yang, X.: Photocatalytic enhancement of Mg-doped ZnO nanocrystals hybridized with reduced graphene oxide sheets. Prog. Nat. Sci. Mater. Int. 24, 6–12 (2014). doi:10.1016/J.PNSC.2014.01.002

253. Briggs, R.J., Ramdas, A.K.: Piezospectroscopic study of the Raman spectrum of cadmium sulfide. Phys. Rev. B. 13, 5518–5529 (1976). doi:10.1103/PhysRevB.13.5518

254. S. O. Kasap: Principles of Electronic Materials and Devices. McGraw-Hill, New York (2006)

255. Cha, S.N., Seo, J.-S., Kim, S.M., Kim, H.J., Park, Y.J., Kim, S.-W., Kim, J.M.: Sound-Driven Piezoelectric Nanowire-Based Nanogenerators. Adv. Mater. 22, 4726–4730 (2010). doi:10.1002/adma.201001169

CURRICULUM VITAE

Name	Ibrahim
Nationality	Pakistan
Date of Birth	5th Jan 1983
Academic Background	Ph.D. in Chemistry
Cell Numbers:	+966-54-6889540 & +92-345-9369499
E-mail Address:	ebraheem@kfupm.edu.sa; ebraheem.chemist@gmail.com
Mailing Address:	Lab 116 A, Building-1, King Fahd University of Petroleum and Minerals (KFUPM), Dhahran, Dammam KSA. 31261
Google Scholar:	https://scholar.google.com/citations?user=3ZxOgLgAAAAJ&hl=en

Research Statement and Objectives

Over the years, I have developed multi-dimensional research skills, while working on various research projects and in academia. During Ph.D., I choose to work on the development of 0D, 1D, 2D and 3D metal and semiconductor nanomaterials via solvothermal, sol-gel, physical vapor deposition (PVD) and electrochemical methods (anodization and electrodeposition). The architectured nanostructures (pure) and their nanocomposites/heterostructure were used for energy harvesting applications such as water splitting and CO_2 reduction via electrochemical techniques. I am fully trained with basic characterization instruments used in these studies such as SEM, XRD, XPS, in-situ Raman. During these years, I have also mastered scientific reports/manuscript/review and research proposal writing for academic and industrial projects. I have coauthored and published over 25 research articles in peered review journals (mostly Q1 category), while 6 patents on our discoveries are under review by the US Patent and Trademark Office. I am also the invited reviewer of few prestigious research journals such as RSC advances, International Journal of Hydrogen Energy etc.

In future, I strongly intend to continue my research in the following dimensions:

- The synthesis of advanced nanomaterials for related renewable energy harvesting technologies, such as Water Splitting, CO_2 conversion, Lithium-ion batteries and energy storage.
- Thorough investigation of the kinetics and mechanism of interfacial electrodes processes via different electrochemical methods such as Mott-Schottky, Tafel plots, Pourbaix diagram and Electronic Impedance Spectroscopy (EIS).
- Owing basic computational chemistry knowledge, I would like to apply it to the designing and parameters studies of nanomaterials

1. Academics

1.1 Ph.D. Chemistry with Research (01/2014 – 04/2018; GPA=3.47/4.0)

Dissertation title **"*Hybrid Metal Oxide Nanoarrays: Fabrication, Properties and Energy Conversion Applications"***. Dissertation Advisor: Dr. Ahsanulhaq Qurashi (Associate Prof.), King Fahd University of Petroleum and Minerals (KFUPM), Dhahran, Dammam, KSA.

1.2 M.Phil. Chemistry with Research (06/2011 – 11/2013; GPA=3.3/4.0)

Thesis title ***"Effect of Single-Walled Carbon Nanotubes (SWNTs) on the Properties of Polymeric Materials".***

Thesis Advisor: Dr. Khalid Saeed (Associate Prof.), University of Malakand, KP Pakistan.

1.3 Master of Chemistry (M.Sc.) with Research (09/2007 – 03/2010; Grade A: 886/1100)

Thesis title **"*Adsorption of Phenol on the Surface of Modified Banana Peel*"**. Advisor: Dr. M. Yousaf, (Associate Prof.), University of Malakand, KP Pakistan.

2. Research Details

2.1 Research Project Completed

1. Fabrication of well-aligned hetero-nanostructured oxide arrays and their graphene nanoarchitectures for solar driven hydrogen production applications;
2. Engineering of ZnO based piezoelectric nanogenerators for energy harvesting;
3. Metal oxide/composites nanomaterials for Hydrogen gas sensing applications;

4. Effect of single-walled Carbon nanotubes (SWNTs) on the properties of polymeric materials (M. Phil Project.

2.2 Instruments Utilized during Experiments (Fully Trained and Utilized)

FTIR, Raman, UV-Vis/DRS, Photoluminescence (PL), XRD, XPS, Magnetron Sputter Machine for films, SEM, Particle Size Analyzer (DLS), TG-DSC, BET etc.

2.3 Computational and Data Software for Research Work

- GAUSSIAN software, Material Studios 7.0 with CASTEP, Quantum ESPRESSO, Avogadro, Chem Draw and Chem 3D, VEDA 4, Crystal Maker etc. for structure designing of materials/Molecules and different properties studies.
- Excel, Origin, and GAMESS for Spectral Analysis, etc.

3. Research Outcomes Total Impact Factor > 100, RG Score = 31

3.1 Publication list

1. **Ibrahim Khan**, Nadeem Baig, Ahsanulhaq Qurashi, Pulse sonochemical tailoring of graphitic carbon nitride impregnated niobium oxide (g-C_3N_4/Nb_2O_5) Type (II) heterojunctions and its synergetic solar-driven hydrogen generation, ACS App. Eng. Mater. ID: ae-2018-00164z **(1st Revision received)**
2. **Ibrahim Khan**, A. Qurashi, Sonochemical assisted *in-situ* electrochemical synthesis of Ag/α-Fe_2O_3/TiO_2 nanotube-arrays for photoelectrochemical energy harnessing from water splitting, ACS Sus. Chem. Eng, ID: sc-2017-02848s.R1 **(2nd Revision Submitted)**
3. N. Ullah, M. Mansha, **Ibrahim Khan**, A. Qurashi, Nanomaterial-based optical chemical sensors for the detection of heavy metals in water: Recent advances and challenges, TrAC Trends Anal. Chem. 100 (2018) 155-166. **IF = 8.44**
4. **Ibrahim Khan**, A. Qurashi, G. Berdiyorov, N. Iqbal, K. Fuji, Single-step strategy for the fabrication of GaON/ZnO nanoarchitecture photoanode and their experimental and computational photoelectrochemical water splitting, Nano. Eng. 44 (2018) 23-33. **IF = 12.34**

5. **Ibrahim Khan**, A. Qurashi, Shaped Controlled Synthesis of Copper Vanadate Platelet Nanostructures, Their Optical Band Edges and Solar-Driven Water Splitting Properties, Sci. Rep. 7 (2017) 14370 **IF = 4.26**
6. **Ibrahim Khan**, S. Ali, M. Mansha, A. Qurashi, Sonochemical assisted hydrothermal synthesis of pseudo-flower shaped Bismuth vanadate ($BiVO_4$) and their solar-driven water splitting application, Ultrason. Sonochem. 36 (2017) 386–392. **IF = 4.22**
7. **Ibrahim Khan**, A.A.M. Ibrahim, M. Sohail, A. Qurashi, Sonochemical assisted synthesis of RGO/ZnO NAs for photoelectrochemical water splitting, Ultrason. Sonochem. 37 (2017) 669–675. **IF = 4.22**
8. N. Iqbal, **Ibrahim Khan**, Z.H. Yamani, A. Qurashi, Solvothermal Synthesis of Gallium Oxynitride Nanosheets and their Solar-Driven Photoelectrochemical Water-Splitting Applications, Sci. Rep. 6 (2016) 32319. **IF = 4.26**
9. S. Ali, **Ibrahim Khan**, S.A. Khan, M. Sohail, Z.H. Yamani, M.A. Morsy, M. Qamaruddin, Plasmon aided $(BiVO_4)x$ $-(TiO_2)_{1-x}$ ternary nanocomposites for efficient solar water splitting, Sol. Energy. 155 (2017) 770–780. **IF = 4.02**
10. **Ibrahim Khan**, A. Abdalla, A. Qurashi, Synthesis of hierarchical WO_3 and Bi_2O_3/WO_3 nanocomposite for solar-driven water splitting applications, Int. J. Hydrogen Energy. 42 (2017) 3431-3439. **IF = 3.58**
11. **Ibrahim Khan**, K. Saeed, I. Khan, Nanoparticles: Properties, applications and toxicities, Arab. J. Chem. (2017). doi:10.1016/j.arabjc.2017.05.011. **IF = 4.55**
12. M. Mansha, **Ibrahim Khan**, N. Ullah, A. Qurashi, M. Sohail, Visible-light driven water splitting by poly(phenylene cyanovinylenes), Dyes. Pig. 143, 95-102 **IF = 3.47**
13. S. Ali, **Ibrahim Khan**, S.A. Khan, M. Sohail, R. Ahmed, A. ur Rehman, M.S. Ansari, M.A. Morsy, Electrocatalytic performance of Ni@Pt core-shell nanoparticles supported on carbon nanotubes for methanol oxidation reaction, J. Electroanal. Chem. 795 (2017) 17–25. **IF = 3.01**
14. **Ibrahim Khan**, A. Khalil, F. Khanday, A. M. Shemsi, A. Qurashi, K. S. Siddiqui, Synthesis, Characterization and Applications of Magnetic Iron Oxide Nanostructures, Arab J Sci Eng. (2017) DOI: 10.1007/s13369-017-2835-1 **IF = 2.87**

15. N. Iqbal, **Ibrahim Khan**, Z.H.A. Yamani, A. Qurashi, A facile one-step strategy for in-situ fabrication of WO_3 -$BiVO_4$ nanoarrays for solar-driven photoelectrochemical water splitting applications, Sol. Energy. 144 (2017) 604–611. **IF = 4.02**
16. S. Ali, S.A. Khan, **Ibrahim Khan**, Z.H. Yamani, M. Sohail, M.A. Morsy, Surfactant-Free Synthesis of Ellipsoidal and Spherical Shaped TiO_2 NPs and Their Comparative Photocatalytic Studies, J. Environ. Chem. Eng. 5 (2017) 3956-3962. **IF = 3.83**
17. A.H.Y. Hendi, M.F. Al-Kuhaili, S.M.A. Durrani, M.M. Faiz, A. Ul-Hamid, A. Qurashi, **Ibrahim Khan**, Tunable visible light absorption of MoO_3 -CdTe composite thin films, Thin Solid Films. 636 (2017) 137–143. **IF = 1.88**
18. H. Ullah, **Ibrahim Khan**, Z.H. Yamani, A. Qurashi, Sonochemical-driven ultrafast facile synthesis of SnO_2 nanoparticles: Growth mechanism structural electrical and hydrogen gas sensing properties, Ultrason. Sonochem. 34 (2017) 484–490. **IF = 4.22**
19. A.H.Y. Hendi, M.F. Al-Kuhaili, S.M.A. Durrani, M.M. Faiz, A. Ul-Hamid, A. Qurashi, **Ibrahim Khan**, Modulation of the band gap of tungsten oxide thin films through mixing with cadmium telluride towards photovoltaic applications, Mater. Res. Bull. 87 (2017) 148–154. **IF = 2.45**
20. M. Mansha, **Ibrahim Khan**, N. Ullah, A. Qurashi, Synthesis, characterization and visible-light-driven photoelectrochemical hydrogen evolution reaction of carbazole-containing conjugated polymers, Int. J. Hydrogen Energy. 42 (2017) 10952-10961. **IF = 3.58**
21. A.A.M. Ibrahim, **Ibrahim Khan**, N. Iqbal, A. Qurashi, Facile synthesis of tungsten oxide – Bismuth vanadate nanoflakes as photoanode material for solar water splitting, Int. J. Hydrogen Energy. 42 (2017) 3423-3430. **IF = 3.58**
22. H.M. Badawi, **Ibrahim Khan**, A comparative study of the vibrational spectra of the anticancer drug melphalan and its fundamental molecules 3-phenylpropionic acid and l-phenylalanine, J. Mol. Struct. 1109 (2016) 171–178. **IF = 1.75**
23. H.M. Badawi, **Ibrahim Khan**, A Study of the Molecular Conformations and the Vibrational, 1H and 13C NMR Spectra of the Anticancer Drug Tamoxifen and Triphenylethylene, J. Mol. Struct. 1117 (2016) 22-29. **IF = 1.75**
24. K. Saeed, **Ibrahim Khan**, Preparation and characterization of single-walled carbon nanotube/nylon 6, 6 nanocomposites, Instrum. Sci. Technol. 44 (2016) 435–444.

25. M. Mansha, A. Qurashi, N. Ullah, F.O. Bakare, **Ibrahim Khan**, Z.H. Yamani, Synthesis of In2O3/graphene heterostructure and their hydrogen gas sensing properties, Ceram. Int. 42 (2016) 11490-11495. **IF = 2.99**
26. V. Avasare, Z. Zhang, D. Avasare, **Ibrahim Khan**, A. Qurashi, Room-temperature synthesis of TiO_2 nanospheres and their solar driven photoelectrochemical hydrogen production, Int. J. Energy Res. 39 (2015) 1714–1719. **IF = 2.60**
27. K. Saeed, **Ibrahim Khan**, Preparation and properties of single-walled carbon nanotubes/poly(butylene terephthalate) nanocomposites, Iran. Polym. J. 23 (2014) 53–58. **IF = 1.42**
28. **Ibrahim**, K. Saeed, Carbon nanotubes-properties and applications: a review, Carbon Lett. 14 (2013) 131–144. **IF = 2.11**

3.2 Publications under review

1. Dmitri Spetter, Muhammad Nawaz Tahir, **Ibrahim Khan**, Ahsanulhaq, Qurashi, Hao Lu, Tobias Weidner, Wolfgang Tremel, Solvothermal Synthesis of Molybdenum-Tungsten-Oxides and Their Application for the Photoelectrochemical Hydrogen Evolution Reaction, **(under review)**
2. **Ibrahim Khan**, Muhammad Qamaruddin, Oluwole Olagoke Ajumobi, Saheed Adewale Ganiyu, Zain H. Yamani, Ahsanulhaq Qurashi, Synthesis and characterization of Sulfur Incorporated Ceria-Titania (S-$CeTiO_{4-X}$) Nanocomposites for Enhanced Solar Driven Electrochemical Water Splitting **(under review)**

3.3 Patents

1. **Ibrahim Khan,** Ahsanulhaq Qurashi: Synthesis of Tin oxide nanoarrays by anodization method. US Patent and Trademark Office, Oblon Ref: 504362US (**Submitted**)
2. **Ibrahim Khan,** Ahsanulhaq Qurashi: Synthesis of In_2O_3 Nanoarrays by Electrochemical anodization technique. US Patent and Trademark Office, Oblon Ref: 504373US (**Submitted**)
3. Shahid Ali, Safyan A. Khan, **Ibrahim Khan**, Manzar Sohail, Mohamed A. Morsy, "Plasmon Aided $(BiVO_4)_X$–$(TiO_2)_{1-X}$ Ternary Nanocomposites for Efficient Solar Water Splitting" File # 2017-131. (**Submitted**)

3.4 Book Chapters

1. **Ibrahim Khan**, Muhammad Mansha, Jafar Muzamdar: "Polymer Blends" Springer link (**accepted**)

4. Posters, Seminars, and Conferences attended/Proceedings

- **Oral Presentation** on "Pulse sonochemical tailoring of graphitic carbon nitride impregnated niobium oxide (g-C_3N_4/Nb_2O_5) type (II) heterojunctions and its synergetic solar-driven hydrogen generation" in 9th KFUPM student research forum (05/2018), organized by KFUPM.
- **Oral Presentation** on "Sonochemical-assisted *in-situ* electrochemical synthesis of Ag/α-Fe_2O_3/TiO_2 nanoarrays to harness photoelectrochemical energy from water splitting" in 8th KFUPM student research forum (10/2017), organized by KFUPM.
- Attended international conference on sustainable energy technologies arranged by US-PCAS-E (12-13th Sep 2017) in Pakistan and poster presentation on "Newly developed GaON/ZnO heterostructure photoanodes for solar-driven photoelectrochemical water splitting"
- Poster presentation on "Single-step strategy for the development of hybrid GaON/ZnO/FTO photoanodes for enhanced water oxidation" in the department of chemistry KFUPM.
- Participated as a member of organizers team in "The 4th Saudi International Nanotechnology Conference 2016 (SINC 2016)" on 25-26th Oct 2016.
- Attended a conference on "Catalysis for artificial photosynthesis" held by KAUST catalysis center (KCC-KICP) from 1-3 Feb 2016 and poster presentation on "Room temperature synthesis of In_2O_3 and Au-In_2O_3 nanoarrays and their water splitting applications".
- Conference paper Presentation Title "Single-step synthesis of Ag/α.Fe_2O_3/TiO_2 and their water oxidation" in the nano energy conference, Manchester (UK) 1-3 Jun 2015.
- Attended 11th international & 23rd national chemistry conference (INCC-2012), University of Peshawar held on 15-17 November 2012 and poster presentation on "effect of SWNT on the properties of SWNT/PBT nanocomposite".

5. Professional Achievements and Awards

- **First Position in Presenting Research Article** in 9th KFUPM Student Research Forum (05/2018)
- **Poster Award Winner** in International Conference on Sustainable Energy Technologies arranged by US-PCAS-E (09/2017).
- **Poster Award Winner** in Research Poster Day arranged by KFUPM and ACS Arabian Chapter (01/2017).
- **Research Assistant** in NSTIP funded project (awarded by National Plan for Science, Technology, and Innovation (MAARIFAH), entitled: "Fabrication of well-aligned hetero-nanostructured oxide arrays and their graphene nanoarchitectures for solar driven hydrogen production applications" Project code: **13-NAN1600-04**.
- Selected as **Research Associate** in HEC funded project entitled: "*To Study the Effect of SWNTs on the Properties of PBT Polymer*", Project code: **20-1470/R&D/095880**.
- **Gold Medalist** in Academics.

Note:

I confirm that all the information given in the vitae is correct to the best of my knowledge.

(Date 09/05/2018)